Modeling and fabrication of tunable 3D integrated Mirau micro-interferometers

Wei Xu

UNIVERSITE PARIS-SUD

ÉCOLE DOCTORALE : Sciences et Technologies de l'Information des télécommunications et des Système (*STITS*)

Laboratoire: Institut d'Electronique Fondamentale

***DISCIPLINE**: PHYSIQUE*

THÈSE DE DOCTORAT

soutenue le 12/12/2014

par

Wei XU

Modélisation et fabrication de microinterféromètres Mirau accordables intégrés 3D

Modeling and fabrication of tunable 3D integrated Mirau micro-interferometers

Directeur de thèse :	Alain BOSSEBOEUF	Directeur de Recherche CNRS, Univ. Paris Sud

Composition du jury :

Président du jury :		
Rapporteurs :	Tarik BOUROUINA	Professeur (ESIEE, Paris)
	Christophe GORECKI	Directeur de Recherche CNRS (FEMTO-ST, Besançon)
Examinateurs :	Arnaud DUBOIS	Professeur (LCFIO,Palaiseau)
	Veronique BARDINAL	Directeur de Recherche CNRS (LAAS, Toulouse)
	Paul MONTGOMERY	Chargé de Recherche CNRS (Icube, Strasbourg)
	Pierre BLONDY	Professeur (XLIM, Limoges)

Acknowledgements

First of all, I gratefully acknowledge my PhD supervisor, Alain Bosseboeuf, senior CNRS researcher. Thank you for your professional guidance, advices, enormous encouragements, and continuous support of my research progress in this tough subject. Then I would like to thank my parents for their understanding and support of my three years' foreign study, and Pro. Sihai Chen who has guided me to this attractive and competitive research field.

I would like to extend my gratitude to permanent staffs in the 'Microsystems and nanobiotechnologies' group of IEF: Johan Moulin, Emile Martincic, Fabien Parrain, Sylvain Perrot, Philippe Coste, Filippo Fabbri, Marion Woytasik, Elie Lefeuvre, Samson Edmond, Nathalie Isac and Xavier Leroux.

Then I want to appreciate the help from the engineers and technicians of CTU: Benoît Belier, David Bouville, Antoine Martin, Cédric Villebasse, Jean-Luc Perrossier, François Maillard, Fabien Bayle, Marie-Paule Planté, Abdelhanin Aassime and Jean-René Coudeville.

Finally, I also want to thank all the interns, PhDs and post-docs in our research group. It has really been an enjoyable and unforgettable working and learning experience with all of you.

Xu Wei

20-11-2014

Orsay

List of abbreviations

APDL	ANSYS Parametric Design Language
ARDE	Aspect Ratio Dependent Etching
BCB	Benzocyclobutene
BHF	Buffered Hydrofluoric acid
CAD	Computer Aided Design
CCD	Charge Coupled Device
CMOS	Complementary Metal Oxide Semiconductor
CMP	Chemical Mechanical Planarization
DI water	Deionized water
DRIE	Deep Reactive Ion Etching
DSOI	Double Silicon On Insulator
DUV	Deep Ultra Violet
EUV	Extreme Ultra Violet
FEM	Finite Element Method
FFT	Fast Fourier Transform
FTIR	Fourier Transform Infrared Interferometry
FWHM	Full Width at Half Maximum
IEF	Institut d'Electronique Fondamentale
ICP	Inductively Coupled Plasma
LED	Light Emitting Diodes
LPCVD	Low Pressure Chemical Vapor Deposition
LWIR	Long Wavelength Infrared
MEMS	Micro-Electro-Mechanical System
MOEMS	Micro-Opto-Electro-Mechanical System
MWIR	Middle Wavelength Infrared
NIR	Near Infrared
OCT	Optical Coherence Tomography
OPD	Optical Path Difference
PECVD	Plasma Enhanced Chemical Vapor Deposition
RMS	Root Mean Square
SEM	Scanning Electron Microscope
SOI	Silicon On Insulator
TLP	Transient Liquid Phase

TTV	Total Thickness Variation
UV	Ultra Violet

Table of contents

1. Introduction

Initially, Micro-electro-mechanical systems (MEMS) were defined as miniaturized systems integrating electromechanical transductions of the motion or deformation of mechanical parts having dimensions down to the micrometer range [Kaajakari-2009]. They were mainly fabricated by surface or bulk micromachining processes developed with silicon microelectronics technological tools. Along the years, this strict definition was extended to any miniaturized systems with free standing parts which are used for sensing, actuation functions and a broad range of different technologies (glasses, polymers…) and specific fabrication processes have been developed. Since the introduction of MEMS in the 80's, the range of applications and the market of MEMS have largely increased with a burst in the recent years. Microsystems are now combining many engineering disciplines, including mechanics, electrics, thermics, (electro)magnetics, chemistry, micro-fluidics, optics and biology.

Optical MEMS or Micro-opto-electro-mechanical system (MOEMS) constitute a subset of the MEMS family which merges MEMS and micro/nano optics technologies for light manipulation or for optomechanical sensing/actuation [Motamedi-2005]. MOEMS include a wide variety of devices such as optical switches [Toshiyoshi-1996], Digital Micro-Mirror Devices (DMD) [Hombeck-1997], tunable optical devices (lasers, filters…) [Chang-2000], micro-bolometers [Niklaus-2007], etc. These devices have existing and promising applications in optical communication, imaging display, scanning systems and micro-optical platforms.

The device investigated in this thesis is a 3D integrated (multi-wafer) optical MEMS. More precisely it is a tunable Mirau micro-interferometer designed for its implementation in a surface interferometric optical profiler and with the potential application of replacing conventional large-size components. In the following content, we will present the motivation, objective and environment of this project, as well as the organization of the thesis text.

Motivation

MEMS fabrication always needs a precise control of processing conditions and mechanical properties of materials. Characterization of the static and dynamic behavior of fabricated devices is required during various stages of their development process. Optical interferometric profilometry is one of the most widely spread measurement techniques for the characterization of MEMS and released structures because it can provide full-field, non-contact and fast 3D measurements of surface

topography, deformations and vibration modes with high vertical and lateral resolutions [Bosseboeuf-2003]. It can also be used for film thickness, spectral reflectivity mapping, and hermeticity testing of wafer-level packaging [Bosseboeuf-2007]. Among the typical configurations of optical interferometric profilers, Mirau-type is the most widely used in semiconductor field, because it covers a large range of medium magnifications (10× to 50×) which are well suitable for surface topography and micro device characterization.

Conventional Mirau interferometers are fabricated with macroscopic optical and mechanical components, and their Optical Path Difference (OPD) is varied by an external piezoelectric actuator associated with a feedback loop for precise control. Although they have now been maturely commercialized, they still endure the drawbacks of expensive cost, large size and long-time consuming of serial measurements. The replacement of these bulky and heavy macroscopic Mirau interferometers by a miniaturized version is expected to have many potential advantages:

- A more compact volume allowing their operation with larger magnification and shorter working distance objectives;
- a lower cost resulting from batch fabrication;
- an easier adaptation to various wavelength ranges from deep ultraviolet (UV) to near infrared (NIR), while commercial macroscopic interference objectives are essentially only available for the visible range;
- The ability to be implemented in an array for parallel measurements, which could solve the bottleneck of time-consuming serial inspection on large size wafers.

Only very few authors have reported the design and fabrication of integrated Mirau interferometers. Chim, Beck and Kino were the first, more than 20 years ago, to build a partially integrated micro-machined Mirau interferometer [Chim-1990] which was integrated in a microscope and successfully used for surface profiling of resist trenches and integrated circuits [Kino-1990]. Later, they extended the working spectral range to UV light (325 nm) with a specifically developed nitrogen-rich SiN film deposited by Low Pressure Chemical Vapor Deposition (LPCVD) [Chang-1998]. Fabrication of integrated Mirau interferometers was only reconsidered recently by Albero et al. who fabricated an array type of Mirau interferometers to perform static measurement and parallel inspection of MEMS [Albero-2011]. These later Mirau interferometers are based on glass-Si bonding technology and integrate a micro-lens and diffractive optical elements for aberrations correction.

Unlike macroscopic interferometers which are implemented with external actuators, miniaturized interferometers fabricated by MEMS technology are well suitable for the integration of internal actuators. Tunability with an integrated reference mirror is desirable for fast measurement by phase shifting interferometry or low coherence interferometry, because smaller motion inertia and faster scanning speed are expected. The first attempts towards a tunable fully integrated Mirau interferometer are proposed in this work and in an ongoing European project performed by FEMTO-ST institute and Fraunhofer ENAS [VIAMOS]. This project is still under progress, and more details of the differences between these two works can be found in section 2.4. It is worth emphasing our original design of self-aligned vertical electrostatic comb-drive scanner based on double SOI wafer. This allows a large range, bidirectional and symmetric vertical translation of the scanner, which is

essential for low coherence interferometry that needs a large motion range. It is also desirable for micro-interferometer made by 3D hybrid integration because it allows a compensation of interferometer gap variations resulting from any technological defects.

Objective

The target of this thesis was to develop a new tunable 3D integrated Mirau interferometer for its use in a surface optical profiler. This micro-machined interferometer is constituted by two functional elements: a scanning mirror and a beam splitter. The scanning mirror is required to be translated vertically with high accuracy (essentially for phase-shifting interferometry) and with large tunable range (essentially for low coherence interferometry). The whole optical system, especially the beam splitter, should have wide working spectral range, in the NIR, visible and/or (deep) UV ranges. A low response time (at least lower than one video frame time which is normally around 40 ms) and good immunity to exerternal disturbance during operiation are preferred. Due to some possible fabrication defects, the capacity to compensate interferometric gap variation at final nbonding process should also be considered. Finally, with all these requirements a prototype with preliminary characterization was expected to be demonstrated.

Project Environment

This thesis, financially support by China Scholarship Council (CSC), has been carried out in the Institut d'Electronique Fondamentale (IEF), a joint laboratory of Université Paris Sud and Centre National de la Recherche Scientifique (CNRS). The whole research work was conducted in the research team "MN(O)EMS & Instrumentation" within the research department "Microsystèmes et Nanobiotechnologies". The experimental fabrication work was performed in the clean room of Centrale de Technologie Universitaire (CTU) hosted by IEF. Some previous works in the field of MOEMS have been accomplished in this research team, such as the investigation of UV, laser and e-beam 3D lithography processes for micro-optics fabrication, the development of fabrication processes of Si refractive and diffractive micro-lenses, the design of an integrated Schwarzchild micro-objective, the development of concave and convex micro-mirrors fabrication processes for this objective, and the design and partial realization of an array of tunable Fabry-Pérot filters for multispectral imaging [Bertin-2013]. This thesis is a new stage of MOEMS development in the research group.

Organization of thesis content

The whole thesis text is splitted in five chapters. The second chapter will explain the basics of interferometric optical profilers and Mirau interferometers, and will review the state of the art of integrated micro-interferometers. Then the third chapter will present the design and modeling of Mirau micro-interferometers, including optical design, electromechanical design and their links. The fourth chapter will describe the proposed fabrication process, the technological steps tests and the whole fabrication tests of tunable scanning mirrors. Finally the fifth chapter will give the conclusions and perspectives of this thesis work.

2. State of the Art of Mirau Interferometers and their Applications

Introduction

Compared to other types of optical interferometers like Fabry-Pérot, Michelson and Mach Zehnder interferometers, Mirau interferometers have been used for a limited number of applications despite their compactness and their simpler configuration and adjustment. The main application of Mirau interferometers is the building of interference objectives for their implementation in full field 3D optical surface profilometers and related interferometric techniques (vibrometry, optical coherence tomography) . This is also the main application that was targeted in this thesis.

In section 2.1 we will review the basics of interferometric optical profilers and their working principle based on phase shifting interferometry and low coherence interferometry. Two examples of commercial products available in our laboratory are given and listed with their key features.

Conventional interference objectives have three different configurations: Michelson, Mirau and Linnik. Section 2.2 will present the reason of choosing Mirau-type rather than the two other types for the investigations made in this thesis.

Section 2.3 will summarize some recent works on new configurations of macroscopic Mirau interferometers that were developed for more advanced measuring techniques and some specific applications.

Very few attempts were performed to fabricate integrated versions of Mirau interferometers and up to 2014 they were all non tunable and mainly intended for their use with monochromatic light. Section 2.4 will make a survey of these published works.

As the mirror scanner developed in this thesis might be also useful for other micro-interferometers, we will do by a rapid survey of other types of integrated tunable micro-interferometers in the last section of this chapter.

2.1 Basics of Interferometric Optical Profilometry

In this section, we will summarize the main characteristics and mode of operation of an interferometric optical profilometer. More details can be found in various papers and books [Bosseboeuf-2003] [Malacara-2007] [Hariharan-2003].

Interferometric optical profilers are widely used optical instruments for the measurement of surface height 3D profiles with high vertical and lateral resolution. They offer the advantage of non-contact measurement, what is essential for fragile or vulnerable samples such as totally released MEMS structures or biological living cells. They are highly performing for surface 3D topography mapping and vibrating mode characterization, with a vertical resolution in the (sub)nanometer range and a lateral resolution down to a fraction of micrometer. Generally its resolution is already high enough for most of applications, and the field view of the microscope and magnification required are always the most important considerations during system design and determination.

Figure 2-1 shows the typical configuration of an optical profilometer based on a Michelson interference objective. It is basically an optical microscope equipped with a CCD or CMOS camera and a monochromatic or broadband light source. The light from lighting system is firstly reflected by a beam splitter and then is focused on the sample through an interference objective. Reflected light will return and transmit through a long optical tube, and is finally imaged on the top camera.

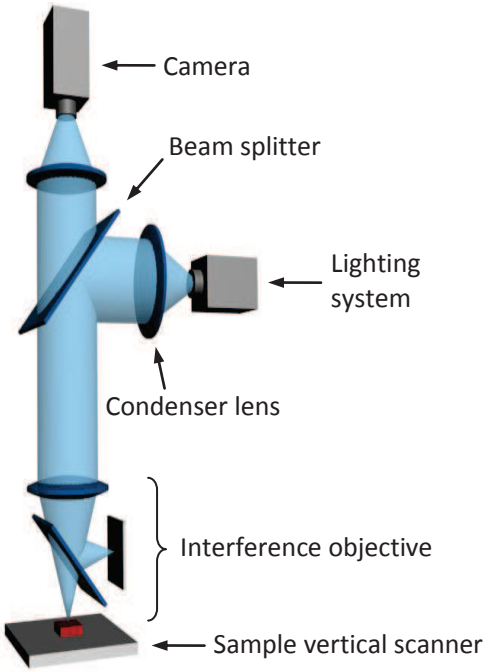

Figure 2-1. Schematic drawing of an interferometric optical profilometer, in the case of a Michelson interference objective and a sample vertical scanner.

The main difference between this interferometric microscope and a classical optical microscope is the use of an interference objective. A more detailed drawing of one Michelson interference objective is shown in Figure 2-2. A large volume cubic beam splitter placed in the middle of optical path splits the incident light into two beams by amplitude division. These two light beams, reflected by

the sample and reference mirror, will propagate along almost the same optical distance, and are re-combined by a beam splitter. The resulting interference patterns are generated by superimposition of these two lights beams, and can be visualized with oculars or imaged on the camera. Thus the height difference between the sample and reference mirror will contribute to the intensity map of these interference patterns. Generally the sample, the interferometer and/or the reference mirror can be tilted to compensate the tilt between sample and reference mirror wavefronts.

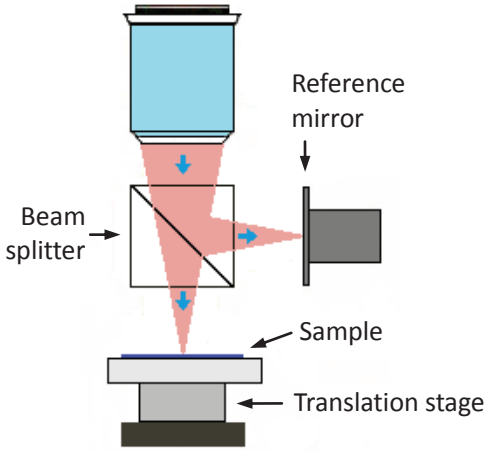

Figure 2-2. Michelson interference objective implemented in the interferometric optical profilometer.

Two examples of interference patterns recorded at IEF with an optical profilometer are shown in Figure 2-3. The first one was recorded on a pressurized metallic membrane with a curved surface. Observed fringers are contour lines of equal height with fringe spacing equal to half mean effective wavelength $\lambda_{meff}/2$ which slightly depends on numerical aperture of the objective. The other one corresponds to a tilted, free-standing, flat and square silicon nitride membrane fabricated on a silicon wafer. The slight discontinuity of the fringe patterns at the membrane periphery is due to the difference of reflection phase shifts between the silicon nitride membrane suspended in air and the silicon nitride film deposited on silicon. .

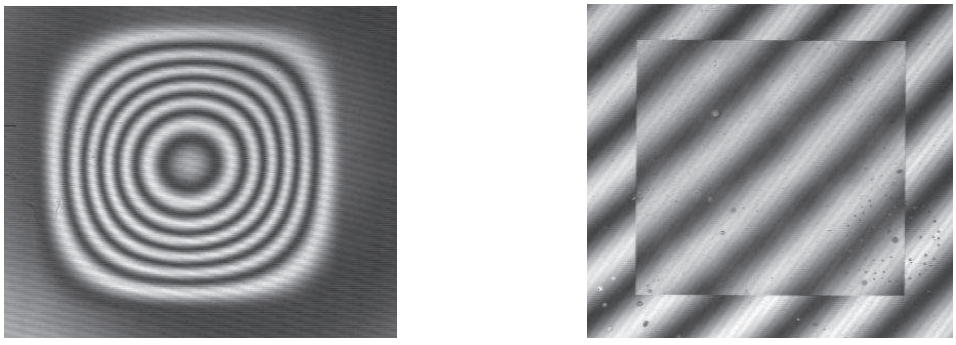

a) b)

Figure 2-3 Fringe patterns recorded a) on a pressurized metallic membrane and b) on a transparent silicon nitride membrane on silicon.

After recording of the fringe sample patterns by the camera, an analysis of these interferograms needs to be performed to extract height variation information. This can be achieved on a single interferogram by using FFT analysis or by other techniques, but the most common procedures are phase shifting interferometry and low coherence interferometry.

Phase shifting interferometry

Phase shifting interferometry requires several interferograms recorded for different values of the Optical Path Difference (OPD) between the two arms of the interferometer [Creath-1988]. These values are typically equidistant fractions of the fringe spacing. Different values of OPD can be obtained either by vertical translation of the sample, by translation of the interferometer or by translation of the reference mirror. This translation is usually achieved with a macroscopic piezoelectric actuator integrating a capacitive or a strain gage position sensor to obtain (sub)nanometric resolution in a close loop configuration.

These interferograms are the result of the cross correlation of the light beam reflected from the sample and from the reference mirror. We can define the wavefronts of the sample light and reference light by, respectively:

$$\omega_s(x,y)=a_s(x,y)e^{i\phi_s(x,y)} \tag{2.1}$$

$$\omega_r(x,y)=a_r(x,y)e^{i\phi_r(x,y)} \tag{2.2}$$

where $a_s(x,y)$ and $a_r(x,y)$ represent wavefront amplitude, $\phi_s(x,y)$ and $\phi_r(x,y)$ represent the corresponding wavefront phase. The interference pattern can then be described by the following equation:

$$\begin{aligned} I(x,y) &= \left|\omega_s(x,y)+\omega_r(x,y)\right|^2 \\ &= \left|a_s(x,y)\right|^2+\left|a_r(x,y)\right|^2+2a_s(x,y)a_r(x,y)\cos\left[\phi(x,y)\right] \\ &= I_s(x,y)+I_r(x,y)+2\sqrt{I_rI_s}\cos\left[\phi(x,y)\right] \end{aligned} \tag{2.3}$$

in which $\phi(x,y)=\phi_s(x,y)-\phi_r(x,y)=\Delta\phi(x,y)+\delta(t)+\Delta\varphi_{rs}(x,y)$ (2.4)

$\delta(t)$ is the time-varying phase shift introduced between two light beam by external actuator, and $\Delta\varphi_{rs}(x,y)$ is the reflection phase shift difference between the sample and the mirror at position x,y. $\Delta\phi(x,y)$ represents the wavefront variations produced by the surface height profile under test, and can expressed as:

$$\Delta\phi(x,y)=4\pi h(x,y)/\lambda \tag{2.5}$$

Thus by phase demodulation, the 3D surface profile $h(x,y)$ of the measured sample can be retrieved. Several methods employing different algorithms and different numbers of phase shifts can be used for this phase demodulation. But at least 3 phase shifts must be applied and a larger number is preferable to limit errors due to phase steps inaccuracies. These phase shifts are typically an integer fraction of 2π and must be controlled with (sub)nanometer accuracy to get high accuracy measurements of the surface profile.

Let us take as an example the case of a four-frame phase shifting algorithm, where phase shifts are equal to 0, $\pi/2$, π and $3\pi/2$. An alternative representation for equation 2.3 could be rewritten as:

$$I(x,y) = I_s(x,y) + I_r(x,y) + 2\sqrt{I_s(x,y)I_r(x,y)}\cos\left[\Delta\phi(x,y) + \Delta\varphi_{sr}(x,y) + (n-1)\pi/2\right] \quad n = 1,...,4 \tag{2.6}$$

In this case, the total phase difference could be calculated as [Hariharan-2003]:

$$\tan(\Delta\phi) = \frac{I(3\pi/2) - I(\pi/2)}{I(0) - I(\pi)} \tag{2.7}$$

Another common used algorithm adopts five different frames, in which n=-2, -1, 0, 1 and 2. The corresponding formula for phase map could be expressed as:

$$\tan(\Delta\phi) = \frac{2I(-\pi/2) - I(\pi/2)}{I(-\pi) - 2I(0) + I(\pi)} \tag{2.8}$$

However, in all cases the obtained phase map is wrapped within the range of 0-2π. A problem so called 2π phase ambiguities arises for determining the number of 2π to be added to the raw values to obtain the actual phase difference. Thus only surfaces with quasi continuity (steps height < λ_{meff} /2) between adjacent pixels can be successfully unwrapped to get its profile. A vertical resolution and repeatability below 0.5 nm can then commonly be achieved. The vertical measurement range is limited by the depth of focus of the objective or eventually by the coherence length of the light source. It is typically in the 1-60 μm range.

Low coherence interferometry

For the profiling of discontinuous surfaces or of continuous surfaces with large height variations, low coherence interferometry is generally used although multiple wavelengths interferometry could also be used. With a broadband light source, the intensity at any position in the image plane can be written as:

$$I(x, y) = I_s(x, y) + I_r(x, y) + 2\sqrt{I_r(x,y)I_s(x,y)}\, E(x, y, h - z)\cos\Delta\varphi'(x, y, z) \tag{2.9}$$

and

$$\Delta\varphi' = \frac{4\pi(z-h)}{\lambda} \tag{2.10}$$

where *z* represents the moving distance brought by the external actuator, *h* represents the height information of the measuring sample, and *E* is a coherence envelope function that depends on reflected light source spectrum.

This technique relies on the fact that for a low coherence light source, like a white light source, the fringe intensity will reach its maximum when Optical Path difference (OPD) of the two optical beams is equal to zero, since all light components at different wavelengths have their maxima at this position. Then the fringe intensity decreases fastly for positive or negative OPD and have smaller amplitudes at other peaks. Figure 2-4 shows a typical variation of the fringe intensity surrounded by its envelopes as a function of the OPD.

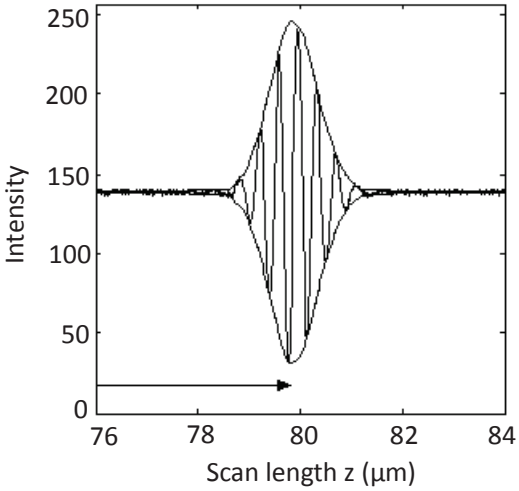

Figure 2-4. Pixel intensity recorded as function of sample translation with a white light scanning optical profilometer on a Al/Si sample.

The surface topography $z(x,y)$ can then be determined by varying the OPD and recording for each pixel the ODP value for which the envelope of fringe pattern $I(x,y,z)$ is maximum. The vertical resolution of low coherence interferometry depends on the width of the light source spectrum and on the motion accuracy of the vertical scanner. It is typically in the 3-10 nm range and can be reduced below 1 nm by combining fringe amplitude detection and phase shifting techniques, but in that case the measurement become more affected by reflection phase shift variations. The vertical measurement range is equal to the scan range less about twice the coherence length. In commercial systems it is typically in the 100 µm-1 mm range.

Two examples of 3D profiles measured by phase shifting interferometry and white light interferometry are shown in Figure 2-5 below. The first profiler is measured on a hollow surface etched by KOH solution using phase shifting interferometry, and the latter is measured on MEMS resonator by white light interferometry.

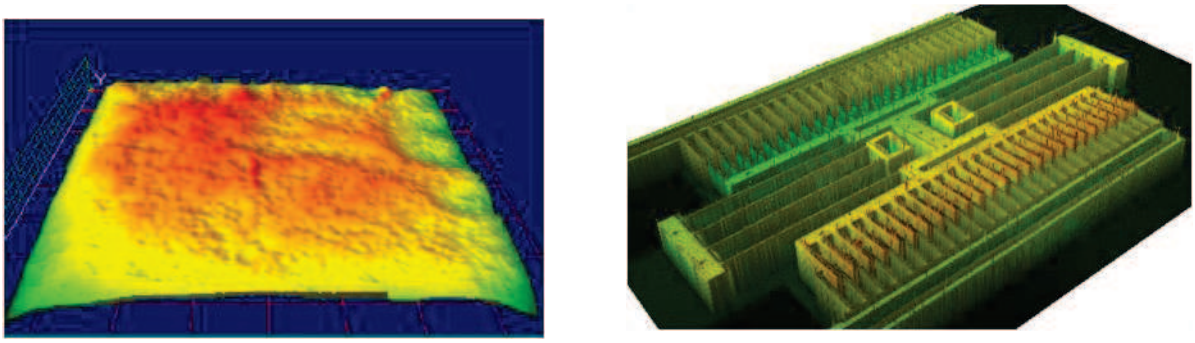

a) Hollow surface after KOH etching, depth 420 µm, roughness r_q=15 nm;

b) MEMS resonator (poly MUMPS).

Figure 2-5. Two examples of 3D profiles measured by (a) phase shifting interferometry and (b) white light interferometry.

Then, the pictures and key features of two versions of optical interferometric profilometers-vibrometers available at IEF and commercialized by Fogale Nanotech Company are listed in Table 2-1 below. Finally let us emphasize that interferometric profilometers can also be used for full field 3D

vibration measurements by using time-averaged interferometry or stroboscopic interferometry with similar lateral and vertical resolutions [Petitgrand-2004].

Table 2-1 Commercial optical interferometric profilometers

	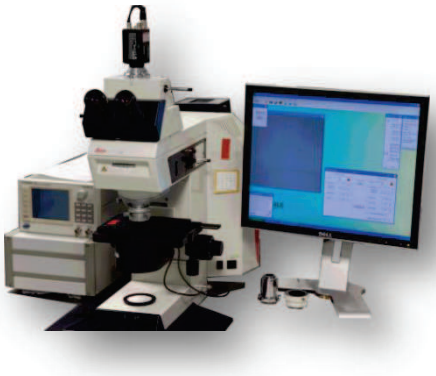 **Microsurf 3D, Fogale Nanotech** (IEF Prototype version)	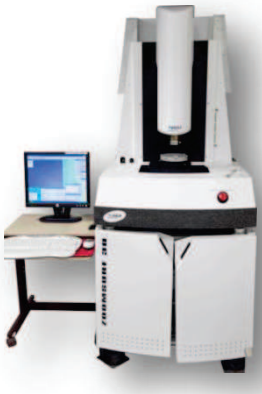 **ZoomSurf 3D**
Light sources	Two among Na lamp, tungsten halogen or continuous or pulsed LED source (red, green, amber) (Manual adjustment)	Red and white continuous or pulsed LED sources (automated)
Objectives	5×, 10×, 20×, 40× 1×, 0.63× or 0.5× imaging lens	5×, 10×, 20×, 50×, compensated for glass window + automated zoom 0.35× - 1.6×
OPD variation	Piezoelectric sample translation with capacitive sensor	Objective piezoelectric translation with capacitive sensor
X,Y,Z stage	Manual sample stage X,Y (Sample stage): 60 mm × 60 mm Z (Sample stage): 50mm translation	Motorized sample stage X,Y (Sample stage): 200 mm × 200 mm Z (objective): 150mm translation Vacuum chamber or probe station can be added
Vertical resolution	Down to 0.3 nm	Down to ~0.3 nm
Vertical measurement range	120 µm	150 µm
Lateral resolution	0.5-5 µm	0.36-9.5µm
Field of view	up to ~1.5mm	60 nm × 80 nm to 5.4 mm × 7.2 mm

2.2 Different Types of Interference Objectives

According to measuring principle and magnification needed, classical optical interferometric microscopes are mainly based on three different configurations of interference objectives: Michelson, Mirau and Linnik [Malacara-2007], as shown in Figure 2-6 below. All these objectives are working on similar interference principle as described in previous section. A beam splitter (cube structure or membrane-based) split the incident light into two identical parts, which are reflected by the sample and by a reference mirror, respectively. Then these two light beams will interfere and their resulting interference images are collected by a camera and used for further computer-based analysis.

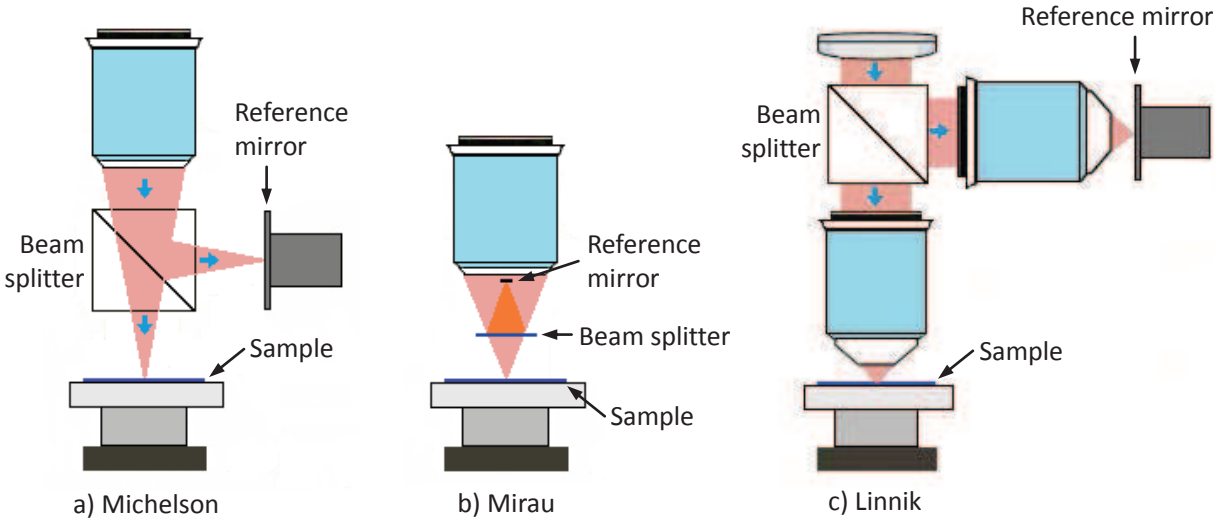

Figure 2-6: Main configurations of interference objectives used in optical profilometers.

Michelson interference objective (Figure 2-6a), which has a cube beam splitter and a lateral reference mirror inserted between the objective and sample, is typically used for small magnifications (<10×), since a large working distance is required for the insertion of these optical components. For magnifications up to 50×, a more compact Mirau interference objective (Figure 2-6b) is adopted instead. This configuration employs a semi-transparent plate serving as a beam splitter and a reference mirror placed parallelly in the incident optical path. But the reference mirror would obscure too much incident light, if the magnification became even larger (>50×). Then in this case, a Linnik configuration (Figure 2-6c) must be used. In the Linnik configuration, two identical objectives are respectively placed in the sample arm and in the reference mirror arm of the interferometer. But drawbacks brought by this use of two objectives are consequently a large volume, a difficult interferometer adjustment and possibly a larger sensitivity to ambient disturbances.

Among the three configurations described above, the Mirau interference objective is the most widely used in semiconductor field, because it covers a large range of medium magnifications (10× to 50×) which are well suited for surface roughness and micro devices characterization. In addition, its simpler and planar configuration is favorable for its miniaturization by using MEMS technologies. It can be easily converted to a stack of multi-wafers (3D integration) which constitute different components of the objective (micro-lens, beam splitter and MEMS actuator). Another great interest for integrated Mirau interferometer is the possible development of array-type Mirau matrix which is suitable for parallel measurements. In this case, the Mirau matrix can be designed into two different

types: mirror array with a common scanner and mirror array with individual scanners. The first conception is easier to be modulated and suitable for measurement of sufficiently flat surface, and the latter has more adjustment flexibility and consequently more difficult to be modulated.

Based on the advantages and potentials of Mirau interferometer listed above, we will focus our investigation on the miniaturization work of this interferometer, and develop its application in surface topography measurement.

2.3 Recent Research Development on Macroscopic Mirau Interferometers

Macroscopic Mirau interferometers for the visible wavelength range are commercialized and widely used for a long time for their implementation in non-contact 3D profiling tools. Recently new versions of Mirau interferometers were developed for polarization interferometry, immersion interferometry and for other spectral ranges.

Polarization Mirau interferometry

Conventional Mirau interferometer divides the illuminating light into two parts (reference beam and testing beam), then re-combine them and record their interference fringe patterns. A polarization-based improvement of it, namely Polarization Mirau Interferometer (PMI) is constructed by introducing polarizers and waveplates in the optical path and by polarizing two divided light beams orthogonally. A schematic diagram of a PMI is shown in Figure 2-7. Many benefits could be brought by PMI such as achromatic phase shifting, equalization of two light beam intensities and simultaneously acquisition of different interference patterns.

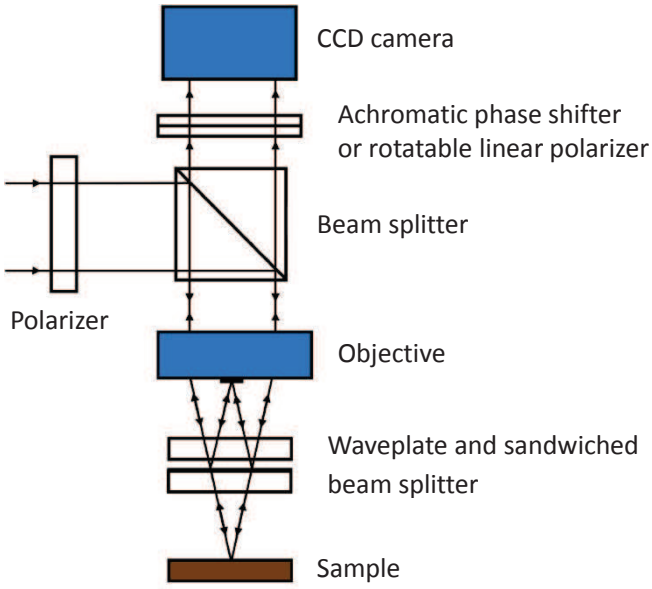

Figure 2-7. Schematic diagram of a polarization Mirau interferometric profiler.

Firstly, PMI could implement achromatic phase shifting which facilitates and improves the use of phase shifting in the white light interferometry [Schmit-2007]. Standard Mirau interferometer needs to record interferograms with arbitrary phase shifts that are introduced by changing of Optical Path Difference (OPD). However, these phase shifts $\phi = 2\pi nd/\lambda$, varies with the reciprocal of wavelength. To overcome this problem, a phase shifter operating on the geometric (Pancharatnam) phase was installed and placed at the output beam to produce phase shift that are independent of wavelength. The two waveplates shown in Figure 2-7 are replaced by two achromatic $\lambda/4$ retarders, and the upper surface of second retarder is coated with 50% reflecting film to functionalize as a beam splitter. The principal axis of first retarder is set parallel to the polarization direction of incident beam (azimuth 0°), while the second retarder is set with its principal axis at 45° (azimuth 45°). With this arrangement, the beam reflected back by the beam splitter remains its polarization unchanged, and the beam transmitted

through the beam splitter emerges with its polarization rotated by 90°. Then another $\lambda/4$ plate with its principal plane set at 45° followed by a rotatable linear polarizer can be placed at the output beams (at the position of achromatic phase shifter shown in Figure 2-6). Rotation of the polarizer through an angle θ introduces a phase difference of 2θ between the two beams, thus acts as an achromatic phase shifter.

Secondly, PMI allows the adjustment of the intensity of two light beams (reference beam and testing beam) to maximize the interferometric fringe contrast [Tapilouw-2013]. A.M. Tapilouw et al. have developed a polarization Mirau interferometer that can work with white light interferometry, while other researchers are constrained with quasi-monochromatic light source. Their main novelty is the home-made reflective-type waveplate fabricated by electron beam evaporation (Ta_2O_5/Ag/Ta_2O_5) on a BK-7 substrate [Jen-2012]. This waveplate can rotate the polarization of incident light by 90° with a conversion efficiency exceeding 0.9 (simulated) or 0.80 (measured) for a light incident angle ranging from 0° to 12° at wavelengths between 450 and 700 nm. By using this waveplate and placing a rotatable linear polarizer in front of the imaging camera, the intensity of each light beam can be adjusted to find the maximum contrast of interferograms, thus to improve measurement accuracy of the whole system.

Thirdly, PMI enables the simultaneous acquisition of different interference patterns [Lyulko-2013] Instead of collecting time-sequential multi phase shifted interference patterns, these images can be recorded simultaneously by spatially separated light beams. Their phase differences are brought by former mentioned polarization elements and waveplates. Main advantage of this implementation is its vibration-insensitive property thanks to this simultaneous imaging.

Immersion Mirau interferometry

Optical coherence tomography (OCT) is increasingly used in cell biology to obtain a 3D tomography image without invasive effect. Mirau interferometers which are compact and have a sufficient high resolution are well suitable for this task. Standard Mirau interferometers are only designed to work in air, and will suffer from poor resolution and degradation of depth resolution when employed for the measurement of biological sample preserved in liquid. Immersion Mirau Interferometry (IMI) was developed to solve these problems [Montgomery-2010]. The only difference between a standard Mirau interferometry and IMI is the working medium of the interference objective. Figure 2-8 shows the schematic drawing of the immersion Mirau interferometric objective where both the test light beam and the reference light beam are propagating in the same liquid.

S.H. Lu et al. have developed a water immersed Mirau interference microscope (Magnification 10×, NA 0.3) and demonstrated its use for full-field optical coherence tomography measurement [Lu-2013]. Their light source was chosen as a near infrared LED with a central wavelength of 840 nm and spectral half width of 50 nm. Final achieved axial resolution of the system is approximately 4.7 μm, and its imaging area is 540 μm× 500 μm. Furthermore, O.V. Lyulko et al. have also developed their own IMI, and even modified it to get a vibration-insensitive apparatus called Simultaneous Immersion Mirau Interferometry (SIMI) [Lyulko-2013]. Both the concept of polarization Mirau interferometry and immersion Mirau interferometry were adopted and combined together to establish this apparatus. A custom interferometric attachment compatible with a threaded Leica N PLAN objective (Magnification 50×, NA 0.5) was designed, constructed and successfully used in the experiment.

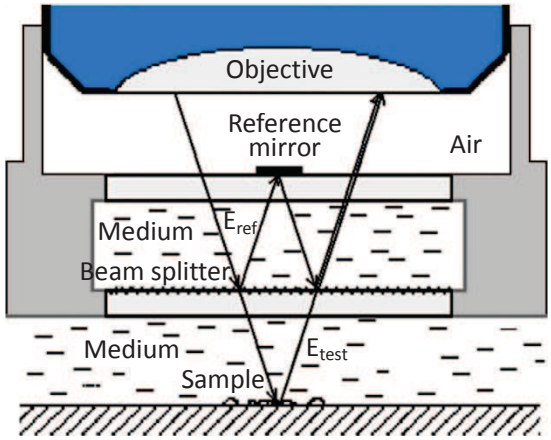

Figure 2-8. Schematic diagram of an immersion Mirau interference objective.

Extension of the working spectral range

Commercial macroscopic optical interferometers are essentially only available for the visible range. Extending the working spectral range to deep ultra violet (DUV) and near infrared (NIR) is also very interesting.

Since the lateral resolution of optical imaging instrument is limited by its operating wavelength, extending the working spectral range to UV or even DUV for Mirau interferometry is attracting to obtain higher resolution [Montgomery-1999]. K. Hamamoto et. al. have constructed an Extreme Ultra Violet (EUV) Mirau interference microscope (13.5 nm) used for inspection of lithography mask for next generation lithography (EUVL) [Hamamoto-2005]. This microscope is composed of Schwarzschild optics (Magnification 30×, NA 0.3), a Mirau interferometer, an X-Y sample stage and an imaging system, as shown in Figure 2-9. Its test results of microscope images were only given without the Mirau interferometer.

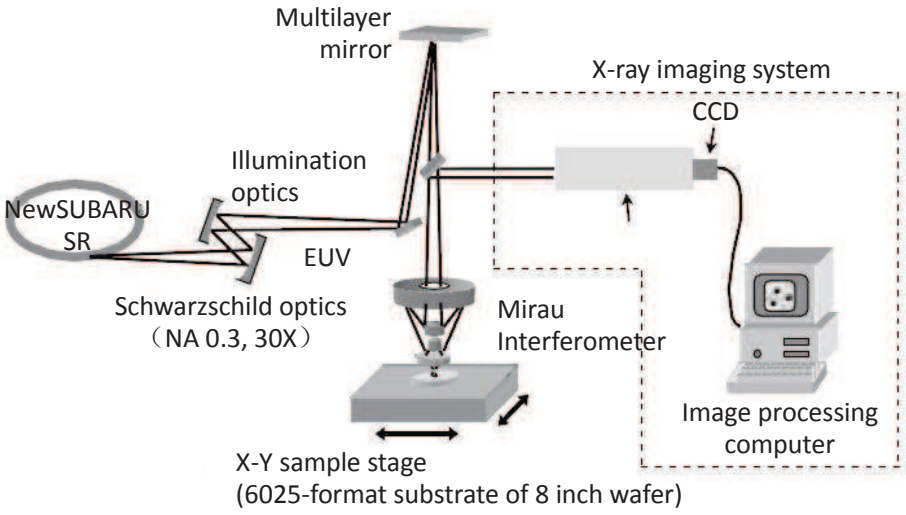

Figure 2-9. Configuration of an EUV interferometric microscope.

The building of a DUV optical profilometer had also been launched in our research group in 2008. A macroscopic 100× DUV Linnik interferometer had been designed and fabricated and part of the

optomechanics of this DUV profilometer had been realized, but this project is in standby because of budget and working force issues.

Likewise, since silicon is transparent for wavelength above 1.1 μm, NIR optical profilometry would also be very interesting notably for buried interface profiling in silicon technology or for the measurement of deformations or vibrations of Si wafer-level packaged MEMS [Montgomery-1997]. X.J. Chou et al. have built a Linnik interferometer using medium objectives (Magnification 40×, NA 0.65) and a near infrared light source with 1127 nm center wavelength and 200 nm bandwidth [Chou-2010]. With this apparatus, internal profile of GaAs microstructures was successfully measured after transmitting through about 100 μm thickness GaAs layer. Notably, there are also some attempts trying to measure buried interface under a transparent layer by using white light interferometry [Benhaddou-2000].

For the same purpose, a large field of view (up to 30 mm) multispectral optical profilometer able to work in visible and NIR range has been built recently in our research group in the frame of the joint lab Metro3D with Fogale Nanotech Company. Preliminary tests in the NIR range have been achieved.

2.4 Research Development on Integrated Mirau Interferometer

Unlike macroscopic Mirau interferometers, very few authors have reported the design and fabrication of integrated Mirau interferometers. Chim, Beck and Kino were the first, more than 20 years ago, to build a partially integrated micro-machined Mirau interferometer [Chim-1990] [Kino-1990] [Chim-1991]. A schematic drawing of their interference microscope is shown in Figure 2-10a. The reference mirror holder was integrated by using a single membrane technology on silicon. A silicon nitride membrane (thickness 100 nm) supporting the thin film mirror was fabricated by backside anisotropic and selective etching of the Si wafer in a KOH solution. A cross section drawing of this device is shown in Figure 2-10b. Then this interferometer was integrated in a microscope and successfully used for surface profiling of resist trenches and integrated circuits.

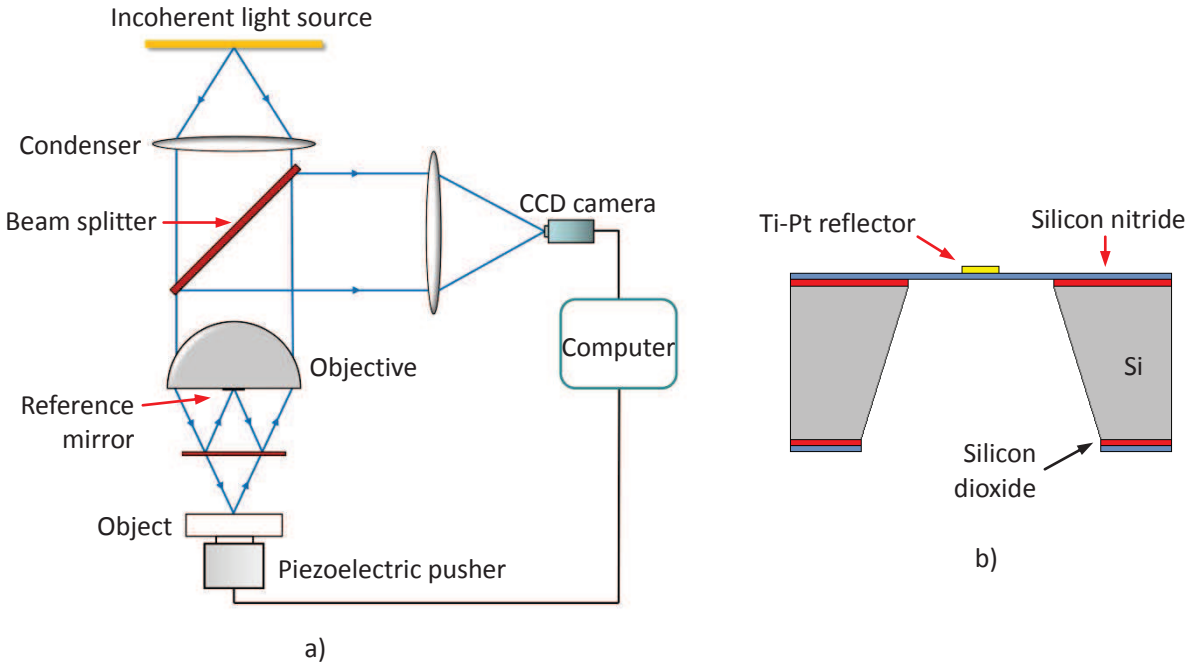

Figure 2-10. (a) Schematic of an interference microscope with a micro-machined Mirau interference objective, (b) cross section drawing of the micro-fabricated mirror of the Mirau interferometer.

Later, Chang and Kino have reported their results on the building of a 325 nm Mirau interference microscope [Chang-1998]. The integration of their micro-fabricated interferometer and an UV objective lens (NA 0.9, Working Distance=200 μm) is shown in Figure 2-11. In this figure, the diamond-shaped reference mirror is suspended by four narrow silicon nitride strips and coated with an aluminum film with high reflectivity. The beam splitter with more than 95% UV transparency is fabricated on another Si wafer by deposition of a nitrogen-rich SiN film (thickness 50 nm, area 3 mm × 3 mm) by Low Pressure Chemical Vapor Deposition (LPCVD) and backside release by Si etching [Chang-1997]. A fully integrated Mirau interferometer is obtained by bonding the two wafers.

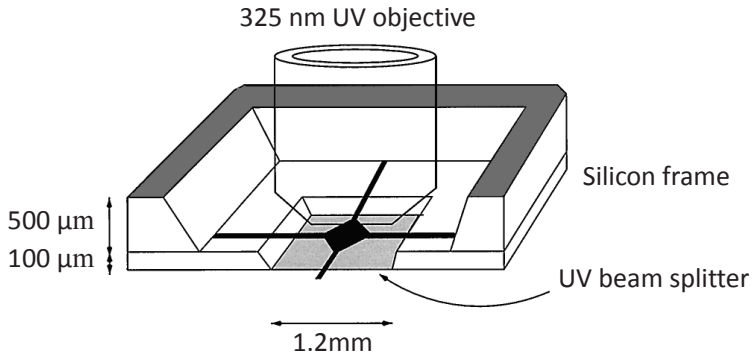

Figure 2-11. Schematic drawing of an integarated Mirau interferometer integrated with an UV objective lens.

Fabrication of integrated Mirau interferometers was only reconsidered recently by Albero et al. in FEMTO-ST institute (Besançon, France). This first work was performed in the frame of an Europe project named SMARTIEHS to develop a novel interferometric test station for massive parallel inspection of MEMS production [Gastinger-2009]. In this concept, two different interferometers: a low coherence interferometer based on Mirau configuration [Albero-2011] and a laser interferometer based on Twyman-Green [Oliva-2012], were both implemented for different functionalities. The Mirau interferometer is specialized in static measurements, while Twyman-Green interferometer is used for dynamic characterizations. The schematic view of the proposed Mirau interference microscope is shown in Figure 2-12. Interferometer surrounded in the dashed box was fabricated principally by employing a glass-Si bonding technology as shown in Figure 2-13. Prior the bonding, microlenses were formed by photoresist reflow on glass wafer or thermal reflow of glass in silicon mould and Diffractive Optical Elements (DOE) were fabricated by variable dose laser lithography to correct optical aberrations of the microlens [Gorecki-2011].

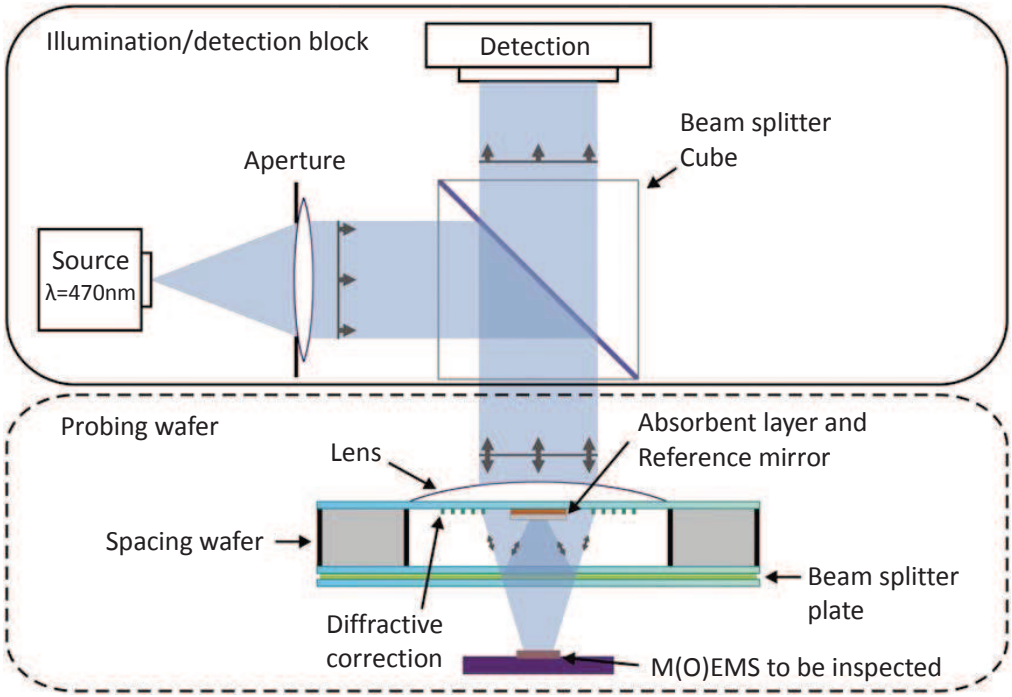

Figure 2-12. Schematic view of Mirau interference microscope investigated in the SMARTIEHS European project.

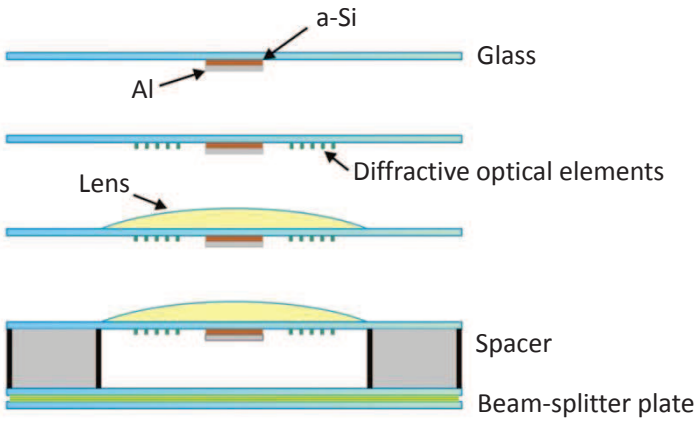

Figure 2-13. Fabrication process the integrated Mirau interferometer in SMARTIEHS project.

Recently, in the frame of another European project (VIAMOS), FEMTO-ST institute in collaboration with Fraunhofer ENAS investigates array-type Mirau-based Optical Coherence Tomography (OCT) microsystem used for early diagnosis of skin cancer [Lullin-2014]. The whole system can work on heterodyne interferometry with the incident light sweeping on wavelength introduced by a Fabry-Pérot interferometer [Krauter-2014], and phase shifting interferometry with the integration of a vertical moving scanner. The schematic drawing of the interferometer and more detailed view of Mirau block are shown in Figure 2-14 and 2-15 respectively.

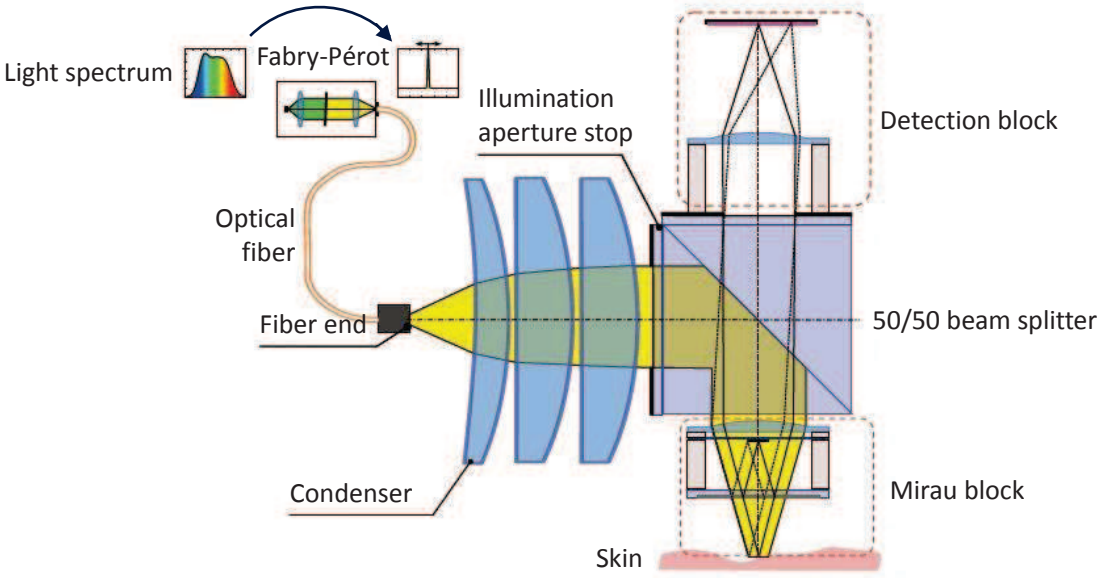

Figure 2-14. Schematic layout of the interference profilometer proposed in VIAMOS project.

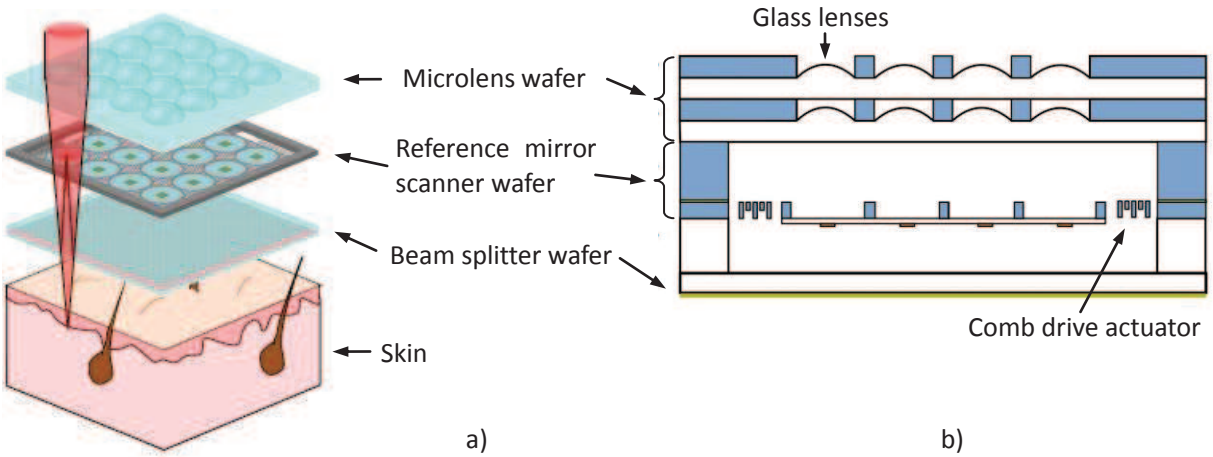

Figure 2-15. Schematic drawing of the tunable Mirau interference objective investigated in VIAMOS project.

The general 3D architecture of the tunable Mirau interferometer has some similarities with the one investigated in this thesis but with some noticeable differences: the scanner investigated in FEMTO-ST is mainly intended for parallel phase shifting interferometry, so the scanner range is 0-1.5 µm , and it was designed to simultaneously translate an array of mirrors. We will see that the scanner investigated in this thesis is intended for a single mirror and has a translation range of ±20µm suitable for both phase shifting and for low coherence scanning interferometry. The fabrication technologies investigated are also very different (Figure 2-16a). In FEMTO-ST project, the mirrors are supported by glass membranes fabricated by Si-glass wafer bonding while there are free-standing in our design. Likewise, the scanner investigated at FEMTO-ST uses low range unidirectional vertical electrostatic comb drives in SOI technology while we will see that our design is based on bidirectional vertical combs in double SOI technology. Finally the beam splitter is the VIAMOS project is made from a glass wafer while our design is based on a dielectric multilayer membrane.

To our knowledge the project above and the work done in this thesis are the only and first attempts to build integrated tunable Mirau interferometers.

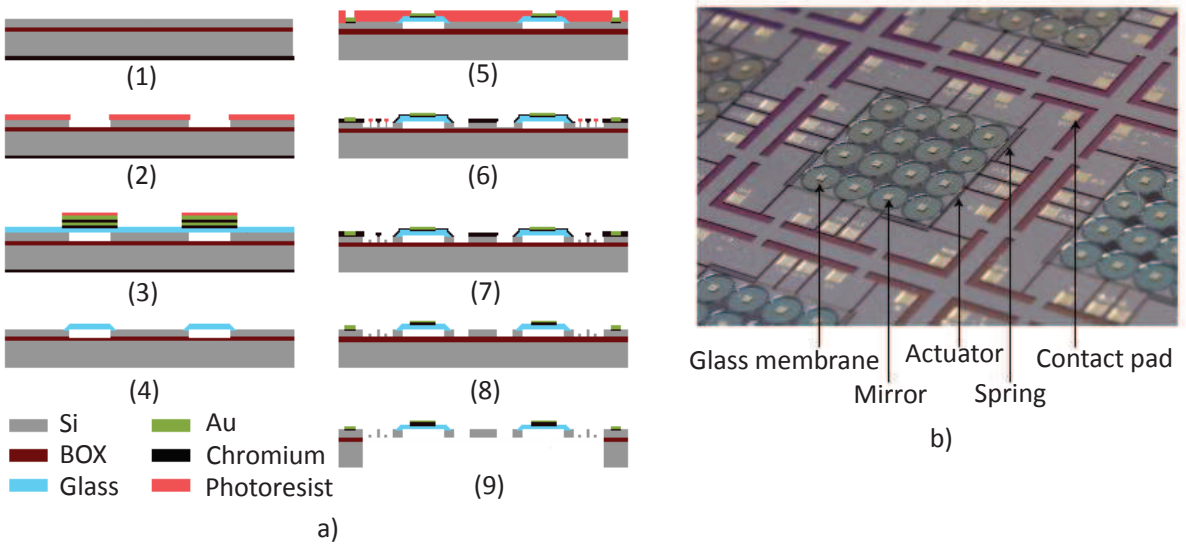

Figure 2-16. (a) Process flow chart and (b) picture of their integrated tunable Mirau interferometer array.

2.5 Other Tunable Micro-Interferometers

Beside the Mirau interferometer discussed above, there are also many other micro-interferometers that were investigated and developed by researchers worldwide. Here we will only review several representative examples to present research progress in neightbouring fields.

Fabry-Pérot interferometers

Fabry-Pérot interferometers are believed to be one of the most widely investigated micro-interferometers. They have various applications in optical filters [Tran-1996], spectrometers [Neumann-2008] [Ebermann-2010] and sensors [Wei-2008]. Most of the Si-wafer-based Fabry-Pérot interferometers were out-of-plane fabricated by surface micro-machining technology [Keating-2007] [Milne-2007] or bulk micro-machining technology [Neumann-2009], while there are still few examples realized by in-plane structures [Masson-2010] [Gelais-2009]. One of the leading products developed by a German industrial company InfraTec GmbH is shown in Figure 2-17. Several different types of micro-spectrometers were fabricated based on hybrid integration of a pyroelectric detector and a micro-machined Fabry-Pérot interferometer (FPI), which cover the spectral range of Middle Wavelength Infrared (MWIR, 3-5 μm) [Neumann-2008] [Neumann-2009] or Long Wavelength Infrared (LWIR, 8-11 μm). The discrete device of FPI was fabricated by bulk micro-machining approach through bonding of two structure wafer with the aid of intermediate SU8 layer.

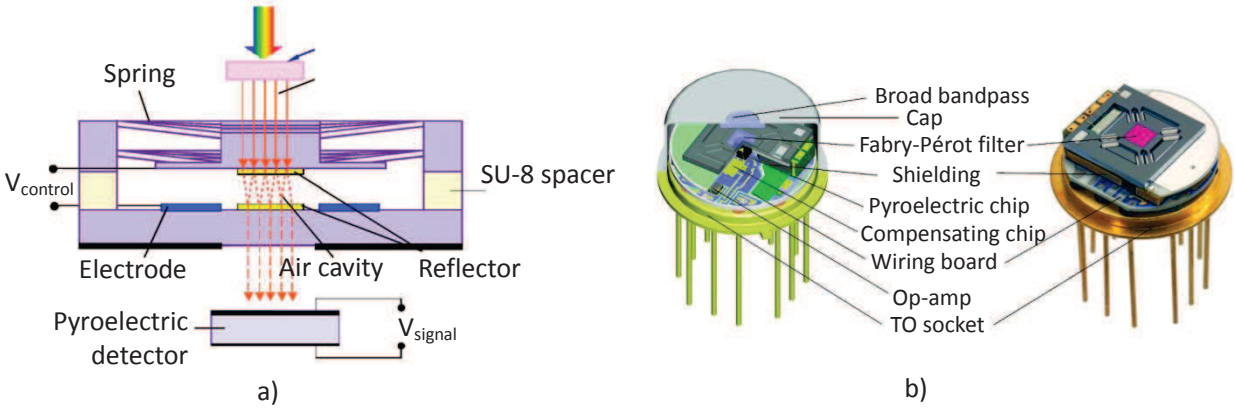

Figure 2-17. (a) Schematic cross section of Micro-machined Fabry-Pérot interferometer, (b) drawing of the commercial product with illustration of the integration composition.

Fourier transform (infrared) spectrometer

Fourier Transform Infrared Spectrometer (FTIR) is commonly a large volume measuring instrument that simultaneously collects spectral data over a large range and then calculates the transmittance or reflectance coefficient of the sample over all the measuring range by using a Fourier transform. Its main structure is based on a Michelson interferometer associated with a movable mirror. Realizing the miniaturization of this instrument could bring in the benefits of smaller volume, lower cost and possible operation in harsh environment where conventional spectrometers are sensitive to shocks and vibrations. Generally, the development on this field can be divided into two types, the first type is trying to realize an all Si-wafer-based spectrometer [Khalil-2011] [Manzardo-1999] (Figure 2-18), while the other is aiming to integrate a micro-machined movable mirror with other macroscopic optical components [Ataman-2006] [Sandner-2008] (Figure 2-19). For the latter one, what needs to be

concerned is the adoption of resonance actuator micro-mirror, which allows a very large motion range (500 μm) and high scanning speed (*f*=5000 Hz).

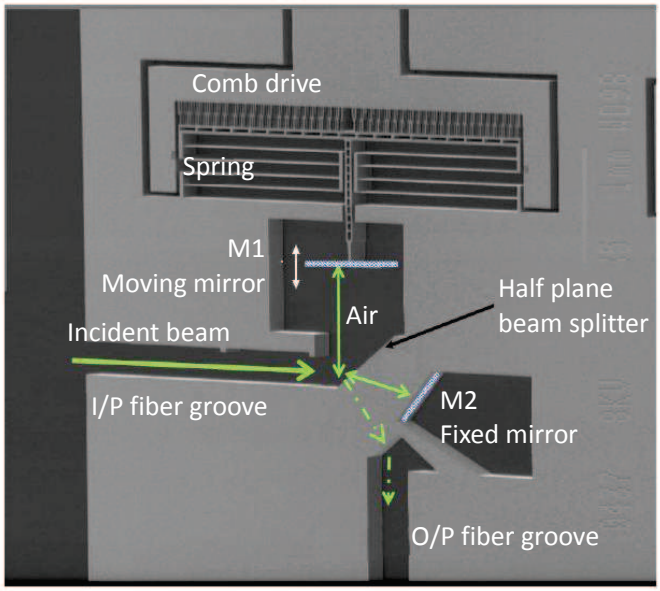

Figure 2-18. FTIR microsystem fabricated on one Si wafer.

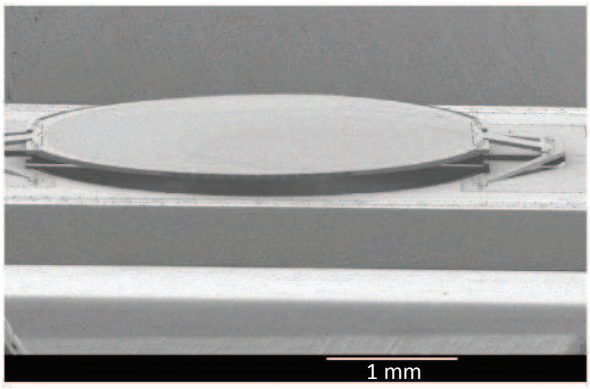

a)

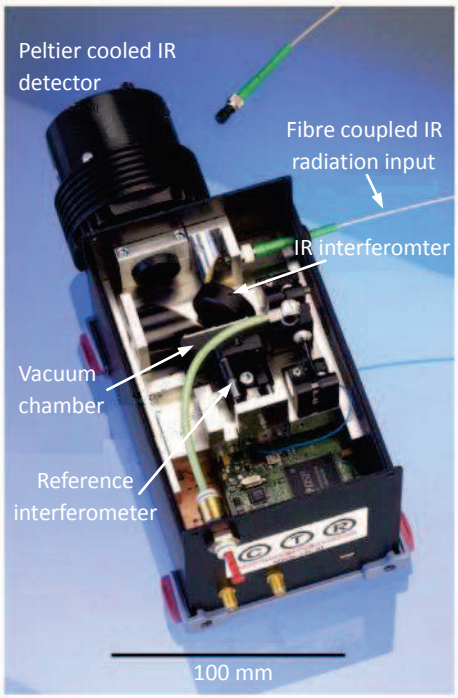

b)

Figure 2-19. (a) SEM image of large motion range, resonance actuated micro scanning mirror, (b) assembly illustration for a FTIR prototype system.

Mach Zehnder integrated interferometers

Integrated single point Mach Zehnder interferometers have been largely investigated for a broad range of applications in telecommunications [Liao-2005], Biomedical OCT [Yurtsever-2014] and

chemical/bio sensor [Sieger-2013]. They have been realized by various waveguides technologies, in different materials and for various wavelengths. As an example, Figure 2-20 shows the configuration of an Optical Coherence Tomography systems based on an integrated Mach Zehnder interferometer chip [Yurtsever2014].

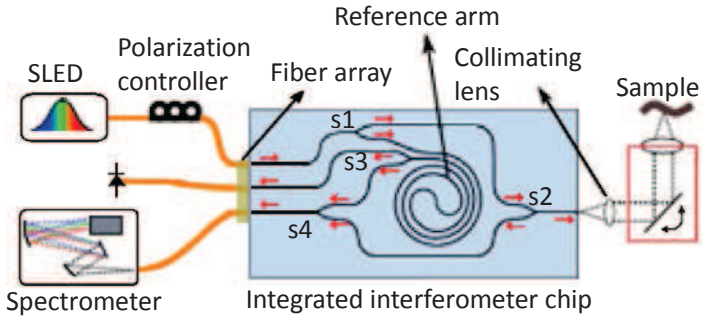

Figure 2-20. Schematic layout of an OCT setup with an integrated Mach Zehnder interferometer chip.

Michelson integrated interferometers

An in-plane integrated Michelson interferometer was also designed and fabricated for its implementation in a surface optical profiler in ESIEE research labs [Malak-2013]. It was mainly fabricated on the top Si layer of a SOI wafer and two different operation approaches have been studied: wavelength sweeping with FFT and monochromatic light modulated with external actuator. A main innovation of this interferometer is the use of vertical air-silicon Bragg mirrors fabricated by Deep Reactive Ion etching. Such mirror technology was also investigated in the research team of Prof. Yves-Alain Peter in Ecole Polytechnique de Montreal.

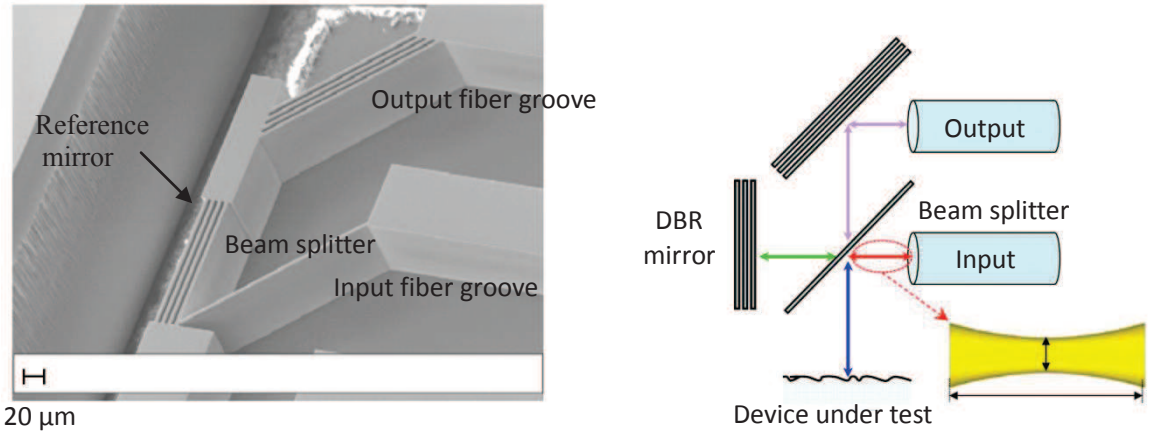

Figure 2-21. SEM image of fabricated Michelson integrated interferometer.

2.6 Conclusion

Mirau interferometers interferometers are two beams coaxial structures that have been widely used for surface topography or vibration mode measurements. In order to fully understand the working principle of this kind of interferometric optical profilometry, the background knowledge of Mirau interferometer based on phase shifting interferometry and low coherence interferometry was firstly reviewed. Macroscopic optical interferometric profilometers commonly achieve a vertical measurement resolution down to 0.3 nm and a lateral resolution reaching 0.6 μm and two examples of available systems at IEF were given.

Then, among the three conventional configurations of interference objectives, Mirau-type was finally chosen for this thesis work, because of its medium magnification and simple structure suitable for MEMS fabrication and multiwafer stacking assembly.

State of the art on Mirau intetferometer was presented on macroscopic and integrated versions respectively. On a macroscopic scale, several new developments have been made recently for the use with polarized light and/or liquids or for non-visible wavelength. Conversely, there is very little work on the implementation of integrated Mirau micro-interferometers and most are still individual non tunable interferometers for their use in monochrome light. It is only very recently that the design and construction of adjustable versions and Mirau micro-interferometer arrays were undertaken. This thesis is one of the few attempts with the particular aims of a wide scanning range of the mirror and an operation in a wide spectral range. Since the work on this type of micro-interferometer is limited, a general review of some other related micro-interferometers was also presented for a better understanding of this scientific research field.

3. Design and Modeling of an Integrated Tunable Mirau Micro-interferometer

Introduction

Through former analysis and comparison of different types of optical interferometer, we have chosen Mirau interferometer for the investigations performed in this thesis. In this chapter, we will first describe the benefits and requirements of integrated tunable Mirau interferometers which are intended to replace the large size macroscopic interference components of the commercial products.

Then section 3.2 will present the technological choices to fulfill this goal and their limitations.

Details of the general design of this integrated interferometer are given in section 3.3. We will see that the micro-interferometer is mainly composed of two parts, a broadband beam splitter and a scanner of the reference mirror of the interferometer.

The optical design work is mainly based on a multilayer membrane previously developed in our group. In section 3.4, the performances of this membrane applied to interference measurements will be analyzed.

The following sections, which also compose the largest content of this chapter, are devoted to a detailed presentation of the electromechanical design of the scanner. The analysis of electrostatic actuation and flexible spring will be present in section 3.5 and 3.6 respectively. Based on these two results, the design, optimization and modeling of the whole scanner have been performed with a final determination of different dimensions of this scanner (section 3.7).

3.1 Benefits and Requirement of Tunable Mirau Micro-interferometer

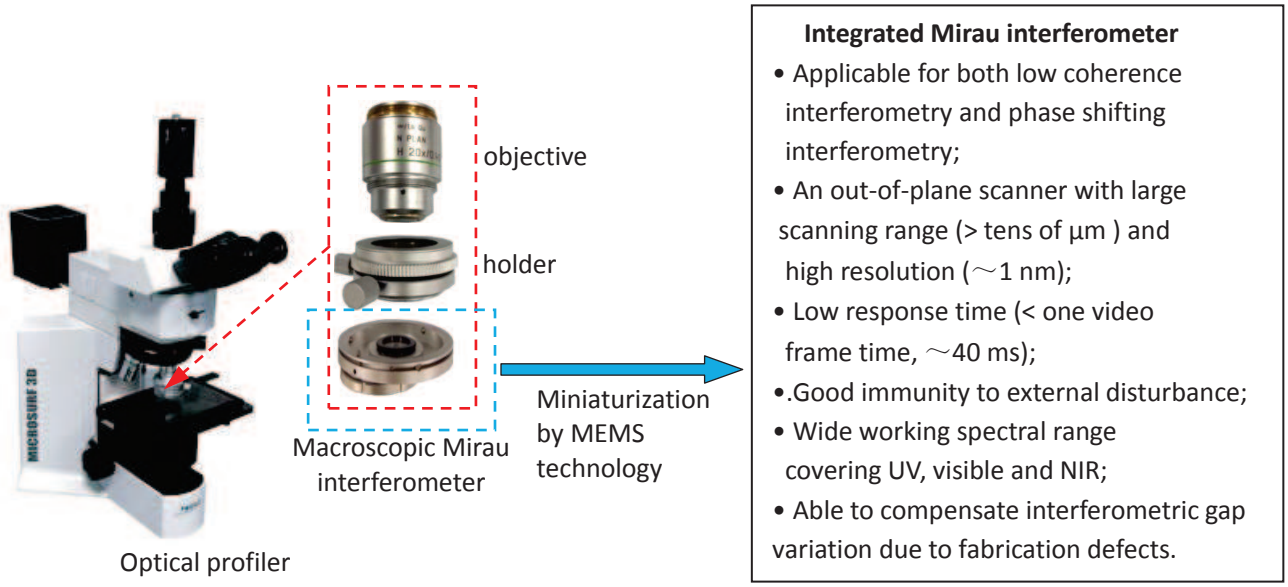

Figure 3-1. Illustration of the work performed in this thesis: miniaturization of macroscopic Mirau interferometer by an integrated version.

Optical profiler is a large size inspection instrument which consists of mechanical, optical and electronic components. In this thesis, only the probing end (Mirau interferometer) is investigated, with the purpose of replacing the macroscopic one by an integrated version as shown in Figure 3-1 above.

Conventional Mirau interferometers are fabricated with large size optical and mechanical components. Although nowadays these commercial components have been made sufficiently compact for their insertion under a long working distance microscope objective of medium magnification, they are still too bulky for large magnification (>50×) objectives with a short working distance. In this case, a Linnik interferometer which is complex to adjust must be used. This issue can be solved by using partially or fully integrated Mirau interferometers fabricated by micro-machining technology. New version of integrated interferometers will bring the merits of a more compact volume, less power consumption and lower fabrication cost arising from batch production.

Beside, with the development of MEMS production, there exists a huge bottleneck for the mass production against single channel measurement approach of today's standard equipment [Gastinger-2009]. An array-type integrated Mirau interferometers could overcome this problem by parallel measurements to save a lot of characterization time.

Moreover, the optical path difference (OPD) of traditional Mirau interferometers is generally varied by scanning the interference objective or the sample with a large size external piezo-actuator. Replacing this large-size actuator with an integrated MEMS scanner is desirable for fast measurement by phase shifting interferometry or low coherence interferometry, because smaller motion inertia and faster scanning speed are expected.

For all the given reasons above, investigation and development of a new 3D integrated tunable Mirau interferometer have great potential and have been targeted in this thesis. At the beginning of this work, it was believed to be the first attempt to realize such novel conception, although another similar

project was also launched recently (described in section 2.4). Both phase shifting interferometry and low coherence interferometry are intended to be realized by this Mirau micro-interferometer. Thus, some essential requirements that must be fulfill for its application for interferometric optical profilometry are given as follows:

- For monochromatic measurements with phase shifting interferometry, the scanning range must be at least slightly larger than $\lambda/2$, be highly linear and the scanner resolution must be in the (sub)nanometer range. The measurement range is limited either by the light source coherence length or by the depth of focus of the objective.

- For low coherence interferometry the scanning range must be at least larger than a few times the coherence length of the light source (or the depth of focus of the objective used whichever is the lowest) and the scanner resolution must be <10 nm. Actually a larger scanning range is needed because it should be able to compensate the OPD difference generated by transmission in the beam splitter. This point will be examinated in more details in the optical design part below. Let us emphasize that the scanning range value approximately gives the maximum height variation than can be measured.

- The proposed scanner should have high resonance frequency to ensure a low response time (at least smaller than one frame time) and good immunity to external disturbance (larger than several kHz) [Montgomery-2008] [Montgomery-2011].

- Actually, in any case a large scanning range is desirable to be able to compensate interferometer gap variations resulting form technological defects. For both modes of operation, the interferometer geometry should be designed from lateral resolution and field of view required by the measurement, and depends on the objective and camera employed.

3.2 Design Criteria

3.2.1 Choice of Vertical Scanner

As mentioned in above section, both phase shifting interferometry and low coherence interferometry need very accurate vertical motion, but different minimum scanning range ($\geq\lambda/2$ for phase shifting interferometry and > several microns for low coherence interferometry). A main target of our work is to avoid an external actuator by integrating a reference mirror scanner. As a consequence, a large range and high resolution vertical motion scanner is the main task to realize. Scanning the reference mirror instead of the interferometer or the sample is obviously the best choice for OPD adjustment of an integrated interferometer and it can potentially be fast if a low inertia mirror assembly is designed.

Generally speaking, there are four main existing mechanisms for MEMS actuation: piezoelectric, electro-magnetic, electro-thermal and electrostatic actuations. Piezoelectric actuators could provide a bidirectional and large range translation if a levering mechanism is used as well as a high accuracy with the aid of a feedback loop. However, piezoelectric actuation is not the easiest way for scanner integration as it requires piezoelectric layers with electrodes having potential issues of mechanical stress control as well as an independent position sensor. Electro-magnetic actuation with a coil and magnets is a good candidate for large range motion. Indeed, we demonstrated in our research group that a ±400 µm vertical motion range of a Si membrane can be achieved [Shahosseini-2013]. Nevertheless it also requires an independent position sensor and magnet integration what is not an easy task. Electro-thermal actuation could be used with a levering mechanism but would also require an additional position sensor as well as a temperature regulation to achieve an accurate and stable positioning of the mirror.

Electrostatic actuation is commonly used in MicroElectroMechanical Systems (MEMS) technology. It has well known advantages such as an easier implementation, low power consumption, the possibility to integrate position sensing by capacitive detection, and low temperature dependence. It is nevertheless clear that a configuration with closing gap parallel electrodes is not suitable to obtain a large actuation range. Instead it was demonstrated by various authors that vertical comb drives could produce an almost constant force during motion and a large translation range.

For all these reasons, electrostatic actuation with vertical electrostatic combs was finally chosen for the actuation mechanism of our work.

3.2.2 Working Spectral Range

Commercial macroscopic optical interferometers are essentially only available for the visible range. As detailed in section 2.3, extension of the working spectral range to deep ultra violet (DUV) and near infrared (NIR) is very attractive.

What determine the working wavelength of a Mirau interferometer is mainly the beam splitter and, in a much lesser extent, the mirror material and the supporting material of the reference mirror when it is a plate or a membrane. In the frame of this thesis, our strategy is to design an integrated

tunable Mirau interferometer configuration able to be used for different spectral ranges by only changing the beam splitter and if necessary the mirror material. Likewise, the design was made to be easily modified for various numerical aperture objectives by simply changing the mirror and beam splitter sizes and gap. As detailed below, this could be achieved by using a mirror suspended in air by small size tethers. Details of this configuration design are described in the following of this chapter.

3.2.3 Limitation of Applied Voltage

When a potential difference is applied between two electrodes immersed in a gas, an electric arc may be generated in the electrode gap if the applied voltage is high enough. At macroscopic scale, this breakdown voltage is typically described by Paschen's law:

$$V = \frac{apd}{ln(pd)+b} \tag{3.1}$$

where a=4.36×10^7 V/(atm·m), b=12.8 in air, and d is gap distance in meters, p is the pressure in Atmospheres or Bar. By using this expression, the breakdown voltage would be 367 V when d=5 μm.

However various authors have demonstrated that Paschen's law can no longer be applied for small air gap below 10 μm [Torres-1999] [Hourdakis-2006]. J.M. Torres's result shows that the breakdown voltage in air is around 350 V for a 5 μm gap [Torres-1999], while E. Hourdakis's result gives an even lower value about 160 V [Hourdakis-2006]. Anyhow, these experiments imply that for a gap of 5 μm (case of our design) the electrostatic applied voltage should not exceed 160 V for a reliable actuation.

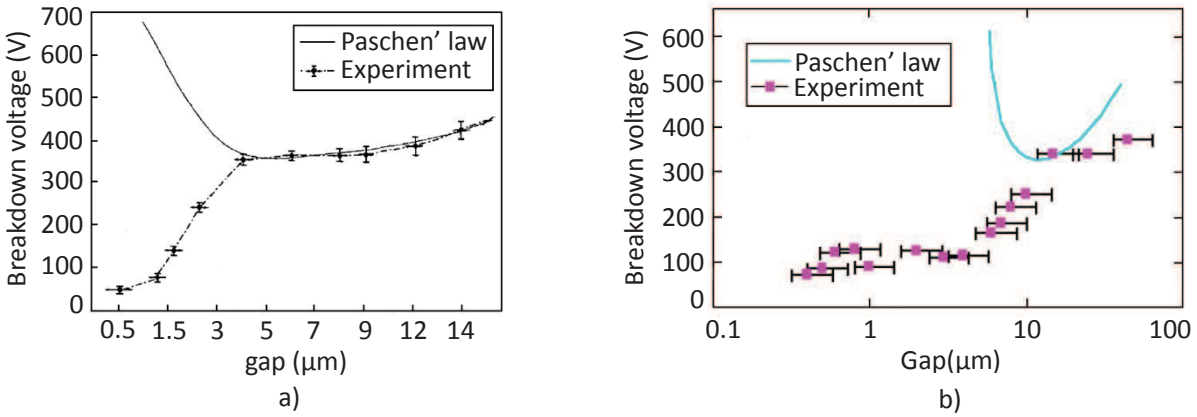

Figure 3-2. Breakdown voltage with a function of gap size published in references (a) [Torres-1999] and (b) [Hourdakis-2006].

3.3 General Design of the Integrated Tunable Mirau Interferometer

Figure 3-3 shows the schematic diagram of our proposed implementation of the tunable integrated Mirau interferometer in an optical profiler. In the frame of this thesis, only the integrated Mirau interferometer, which contains a movable reference mirror and a beam splitter, will be fabricated by micro-machining technology and assembled by 3D integration. Other components will use commercial products for the validation tests. Further integration could be considered as in [Gastinger-2009], where the microscope objective was replaced by micro-lenses and a miniaturized light source and a camera were also integrated. Concerning the integration of an objective, a micro-machined version of an achromatic Schwarzchild objective, which is constructed by an apertured concave spherical mirror and a convex speherical mirror, could be considered. Indeed an integrated Schwarzchild objective was started to be designed and fabricated in IEF in 2010 by Nguyen Phuong Trung Hoa in the frame of a master training and in 2011 by Yifan Zhou during its 1st year thesis. This solution was also investigated recently in FEMTO-ST institute for an on chip confocal microscope by M. K.Baranski [Baranski-2013] and a first prototype of integrated Schwarzchild objective could be successfully demonstrated.

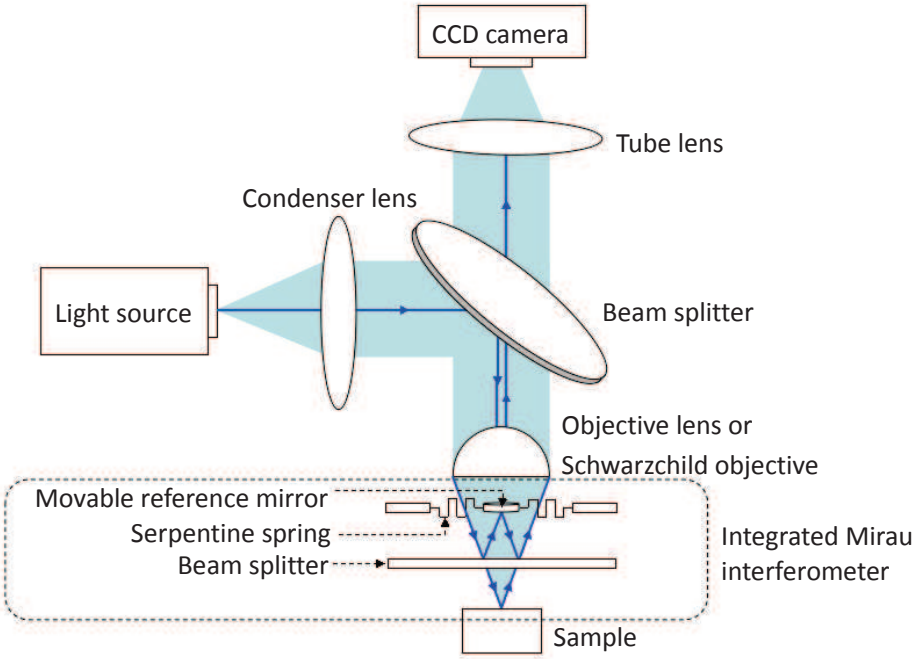

Figure 3-3. Schematic diagram of proposed optical profiler.

The tunable integrated Mirau interferometer, which is surrounded by dashed lines in Figure 3-3, is drawn in 3D in Figure 3-4. As shown in the drawing, this interferometer comprises two functional Si wafers. On the first wafer, a movable reference mirror with two vertical directions motion ability is suspended by serpentine springs and actuated by vertical electrostatic comb fingers. The second Si wafer, which holds a dielectric multilayer semi-reflecting membrane, acts as the beam splitter. A fully integrated Mirau interferometer could finally be obtained by thickness adjustment and bonding of these two wafers.

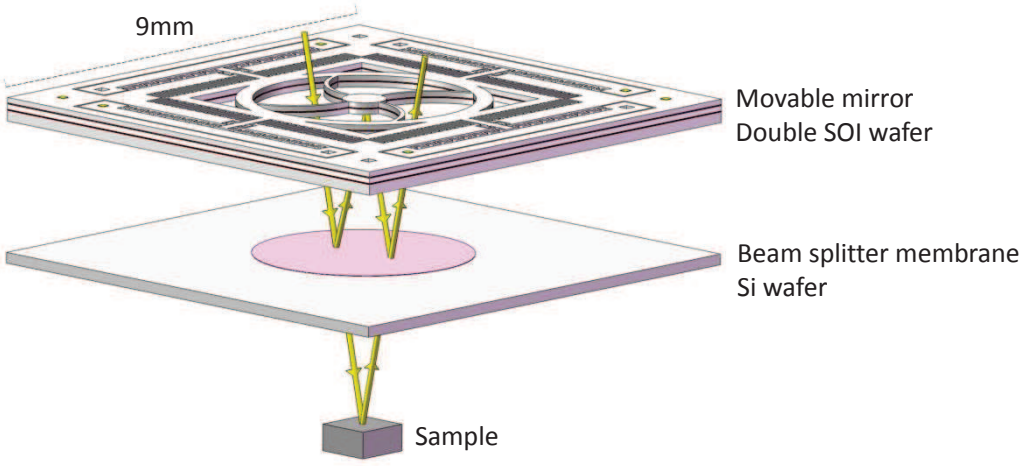

Figure 3-4. Schematic 3D drawing of the tunable Mirau interferometer.

A more detailed view of 1/4 of the movable mirror scanner wafer is shown in Figure 3-5. It is intended to be fabricated from a highly doped double SOI wafer ($Si/SiO_2/Si/SiO_2/Si$, thickness 25/1.5/25/1/380 μm). The central movable reference mirror is connected to an open frame by four curved beams. This curved shape was chosen to reduce effect of (unknown) mean residual stress in the double SOI wafer. Then this open frame serves as optical aperture with the advantage of transmitting light regardless of its wavelength and spectrum. As a result, this configuration is applicable for various spectral ranges by only changing other optical components, such as light source, beam splitter and camera. The open frame is surrounded by a large number of electrostatic comb fingers that act as vertical actuators, and is suspended by serpentine springs which will be designed to be highly flexible in the vertical direction in order to limit frame deformation. Four different electrodes are deposited both on upper and lower layers of the double SOI wafer within movable and fixed area.

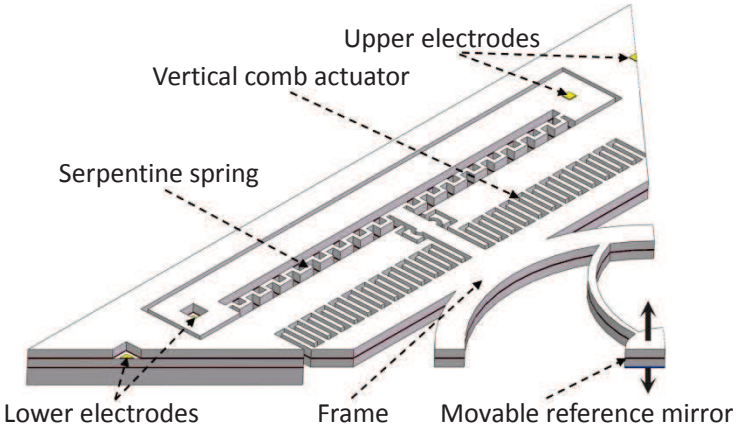

Figure 3-5. Detailed view of 1/4 of movable mirror wafer.

Part of the vertical comb-drive actuator with $Si/SiO_2/Si$ layers stack is depicted in Figure 3-6. Top and bottom Si layers with different electrodes are electrically isolated by an intermediate buried oxide layer and by deeply etched trenches. In this way, it will be possible to apply four different potential. Initial offset between biased parts required for vertical motion is simply obtained by applying a voltage difference between V_1 and V_4 or between V_2 and V_3. The movable comb can translate both in upward and downward directions. By changing the structure configuration, as shown in Figure 3-7 and Table 3-1, a slight in-plane movement and a tilt adjustment could be added [Tsou-2005].

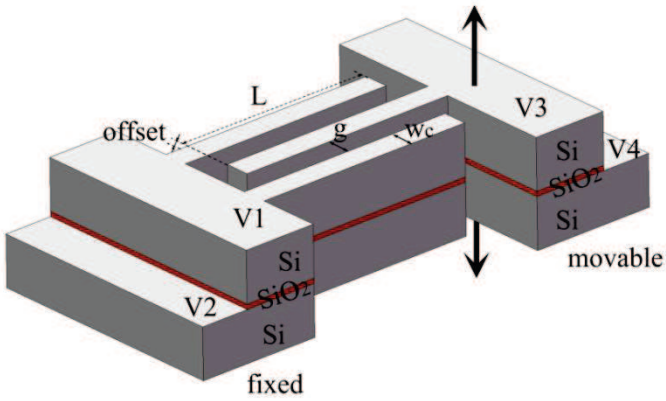

Figure 3-6. Schematic drawing of a pair of fingers of the bidirectional vertical comb-drive actuators.

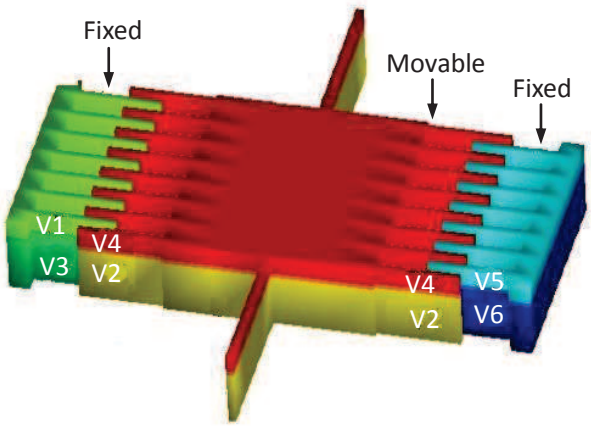

Table 3-1. Different motion principle.

Motion	Apply voltage
upward	V_1,V_5& V_2
downward	V_3,V_6& V_4
left	V_1,V_3&V_2, V_4
right	V_2, V_4& V_5, V_6
↻rotation	V_1&V_2, V_4&V_6
↺rotation	V_3&V_4, V_2&V_5

Figure 3-7. Schematic structure of multi-directional motion actuator.

The maximum motion range of the actuator is close to the total thickness of Si/SiO_2/Si multilayer (25/1.5/25 μm). This means that for the chosen DSOI wafer, a vertical bidirectional motion of ±25 μm is expected to be achievable. Let us emphasize that the same low stress, single crystal material (silicon) and thickness is used both for the top and bottom part of the fingers of the electrostatic combs. This is quite favorable to obtain a scanner with good symmetry, reproducibility and reliability.

3.4 Optical Design

A simplified schematic drawing of Mirau interferometer is shown in Figure 3-8. The integrated interferometer was designed for a Nikon CFI S PLAN Fluor ELWD objective with a 0.6 NA, 40× magnification and 2.8-3.6 mm adjustable working distance. This objective was chosen because of its high resolution and magnification, its large working distance and wavelength range (340-1100 nm) and the possibility to compensate a cover glass thickness in the 0-2 mm range. This latter characteristic is interesting as a beam splitter will be inserted below the objective. The measured diameter of its output aperture is 6 mm, which essentially determines the input optical aperture of the frame of the movable reference mirror. Besides, the selected imaging camera is a Sony XC8500CE having 782×582 pixels and a 8.3×8.3 μm^2 pixel size.

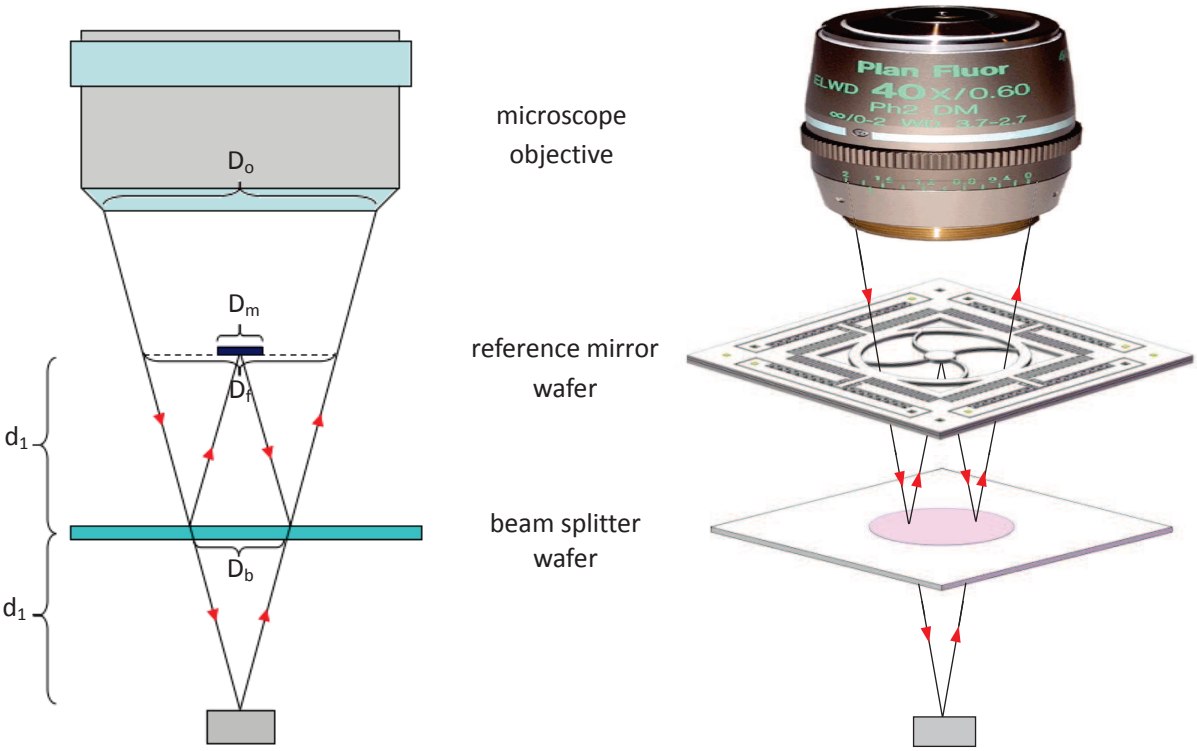

Figure 3-8. Schematic diagram of the Mirau interferometer.

For the purpose of fully imaging the sampling area, the diameter D_m of the movable reference mirror should be larger than the field of view, which is generally adjusted to the imaging area of the camera divided by the magnification of the objective. The obtained value (162×120 μm^2) determines the diameter of reference mirror D_m which was chosen to be larger than 201 μm. On the other hand, the diameter of the reference mirror must not be too large as it induces a central obscuration of the incident light beam. The sampling spot size given by the objective could be roughly calculated as 1.5 mm, which ensures a future extension of the camera's sensitive area. By taking into account of the trade-off, the essential dimensions of the interferometer are listed in Table 3-2.

Table 3-2. Essential dimensions of optical system.

Objective	0.6 NA, 40× magnification, 2.8-3.6 mm adjustable working distance
Camera	782×582 pixels, 8.3×8.3 μm^2 pixel size, 162×120 μm^2 field of view
Geometrical parameters	D_o=6 mm, D_f=4 mm, D_m=0.8 mm, D_b>2 mm, d_l=1 mm

The presence of central reference mirror will obscure part of the incident light (4% of the aperture area), will reduce the effective NA from nominal value 0.6 (0-36.87°) to actual 0.47 (8.53-36.87°), and will increase the fringe spacing by a factor of 1.12 (apodization parameter n=0, corresponding to a constant angular variation condition, Herschel) or 1.11 (n=0.5, perfect aplanatic condition, sine) [Sheppard-1995, Dubois 2000].

Then, four curved arms which connect the central reference mirror are also placed in the optical path and may introduce some diffraction effects. Its impact is believed to be negligible based on previous experience of our research team. Indeed, no obvious effect had been observed for a formerly developed macroscopic Mirau interferometer having a suspended mirror arms width w_a=0.5-0.7 mm for a , diameter of open aperture D_f=24 mm, while our miniaturized version has a similar w_a/D_f ratio but a shrinked size (w_a =100 μm, D_f =4000 μm).

3.4.1 Design of the Beam Splitter

The beam splitter plays a very important role in this optical system. It was conceived to achieve a light transmittance/reflectance ratio of 50/50 under 0-36.87° oblique incidence. This angle range corresponds to the cone of incident angle for the Numerical Aperture (NA) of the chosen Nikon objective (NA=0.6). As mentioned above, our device is intended to work in the spectral range from visible to near infrared (NIR). The possibility to realize a large area and broadband semi-reflective membrane was already demonstrated in our laboratory by Hervé Bertin [Bertin-2013]. This was achieved by deposition of a SiN_x/SiO_2 multilayer by plasma enhanced chemical vapor deposition (PECVD) followed by a high temperature annealing for residual stress control. The membrane was released by Si wafer Deep Reactive Ion Etching (DRIE) in a SF_6+C_4F_8 plasma (Bosch process) followed by a highly selective XeF_2 etching. Such a beam splitter membrane is similar to a Bragg mirror with a stack of alternating dielectric material layers with high (SiN_x) and low (SiO_2) refractive indices. Its design was optimized by simulations with TFCALC optical software to obtain broad spectral range coverage.

We used the multilayer design previously optimized by Hervé Bertin for a Fabry Pérot tunable filters array [Bertin-2013-2]. This design, given in Table 3-3, is based on a 12 layers stack. It provides a normal incidence reflectance coefficient of approximately 50% in the 550-850 nm range (Figure 3-9). For our Mirau interferometer, we simulated the reflectance under 36.87° angle which corresponds to arcsin(NA) where NA is the numerical aperture of the chosen objective. Experimental values of optical constants and their dispersion measured previously by spectroscopic ellipsometry were used for the calculations. The result, plotted in Figure 3-9, shows that the variation of incident angle has a little influence on the reflectance and thus on the transmittance to reflectance ratio of the beam splitter. However, a significant shifts of the starting wavelength (-33 nm) and of the ending wavelength (-54

nm) of the working spectral range can be observed when the angle of incidence is varied from 0° to 36.87°. The wavelength range for optimum use of this beam splitter is then predicted to be 550-800nm.

Table 3-3. Multilayer Bragg mirror membrane design

SiN_x (H)/ SiO_2 (L) (nm)
Air/L 108/ H 117/ L 19/ H 181/ L 205/ H 53/ L 228/ H 90/ L 116/ H 84/ L 112/ H 79/Air

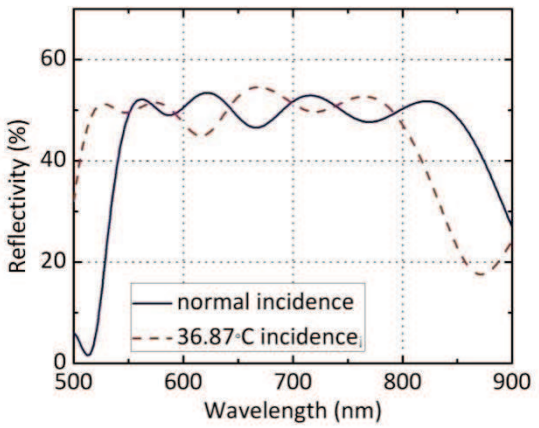

Figure 3-9. Optical reflectance at normal and 36.87°C incidence with a function of wavelength.

3.4.2 Initial Optical Path Difference

Ideally, when constructing a Mirau interferometer, the two optical paths of the reference beam and of the sample beam must initially be equal or their difference must be at least lower than the coherence length of the light source. Otherwise, the contrast of the interference fringes would be too low for measurements. The coherence length L_c of a light source with a Gaussian spectrum with a Full Width at Half Maximum (FWHM) $\Delta\lambda$ and a central wavelength λ_0 is is given by:

$$L_c = \frac{2ln(2)}{\pi \cdot n}\frac{\lambda_0^2}{\Delta\lambda} = 0.441\frac{\lambda_0^2}{\Delta\lambda} \tag{3.2}$$

where n is the refractive index of the medium. In our case, n=1 for air. The computed values for some chosen LED are listed in Table 3-4.

Table 3-4. Typical coherence length of LED light sources.

	Working wavelength (λ_0)	**Spectrum range ($\Delta\lambda$)**	**Coherence length (L_c)**
Red LED	650 nm	50 nm	3726 nm
NIR LED	900 nm	40 nm	8930 nm
White LED	550 nm	200 nm	667 nm

In a Mirau interferometer configuration with a suspended mirror, the optimum beam splitter, from the point of view of optical path compensation, is a semitransparent ultrathin metallic layer sandwiched between two identical transparent substrates (such as glass plates) or between the same two transparent films. In that case an almost fully compensated Mirau interferometer could be obtained although a compensation defect would still be present because of the reflection phase shift difference between the reference mirror and the sample [Dubois-2004]. However such a beam splitter

is suitable only for monochromatic illumination because the transmission of the metallic film is highly variable with wavelength.

In our proposed design, the beam splitter is a non absorbing dielectric multilayer membrane freestanding in air as it is totally released by backside silicon substrate etching. The initial optical path difference (OPD) caused by such a beam splitter is inherently different from zero. For a highly monochromatic light source like a laser diode this is not an issue as the coherence length is very large but for a quasi monochromatic LED source or a white LED source it is more problematic. Indeed, because the light will tramsitt or be reflected by the beam splitter, the initial OPD must be below $L_c/2 \approx 1.86$ µm for a red LED and below $L_c/2 \approx 333$ nm for a white LED source to get high contrast interference fringes.

For a tunable Mirau interferometer, the initial compensation condition can eventually be less restrictive because the mean OPD can be reduced and even cancelled by moving the reference mirror if the tuning range is sufficiently large. However, this OPD tuning is the same for all wavelengths while the initial OPD is generally wavelength-dependent notably because of light dispersion in the films of the beam splitter. Thus it remains necessary to get an initial optical difference variation with wavelength lower than half the coherence length. As detailed below, calculation of the initial optical path difference is not straightforward.

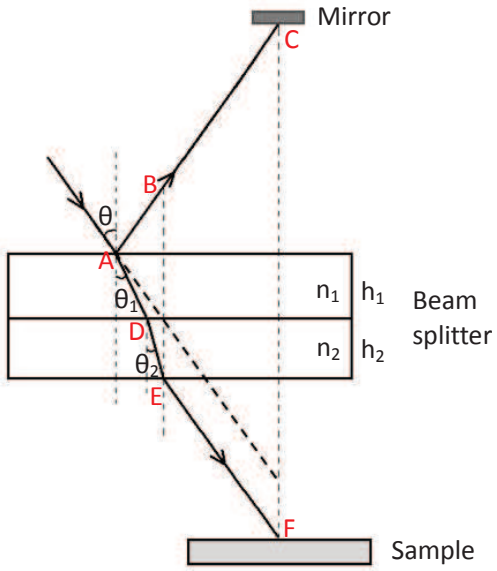

Figure 3-10. Optical beams reflection and propagation on/in a multilayer beamsplitter.

Let ϕ_r represent the phase lag of the reference wave reflected on the beam splitter and ϕ_t represent the phase lag of the sample wave just after its transmission through the beam splitter (Points A and E in Figure 3-10 corresponding to the case of a two layer beam splitter). For a broadband light source and a low refractive index contrast of the films composing the beam splitter membrane, we can neglect, as a first approximation, multiple interference in the films of the beam splitter. Then, for given angle of incidence θ and wavelength λ, the optical path difference $\Delta c1$ between the transmitted (optical path AE in Figure 3-10) and reflected wave amplitudes is:

$$\Delta_{c1} = \frac{\lambda}{2\pi}(\phi_t - \phi_r) = \sum_{i=1}^{n} \frac{n_i h_i}{\cos(\theta_i)} - \frac{\lambda}{2\pi}\phi_r = \sum_{i=1}^{n} \frac{n_i^2 h_i}{\sqrt{n_i^2 - \sin^2(\theta)}} - \frac{\lambda}{2\pi}\phi_r \qquad (3.3)$$

where n_i, h_i are respectively the refractive index and thickness of layer i , and ϕ_r is the beam splitter reflection phase shift. In the right part of equation 3.3, the Descartes law $\sin(\theta)=n_i\sin(\theta_i)$ was used.

A decrease of the optical path difference Δc2 also arises from the lateral shift of the transmitted beam (additional path AB of the reflected beam in Figure 3-11). The corresponding optical path difference is given by:

$$\Delta_{c2} = -\sum_{i=1}^{n} \frac{h_i \tan(\theta_i)}{\sin(\theta)} = -\sum_{i=1}^{n} \frac{h_i}{\sqrt{n_i^2 - \sin^2(\theta)}} \tag{3.4}$$

So the total optical path difference introduced by the beam splitter is [Chim-1990]:

$$\Delta_c = \Delta_{c1} + \Delta_{c2} = \sum_{i=1}^{n} \frac{(n_i^2 - 1)\, h_i}{\sqrt{n_i^2 - \sin^2(\theta)}} - \frac{\lambda}{2\pi}\phi_r \tag{3.5}$$

Equation 3.5 shows that the first term of OPD is maximum when the angle of incidence is maximum and for the lowest wavelength of the light spectrum and is increasing with the total thickness of the layer stack and thus with the number of layers composing the beam splitter.

For unpolarized light, ϕ_r can be computed from equation [Dubois-2004]:

$$\phi_r = \arg\left[\, |r_s| \exp(i\phi_s) + |r_p| \exp(i\phi_p)\right] \tag{3.6}$$

Where $|r_s|\exp(i\phi_s)$ and $|r_p|\exp(i\phi_p)$ are respectively the amplitude reflection coefficients for perpendicular and parallel polarisations computed from Fresnel equations. Note that for normal incidence, if internal and backside reflection are neglected ϕ_r is simply equal to 0 or π.

Actually, the OPD of interfering beams in a Mirau interferometer is equal to $2L_c$ because the beams are reflected twice by the beam splitter or transmitted twice through the beam splitter. Calculated values of $2L_c$ are plotted as function of wavelength in Figure 3-11 for the 12 layers beam splitter of Table 3.3 and for θ=36.87°.The results show that the maximum value in the 550-850 nm range is about 2660 nm.This maximum value of 2Δc is smaller than or equal to the coherence length calculated before for red and NIR LED light sources but it is significantly larger than the coherence length of a white LED. The Mirau interferometer can thus be used without tuning for phase shifting measurements with quasi monochromatic light in the 550-800 nm range. For a white light LED, the Mirau interferometer is too much unbalanced to get interference fringes without tuning. The mean OPD difference can be nulled by interferometer tuning nevertheless the OPD variation with wavelength (530 nm) must be considered. It is slightly lower then the coherence length L_c. for white LED. This means that low coherence interferometry should be possible but with a limited fringe contrast and thus with degraded performances.

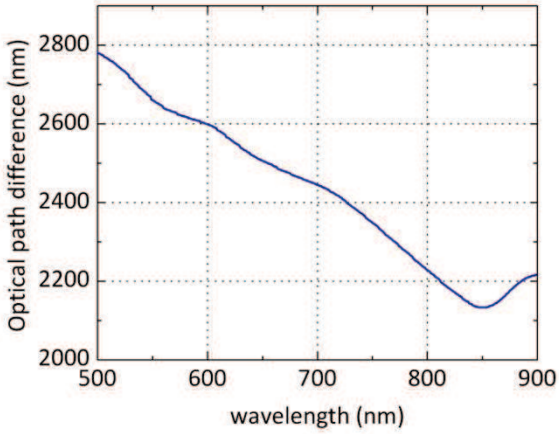

Figure 3-11. Optical path difference of the proposed multilayer Bragg mirror membrane calculated by neglecting internal reflections for θ=36.87° as function of wavelength.

The calculation above was made for a single wavelength and a single angle of incidence. In a Mirau interferometer the beam splitter is actually illuminated by a partial truncated cone having a length equal to ~W/2 where W is the mirror to sample distance, and an angle of incidences range from θ_0=atan(R/W) to θ_{max}=arcsin(NA), where R is the radius of the reference mirror and NA is the numerical aperture of the objective for which the interferometer is designed. For a complete calculation of the optical path difference, it should be integrated in this partial truncated cone. Note that this integration differs from the case of fringe spacing calculation because in this later case the solid angle cone is not truncated [Dubois-2000].

The final mean optical path difference should be computed by performing another integration on the wavelength range of the light source by using a weighting function given by the wavelength spectrum of the amplitude of the electrical field.

Finally, for a more rigorous treatment, reflection and transmission phase lags should be computed by taking into account remaining multiple internal reflections and the partial coherence of the light source. This could be done for example by using recent models of reflectance and transmittance calculations in a stratified media with a partially coherent light source [Lahiri-2012, Lahiri-2013, Santbergen-2013, Katsidis-2002].

This discussion shows that exact full calculation of the initial optical path difference and its variation with wavelength is not easy and requires extensive calculations. This calculation could not be undertaken during this thesis but it should be done in the future. Alternatively it could be determined from experiments.

3.4.3 Optical aberrations due to the beam splitter

When a convergent light beam passes through a transparent optical lens, plate or film, the paraxial rays and marginal rays may not meet at one focal point, this phenomenon is called spherical aberration. When a thicker film and larger NA objective are employed, a greater spherical aberration of the focused beam will be produced. The radius of the aberrated beam r_A can be calculated by the following formula [Chim-1990]:

$$r_A = HF = \Delta h \cdot tan\theta = h \cdot tan\theta \cdot \left(\frac{1}{n} - \frac{cos\theta}{\sqrt{n^2 - sin^2\theta}} \right) \tag{3.7}$$

where h is the thickness of the plate and n is its refractive index. This formula only corresponds to a single layer. The aberration of the multilayer layer given in Table 3-3 can be calculated as the sum of contributions of all different layers.

The effect of spherical aberration can be considered negligible only if the calculated radius r_A is much smaller than the radius r_D limited by diffraction theory. For an objective of numerical aperture NA=sin(θ), r_D is given by

$$r_D = 0.61\lambda / sin\theta \tag{3.8}$$

The beam aberration generated by a transparent film is illustrated in Figure 3-12a. Calculated values of r_A/r_D versus wavelength are plotted in Figure 3-12b. From this curve, it can be seen that r_A/r_D is restrained under an acceptable range in the visible-NIR range. However, if large NA objective with higher magnification would be employed with the integrated Mirau interferometer, the r_A/r_D would increase rapidly.

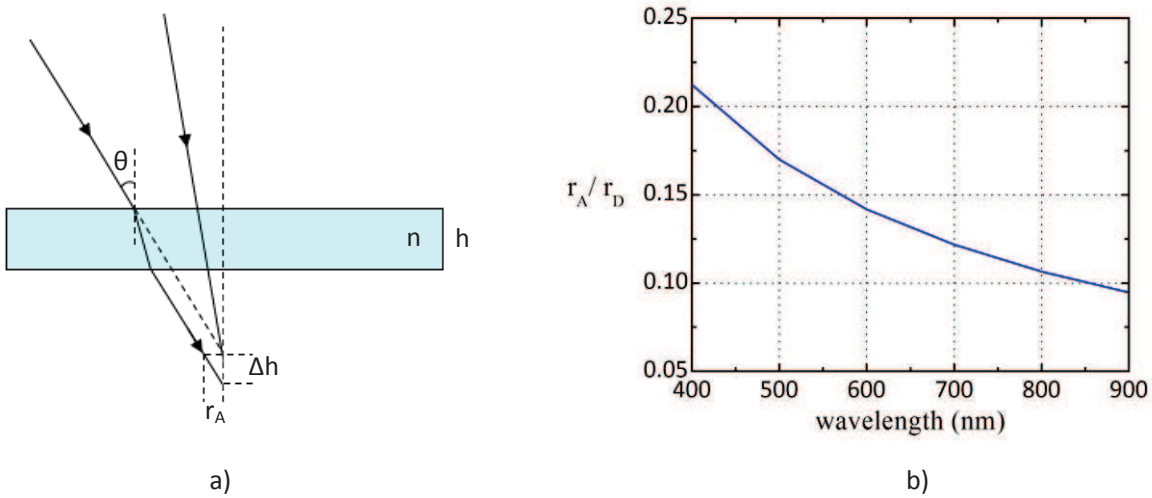

Figure 3-12. (a) Illustration of beam aberration from a transparent film and (b) plots of r_A/r_D versus wavelength For the 12 layers beam splitter.

3.5 Electrostatic Actuation

The key element for the tunability of the investigated Mirau interferometer is the reference mirror scanner. This mirror scanner will be actuated by vertical electrostatic comb drives, and an illustration drawing of this kind of actuation is shown in Figure 3-13. Vertical motion can be realized by the attraction between movable and fixed comb finger with different heights.

As a main novelty of this work, electrostatic vertical comb-drives in our case will be fabricated by double SOI technology in order to obtain a large range and bidirectional vertical translation with a high accuracy. The gap between the different fingers was set to be 5 µm in order to limit the gap aspect ratio (height/width) to a value of about 10. Likewise, the finger length L and width w_c (top view) were chosen to get aspect ratios L/w_c below 50 in order to limit fabrication issues. The dimensions of proposed vertical comb fingers are listed in Table 3-5.

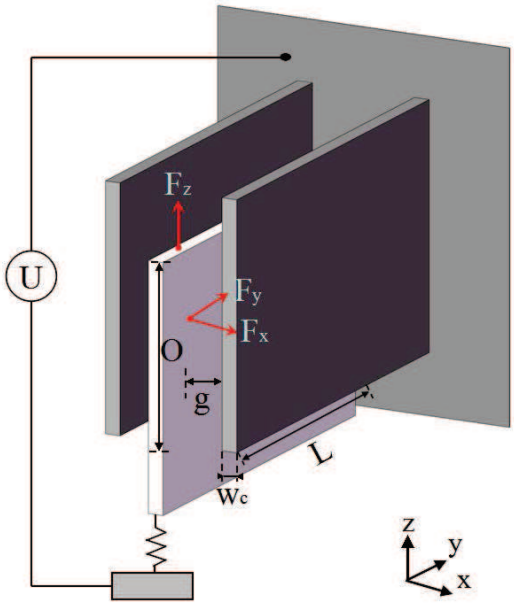

Figure 3-13. 3D drawing of conventional vertical comb fingers with applied potential.

Table 3-5. Dimensions of vertical comb fingers

Items	Values
w_c	10 µm
g	5 µm
L	400 µm

3.5.1 Analytical Calculation of Electrostatic Force

When a potential difference is applied between a movable finger and a fixed finger, the resulting electrostatic force will tend to align the fingers in the vertical direction z and longitudinal y direction and to attract the fingers in the transverse direction x. Assuming that the fixed and movable comb fingers already have a certain overlap area along z direction, and ignoring fringe field effect, the electrostatic energy is given by:

$$\because W(x,y,z) = \frac{1}{2}CU^2 = \frac{\varepsilon LO}{2g}U^2 \tag{3.9}$$

where C is the air gap capacitance, $O(z)$ is the overlapping height, $L(y)$ is theoverlapping finger length, $g(z)$ is the lateral air gap, ε is the permittivity of medium between fingersand U is the appliedvoltage difference (see Figure 3-13).

The resulting components of the electrostatic force are:

$$\therefore F_{\mathrm{x}} = \frac{\partial W}{\partial x} = \frac{\varepsilon LO}{2\mathrm{g}^2}U^2,\ F_{\mathrm{y}} = \frac{\partial W}{\partial \mathrm{y}} = \frac{\varepsilon O}{2\mathrm{g}}U^2,\ F_{\mathrm{z}} = \frac{\partial W}{\partial z} = \frac{\varepsilon L}{2\mathrm{g}}U^2 \tag{3.10}$$

Properly aligned comb fingers will generate numerically equal but directionally opposite F_x by two adjacent fingers. And F_y will also be balanced by its counterpart since the whole geometry is symmetrical. Only vertical forces (F_z) will work, and will pull up the movable finger, in the case of Figure 3-13.

The total force exerted on one movable finger by two adjacent fixed fingers can be expressed as:

$$\therefore F_{x,one} = F_x - F_x = 0,\ F_{y,one} = 2F_y = \frac{\varepsilon O}{\mathrm{g}}U^2,\ F_{z,\,one} = 2F_z = \frac{\varepsilon L}{g}U^2 \tag{3.11}$$

However, if the gap on both sides of a movable finger is not equal, due to some fabrication issues or misalignment between movable and fixed fingers, there will be a large lateral electrostatic force. Then an instability in the form of lateral pull-in may occur. Assuming g_1=g-x, g_2=g+x, then:

$$F^*_{x,one} = F_{\mathrm{x1}} - F_{x2} = \frac{\varepsilon LOU^2}{2(g-x)^2} - \frac{\varepsilon LOU^2}{2(g+x)^2} = \frac{2gx\varepsilon LOU^2}{(g^2-x^2)^2} \tag{3.12}$$

The ratio of $F^*_{x,one}/F_{z,one}$ exerted on one movable finger is given by:

$$F^*_{x,one}/F_{z,one} = \frac{2g^2Ox}{(g^2-x^2)^2} \tag{3.13}$$

The value of $F^*_{x,one}/F_{z,one}$ is plotted as function of the misalignment x/g for different values of O/g in Figure 3-14.

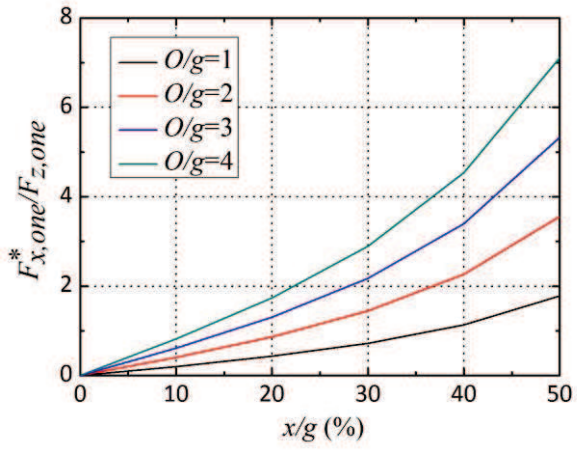

Figure 3-14. Ratio of transverse to vertical electrostatic force as function of misalignment ratio x/g for different values of O/g.

Figure 3-14 shows that the ratio $F^*_{x,one}/F_{z,one}$ increases with overlapping area and also with misalignment. For a gap g=5 µm and a misalignment x≤1µm (e.g. x/g≤20%) the ratio $F^*_{x,one}/F_{z,one}$ is always below 2. However the $F^*_{x,one}/F_{z,one}$ ratio become larger than 7 for a misalignment x=2.5 µm and an overlap O equals to 20 µm. Consequently, the springs must be much stiffer in x direction than in z direction to avoid lateral pull-in effect. This point will be discussed in more details in a later section.

3.5.2 FEM Simulation of Electrostatic Forces

Since fringe field effects are not taken into account in the analytical calculation described in previous section, Finite Element Modeling (FEM) simulations using ANSYS software were performed to obtain more accurate electrostatic force created by the vertical electrostatic combs. A comparison between these two methods will be first given, for different cases (Figure 3-15a); starting from two simple electrodes in infinite space ①, to three electrodes ②, then to electrodes with conductors ③, and finally two electrodes with conductors and insulators ④ which is the closest case to the real configuration we desire . Figure 3-15a shows cross section of these four configurations analyzed in FEM simulations, and Figure 3-15b plots the electrostatic force per unit length as a function of the overlap between movable and fixed comb fingers in the four different cases.

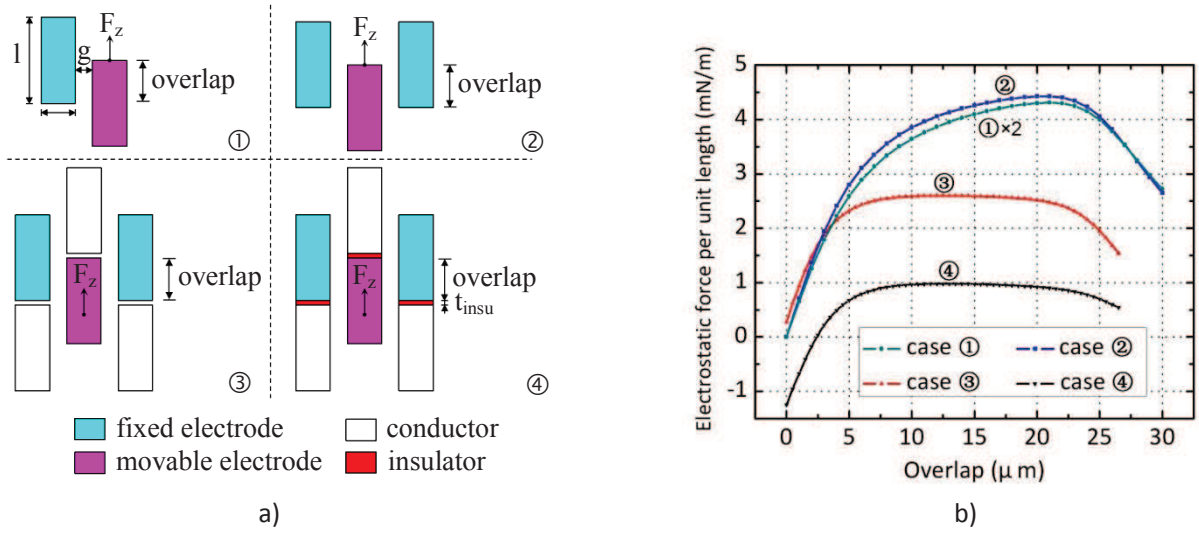

Figure 3-15. (a) Cross section of different configurations analyzed by FEM simulation with a potential difference applied between cyan and purple box, ①: two simple electrodes in infinite space, ②: two fixed electrodes with one movable electrodes, ③: multilayer electrodes with additional conductors (white boxes), ④: multilayer electrodes with conductors and insulators (red boxes). (b) Electrostatic force per unit length as a function of overlap under the condition: l=25 µm, w=10 µm, g=5 µm, U=50 V, t_{insu}=1.5 µm.

By using formula (3.10), the vertical electrostatic force F_z could be calculated as 2.21 mN/m, which exactly approximates the maximum value of two simple electrodes in infinite space (case ① in Figure 3-15a). For the three electrodes configuration (case ②), the total force also satisfies the double value of case ①. However, when conductors are added, the produced force will be halved because of changing of electric field distribution. Another reducing by half could also be observed when insulators are added. Zero positions are the same for first two cases, but shift slightly for case ③ and largely for case ④.

As a conclusion, FEM simulations of two and three electrodes in infinite space are in agreement with analytical results. But when other components such as conductors or insulators are added, the resulting electric field will be influenced, and the total produced electrostatic forced will be reduced. The final configuration that is similar to our proposed design could only generate approximately 1/4 of the force comparing to analytical results, but its value remains constant in a large motion range.

Elaborate simulation of our real configuration with comb fingers (light and dark gray areas, not meshed in the following analysis), buried silicon oxide (magenta area, $\varepsilon_r = 3.9$) and air space (light and dark blue area, $\varepsilon_r = 1$) were performed and are shown in Figure 3-16. Periodic boundary condition and infinite space condition were set for the four sides of the whole geometry (Figure 3-16a). And rectangular mesh with regular shape was applied for this analysis (Figure 3-16b). These meshes are already fine enough, because only less than 2% variation of the obtained force values was observed when the mesh size was halved.

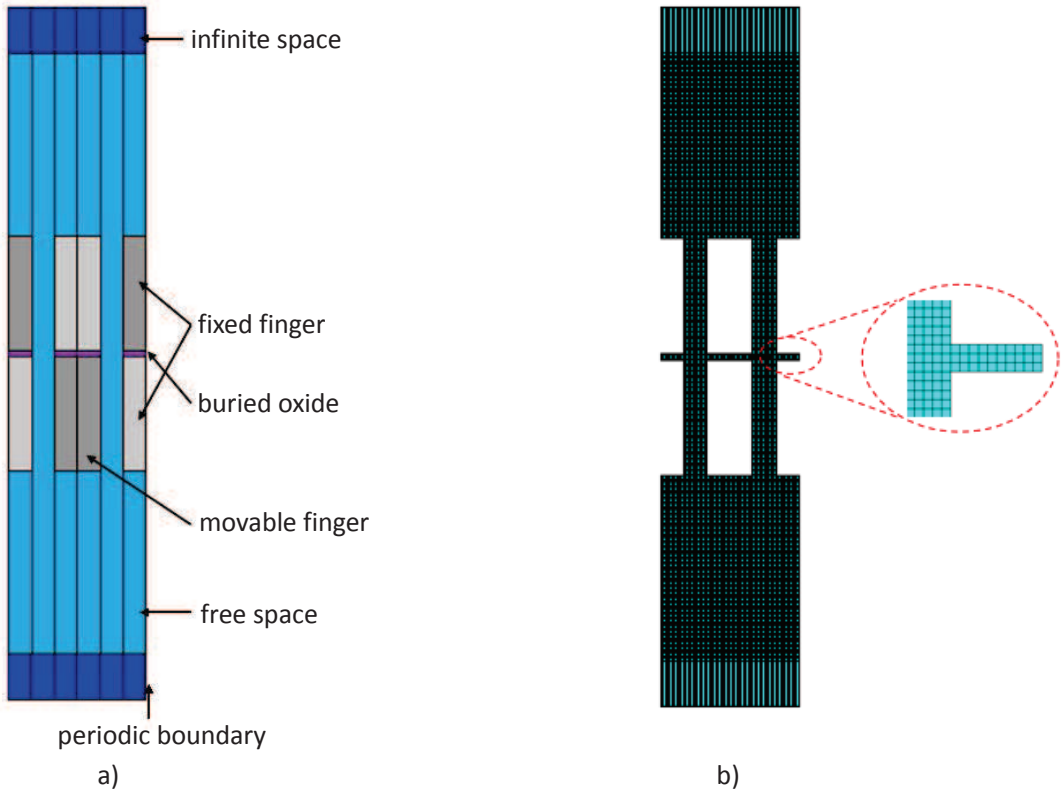

Figure 3-16. (a) Single pair of comb finger modeled by finite element simulation with infinite and periodic boundary condition. (b) Rectangular mesh with regular shape used for the simulation.

Electrical potential distributions produced by one pair of fixed lateral comb fingers for different values of displacement are depicted in Figure 3-17. They show that at the initial step (vertical displacement D=0), a non zero electric field is produced by fringing field effect. It then progressively dominated by the field produced by overlapping parallel faces of the movable and fixed fingers when the central movable finger moves upwards.

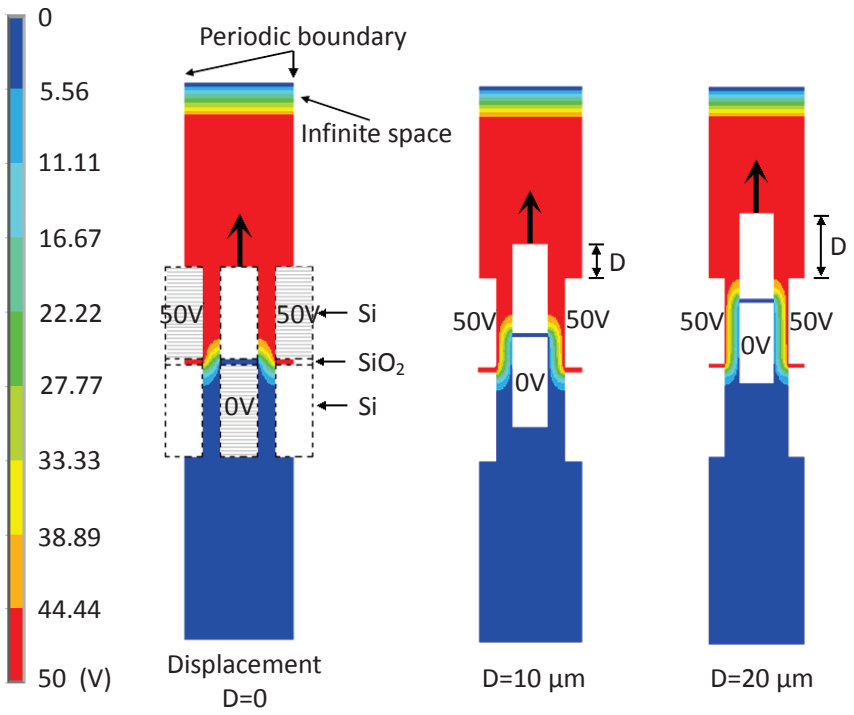

Figure 3-17. Contour plot of electric potential distribution of one pair comb finger, under the condition that two electrodes are biased at 50 V and other two electrodes are discarded with floating potential. Note that, Displacement (D)=1.5 µm + Overlap (O)

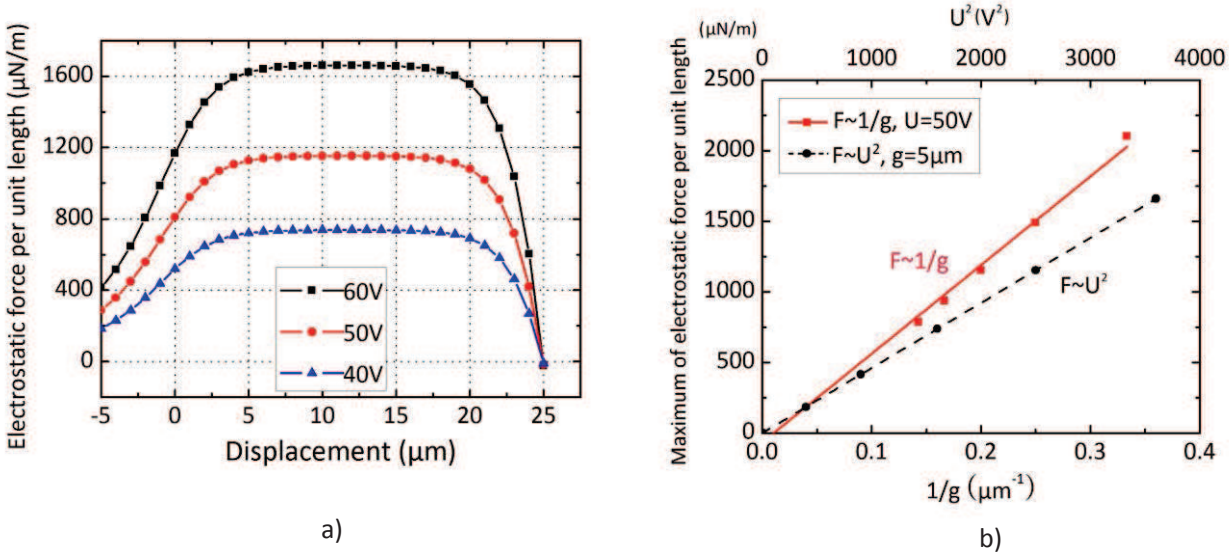

Figure 3-18. (a) Electrostatic force per unit finger length versus vertical displacement under the condition: l_{si}=25 µm, l_{sio2}=1.5 µm, w=10 µm, g=5 µm. (b) The relationship of F between 1/g and U^2.

Simulated force per unit length is plotted in Figure 3-18a as a function of vertical displacement of the movable finger in upward direction for different applied voltages. A similar curve would be obtained for a downward direction by applying the voltage difference between the bottom part of fixed fingers and the upper part of the movable finger. As expected, the force initially increases, stays approximately constant in the displacement range +5 µm to +20 µm and then tends to zero when the displacement reaches the Si thickness (25 µm). This means when D=20 µm, or O=18.5 µm, we can still obtain an electrostatic force very close to its maximum value. The force at zero displacement is

about 30% lower than its maximum value and is 50% lower if D=-2 μm, corresponding to an initial self-drop of the movable part due to the gravity. These forces at rest position are significantly lower than their maximum values but still sufficiently high to allow an actuation.

Since the vertical electrostatic force could no longer be simply calculated by formula (3.10), we have tried to analyze different parameters contributing to the final value. The relationship of F with $1/g$ and U^2 are plotted in Figure 3-18b. It proves that these relationships still can be fitted by a straight line. According to the results of calculations, an approximate expression for the maximum value of the vertical electrostatic force can be summarized as:

$$F_{\text{z, one,per L}} \approx \frac{0.274\varepsilon U^2}{g}, \quad F_{\text{z,one}} \approx \frac{0.274\varepsilon L U^2}{g} \tag{3.14}$$

3.6 Serpentine Springs Analysis

A serpentine spring gets its name from the meandering snake-like shape. This spring shape was chosen for our work because it allows the design of very flexible springs with a small spring surface area. This feature is beneficial for the foot print of the whole device. A schematic diagram of a serpentine spring is drawn in Figure 3-19. As depicted in the figure, the spring is composed of two different types of segments: span beams and connector beams. In order to simplify the calculation, we assumed that all the beams have the same width w_s. In the following, the length of span beams and connector beams will be noted a and b respectively, and n will represent the number of connector beams employed, for example in the Figure 3-19 below, n=8. Because of the symmetry of whole scanner structure, the serpentine springs motion are governed by a guided-end boundary condition, which means that only motion in preferred directions is allowed.

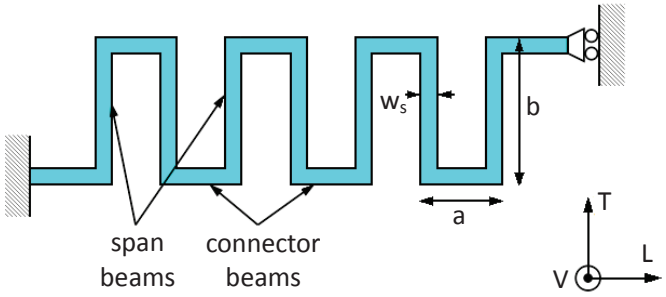

Figure 3-19. Schematic diagram of a serpentine spring.

3.6.1 Analytical Calculation of the Spring Constant

A detailed analytical derivation of the static spring constant under guided end condition is given in the thesis of Gary Keith Fedder [Fedder-1994]. It is based on energy methods with a solving of the boundary condition equations. The resulting formulas are listed below:

For even n, the spring constants in longitudinal direction (x direction in Fig 3-19), transverse direction (y direction) and vertical (out-of-plane, z direction) are given by:

$$k_L = \frac{12EI_{V,b}\left[\left(\tilde{a}+b\right)n^2 - 3bn + 2b\right]}{b^2\left[\left(3\tilde{a}^2 + 4\tilde{a}b + b^2\right)n^3 - 2b\left(5\tilde{a}+2b\right)n^2 + \left(5b^2 + 6\tilde{a}b - 9\tilde{a}^2\right)n - 2b^2\right]} \tag{3.15}$$

$$k_T = \frac{12EI_{V,b}\left[\left(3\tilde{a}+b\right)n - b\right]}{a^2 n\left[\left(3\tilde{a}^2 + 4\tilde{a}b + b^2\right)n^3 - 2b\left(5\tilde{a}+2b\right)n^2 + \left(5b^2 + 6\tilde{a}b - 9\tilde{a}^2\right)n - 2b^2\right]} \tag{3.16}$$

$$k_V = \frac{12S_{ea}S_{eb}S_{ga}S_{gb}}{\left\{\begin{array}{l} S_{eb}S_{ga}a^2\left(S_{gb}a + S_{ea}b\right)n^3 - 3S_{ea}S_{eb}S_{ga}a^2bn^2 + \\ S_{ea}b\left(2S_{eb}S_{ga}a^2 + 3S_{eb}S_{gb}ab + S_{ga}S_{gb}b^2\right)n - S_{ea}S_{ga}S_{gb}b^3 \end{array}\right\}} \tag{3.17}$$

For odd *n*,

$$k_L = \frac{12EI_{V,b}\left[\left(\tilde{a}+b\right)n-b\right]}{b^2\left(n-1\right)\left[\left(3\tilde{a}^2+4\tilde{a}b+b^2\right)n+3\tilde{a}^2-b^2\right]} \tag{3.18}$$

$$k_T = \frac{12EI_{V,b}}{a^2 n\left[\left(\tilde{a}+b\right)n^2-3bn+2b\right]} \tag{3.19}$$

$$k_V = \frac{12S_{ea}S_{eb}S_{ga}S_{gb}(\,S_{ga}b(n-1)+S_{en}an)}{\left\{\begin{array}{l} S_{eb}S_{ga}a^2\left(S_{eb}S_{gb}a^2+\left(S_{ea}S_{eb}+S_{ga}S_{gb}\right)ab+S_{ea}S_{ga}b^2\right)n^4- \\ S_{eb}S_{ga}a^2b\left(\left(3S_{ea}S_{eb}+S_{ga}S_{gb}\right)a+4S_{ea}S_{ga}b\right)n^3+ \\ +S_{ea}b\left(2S_{eb}^2S_{ga}a^3+\left(5S_{eb}S_{ga}^2+3S_{eb}^2S_{gb}\right)a^2b+4S_{eb}S_{ga}S_{gb}ab^2+S_{ga}^2S_{gb}b^3\right)n^2- \\ 2S_{ea}S_{ga}b^2\left(S_{eb}S_{ga}a^2+2S_{eb}S_{gb}ab+S_{ga}S_{gb}b^2\right)n+S_{ea}S_{gb}b^2\left(S_{ga}^2b^2-3S_{eb}^2a^2\right) \end{array}\right\}} \tag{3.20}$$

In the formulas above, $\tilde{a} \equiv a\, I_{V,b}/I_{V,a}$, $S_{ea} \equiv EI_{L,a}$, $S_{eb} \equiv EI_{L,b}$, $S_{ga} \equiv GJ_a$ and $S_{gb} \equiv GJ_b$.

I is the bending moment of inertial of one beam. It can be calculated as : $I_L = \int_{-w/2}^{w/2}\int_{-t/2}^{t/2} z^2 dxdz = \frac{t^3 w}{12}$, $I_V = \int_{-t/2}^{t/2}\int_{-w/2}^{w/2} x^2 dxdz = \frac{tw^3}{12}$. In our case, w_a=w_b=w_s, so $I_{L,a} = I_{L,b} = \frac{t^3 w_s}{12}$, $I_{V,a} = I_{V,b} = \frac{tw_s^3}{12}$, $\tilde{a} = a$.

J is the torsion constant for one beam of rectangular cross-section. It is given by: $J = \frac{1}{3}t^3 w\left(1-\frac{192}{\pi^5}\frac{t}{w}\sum_{i=1,odd}^{\infty}\frac{1}{i^5}\tanh\left(\frac{i\pi w}{2t}\right)\right)$, where $t < w$. And if $t > w$, the role of *t* and *w* need to be switched.

The formulas 3.15 to 3.20 were established for a spring made in an isotropic material. In the proposed DSOI technology of fabrication proposed for the scanner, the springs will be made in $Si/SiO_2/Si$ multilayer. Monocrystalline silicon is a cubic material with 3 independent elastic constants. In the general case it is an anisotropic material: the elastic constants of monocrystallline silicon depend on crystalline plane and on the direction in this plane. The crystallographic planes and directions are identified by miller indices *hkl* and are given for silicon in Figure 3-20 [Hopcroft-2010]. Ideally MEMS should be fabricated in (111) oriented Silicon because elastic constants are isotropic in this particular plane. Unfortunately double SOI wafers are only available in (100) crystallographic orientation (Figure 3-20b).

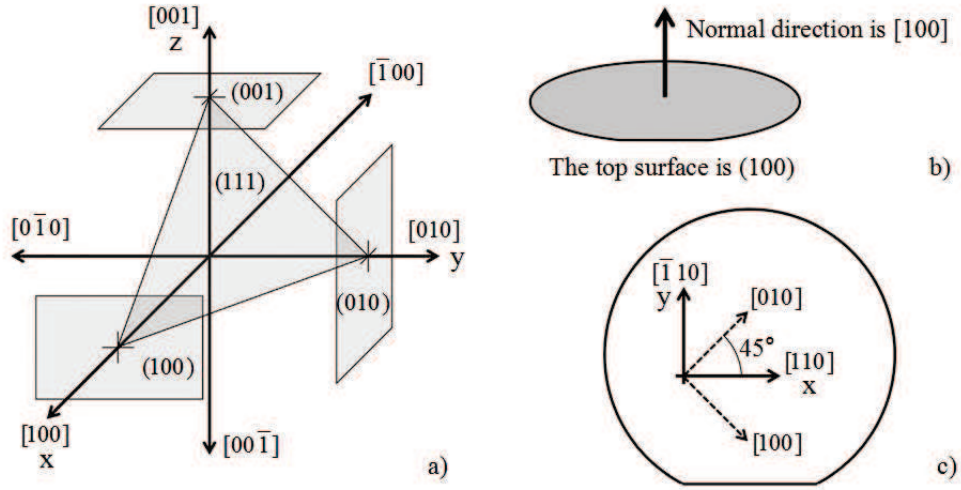

Figure 3-20. (a) Miller Indices in a cubic crystal. Typically [hkl] represents a direction vector given by hkl, and (hkl) represents the crystal surface perpendicular to vector [hkl]. And <hkl> represents the family of symmetric directions vectors equivalent to direction hkl, (b) a standard (100) Si wafer, (c) the primary flat of (100) wafer is along [110] direction.

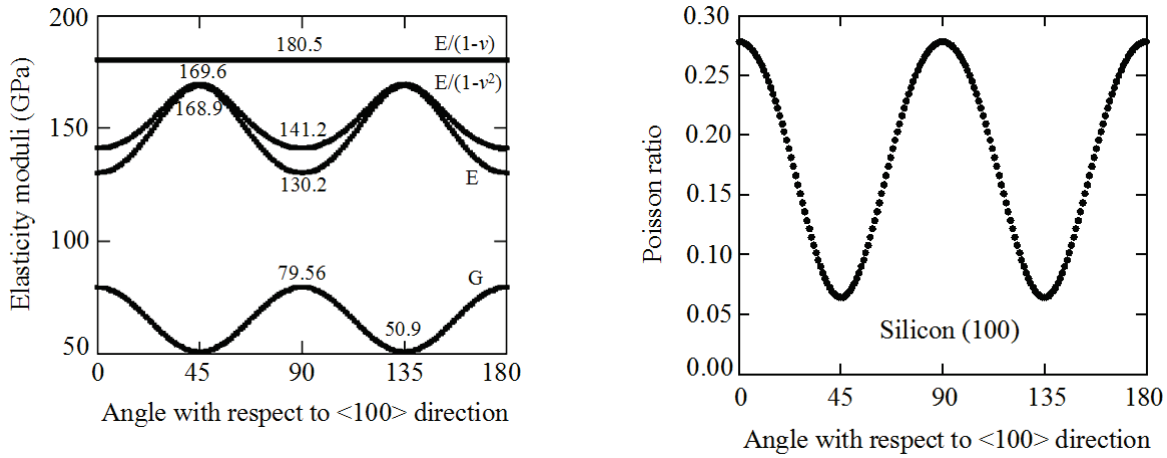

Figure 3-21. Variation of elastic constants of (100) silicon as function of direction in the plane, E=Young's Modulus, G= Shear modulus, ν= Poisson ratio.

As shown in Figure 3-21, in (100) planes, the Young's modulus varies from 130 GPa (in <100> directions) to 169 GPa (in <110> directions), the shear modulus varies from 79.6 GPa (<100> directions) to 51 GPa (<110> directions) and the Poisson ratio varies from 0.28 (<100> directions) to 0.064 (<110> directions). Let us recall that for (100) silicon the wafer main flat is along [110] direction which makes a -45° angle with [100] direction (Figure 3-20). In practice, it is much easier to align the scanner geometry with respect to the primary. So the orthotropic elastic constants used for the serpentine springs are:

$$E_x = E_y = 169GPa\,,\ E_z = 130GPa\,,\ v_{yz} = 0.36\,,\ v_{zx} = 0.28\,,\ v_{xy} = 0.064\,,$$

$$G_{yz} = G_{zx} = 79.6GPa\,,\ G_{xy} = 50.9GPa$$

3.6.2 FEM Simulation of Spring Constant

Finite Element Modeling of the spring constant was carried out by using ANSYS software. Two different interfaces are available for this software, APDL product launcher and Workbench platform. With a consideration of the feasibilities and conveniences of different interfaces, 2D modeling with scripts programming was realized by APDL launcher, and 3D modeling was performed with Workbench platform.

Separately constructed configurations and applied meshes for a same structure are shown in Figure 3-22. The obtained results are compared between analytical formula calculation, 2D modeling and 3D modeling in Table 3-6.

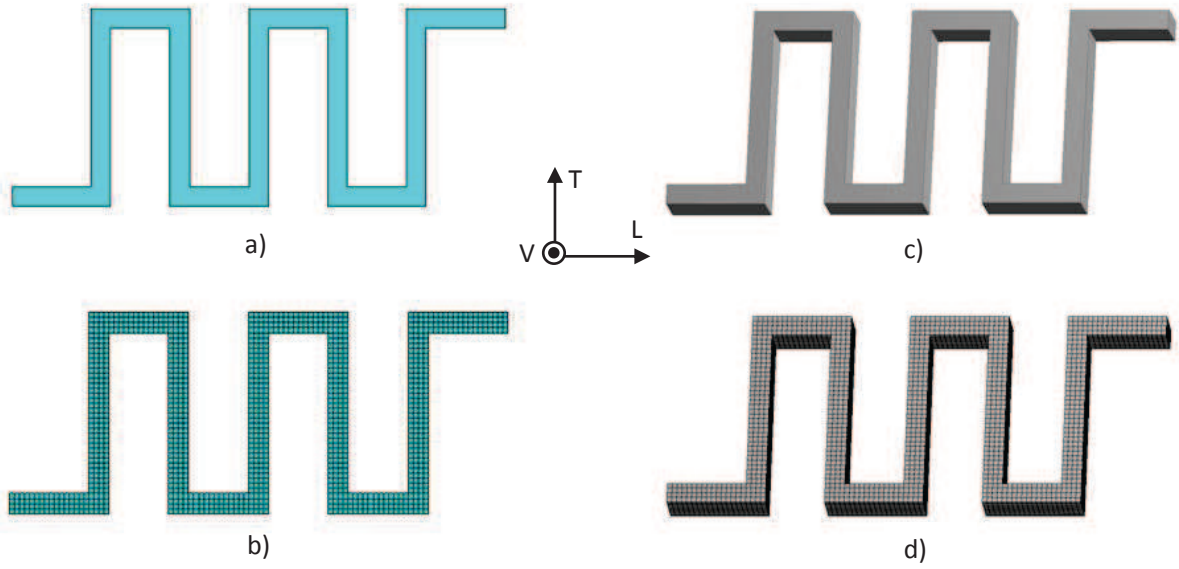

Figure 3-22. Geometric model (a) with applied rectangular mesh (b) for 2D modeling, and 3D geometry (c) with applied rectangular parallelepiped mesh (d) for the same serpentine spring. Dimension: n=6, a=10 µm, b=20 µm, w_s=2 µm, t=4 µm, orthotropic elastic constants.

Table 3-6. Result comparison between analytical calculation and FEM simulation.

Spring constant	**Analytical calculation** k_{Anal}	**2D modeling** k_{2D}	**3D modeling** k_{3D}	$(k_{Anal} - k_{3D})/k_{3D}$	$(k_{2D} - k_{3D})/k_{3D}$
k_L (N/m)	72.99	68.73	56.79	28.5 %	21 %
k_T (N/m)	22.24	20.61	19.15	16.1%	7.6%
k_V (N/m)	28.69	29.12	29.73	-3.5%	-2.1%

If we consider that values computed from 3D FEM simulations are the most accurate, we can see from the Table 3-6 that, for this example, both analytical simulations and 2D FEM simulations significantly overestimate the longitudinal spring constant k_L and the transverse spring constant k_T with the largest discrepancy occurring for k_L analytical values. The agreement between values of calculated out-of-plane spring constant k_V by the different methods is however quite good (error ≤3.5%). One

reason for the relatively large overestimation of spring constants k_L and k_T by analytical calculations might be the choice of length for each segment beam, since there are always overlapping areas between two connected beams. Indeed, when decreasing the width to length ratios of the connector beams (*w/a)* and of the span beams (*w/b)*, the calculated errors were found to decrease. We can conclude from these results that 3D FEM modeling is required for an accurate modeling of the spring constants. However the drawback of 3D simulation is the time-consuming work required for changing the spring geometry. On the contrary, variations of the geometrical parameters are very easy to perform for analytical and 2D FEM simulations and these methods are more suitable for an optimization task by script based programming. In a later section, an optimization work to establish the final choice of serpentine springs geometry will be performed mainly by using analytical calculation and 2D modeling methods.

3.6.3 Multilayer Spring Analysis

In the former two sections, we simplified the analysis of serpentine springs by considering only one silicon layer. But in reality, they are composed of a Si/SiO_2/Si (25/1.5/25 μm) multilayer. Here we evaluate the accuracy of this approximation. Two serpentine springs with the same geometries and similar meshing are modeled by 3D FEM simulation (Figure 3-23).

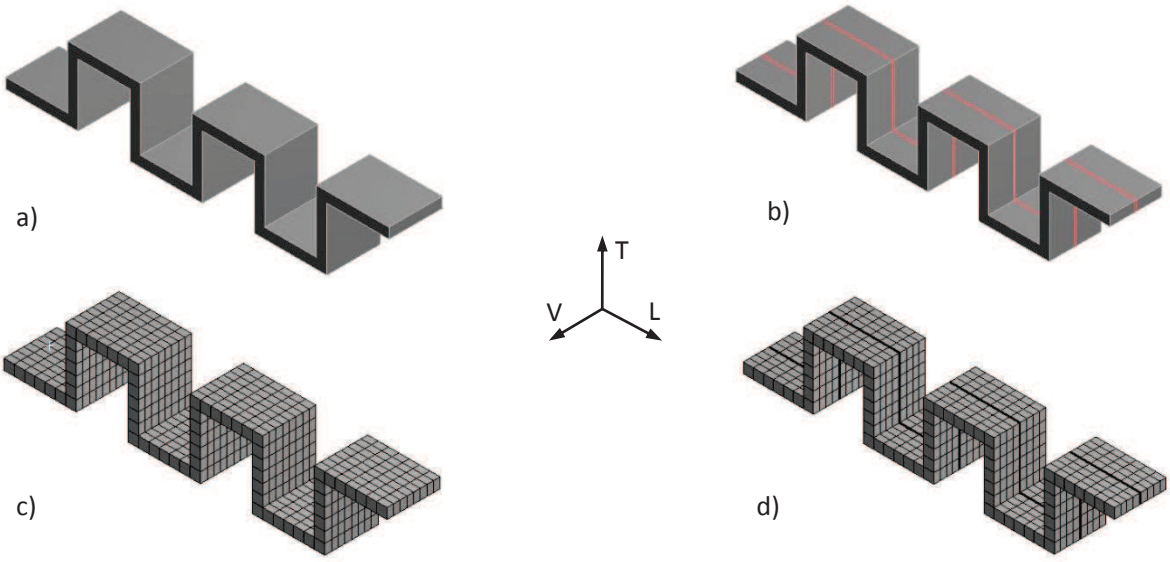

Figure 3-23. Serpentine springs constituted by (a) single polysilicon and (b)a Si/SiO_2/Si (25/1.5/25 μm) multilayer and their corresponding meshing (c), (d). For these two springs, n=6, a=70 μm, b=70 μm, w_s=10 μm, t=51.5 μm, Si layer uses orthotropic elastic constants as given before, SiO_2 uses the isotropic elastic constants: E=70 GPa, v=0.17 [Kim-1996].

Orthotropic elastic constants as given before were used for the Si layer. For the SiO_2 layer, the isotropic elastic constant used are E_{SiO2}=70 GPa and v_{SiO2}=0.17 [Kim-1996], $G_{SiO2}=E/2(1+v)$=29.9 GPa. The obtained results are listed in Table 3-7.

Table 3-7. Spring constants for different serpentine springs under free end and guided end boundary conditions.

	Free end boundary condition			Guided end boundary condition		
	Single layer spring $k_{f,s}$	Multilayer spring $k_{f,m}$	$(k_{f,s}- k_{f,m})/k_{f,m}$	Single layer spring $k_{g,s}$	Multilayer spring $k_{g,m}$	$(k_{g,s}- k_{g,m})/k_{f,m}$
k_L (N/m)	643.87	654.62	-1.64%	161.97	164.64	-1.62%
k_T (N/m)	23.96	24.36	-1.64%	116.9	118.86	-1.65%
k_V (N/m)	102.95	106.34	-3.19%	505.15	520.72	-2.99%

From table 3-7, we can conclude that the spring constants computed by considering only a single layer of silicon are only very slightly underestimated. The maximum relative difference occurs for k_y values and is lower than 3.2%. This is mainly due to the rather thin thickness of SiO_2 layer in the multilayer beam. Consequently, all the following spring optimization work will be based on the single layer approximation for simplification.

3.7 Overall Scanner Structure Design and Modeling

3.7.1 Electrostatic Force and Spring Constant Requirement for the Whole Structure

When considering the whole structure of our proposed movable scanner, all comb fingers are distributed along the four sides of a square frame, as shown in Figure 3-24. Because the structure is symmetrical along *x* and *y* axis, analysis will only be performed in *x* axis. Same results are expected for *y* axis.

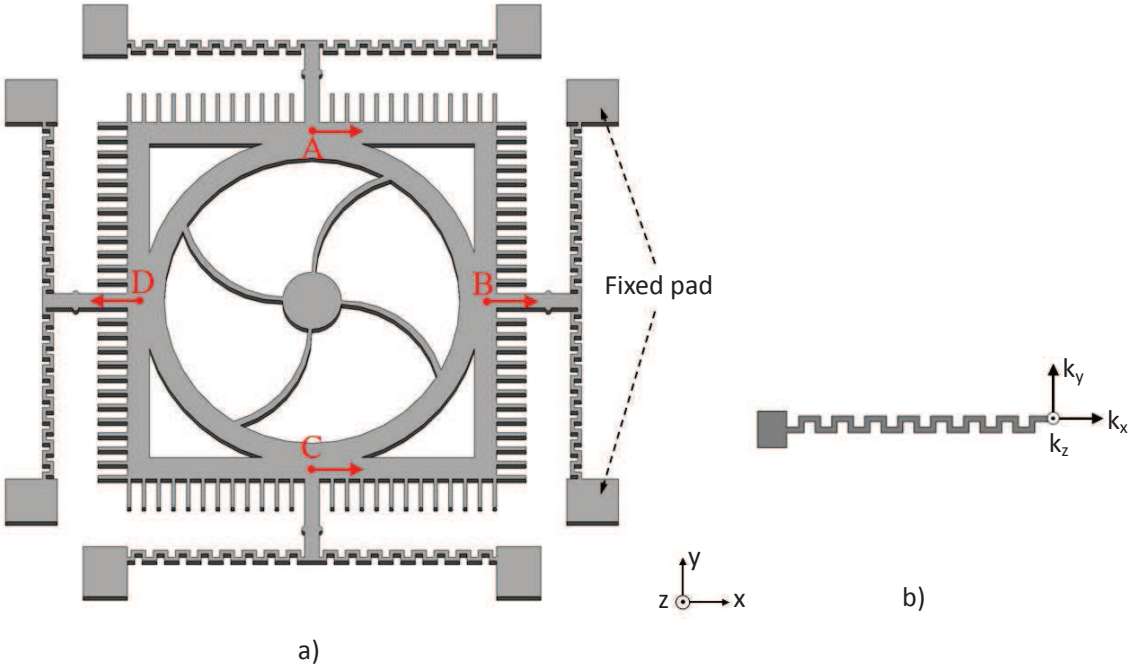

Figure 3-24. (a) Top view of movable part of the proposed scanner with distributed comb fingers and serpentine springs. Red arrows represent x directional electrostatic force applied by four parts of the distributed comb fingers. (b) One serpentine spring with indicated spring constants in different coordinate axis.

From Figure 3-24 above, we can obtain the total spring constants and exerted forces of the whole structure:

$$k_{x,tot} = k_{y,tot} = 4(k_L + k_T) \tag{3.21}$$

$$k_{z,tot} = 8k_V \tag{3.22}$$

$$F_{z,tot} = 4nF_{z,one} \tag{3.23}$$

$$F_{x,tot} = F_A + F_B + F_C - F_D \tag{3.24}$$

with, $F_B = F_D = nF_{y,one}$, $F_A = F_C = nF^*_{x,one}$,

where n is the number of comb finger pairs on one side of the square frame.

In order to fully achieve the maximum motion range, the total spring constant in z direction should fulfill the equation:

$$F_{z,tot} = k_{z,tot} O_{max} \tag{3.25}$$

By combining (3.14) in (3.25), the desired vertical spring constant can be written as:

$$k_V \approx \frac{0.137 n\varepsilon L U^2}{g O_{max}} \tag{3.26}$$

The lateral pull-in force as described before also needs to be considered for the whole structure. Thus the total pull-in force along x direction is given by:

$$F_{x,tot} = 2nF^*_{x,one} = n\varepsilon LOU^2 \left[\frac{1}{(g - x)^2} - \frac{1}{(g + x)^2} \right] \tag{3.27}$$

where n is the number of comb finger pairs on one side of the square frame.

Then, a parameter of lateral instability can be defined as:

$$K = \frac{\partial F_{x,tot}}{\partial x} = 2n\varepsilon LOV^2 \left[\frac{1}{(g-x)^3} + \frac{1}{(g+x)^3} \right] \tag{3.28}$$

$$K_{min} = \frac{4n\varepsilon LO_{max} V^2}{g^3} \quad (x=0,\ O=O_{max}) \tag{3.29}$$

In order to understand the effect of misalignment, the relative instability parameter (K/K_{min}) is calculated as a function of relative misalignment, as plotted in Figure 3-25a. It shows that K increase rapidly with misalignment, when x=0.2g, K=1.26K_{min}, and when x=0.4g, K=2.5K_{min}. As a compromise, the tolerable lateral misalignment due to fabrication issues is set to be 1 μm (x=0.2g) for following design.

To prevent a possible pull-in at maximum motion range ($O=O_{max}$), the total spring constant in x direction should be at least larger than K_{min}.

$$k_{x,tot} = 4(k_T + k_L) > 1.26K_{min} = \frac{5.04n\varepsilon LO_{max} U^2}{g^3} \tag{3.30}$$

which means, $$k_T + k_L > \frac{1.26n\varepsilon LO_{max} U^2}{g^3} \tag{3.31}$$

Then comparing (3.26) and (3.31), we can obtain an important spring constant requirement:

$$\frac{k_T + k_L}{k_V} > \frac{1.26 O_{max}^2}{0.137 g^2} = 125.9 \quad (O_{max}= 18.5\ \mu m,\ g=5\ \mu m) \tag{3.32}$$

As a conclusion for the formula deducing above, two major requirements must be met for the spring design: equation 3.26 for maximum vertical motion range and formula 3.32 for lateral stability.

Besides the requirement for spring design, a half cylinder stopper was designed and placed near the main supporting beam (Figure 3-25b). Since this circular arc can collect both x and y directional displacement, it acts as a stopper in both directions. In case of unwanted pull-in, the contact is made to an unreleased isolated island rather than to the fixed comb fingers to prevent a destructive short-circuit.

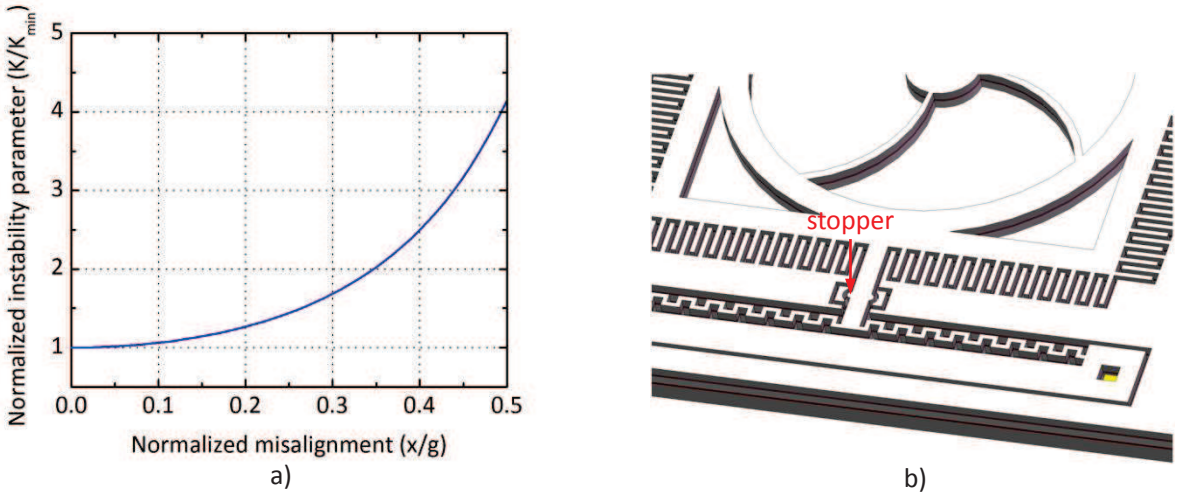

Figure 3-25. (a) Relationship between K/K_{min} and x/g. (b) Part of the movable scanner with collision stopper.

3.7.2 Final Comb Drive Sizing and Serpentine Springs Optimization

Serpentine springs with a low vertical spring constant (k_V) and maximized sum of in-plane spring constants (k_L+k_T) are required according to the analysis above. An optimization has been carried out by combining all the results obtained previously. This optimization was performed by following the methodology described by the flow chart of Figure 3-26.

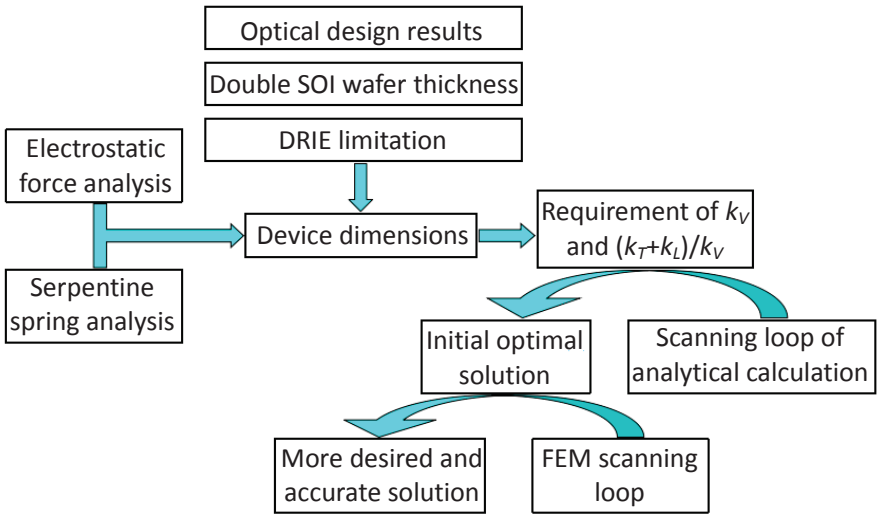

Figure 3-26. Flow chart of optimization sequence.

Firstly we start from the optical design results that give the diameter of open frame. The total length of comb drives and of serpentine springs should not exceed this diameter. Then the thickness of double SOI wafer ($Si/SiO_2/Si/SiO_2/Si$, 25/1.5/25/1/380 μm) does not only define the maximum motion range, but also the minimum surface patterns dimensions. All the springs, frames and electrostatic combs will be fabricated by Deep Reactive Ion Etching (DRIE) and release from the backside of the $Si/SiO_2/Si$ multilayer. Since the DRIE etching of the three layers is not a conventional step, a conservative value of 10 was chosen for the maximum aspect ratio (depth to lateral dimensions) of the patterns etched by DRIE. In order to avoid etching non uniformities resulting from the well-known Aspect Ratio Dependent Etching (ARDE) effect, all trenches during the first patterning were set to have the same width (5 μm). Then the top-view length and width of comb fingers were chosen to be 400 μm and 10 μm respectively, with the purpose to insure in-plane aspect ratio L_c/w_c below 50 in order to limit fabrication issues. The number of comb finger pairs on each side of the open frame (n) could then be calculated to be 156.

In order to reduce the initial bending due to the weight of movable part, we considered that the total generated electrostatic force should be always 10 times larger than the calculated weight. This implies that the applied voltage must be larger than 50V. According to Figure 3-18, we can expect a motion range of D=20 μm, or O_{max}=18.5 μm, where the electrostatic force are still very close to its maximum value. Then by using expressions 3.26 and 3.32, we can compute the desired values of vertical spring constant (k_V) and sum of in-plane spring constants (k_L+k_T). A scanning loop of analytical calculations was firstly programmed to search for an optimal solution for the chosen k_z while maximizing k_L+k_T. The criterion chosen for this scanning are: $w_s \geq g$, $a \geq 3g$, $b \geq 3g$, total length L<2400 μm, expressions 3.26 and 3.32. A trade-off between the maximum value of k_L+k_T and the minimum number of meander beams n was made for the final choice of spring dimensions in order to limit potential fabrication issues. Afterwards, another loop varying only n based on 2D Finite Element Modeling (FEM) was performed to acquire more desired and accurate spring constants.

Different parameters of the analysis or optimization discussed above are listed in Table 3-8. Finally proposed serpentine spring and resulting spring constants are given in Table 3-9.

Table 3-8. Different parameters of the analysis and optimization.

Items	Values
Gap (g)	5 μm
Comb fingers	length (L_c): 400 μm width (w_c): 10 μm thickness (t_c): 51.5 (25/1.5/25) μm
Number of comb finger pairs on one side of open frame (n)	156
Maximum applied voltage (U)	50V
Weight of movable structure	14.5 μN
Total maximum vertical electrostatic force	269.6 μN
Expected motion range	D=20 μm , O_{max}=18.5 μm

Table 3-9. Proposed serpentine spring and resulting spring constants.

Proposed serpentine spring	n=38, a=70 μm , b=70 μm , w=10 μm , t=51.5 μm .
Spring constant of one serpentine spring	Analytical calculation: k_L=267.1 N/m, k_T=0.382 N/m, k_V=1.207 N/m; $(k_L+k_T)/k_V$=221.6 2D FEM simulation: k_L=281.4 N/m, k_T=0.396 N/m, k_V=1.421 N/m; $(k_L+k_T)/k_V$=198.3

3.7.3 Displacement Simulation of Overall Structure

3D FEM simulation of the overall structure loaded by the electrostatic force induced by vertical comb drives was performed. Since this geometry is very complicated, it was firstly built by a 3D mechanical CAD software, then imported to ANSYS Workbench platform for further analysis. The built 3D geometry is shown in Figure 3-27a and applied meshing is shown in Figure 3-25b. Because solver pivot problems were encountered for hexahedral meshing, tetrahedral meshing has been used for this simulation. As shown in Figure 3-27, very fine meshes were used for serpentine springs, and much coarser meshes were applied for other parts. From the result, we could obtain the spring constant of the whole structure: $k_{z,tot}$=11.9 N/m , which is close to 2D FEM result of serpentine spring calculated before: $k_{z,tot}=8k_V=8\times1.421=11.37$ N/m.

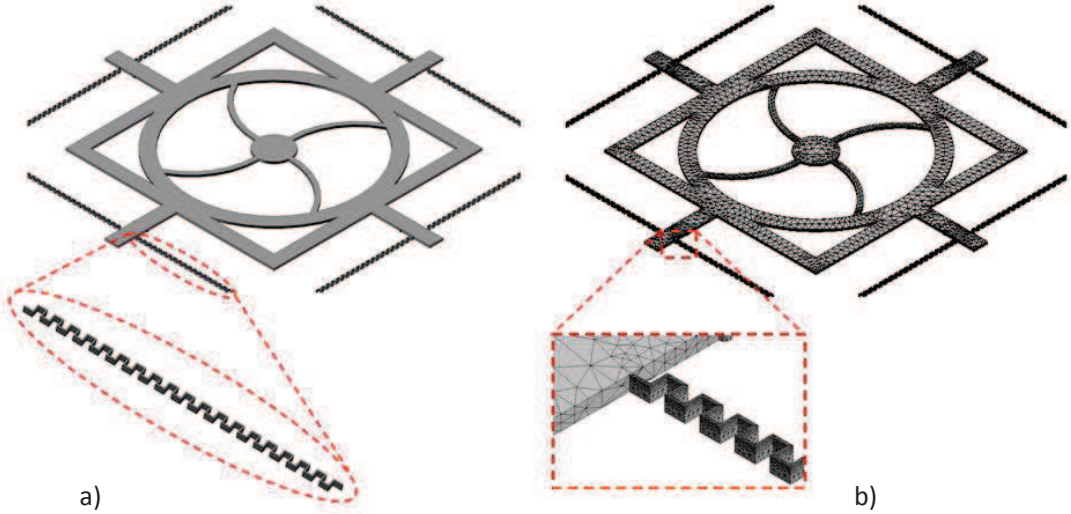

Figure 3-27. (a) 3D geometry of whole structure and (b) applied meshing.

By combining the obtained spring constant and electrostatic force (Table 3-8 and 3-9), we could deduce the final displacement from the intersection point of these two curves (plotted in Figure 3-28).

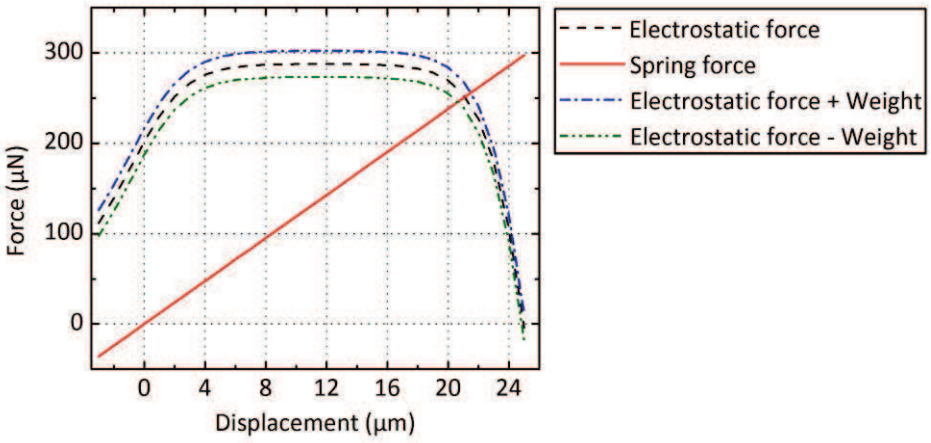

Figure 3-28. Electrostatic force, weight and spring restoring force as function of vertical displacement of the scanner structure and resulting equilibrium positions for a 50 V applied voltage.

Considering the influence of weight, when suspended structure moves upward, F_{elec}-F_{weig}=F_{spring}; when it moves downward, F_{elec}+F_{weig}=F_{spring}. As a consequence, the equilibrium position in Figure 3-28 above indicates that the final achieved displacement is d=20.5 μm for upward movement and is d=21.5 μm for downward movement.

The contour images of displacement and Von Mises stress distribution under 50 V applied voltage are shown in Figure 3-29a and b, respectively. Figure 3-29a demonstrates that most of the displacement is produced only by spring bending while the Si frame remains flat. Reference mirror could keep a peak to valley flatness below 2 nm during motion, which is essential for interferometric measurement. But this simulation only verifies the bending produced by motion, the reference mirror may still suffer from non-negligible bending resulting from internal stress of multilayer and residual stress of metal film deposition, which will be discussed in later chapter. Besides, stress induced by the

motion is mainly concentrated in the springs (see Figure 3-29b) and its maximum value near the anchors (~40 MPa) is far below the facture strength of single crystal silicon (~1-4 GPa).

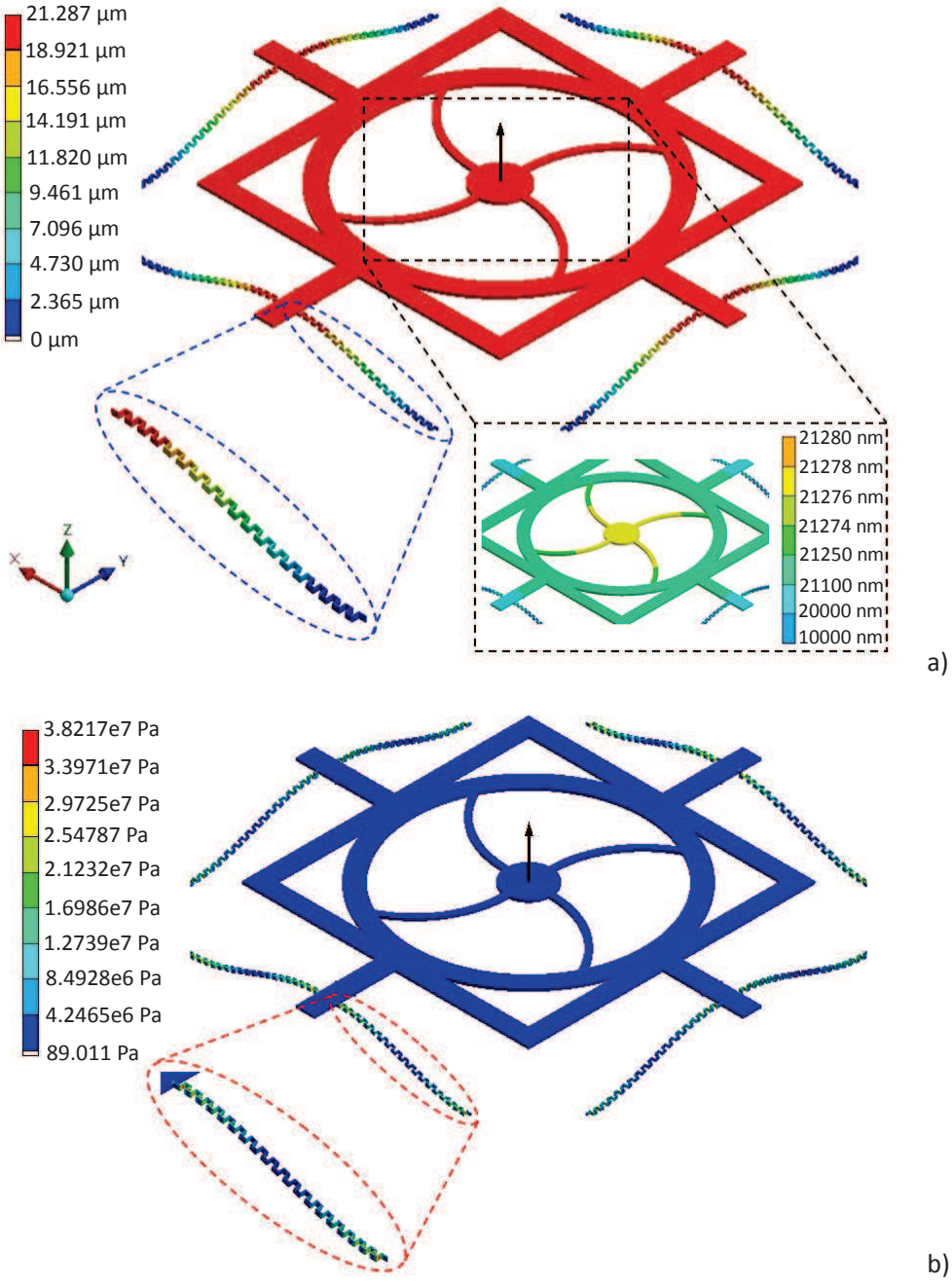

Figure 3-29. Contour images of (a) displacement and (b) stress distribution under 50 V applied voltage.

By using the method described above for finding the equilibrium position with different applied voltages (Figure 3-30a), the resulting curve of vertical displacement versus applied voltage is plotted in Figure 3-30b. Below 45V applied voltage, the equilibrium state is achieved when electrostatic force stays at its maximum value. But above 45V, the electrostatic force at equilibrium position drops dramatically and as a consequence, the achieved displacement is no longer proportional to the square

of applied voltage. This can be seen in Figure 3-30b where a bend of the curve can be observed around 45V. Anyhow, a translation range of ±20 µm should be safely obtained for a voltage range of ± 50 V.

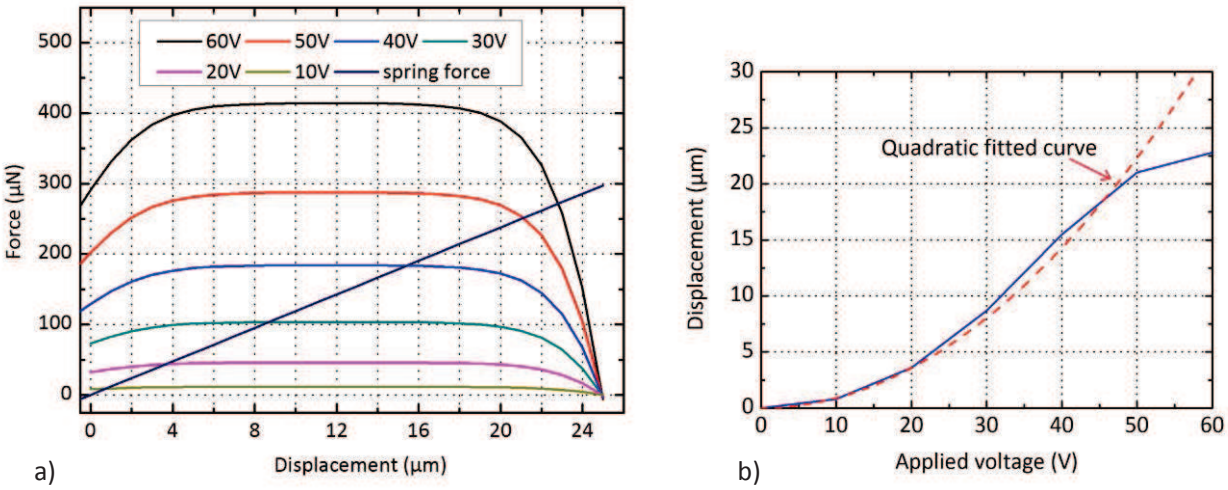

Figure 3-30. (a) Equilibrium position between spring force and electrostatic force with different applied voltage. (b) Curve of displacement with a function of applied voltage.

The average slope is about 0.4 µm/V. For phase shifting measurements the required motion range is below 1 µm. If we reasonably assume a global regulation level better than $5x10^{-4}$ for the applied voltage (including noise, ripple and stability), the open loop scanner resolution in this range would be better than 0.4 nm what is totally suitable for phase shifting measurements. The minimum resolution obtained at the end of the scanning range would be 10 nm what is still acceptable for low coherence scanning interferometry. With a close loop configuration using a capacitive sensor a resolution of 10^{-6} can be expected and the scanner resolution would be very good. The measurement quality should then not be limited by the performances of the MEMS scanner but by drifts and vibrations altering the distance between the beam splitter and the measured sample.

3.7.4 Mechanical Resonance of Overall Structure

To obtain a stable positioning of the mirror in the disturbing environment that can be found in a laboratory room or in a clean room, it is desirable that the resonant frequencies of the mechanical structure of the scanner are above the frequency range where the acoustic and other vibrations sources are large. For a typical environment this means that the resonant frequencies should ideally be above a few kHz. A high fundamental resonant frequency f_0 is also desirable to get a high response time suitable for fast measurements. The response time τ is roughly given by $3/f_0$.

For a simple spring-mass model, the fundamental resonant frequency of a harmonic oscillator is given by:

$$f_0 = \frac{\omega_0}{2\pi} = \frac{1}{2\pi}\sqrt{\frac{k}{m}} \tag{3.33}$$

where k is the spring constant and m is the total mass. Using the numerical values given before, the fundamental resonance frequency of the overall structure was estimated to be:

$$f_0 = \frac{1}{2\pi}\sqrt{\frac{k}{m}} = \frac{1}{2\pi}\sqrt{\frac{11.9}{1.478\times10^{-6}}} = 451.8Hz \tag{3.34}$$

Higher modes of resonance frequencies have also been investigated by FEM modal analysis. Figure 3-31 shows 3D views of the first 8 mode shapes and Table 3-10 gives the corresponding resonant frequencies.

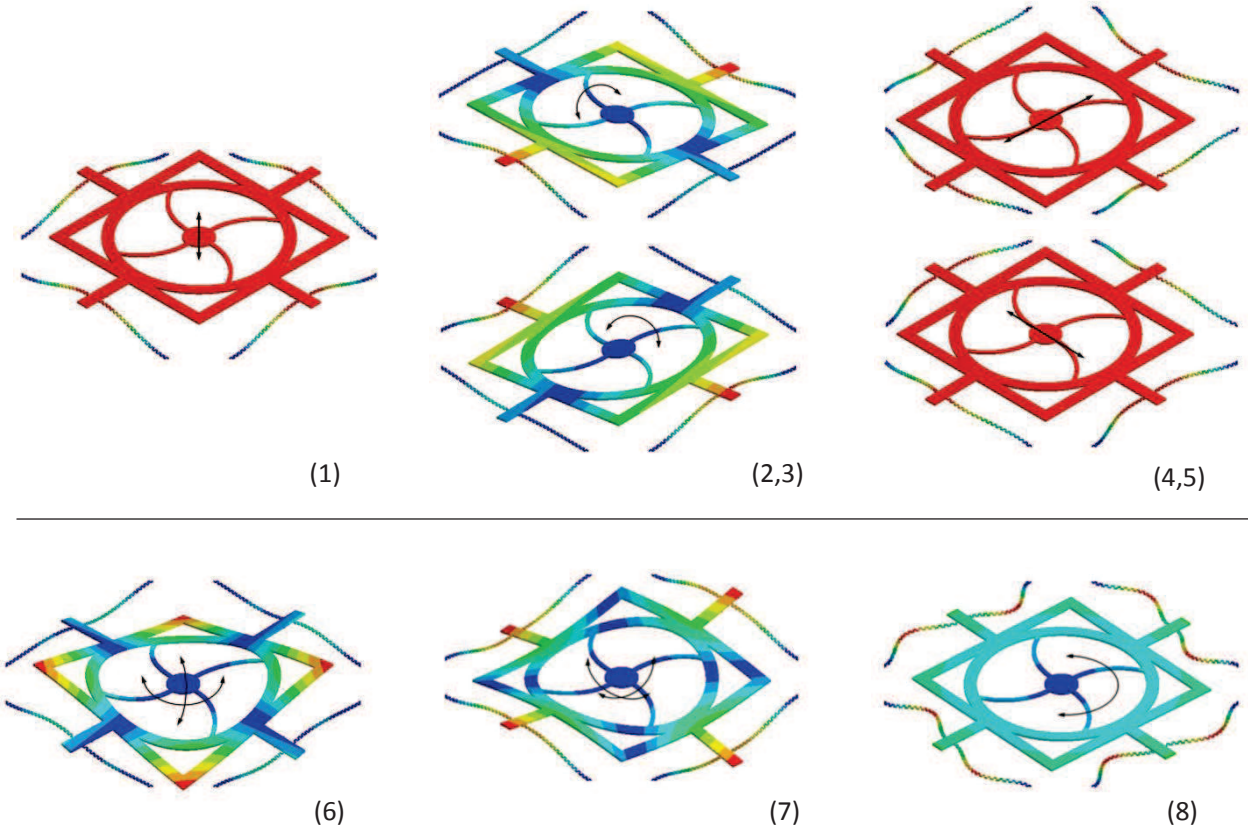

Figure 3-31. Schematic graphic representation of different mechanical resonance modes.

Table 3-10. Frequencies of difference resonance modes.

Resonance Mode	Frequency (Hz)
1	464.6
2	702.5
3	702.7
4	4568.5
5	4628
6	7006.7
7	7407.5
8	8941.1

The first 3 resonant frequencies are relatively low and this is not favorable for the immunity of the scanner to external disturbances if the corresponding quality factors Q of the resonances in air are high. High Q values are possible because the scanner structure is mainly made in monocrystalline silicon and is an open structure. Simulation and experimental evaluation of scanner structure damping in air was not undertaken in this thesis and will have to be made in the future. According to formula 3.33, the relatively low resonant frequencies are mainly due to the heavy mass of movable part and the low stiffness of serpentine springs. In principle the resonant frequencies could be increased by using stiffer springs and by generating a larger electrostatic force. This would be also favorable to reduce the effect of gravity. A larger electrostatic force can be obtained by using larger applied voltages, by reducing the fingers gaps of the electrostatic comb drives, or both. Eventually the scanner weight could also be reduced by using a smaller frame width or thickness but it would then become more deformable and achieve smaller motion range. Some trade-offs of all these influence factors will have to be considered for a future improved version of the scanner.

3.7.5 Electromechanical Stability Analysis of Overall Structure

It is common that due to some fabrication issues or non-uniform property of materials, the fabricated device will not work ideally as expected. Here we analyze the stability of the whole device under asymmetric applied vertical electrostatic force and unwanted lateral force. Then the maximum tolerable error range of the whole device will be determined.

When the device achieves its maximum motion range of 21 μm, if one side of vertical comb fingers has produced 10% larger electrostatic vertical force than others, the open frame will undergo some rotational tilt (Figure 3-32). From an FEM simulation, the produced height difference between edges A and B was found to be 888nm, which corresponds to a tilt of 1.78×10^{-4}°. This angle seems negligible, but the height different is large enough to affect the electrostatic force produced by two adjacent comb fingers. Considering the ratio between this extra force and displacement, we can define $K=F/d=0.1F_{one,side}/H_{differ}$. The spring constant of the whole device is $k_{z,tot}=4F_{one,side}/21$ μm, then we can find $K=0.59k_{z,tot}$., which demonstrates that this extra force can produce more displacement that symmetric applied electrostatic force.

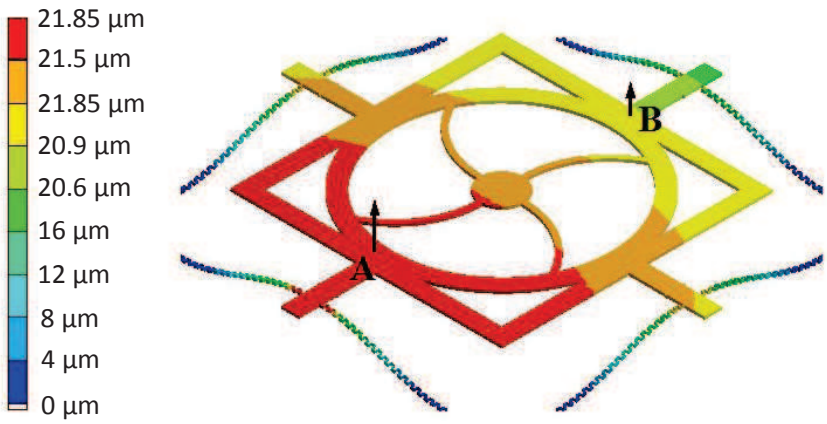

Figure 3-32. Displacement produced by asymmetric vertical electrostatic force under a base displacement of 21 μm.

If the gaps on both sides of a movable finger are not equal, a large lateral electrostatic force will be generated and may produce a side pull-in phenomenon. In order to evaluate the possibility of fingers stiction by pull-in, we first analyzed the spring constant of the whole device in lateral direction by FEM simulation (Figure 3-33a). The obtained result is: $k_{x,tot}$=1172 N/m , not far from 2D FEM result of serpentine spring calculated before: $k_{x,tot}=4(k_x+k_y)$=1127 N/m. Then the generated lateral electrostatic force was simulated by 2D FEM under a base displacement of 21 μm and by varying only gap distance (Figure 3-33b). Finally the curves of lateral electrostatic force and spring force in the case of misalignment are plotted in Figure 3-33c.

As shown in Figure 3-33c above, initially the lateral electrostatic force is smaller than the spring restoring force and no pull-in instability will occur. Then when $\Delta g/g$=0.3 or Δg=1.5 μm , the pull-in threshold position is reached. When Δg becomes larger, the electrostatic force will exceed the restoring force and will push the movable comb fingers until they touch the fixed comb fingers. This side pull-in effect will occur when the motion exceeds 1/3 of the gap. As a consequence, the maximum tolerable misalignment of comb fingers is $\Delta g/g$=0.3 or Δg=1.5 μm .

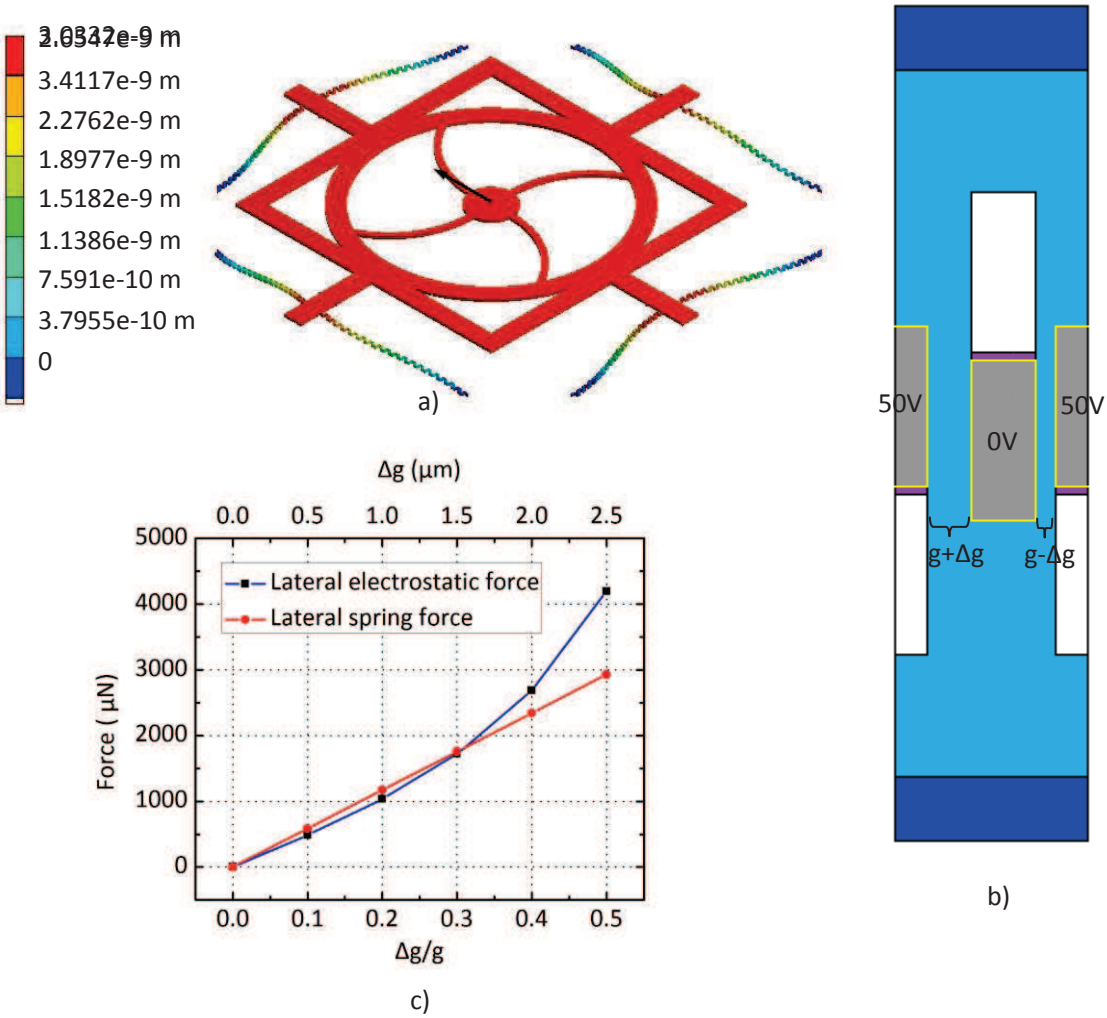

Figure 3-33. (a) Displacement under 4 μN applied parallel force; (b) Electrostatic force simulation under 21μm base displacement; (c) Curve of lateral electrostatic force and spring force with a function of misalignment.

3.8 Conclusion

The proposed integrated tunable Mirau interferometer has two parts that will be bonded at the end of the fabrication process: a reference mirror vertical scanner intended to be fabricated from a double SOI wafer and a multilayer beam splitter membrane that can be fabricated on a Si wafer. The designed mirror scanner is composed of a thick frame which holds the reference mirror by means of stress relaxing curved beams. This frame is suspended by serpentine springs and actuated by vertical electrostatic comb drive actuators. This mirror scanner was designed to have a large translation range (±20µm) suitable for low coherence interferometry. The selected beam splitter has an approximately constant reflectance coefficient (50%) in a broad wavelength range (550-800nm) and for a large range of incidence angles. It is sufficiently thin to limit spherical aberrations but it introduces a too large phase difference in the reflected and transmitted beam for its optimum use with a white light LED or other broadband source. This means that the designed integrated Mirau interferometer is suitable for phase shifting measurements in the 550-800 nm range and for low coherence interferometry measurements but with a limited spectral width (50 nm) and thus a degraded vertical resolution.

Electromechanical modeling and sizing of the scanner were performed from analytical calculations and finite element simulations. They are based on $Si/SiO_2/Si$ (25/1.5/25 µm) composite structure, a maximum value of ~10 for the aspect ratio of the electrostatic gaps and for the length to width aspect ratio of the fingers and a 40-60V maximum actuation voltage. Simulated electrostatic force value is much smaller than analytically calculated ones, and it is found to result from the changing of electric field disctribution due to the adding of conductors and insulators. A correction factor of 0.274 is then given for this approximation. It is also shown that the fringing electrostatic field is sufficient to generate a significant vertical force without the need of a vertical offset between movable and fixed fingers and that the actuation force is constant in most of the 0-20 µm translation range.

Serpentine springs were chosen to get low spring constant with a minimized footprint. Simulated spring constants from different analyzing methods can agree well with each other. The influence of intermediate SiO_2 layer is considered negligible because less than 3.5% difference was found. Optimization by analytical and FEM simulations allowed the sizing of springs with a very high lateral to vertical spring constant ratio ($k_L+k_T=198k_V$).

Global electromechanical simulations showed that a ±20µm mirror translation range can be achieved with an applied voltage of ±50V with a reasonable number of electrostatic fingers (4×156) and a negligible deformation of the reference mirror. In open loop configuration, a translation resolution below 0.5 nm should be possible for translation ranges required for phase shifting measurements while a 10 nm resolution is expected for a translation near 20µm. A close loop operation with capacitive detection should be able to get a resolution largely below 1nm in the full translation range.

The design is relatively robust: the translation generates a maximum stress far below the Si fracture strength and lateral pull-in of the vertical electrostatic combs is predicted to occur only for a dissymmetry of the finger electrostatic gap larger than 1.5 µm. However two limitations could not be avoided: the reference mirror position is significantly affected by weight of the frame structure and the

lowest resonant frequency of the mechanical structure (464 Hz) is likely too low to get a good immunity to external disturbances. It is however sufficiently high to get a fast response time (6 ms) suitable for fast interferometry measurements.

4. Technological Tests and Fabrication of a Micro-Mirror Vertical Scanner

Introduction

As seen in Chapter 3, the electromechanical design of the micro-mirror vertical scanner is based on electrostatic actuation with vertical electrostatic comb drives. In-plane electrostatic combs are used in the MEMS field since the 80's while vertical combs were introduced much later. Many different fabrication processes were proposed for these vertical comb drives, so we found it useful to perform a review of the published methods in order to choose and develop a new fabrication process. This review will be presented in section 4.1.

Then we will describe the original fabrication process we propose for the mirror scanner (section 4.2) and will give the experimental procedures and results of the technological tests of the most critical steps (section 4.3-4.6). This will include double SOI wafer fabrication, double SOI wafer Deep reactive Ion Etching (DRIE) with a dry film masking layer and two levels patterning with a single dry film mask.

Then results of fabrication of the whole electromechanical mirror scanner will be given and discussed in section 4.6.

Another critical part of the Mirau interferometer is the beam splitter. The technology of fabrication of semi-reflective dielectric multilayer mirror membranes was developed previously in IEF by H. Bertin [Bertin-2013-2] and will be only summarized in section 4.7.

4.1 Review of Vertical Comb Drive Technology

An electromechanical mirror scanner based on electrostatic actuation with vertical comb drive micro-scanner has been chosen in this work to realize large range and bidirectional out-of-plane motion. Many authors have proposed fabrication methods based on the requirement of specialized functions and accessibility of different fabrication equipments [Gallagher-2012].

A common critical issue during vertical comb drive fabrication is to minimize the misalignment between movable and fixed comb fingers in horizontal direction that will eventually produces a large lateral force and an unwanted pull-in side instability. Nowadays the common strategy to prevent this issue is the use of self-alignment technology, by which different comb fingers are simultaneously patterned by one single mask level.

Another issue is to obtain a vertical offset or a height difference between movable and fixed fingers in order to get a vertical electrostatic force, event at initial rest position, when the electrostatic combs are biased. This issue has challenged and been creatively solved by many scientific researchers who have proposed various fabrication processes combining of different mature or innovative technologies.

In the following we will review the recent and practical methods which have been proposed in the literatures. Let us emphasize that electrostatic comb drives also have a large number of applications in lateral and rotational actuations. But because of the main requirements of our mirror scanner, only out-of-plane (vertical) actuation will be considered in this review.

1) Electrostatic Levitation

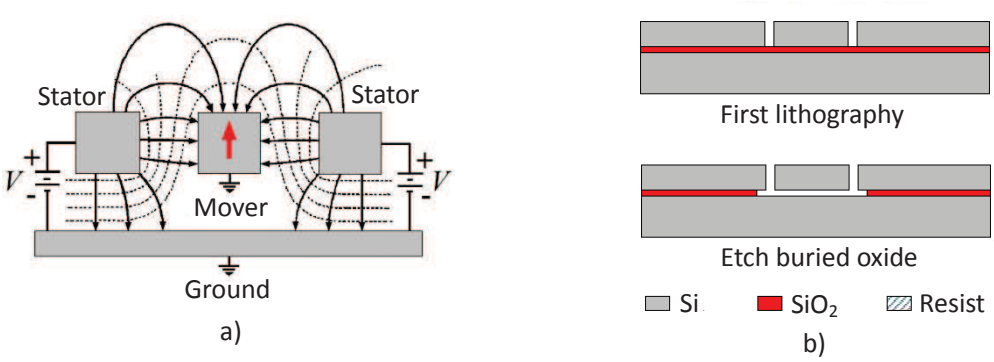

Figure 4-1. (a) Electric field distribution for vertical actuation and (b) simplified fabrication process flow chart of electrostatic levitation method of vertical comb drive.

Electrostatic levitation is usually an unwanted out-of-plane motion of many laterally driven actuators and sensors [Tang-1992]. It arises from the asymmetric electric field when the movable part and the underlying substrate are biased at the same ground potential (Figure 4-1a). Many researches on this topic are aiming to control or eliminate the levitation. However, with proper design and by adding a capacitance feedback, levitation effect can also be utilized for out-of-plane translation. It was for example applied to phase shifting interferometry [Lee-2003], to piezoelectric coefficient measurements [Wooldridge-2013] and to MEMS strain gauges [Azevedo-2008]. This actuation method needs a very simply fabrication process (shown in Figure 4-1b), but severely suffers from a

limited achievable motion range. Without considering the restoring force, the movable parts have a same equilibrium position independent of applied voltage. Maximum vertical travel range is completely limited by this equilibrium position. Referring to published results, their achieved travel ranges are all very small, for instance 1.22 µm in [Tang-1992], 1 µm in [Wooldridge-2013] and 1.2 µm in [Lee-2003].

2) Resonant actuation

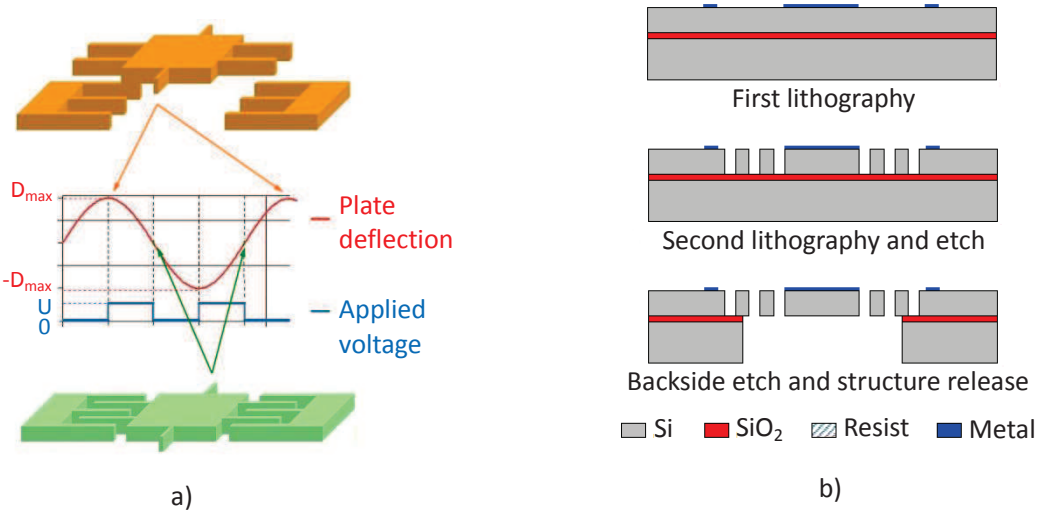

Figure 4-2. (a) Driving principle of electrostatic resonance actuation and (b) its simplified fabrication process flow chart.

It is well known that motion amplitude can be extended by taking benefit of mechanical resonance. Indeed at resonance, the amplitude is increased by a factor Q, where Q is the quality factor. To implement this type of actuation, the vertical comb is driven by a sinusoidal voltage at twice the natural resonant frequency (ω_0) of the movable mechanical part even though the actual device oscillates at its eigenmode. This resonant frequency ω_0 can be chosen to correspond to a vibration mode that is compatible with the desired motion. Actuation by square-wave at frequency of $2\omega_0$ is also possible as shown in Figure 4-2a. Because low damping, stability and precise frequency control are achievable in micro systems, sub harmonic excitation at $\omega=\omega_0/2n$ can also be used [Turner-1998], where n is a positive integer. This actuation method has the advantage of low power consumption and a low sensitivity to environmental shocks and vibrations. Static deformation is unable to be realized by resonant actuation, but it can provide a well controlled 1D or 2D scanning, what has been applied to Fourier transform spectrometers [Sandner-2008] [Ataman-2006] and torsional micro-scanners [Aslihan-2010] [Caglar-2006]. Its fabrication process is very simple (shown in Figure 4-2b) since only in-plane comb fingers fabrication is required. Published works show that a 200 µm stroke can be reached under 500 Pa pressure [Sandner-2008] and a 106 µm stroke under ambient pressure [Ataman-2006]. These values seem to be the largest ones that can be achieved by electrostatic actuation with vertical comb drives.

3) Artificial offset

This method generally adopts the fabrication of springs, movable and fixed comb fingers by a single etching of the top device layer of a SOI wafer. After that, various mechanisms can be utilized to create a vertical offset between movable and fixed comb fingers, as shown in Figure 4-3. K. H. Jeong et al. [Jeong-2005] used the dissimilar thermal expansion coefficients of bimorph cantilevers (silicon

oxide and silicon) to move the fixed part vertically. J.C. Chiou et al. [Chiou-2005] and M. Sasaki et al. [Sasaki-2004] also adopted this mechanism and eventually added a post annealing process to enhance the initial vertical displacement. Whereas, J. Kim et al. [Kim-2006] used a pillar in a lid wafer to push movable part and induce a plastic deformation. According to the reported results, this method can achieve a rather large motion range, e.g. 30 μm in [Jeong-2005] and 50 μm in [Sasaki-2004]. However, its reproducibility and the lateral alignment accuracy of different combs after initial artificial displacement are still questionable.

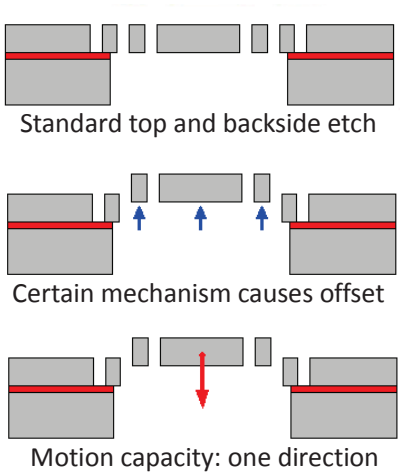

Figure 4-3. Schematic diagram of employed fabrication technology and motion capacity of artificial offset method.

4) Combs with different finger heights

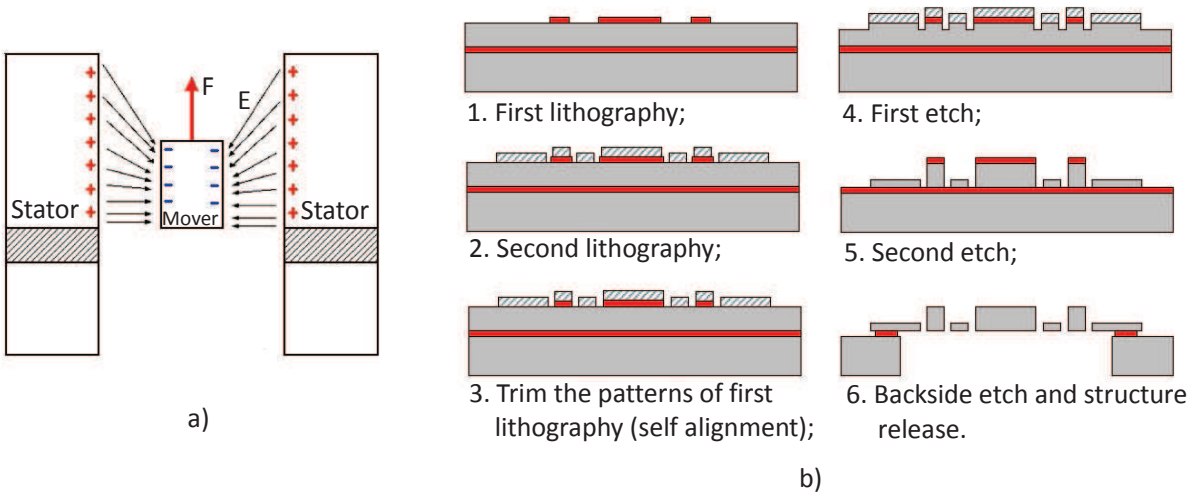

Figure 4-4. (a) Electric field distribution for vertical actuation and (b) simplified fabrication process flow chart of vertical comb drive fingers with different heights.

This method uses two patterning steps on the top surface of a SOI wafer to fabricate movable and fixed comb fingers at the same level but with different heights. It utilizes the asymmetric electric field to pull the movable finger approaching the center axis of fixed part (see in Figure 4-4a), but in practice it is usually not possible to reach this position because of the rapidly decreasing electrostatic force. N. Quack et al.[Quack-2009] adopted exactly the process indicated in Figure 4-4b, and H. Choo et al. [Choo-2007] has added a side wall oxidation process to protect comb fingers from side erosion. M.

Zickar [Zickar-2007] used topside isotropic etching of buried oxide instead of backside silicon etching via the substrate to release the suspended structure.

As we can see, these methods use a very limited number of fabrication steps (Figure 4-4b), which will minimize unpredictable difficulties and improve the processing yields significantly. Its alignment difficulties could be solved by oversizing the initial patterning and trimming these enlarged areas by a second etching. In this way all the critical gaps are only defined by the second photo-lithography step. Clever design of the masks used in the process, could enable tilting motion and even capacitance sensing function [Oda-2012]. However, the drawbacks of this method are also very obvious: first of all, there is no overlapping area change during comb finger motion, which means that all pulling up force is induced by variation of fringe capacitance. Consequently its induced force is comparably smaller. Secondly all these announced actuators could only travel a small percent of comb finger thickness, for example it moves 5% of the thickness in [Quack-2009] (2.5/20 μm) and 3% in [Zickar-2007] (1.5/50 μm).

5) Trench refilling

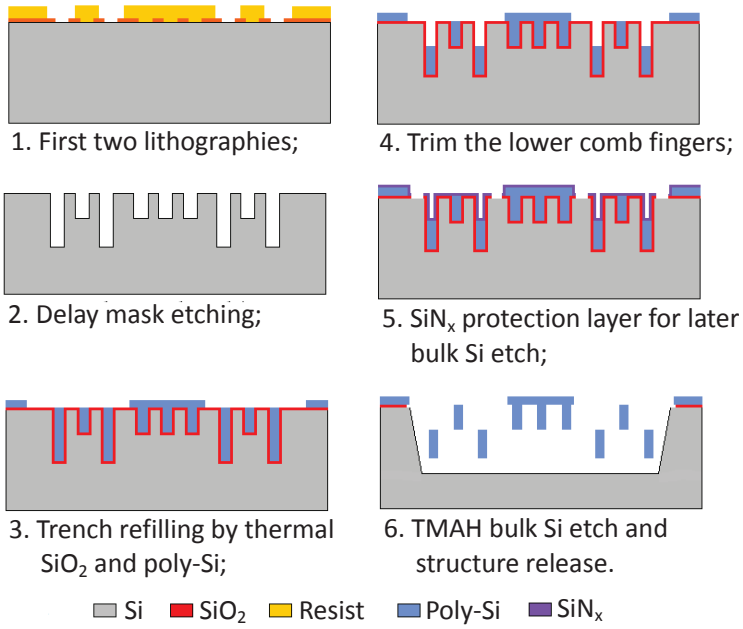

Figure 4-5.Process flow chart of trench refilling method for the fabrication of a vertical comb drive.

Trench-refilled molding processes are suitable for the fabrication of large aspect ratio (depth/width) structures, known as high aspect ratio molded polysilicon (HEXSIL) [Keller-1997] and high aspect ratio polysilicon structures (HARPSS) [Avazi-2000]. Figure 4-5 gives an example of vertical comb drive fabrication process of this method. A delay mask etching is firstly employed to drill trenches with different depths on silicon substrate. Then these trenches are refilled with thermal oxide by high temperature oxidation and by polysilicon deposited by low pressure chemical vapor deposition (LPCVD). The thermal oxide and another deposited silicon nitride film will serve as protection layer for polysilicon structures during following bulk silicon etching process. Finally, silicon substrate that encapsulates and lies beneath the polysilicon structures will be totally removed by wet silicon etching process. M. Wu et al. [Wu-2005] initially used the fabrication steps indicated in Figure 4-5, and then modified the mask delay etching process to fabricate more complex trenches with

three different heights and improved the final silicon lateral etching with open holes [Wu-2006]. In summary, trenching refilling method shows the advantage of, firstly a higher aspect ratio than standard deep etching equipment could achieve, secondly adjustable thicknesses of vertical comb finger, flexible springs and central mirror with respect to their different requirements.

6) Custom SOI bonding

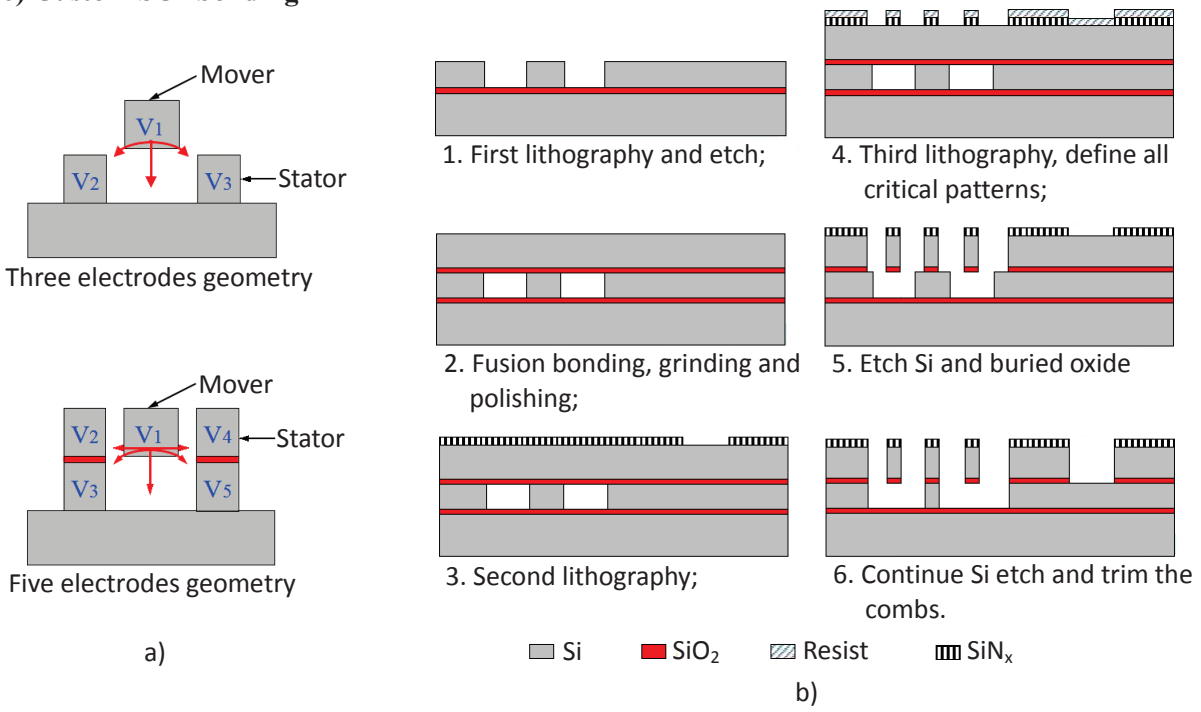

Figure 4-6. (a) Motion capacity of three electrodes and five electrodes geometries, (b) simplified fabrication process flow chart of custom SOI bonding method of vertical comb drive.

Custom SOI bonding method described here generally uses the fusion bonding of an oxidized Si wafer with an already patterned SOI wafer followed by grinding and polishing of the top Si wafer (Figure 4-6b). The patterns on top wafer are narrower than the ones on the lower SOI wafer what provides some self-alignment. Vertical comb fingers with different layer compositions are formed to realize multi-directional motion capacity. As illustrated in Figure 4-6a, geometries with three electrodes [Carr-2006] or with five electrodes [Lee-2004] can be found in published works. Vertical comb drive with five electrodes geometry, in principle, will have two more potential motional directions in the lateral plane than the three electrode geometry. But both these two geometries can only travel in one vertical direction (downward in Figure 4-6a). Most of the authors have chosen a thick substrate layer to fabricate more robust devices except V. Milanovic [Milanovic-2004] who used backside via etching. As a conclusion, this method shows a very versatile potential motion capacity but for only one vertical direction. Its motion range is determined by the thickness of the device layer of the SOI wafer and by the top Si layer after bonding and thinning. As a consequence of the thinning process, the remaining thickness as well as the motion range is generally large (tens of microns).

7) Multilayer

The multilayer method commonly begins with a multilayer wafer, which is fabricated by adding silicon oxide and polysilicon layer on a SOI wafer [Lin-2005] [Tsou-2005] [Carlen-2005] or by two SOI wafer direct bonding followed by thinning [Liu-2013] (Figure 4-7b) . LPCVD polysilicon in [Lin-

2005] [Tsou-2005] was deposited with a thickness of 2μm what largely limits the actuator's motion range. Instead, Epitaxial reactors (Epipoly) deposited polysilicon [Carlen-2005] and two SOI bonding method [Liu-2013] can solve this issue and increase the thickness to 20μm.

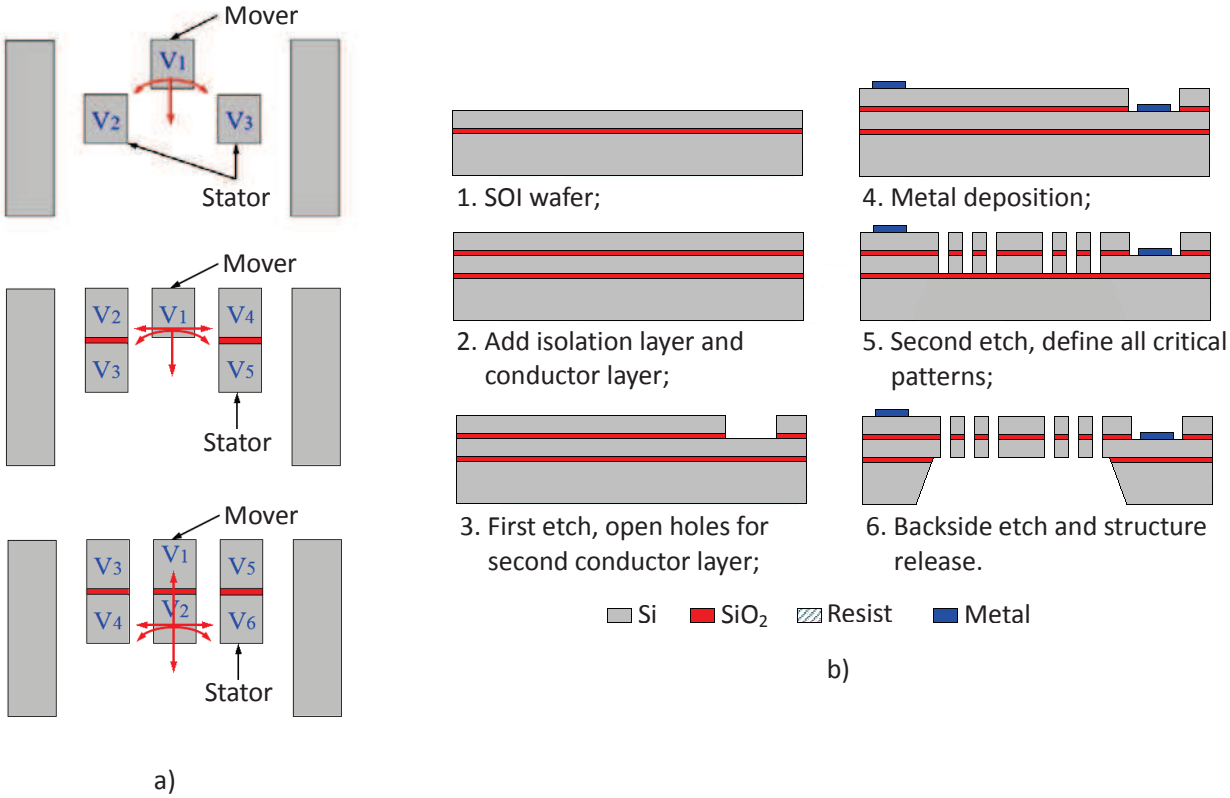

Figure 4-7. (a) Motion capacity of different electrode geometries, (b) simplified fabrication process flow chart of multilayer vertical comb drive.

The fabrication method introduced in [Jeong-2012] is slightly different. It firstly starts with a direct bonding of a SOI wafer with a caved Si wafer, then it is followed by a grinding of the SOI wafer substrate layer to form another device layer. Like the custom SOI bonding method, multilayer vertical comb drives can have different versions of electrode distribution (Figure 4-7a). As shown in Figure 4-7a in the bottom, the six electrodes geometry gives the most versatile motion capacities and needs the simplest fabrication steps because none comb fingers need to be trimmed. Its drawback is the floating voltage of unused electrodes during one directional actuation. But by using this option, the motion range can be doubled.

There are also some other interesting methods for vertical comb drives fabriation, such as polymer based comb finger structure [Chung-2008], silicon etching with oxide protection from lateral silicon etching [Zhang-2005], or boron etch-stop assisted lateral silicon etching (BELST) [Tsai-2004].

As a summary of this review, we can remark that the differences of the proposed fabrication methods are rather numerous:

- achievable motion ranges;
- possible moving directions;
- the strategies to avoid critical alignment requirement;

- the possibilities of separating the movable and fixed comb fingers at different levels and even with certain offset;
- the methods to deal with residual stress of released structures;
- the capacities of varying the thickness of different components according to their requirements;
- the complexities of employed technologies;
- numbers of steps needed for fabrication.

The main judging criterias for our mirror scanner are the achievable motion range and the simplicity of fabrication steps. We found that among all these reviewed fabrication methods of vertical comb drives, the multilayer method is the most attractive for the requirements of our device. Starting from this idea, we have proposed our own fabrication method based on double SOI technology which will be explained in details in the next section. We will see that our method keeps the advantage of a large travelling range, a bidirectional vertical motion capacity, while greatly simplifying the fabrications steps needed when compared to other published methods. In addition, same low stress gradient, single crystal material (silicon) and thickness is used for the top and bottom part of comb fingers. These features are quite favorable to obtain a scanner with good symmetry, reproducibility and reliability.

4.2 Proposed Fabrication Process of Vertical Comb Drive Scanning Micro-mirror

As discussed above, we have chosen multilayer comb drive method with double SOI wafer technology to fabricate the vertical scanning micro-mirror. With the purpose of reducing fabrication steps needed, and thus improving the final production yield, we have designed a six-step fabrication process.

Step 1:

1. Double SOI wafer: $Si/SiO_2/Si/SiO_2/Si$;

a)

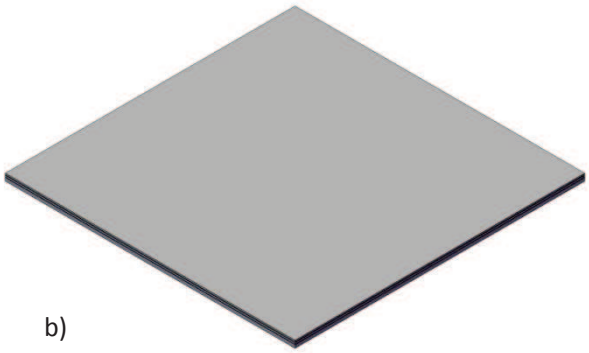

b)

Figure 4-8. (a) Cross section view and (b) bird view of the first fabrication step of vertical scanning mirror.

The fabrication starts from a five-layer double SOI wafer (Figure 4-8) which can be purchased or made by direct bonding of SOI wafer with an oxidized Si wafer followed by a thinning step. Section 4.3 will describe the experimental fabrication tests of double SOI wafer in our clean room. Unfortunately, the fabrication yield was too low to continue the process with these homemade double SOI wafers. As a substitution, we bought double SOI wafers from OKMETIC Company with $Si/SiO_2/Si/SiO_2/Si$ layer stack thicknesses equal to 25/1.5/25/1/380 μm and with top and intermediate silicon layers resistivity equal to 0.01-0.02 Ω·cm.

Step 2:

2. Front side $Si/SiO_2/Si$ DRIE;

a)

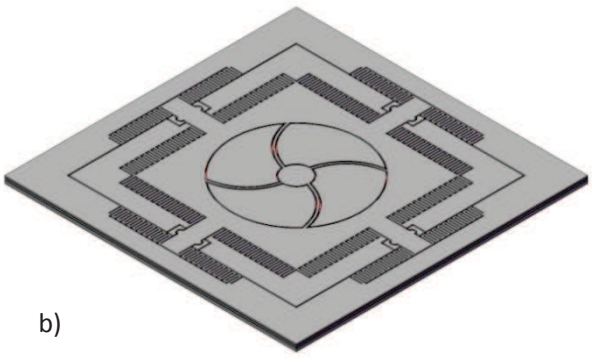

b)

Figure 4-9. (a) Cross section view and (b) bird view of the second fabrication step of vertical scanning mirror.

Then a three layer Deep Reactive Ion Etching (DRIE) masked by a single photoresist layer is performed to define most of the important patterns of the device (Figure 4-9). Because this is not a conventional etching process, a conservative value of 10 was considered for the maximum aspect ratio (depth/width). As shown in the Figure 4-9, the patterns on the DSOI wafer are somehow complicate,

but they have the same trench/hole width of 5 µm everywhere to obtain homogeneous etched depths and sidewall profiles. Three initial validation experiments (Si, SiO_2 and SiO_2/Si etching) were performed before the final test of Si/SiO_2/Si etching to evaluate the manufacturability of our proposed technology. Details of these DRIE etching tests will be presented in Section 4.4.

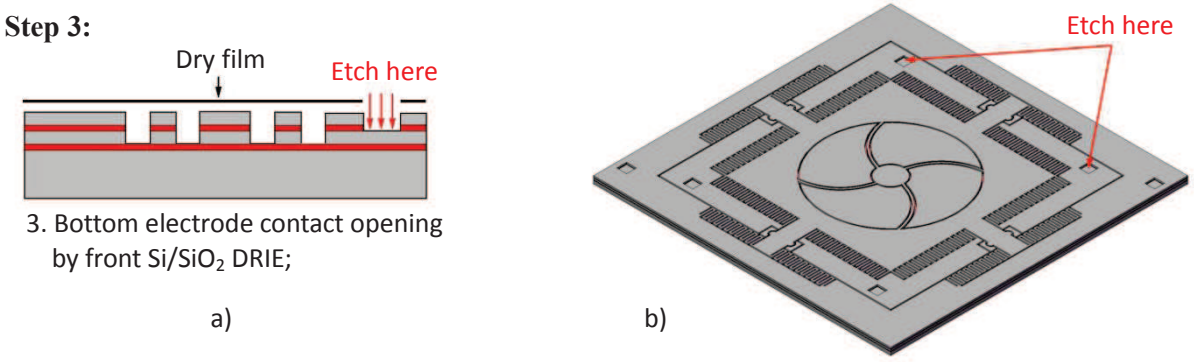

Figure 4-10. (a) Cross section view and (b) bird view of the third fabrication step of vertical scanning mirror.

In order to create large open windows for the contacts on the bottom Si part of the Si/SiO_2/Si layer stack, DRIE etching and BHF wet etching with a laminated dry film photoresist mask are used respectively to etch the top Si layer and the buried SiO_2 layer (Figure 4-10). Dry film technology was finally chosen among many possible options, because it is compatible with highly structured surface and its drawback of low resolution is acceptable for the contact openings which have a large size and a large error tolerance for dimensions and alignment.

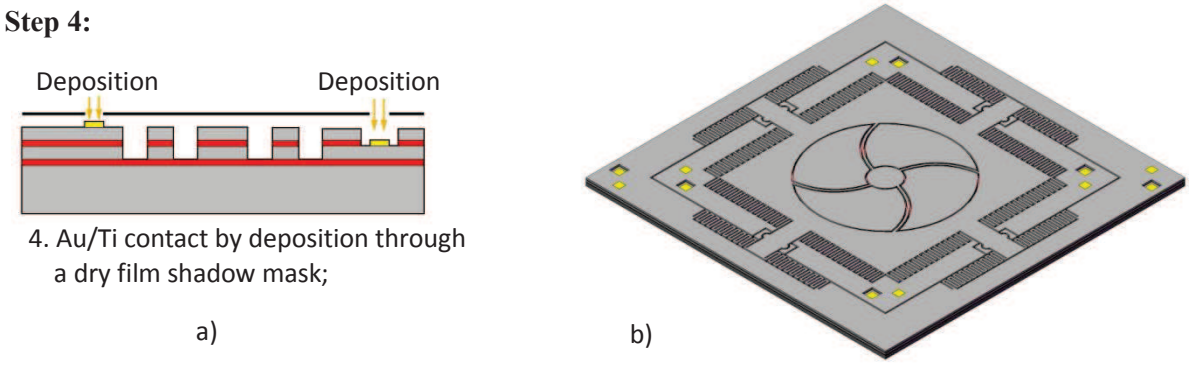

Figure 4-11. (a) Cross section view and (b) bird view of the forth fabrication step of vertical scanning mirror.

Because metallization at two different layers (the upper and lower Si layers of the DSOI wafer) is needed, we have developed a novel technology to realize the metallization at two different levels by only one step. This technology can save one extra lithography and deposition process, but is challenging because of the large height difference between the two levels (21.5 µm). Standard spin coating of photoresist is not satisfactory in this case. Since a laminated dry film can overhang large cavities, we have performed another dry film lithography and an Au/Ti metallization to deposit and pattern metal electrodes simultaneously on both upper and lower Si layers (Figure 4-11). Patterning of the top electrode is made by lift-off while the bottom one is based on shadow masking.

Step 5:

5. Structure release by backside DRIE+BHF etch;

a)

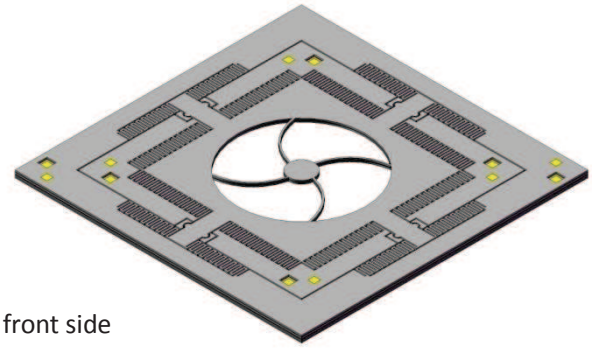

b) front side

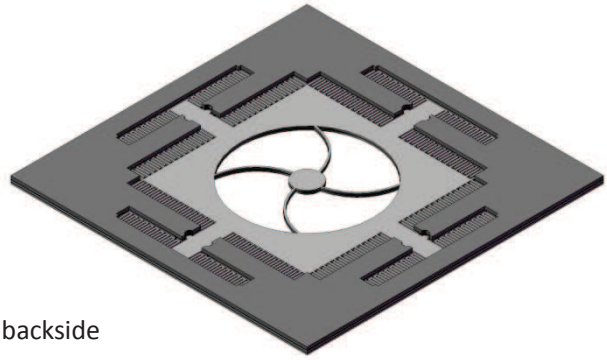

c) backside

Figure 4-12. (a) Cross section view, (b) topside bird view and (c) bottom side bird view of the fifth fabrication step of vertical scanning mirror.

After the topside wafer process is finished, the fifth step of the fabrication process is the structure release step (Figure 4-12). For this, backside DRIE is applied to etch the whole Si substrate until the bottom buried oxide layer which acts an etch-stop layer. Then this SiO_2 layer is wet etched by buffered hydrofluoric (BHF) from backside. During DRIE and BHF etching, the top side is protected by a spin coated photoresist and a temporarily bonded wafer.

Step 6:

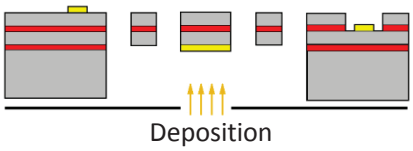

6. Mirror deposition through a shadow mask.

a)

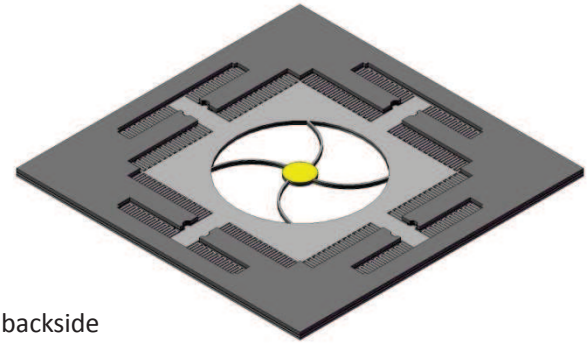

b) backside

Figure 4-13. (a) Cross section view and (b) bottom side bird view of the sixth fabrication step of vertical scanning mirror.

At this stage, the vertical comb drive scanning mirror is almost finished and available for further device test and characterization. If a high reflectivity of the scanning mirror is required, another metal deposition through a shadow mask can be performed from the backside (Figure 4-13).

In conclusion, the fabrication process described above consists of only three DRIE, two metal depositions and five photolithographies without critical alignment. It is mainly based on both front and backside DRIE of a highly doped double SOI wafer to form vertical comb drive actuators. The first lithography of photoresist is the most crucial because it defines most of the important patterns. As detailed above, dry film photoresist masking was adopted for several steps because of its ability to be used on highly structured or open surfaces where standard spin coating of liquid photoresist is not suitable. Another possible option of these lithographic steps is the use of a spray coated resist but dry film was considered as a better choice. This proposed fabrication process with a minimized number of fabrication steps was designed to reduce fabrication issues and time cost. A large range and bidirectional motion ability as well as the implementation of a self aligned technology are also great merits of this proposed vertical comb drive technology when compared to other existing vertical comb drive fabrication methods

4.3 Experimental Fabrication Tests of Double SOI Wafer

Double SOI wafers are essential for the fabrication of our reference mirror scanner with vertical comb drive actuators, because it provides stacks of different device layers and inborns height offset which allows bidirectionnal vertical translation. Three different methods have been considered to fabricate this kind of wafer: LPCVD deposition, epitaxial growth and wafer bonding followed by thinning. Compared to the former two methods, wafer bonding and thinning method could produce a larger thickness and same material for the different Si and SiO_2 layers, has thus finally been chosen for the experimental fabrication tests.

Wafer bonding is a set of technological procedures which permanently seal solid state material with flat and smooth surfaces. It is widely used in MEMS field, since it can split the structure complexity between several wafers during processing, allows the fabrication of multilayer MEMS devices and is largely used for packaging at the wafer level. Generally, this technology consists of direct wafer bonding, anodic bonding and intermediate layer bonding that differ from the operating temperature, bonding material and external loading (pressure, electrical field). Concerning the fabrication of double SOI wafers for our work, direct wafer bonding is the most suitable wafer bonding technique.

Direct wafer bonding, also called fusion bonding or thermal bonding, is connecting two wafer surfaces without any additional material or external electric field excitation. It is always performed in the clean room under following procedures:

- ❖ Cleaning and activation of the surfaces to be bonded;
- ❖ Initial contact and pre-bonding;
- ❖ Final formation of bonding by high temperature annealing.

The double SOI wafer, which is composed by five alternating layers of Si and SiO_2, can be fabricated by direct bonding of a SOI wafer with an oxidized Si wafer, followed by a thinning of the top Si layer to the desired thickness (Figure 4-14). For economical considerations, the first direct wafer bonding experiments were carried out by bonding a Si wafer with an oxidized Si wafer. Its bonding interface is Si-SiO_2/Si, so the results concerning bonding quality should be similar to the case of the bonding a SOI wafer to an oxidized wafer bonding, except the mechanical state after wafer bonding which can be different.

After direct wafer bonding, a thinning process of the top Si layer must be performed to reduce its thickness down to the one of the first buried Si device layer (thickness of the Si layer of the initial SOI wafer). This thinning step could be performed by wet Si chemical etching with suitable protective layers, by Deep reactive Ion Etching (DRIE) or by Chemical Mechanical Planarization (CMP). In this work, we selected CMP as the thinning method as it is an efficient process not requiring protective layers. Ideally such CMP step should be followed by a wet chemical etching to remove the damaged surface layer but to simplify the process this step was avoided. As a first approximation, we considered that this damage layer has a low impact on the scanner's performances.

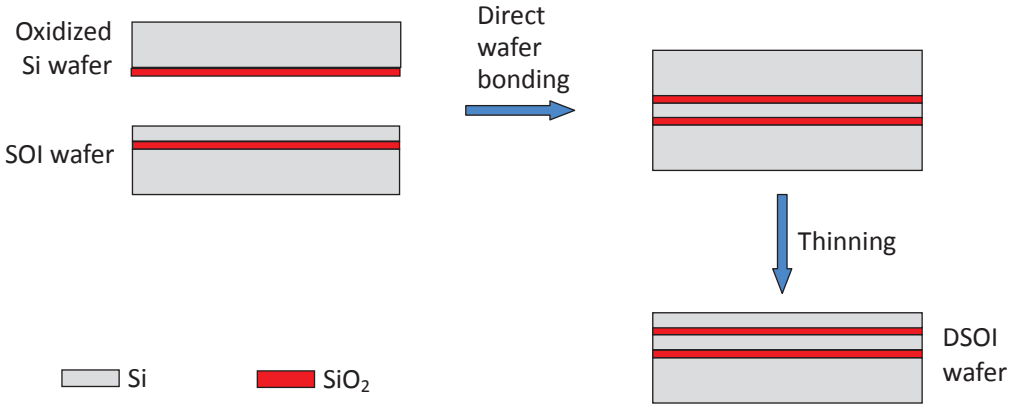

Figure 4-14. Principle of the fabrication process of a double SOI wafer

Details of the fabrication process will be introduced in section 4.3.1, and the measurement results will be given in section 4.3.2. Finally section 4.3.3 will conclude all achieved accomplishments and encountered problems, and will propose a final solution.

4.3.1 Fabrication Procedures of Double SOI wafer

The first fabrication steps of the double SOI wafer were performed in a clean room having a class 1000 (less than 1000 particles with size ≥0.5 μm in 1000 cubic foots of air) with the help of Nathalie Isac (Process engineer) and Samson Edmond (Technician). Firstly, a bare Si wafer was cleaned by the processing steps number 1 to 7 given in Table 4-1 and then wet oxidized in a furnace at 1000℃ during 30 minutes to form a ~200 nm thick SiO_2 layer on the surface (actually 170 nm after measurement). Then both this oxidized wafer and another bare Si wafer were cleaned and activated by processing steps number 1 to 12 in Table 4-1.

Table 4-1. Procedures of surface preparation for wafer bonding.

Step	Chemical treatment	Time
1	Acetone	3min
2	Ethanol	3min
3	DI water+N_2	3min
4	BHF	30s
5	DI water+N_2	3min
6	H_2SO_4+H_2O_2 (3:1)	5min
7	DI water+N_2	3min
8	BHF	30s
9	DI water+N_2	3min
10	RCA 2: HCL+H_2O_2+H_2O (3:1:1)	10min
11	DI water+N_2	3min
12	Drying in N_2 jet gun	

The solvent cleaning at initial two steps aims to remove organic contaminations on the wafer. Then BHF acid was applied to etch the native thin oxide layer on the surface. Piranha solution (H_2SO_4 : H_2O_2 mixture) followed by BHF was intended to oxidize the surface and then remove this oxide under the purpose of removing hydrocarbon and other contaminations. Finally a RCA-SC2 bath ($HCL:H_2O_2:H_2O$ mixture) was used to remove metallic and particle contamination while preserving the surface hydrophilic [Moriceau-2010].

After these cleaning steps, the wafers were blown dried with filtered N_2 and initially contacted at room temperature. A possible improvement of the drying process could be the use of spin drying but there is not a suitable spin dryer available in IEF clean rooms. After the two wafers were contacted, a spontaneous bonding will occur. Let us emphasize that, because of dust and tweezer dust/chemical contaminations during cleaning and handling, it is important to bond two wafers immediately after preparation and to restrict tweezer contact area at only one place. A soaking support without contact should be ideally used.

It is commonly admitted that hydrogen bond, capillary force and Van der Waals attraction cause this spontaneous bonding [Moriceau-2010]. But this bonding at room temperature is still weak. Then, a reinforcement process was applied to the bonded wafers by using EVG®501 Wafer Bonding System (Temperature=400℃ , vacuum pressure=10^{-3} Pa, pressing force=8000 N, bonding time=30 min). Finally, a high temperature N_2 annealing was carried out to consolidate the bonding.

Many authors have investigated the mechanisms of high temperature Si/SiO_2-Si bonding. In agreement with many authors, J.A. Dziuban proposed a three-step process to explain it [Dziuban-2007]. Initially between the pre-bonded surfaces, several monolayers of molecular water are trapped at the interfaces to form spontaneous bonding. Then the first annealing step, at temperatures below 200℃ , induces a loss of molecular water and produces an evolvement of hydrogen bonds (Si-H) and silanol bonds (Si-OH). At the second step, from 200℃ to 1100℃ , the former two types of bonds are replaced by siloxane bonds (Si-O-Si). This leads to an increase of bonding energy and a reduction of interval distance between two contacting surfaces (called gap closing). Finally when temperature increases beyond 1100℃ , the gap is completely closed and two surfaces are totally sealed with a complete consumption of available hydroxide groups.

A compressive thermo-mechanical stress reaching a few hundred of MPa in magnitude is inherently produced in thermal SiO_2 layers. At annealing temperatures above the glass transition temperature of silica (950-1000°C), some stress relaxation can occur leading to a difficult to predict stress state in SiO_2 and Si layers which can affect the released structures. To avoid this issue, at testing stage, high temperature annealing was restricted to temperatures lower or equal to 1000℃ .

The next thinning process of already bonded wafers was performed by a PRESI polishing machine (MECAPOL P 400). The whole process can be divided into two independent parts, first grinding, and second polishing. The initial grinding step was implemented by using abrasive paper P1200 (aluminum oxide abrasive). Each paper was able to reduce the top Si layer thickness by about 50 μm for the experimental conditions used (wafer rotation speed ω_{wafer}=40 rpm, paper support rotation speed ω_{paper}=100 rpm, opposite rotating directions, applied pressurizing force F=20 daN, grinding duration T=6 min). Then, a second polishing step was carried out by using diamond suspension LDP in the sequence of particle diameter from 9 μm, 3 μm, 1 μm to final 1/4 μm. At last,

the polishing process was ended under a continuous spraying of Nalco solution, which is composed by NaOH, colloidal silica and DI water.

After all this thinning process, the bonded wafers were cleaned, dried and transferred to several measurement equipments described in next section to test their qualities.

4.3.2 Measurement Results of Double SOI Fabrication Work

These experiments were the first direct wafer bonding tests performed at IEF, so several measurement methods had to be implemented to evaluate the fabrication quality of our double SOI wafers. The first one is near infrared imaging in transmission mode to find bonding voids; the second one is Fourier Transform Infrared spectrometry (FTIR) to measure wafer and Si layer thicknesses. Finally optical profiler and stylus profiler were used to measure the surface flatness and roughness. Bonding energy measurement by blade test (also called Maszara test or crack opening method), where a razor blade is inserted at the bonded interface and the resulting crack length is measured, was initially planned but in reality not performed, because of non-ideal fabrication results.

4.3.2.1 Infrared images observation

Bonding defects can be visualized by infrared imaging or scanning acoustic microscopy (SAM). In order to detect the non-bonded areas (or voids) of our testing wafers, an infrared imaging set-up in transmission mode was built as shown in Figure 4-15a below. Since silicon is transparent for radiation with wavelength $\lambda > 1.1\mu m$ but not for visible light, a bare silicon wafer was used as NIR filter in this set-up. Examples of recorded images of bonded wafer (after the first direct wafer bonding) before and after annealing are shown in Figure 4-15 b and c.

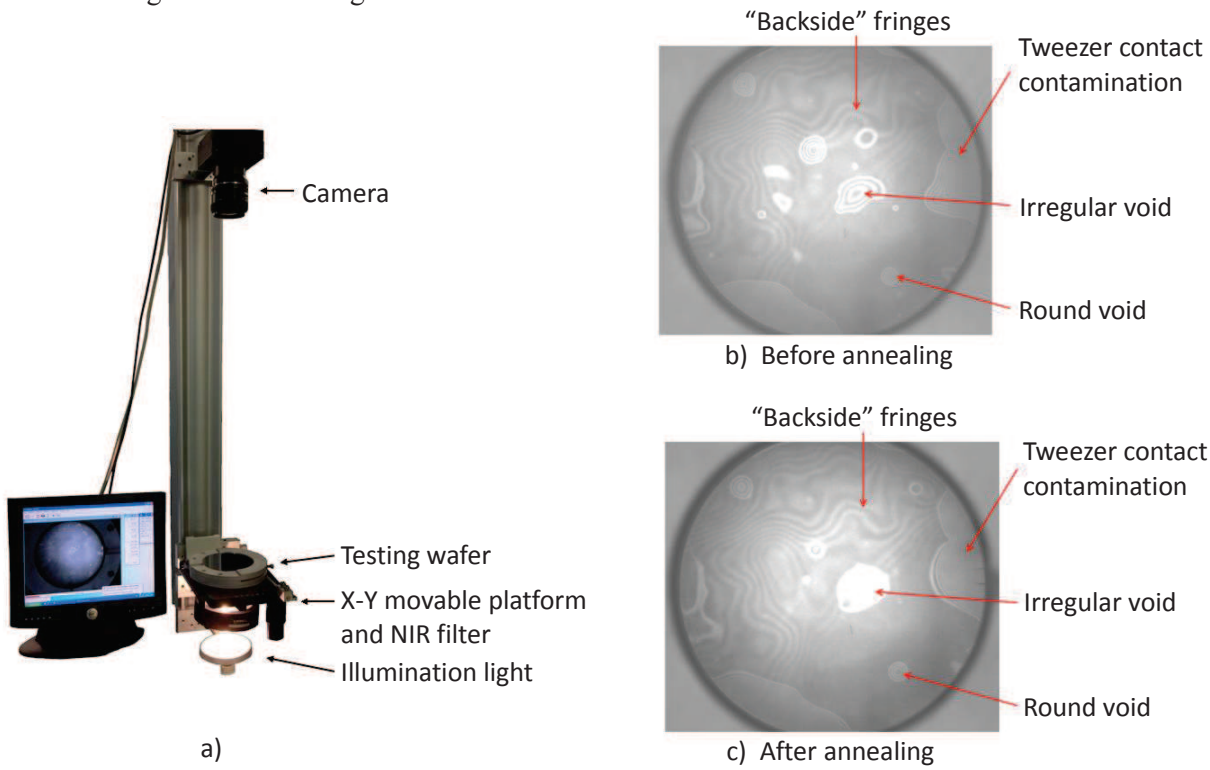

Figure 4-15. (a) Infrared observation set-up and visualized NIR images of bonded wafer (b) before annealing and (c) after annealing.

From these infrared images, we can distinguish different unbonded areas: large area voids related to tweezer contact contaminations, round shape voids and irregular shape voids. Tweezer contact contaminations only occur near the edge, and can be eliminated or restricted to only one place by proper handling so this is not a real issue. Because of their large heights (estimated to be up to several microns from the interference fringes) and large areas (several mm^2), round shape voids were firstly suspected to result from contamination by hard dust particles. However after high temperature annealing, the numbers of their interference rings were found to decrease while their occupying areas were still the same (Figure 4-15b and c). This shows that the heights of the inner cavities have been reduced, rather than their surface areas. So we finally attributed this behavior to gas trapped inside cavities resulting from surface contamination like organic contaminations/dusts possibly combined sometimes with hard dusts. Irregular shape voids were also attributed to the same causes but may also originate from insufficient flatness of bonded surfaces. Until now, it was difficult for us to distinguish different origins for round and irregular voids. Nevertheless, what was consistent during several tests was that it was possible to eliminate small voids by high temperature annealing, while large bubbles with large volume of trapped gas were very difficult to eliminate. We also observed that they could move or become larger by collecting gases trapped elsewhere or generated from surface reactions.

We tried to modify the experimental parameters of wafer bonding experiments, such as initial bonding conditions in the wafer bonder (Temperature=400-500 ℃ , pressurizing force=6000-8000 N) and annealing conditions in a furnace (Temperature=800-1000 ℃ , time=1-2 h). However, all found differences caused by these modifications were negligible when comparing to deterioration brought by surface flatness defects and organic or hard particle contaminations.

We also tried O_2 plasma surface activation before bonding which is known to be able to produce a high bonding energy even at moderate temperature annealing (200-500 ℃) [Wiegand-2000]. In our trial, O_2 plasma treated wafers showed a very different spontaneous bonding behavior when compared to chemical solution activated wafers (Figure 4-16a and b). A few changes have been also observed after high temperature annealing (Figure 4-16c). However large bonding defects are still present. The conclusion of these direct wafer bonding tests is that dust and organic contamination was the main limiting cause of poor wafer bonding quality and prevented a good investigation of the influence of wafer bonding process parameters. Handling and drying procedures as well as particle contamination in rinsing baths will have to be largely improved in the future to get good direct wafer bonding results. Let us emphasize that for these experiments surface preparation were performed in a class 1000 clean room. This partly explains the insufficient control of particle contamination although some labs could obtain good results in similar class clean rooms.

Despite these unsatisfactory results of wafer bonding experiments, we investigated the wafer thinning process by CMP for future works with the help of Cédric Villebasse (technician of clean room facilities). Thinning of a 4 inches silicon wafer has not been previously investigated at IEF. After the bonding process, composite wafers were thinned by grinding and polishing processes. Figure 4-17 shows a fabricated wafer that has endured a whole run of these processes: (a) chemical activation and initial bonding process, (b) high temperature annealing, (c) thinning. From these images, we can find that tweezer contact contaminations have been eliminated and that high temperature annealing helped a lot to eliminate many of the small voids. One interesting finding not discussed above is the observation of what we called “backside” fringes on bonded wafers. These fringes showed no change before and after high temperature annealing unlike bonding voids with gas captured inside. They only disappeared after grinding and polishing as shown in Figure 4-17c. We did not find NIR images of

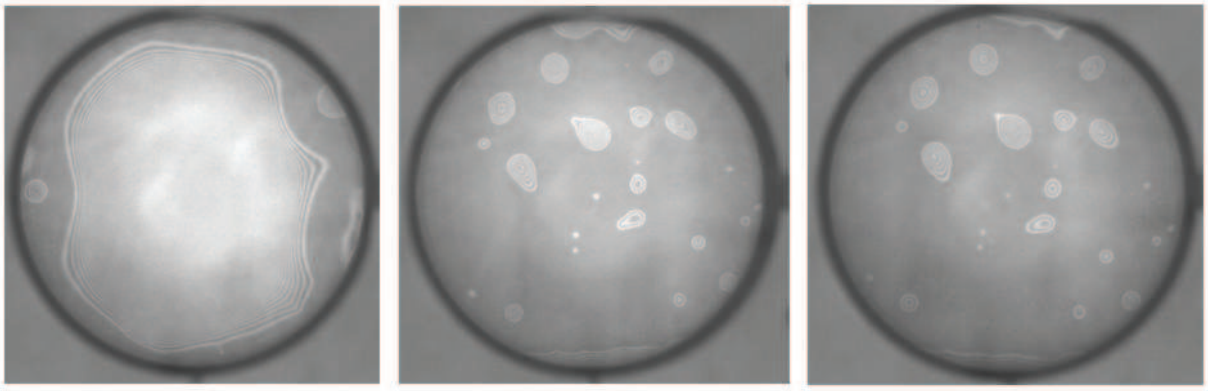

a) Spontaneous bonding after chemical activation

b) Spontaneous bonding after O_2 plasma treatment

c) Wafer of (b) after annealing

Figure 4-16. Infrared images of (a) spontaneous bonded wafer after chemical activation or (b) after O_2 plasma treatment followed by (c) a high temperature annealing.

bonded wafers with such fringes in published works. We believe that they result from a multiple optical interference between two bonded wafers working like a Fabry-Pérot interferometer. They can then clearly be observed only when two wafers have almost same thicknesses and reflectance coefficients and a sufficiently monochromatized light is used. In our case a Si filter and a CCD camera were used so the tramsmitted and detected light should have a rather narrow wavelength range.

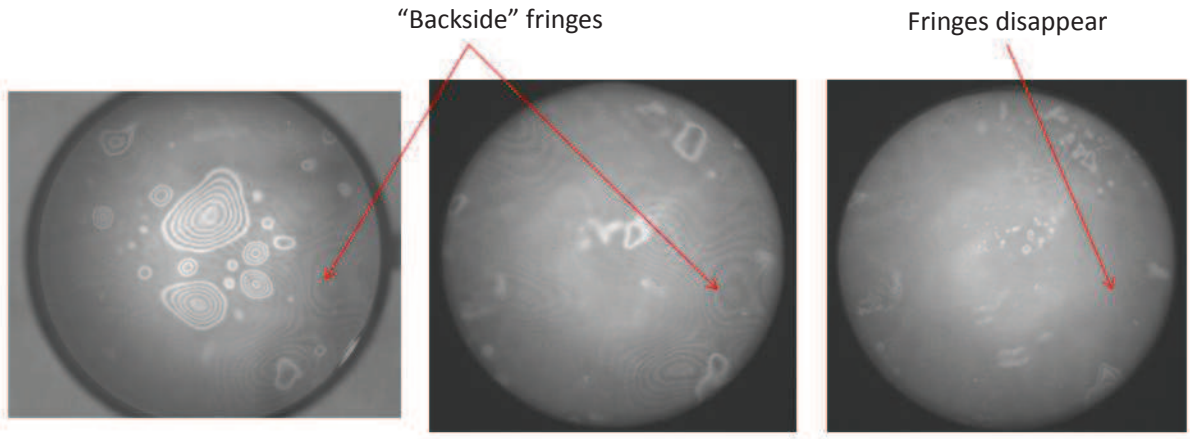

a) After chemical activation and initial bonding process

b) Wafer of (a) after annealing process

c) Wafer of (b) after thinning process

Figure 4-17. Infrared images of a fabricated wafer (a) after chemical activation and initial bonding process, (b) after high temperature annealing, (c) after grinding and polishing processes.

Concerning the wafer thinning process, two evaluation methods were adopted to measure the reduced thickness and surface roughness after polishing.

4.3.2.2 Wafer thickness measurement

Firstly, the thicknesses of bonded wafer before and after thinning process were measured by a comparator which is a direct contacting thickness measuring tool. It works in the principle similar to a caliper and is simple to operate. However, the obtained results are not fully satisfactory because the

thicknesses of the different layers of the composite wafer cannot be separated and it is difficult to locate the measurements at a same place at different measuring times.

A more accurate measurement using Fourier Transform Infrared Spectroscopy (FTIR) was implemented. FTIR is usually used to measure the transmitted or reflected infrared spectrum of different samples. Its operation is based on a two arms Michelson interferometer where light beams reflected by a fixed mirror and by a moving mirror are interfering. Then, a computer-based processing is applied to convert the raw interferogram data (light intensity/mirror position) into a spectrum data (transmittance or reflectance coefficient/wave number) by using Fourier transform algorithm. The schematic image of the processing by FTIR is shown in Figure 4-18a and b. In the case of a double side polished single wafer or bonded composite wafer, the FTIR spectrum contains oscillations related to multiple interference fringes in the Si wafer/layers. Starting from the spectrum given by FTIR, we applied another Fourier transform to demodulate these oscillations and extract different thickness information of measured wafers (Figure 4-18 c and d).

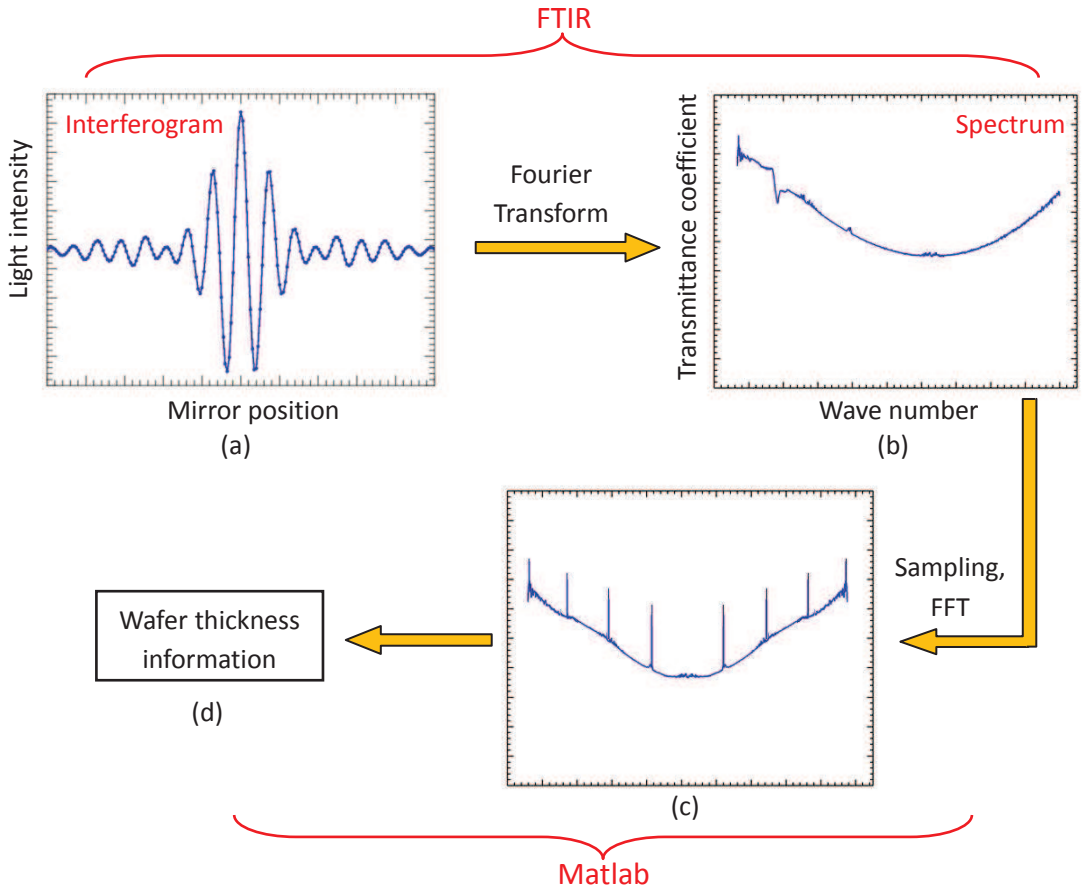

Figure 4-18. Processing flow of thickness measurement based on FTIR.

Before its application to real wafer measurements, this measuring method was evaluated on spectrum data obtained with an optical simulation software (TFCalc). The simulated optical transmittance coefficient of a bare Si wafer (300µm) and composite wafer ($Si/SiO_2/Si$, 300µm/170nm/200µm) are plotted in Figure 4-19. In this simulation, the used optical constants of Si and SiO_2 (refractive index n and extinction coefficient k) were taken from a published handbook [Palik-1998]. Then, a Fast Fourier Transform (FFT) was applied to this optical spectrum data. Because this raw data is not uniformly spaced under wave number unit, a sampling process by using

interpolation in Matlab was performed prior the Fourier transform operation. The obtained spectrum data are shown in Figure 4-20.

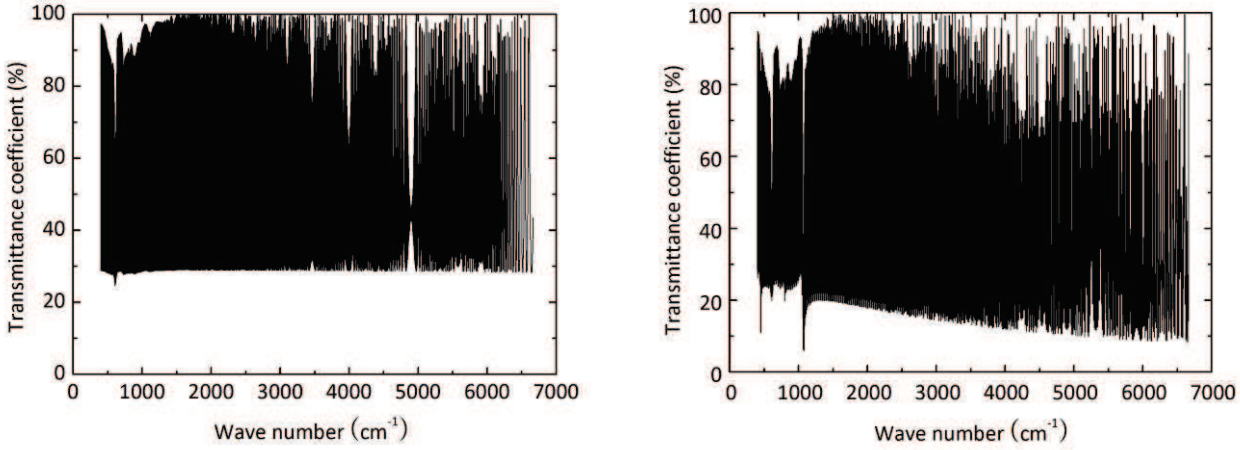

b) Bare Si wafer (300 µm)

a) Composite wafer ($Si/SiO_2/Si$, 300 µm/170 nm/200 µm)

Figure 4-19. Simulated transmittance coefficient versus wave number of (a) a bare Si wafer and (b) a composite wafer.

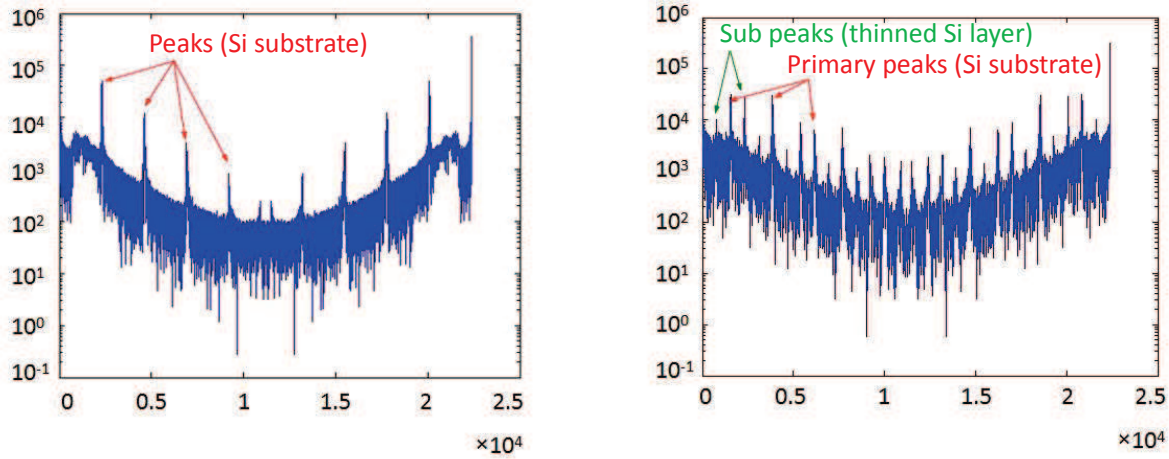

a) Bare Si wafer (300 µm) after sampling and FFT

b) Composite wafer ($Si/SiO_2/Si$, 300 µm/ 170 nm/200 µm) after sampling and FFT

Figure 4-20. Spectrum data from Figure 4-19 after sampling and fast Fourier transform.

From Figure 4-20a, we can see that the Fourier transformed spectrum of the bare Si substrate contains periodic peaks in the whole range. In the case of a SOI wafer (Figure 4-20b), the primary peaks arising from Si substrate remain at the same positions, while new emerging sub peaks with narrower intervals related to the top Si layer are added. By varying the thickness of thinned Si layer, the intervals of sub peaks were proved to be linear with its thickness. and the factor k=interval/thickness (µm) was found equal to 7.55. So by counting all peaks showed in these plots, we can deduce thickness information of measured wafers.

After this verification of the method validity, a real measurement of a thinned composite wafer was carried out. Obtained data after Fourier transform operation are shown in Figure 4-21. It can be

seen that peaks related to the Si different layers are clearly visible in the magnified view. The final calculated values are: $t_{substrate}$=313 µm, and $t_{thinned\ layer}$=63 µm.

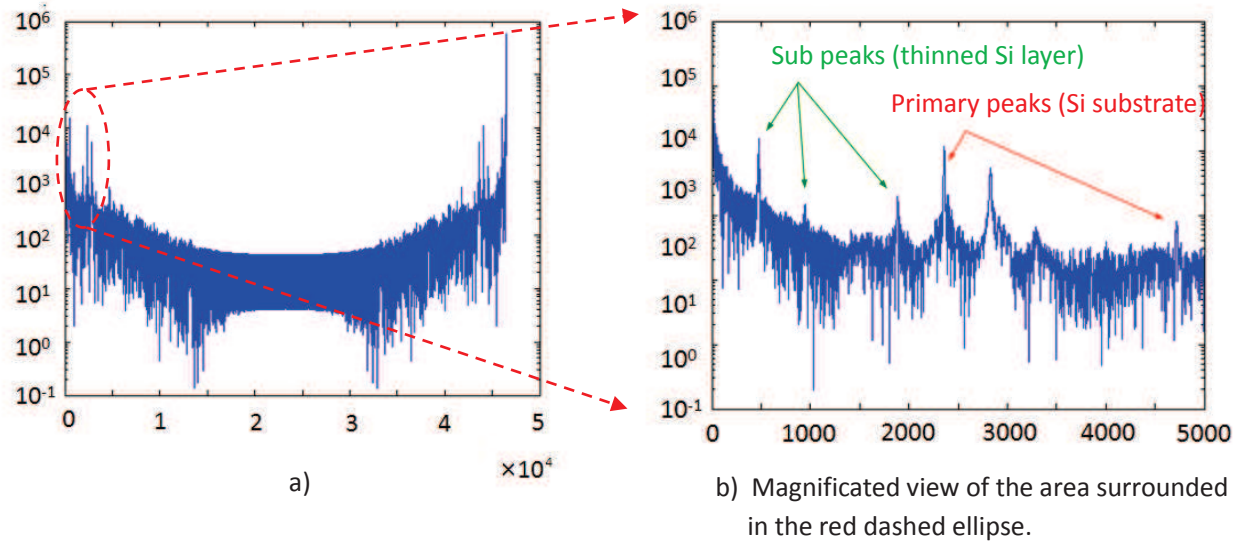

Figure 4-21. Measured spectrum data of a thinned composite wafer after Fourier transform operation.

The thickness values obtained from FTIR measurements are compared with values measured with a comparator in Table 4-2. The numbers in the top line corresponds to the different measurement location spots depicted in Figure 4-22.

Table 4-2. Measured thickness of bonded and thinned wafer by comparator and FTIR.

Thickness (µm)	1	2	3	4	5	6	7	8	9	10	11	12	13
Comparator	412	389	374	373	369	389	389	396	399	382	382	381	388
FTIR	398	384	359	354	341	365	374	389	391	/	376	378	379
(thinned layer +substrate)	85+ 313	72+ 312	47+ 312	42+ 312	40+ 311	53+ 312	61+ 313	75+ 314	78+ 313	?+ 313	63+ 313	65+ 313	65+ 314

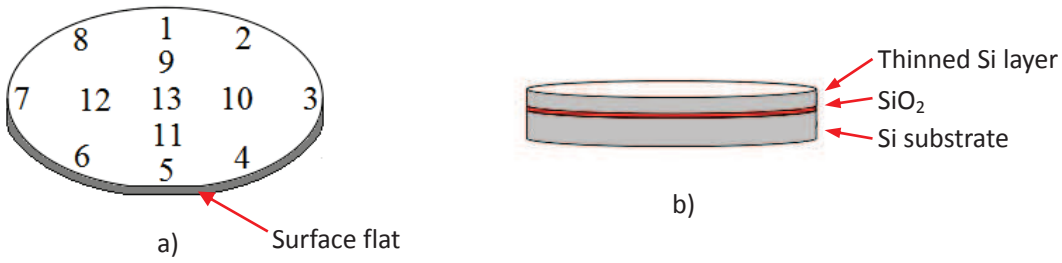

Figure 4-22. (a) Location of different spots during thickness measurement and (b) layer stacks of measured wafer.

Table 4-2 shows that comparator measurements give thickness values slightly larger than the ones by FTIR method. As discussed above, the accuracy of measurements with a comparator is considered to be lower. So for following analyses, we mainly used thickness data from FTIR method. From the results, a thickness lateral gradient can be observed with the highest thickness located at spot location number 1 and the lowest thickness at spot location number 5. The thickness profile along the circular border and a 3D drawing illustrating the top layer Si thickness variation on the 4 inches wafer are shown in Figure 4-23..

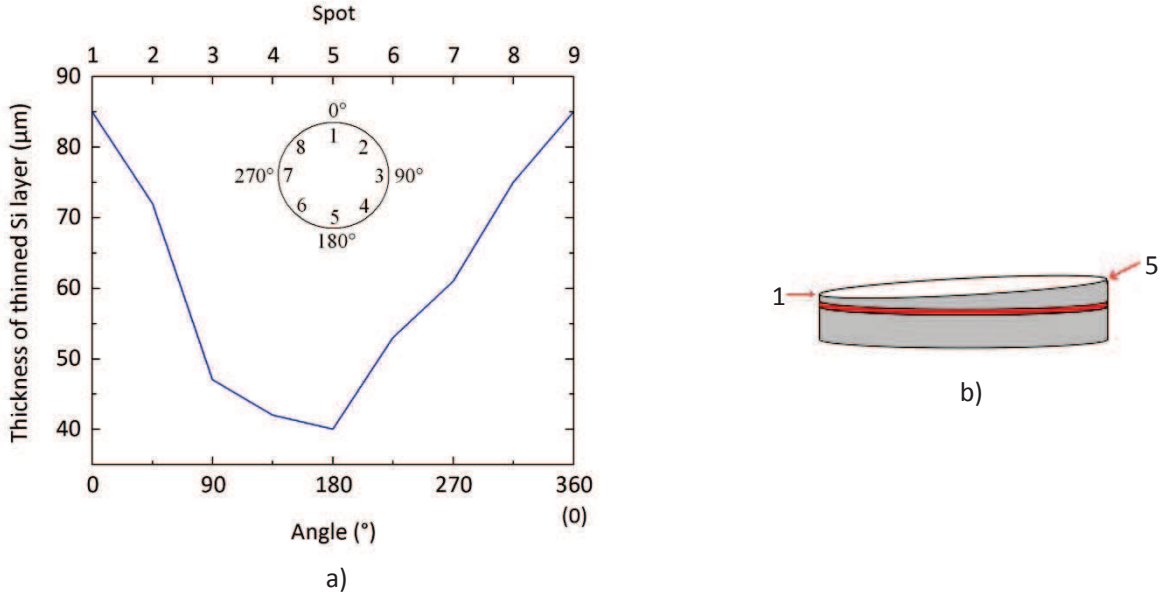

Figure 4-23. (a) Thickness plot of thinned Si layer along the circular border and (b) 3D illustrating drawing of the whole wafer.

Figure 4-23 shows that there is nearly a 45 µm difference between the maximum and minimum thickness values of the thinned Si layer. This variation is unexpectedly very large, as it corresponds to 72% of the mean final thickness (62.1 µm). The reason for this large non uniformity is still not clear for us since both the large volume metal support used for gluing the wafer and the grinding paper placed below the testing wafer are both rotating during the grinding and polishing process. The difference might result from the improper loaded mechanical components and an uneven pressure distribution on the wafer surface. If these are the real causes, debugging and adjusting the polishing equipment was considered to be a too time-consuming task and this work was not undertaken.

4.3.2.3 Surface roughness and wafer bow measurement

Beside thickness measurements, the root mean square roughnesses r_q and the wafer bow of the thinned wafers were also respectively measured by optical profilometry, and by a laser scanning system or a stylus profiler.

Optical interferometric profilometry is a fast and non-contact optical technique for 3D surface topography measurement. It can be operated with a white light source (low coherence interferometry mode) or with a monochromatic light source (phase shifting interferometry mode). Taken into account the low surface roughness to be measured, the phase shifting interferometry mode was selected. Measurements were performed with a 40× Mirau interference objective. The measured results of a wafer at different stages are listed in Table 4-3. They show that a grinded and then polished wafer

having a low roughness comparable to the initial bare Si wafer could be achieved. It should be noted that these values are actually the sum of the optical profilometer reference mirror rms roughness and the sample surface rms roughness, are measured on a small area near the wafer center and includes waviness in this area. The real rms microroughness of Si wafers is usually <0.5 nm.

Table 4-3. Measured roughnesses of a testing wafer at different stages by optical interferometric profilometry.

	Bare Si wafer	Oxidized wafer SiO_2	Bonded wafer after thinning
Roughness	3.2 nm	4.2 nm	4.35 nm

Next, the wafer surface curvature was measured with a laser scanning system from FSM Company. This system detects the deflection variation of a reflected laser beam during a line scan. Its measurement result provides only the shape profile along a line. The explanation of scanning lines used, wafer sides names and the obtained surface profiles along these scanning lines on the different wafer surfaces are shown in Figure 4-24. Stylus profilometry measurements were also performed along the same scan lines. It was checked that the results obtained with these two different methods are quite similar, despite their different measuring principle. So in the following only results obtained with the laser scanning system will be presented.

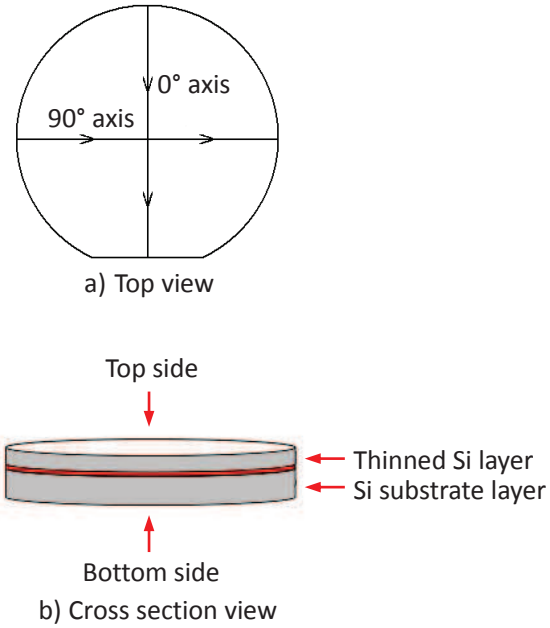

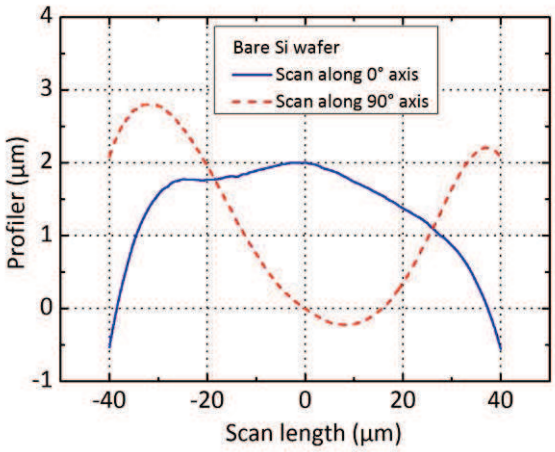

c) Bare Si wafer

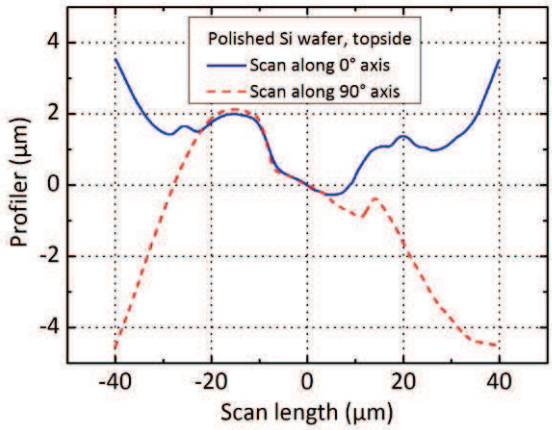

d) Polished wafer, topside

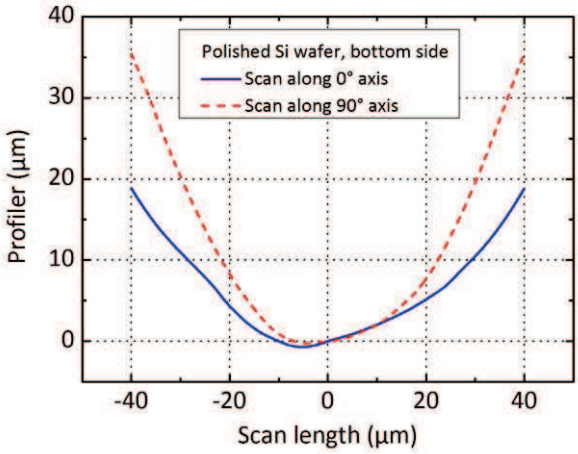

e) Polished wafer, bottom side

Figure 4-24. (a) Drawing of the scanning lines used, (b) definition of wafer sides and (c,d,e) plots of obtained surface profiles along different scanning lines and on different wafer surfaces.

It can be seen in Figure 4-24, the front side which has been polished during thinning process has a low height variation (less that 6 µm) over the whole wafer surface, while the bottom side that has been glued to a support can be found more 35µm's variation. Indeed, the testing wafer was firstly heated to 200℃ for the gluing process on a steel support with the aid of wax, then cooled down to room temperature for thinning process. The large bow found at the bottom side may result from the thermal expansion coefficient difference between steel and Si.

4.3.3 Conclusion on Double SOI Wafer Fabrication Work

From all the details of double SOI wafer fabrication discussed before, the obtained results can be concluded as follows:

1. Direct wafer bonding should totally seal two interfaces (Si/SiO_2-Si) after chemical activation, pre-bonding and high temperature annealing. The voids observed by infrared imaging set-up showed that some gas was captured inside inner cavities resulting from surface contaminations, dust and flatness defects. Contamination brought by tweezer contamination can be avoided by proper operation so the key parameters to eliminate observed bonding voids are still wafer cleanness and flatness. For further improvement, better starting wafers, careful preparation and cleaner environment are required.

2. O_2 plasma treatment can help to improve the bonding energy, but will bring in more unwanted contaminations from wafer transfer and reaction chambers. Improving its results also need cleaner environment and cleaner reaction chamber.

3. Top Si layer thinning by CMP was both measured with comparator and by a FTIR based method. The latter method needs the application of a Fourier transform operation to the raw data obtained from the FTIR instrument. Its results are believed to be more accurate and useful for the study of the polishing process performances.

4. The tested thinning process produces a large thickness slope on the surface with nearly 45 µm thickness variation for a 250 µm mean thickness. This difference may come from an uneven applied pressure on the wafer surface during grinding. To get better performances, a large effort will have to be spent to debug and adjust the equipment or a new system will have to be acquired. Roughness measurements prove that the wafer polishing process is able to provide a smooth surface comparable to the initial bare Si wafer. Nevertheless, wafer bow measurements show that the glued surface has a large bow after thinning, while the grinded and polished surface has a good flatness. This bow seems to be related to the gluing process as the support has a good flatness..

Until now, current fabrication results of double SOI wafer do not satisfy the requirements for its further exploitation. The performances of our DSOI wafer fabrication process are mainly limited by particle contamination of the clean room and equipments and possibly chemical products, and the insufficient performances of the polishing equipment. In order to be able to continue our Mirau interferometer project, we adopted as a substitute plan, the purchase of DSOI wafers from a commercial supplier. We could very luckily benefit from the existence of a remaining lot of DSOI wafers fabricated by Okmetic Company for a customer. The bought double SOI wafers have five alternating stacks of layers ($Si/SiO_2/Si/SiO_2/Si$) with thickness equal to 25/1.5/25/1/380 µm. And the top and intermediate silicon layers are highly doped with resistivity equal to 0.01-0.02 Ω·cm. All the design and fabrication works on tunable 3D integrated Mirau interferometers presented in this thesis are based on these double SOI wafers.

4.4 Fabrication Tests of First Top Side Patterning

After the double SOI wafer is obtained, what follows is the patterning of the top two Si layers. It is performed by a three layer ($Si/SiO_2/Si$) Deep Reactive Ion Etching (DRIE) with a single photoresist masking layer. This step is very critical because it defines most of the important patterns of the reference mirror scanner including the outlines of vertical combs and serpentine springs. In order to obtain the same sidewall profiles and homogeneous etched depths everywhere, all the patterns at this step were designed to have the same trench width of 5μm everywhere. A more detailed fabrication process flow of this surface micromachining step is shown in Figure 4-25.

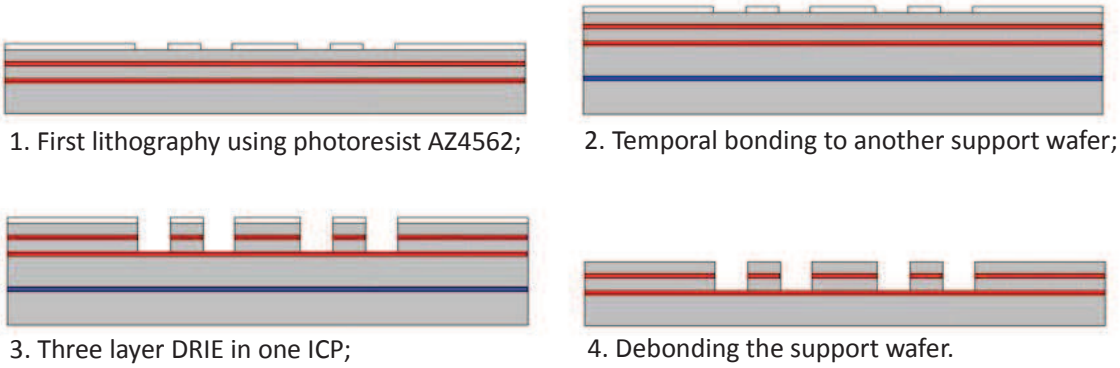

Figure 4-25.Fabrication process flow chart of first topside patterning.

Firstly, a thick AZ4562 photoresist layer was spin coated on a well cleaned double SOI wafer, exposed to Ultra Violet (UV) light and then developed in diluted AZ400K solution to form a masking layer (Figure 4-25.1). Next, the patterned wafer was temporally bonded to an oxidized Si wafer at around 70°C by using thermal grease (Figure 4-25.2). This oxidized Si wafer serves as a support wafer that will be clamped in the etching chamber. After that, the whole bonded wafer was introduced into an ICP chamber and underwent three independent etchings by changing the reaction gases and recipes in turns (Figure 4-25.3). Finally, the double SOI wafer was debonded from the support wafer by heating at 70 ℃ again (Figure 4-25.4), and cleaned in isopropanol then in acetone to remove the residual thermal grease and photoresist respectively.

4.4.1 Optimization of Lithography with Photoresist AZ4562

AZ4562 is a positive photoresist that is suitable for large thickness coating (3-30 μm). In our research group, AZ4562 thickness up to 30 μm was already successfully tested. Concerning the need of this experiment (etching mask for $Si/SiO_2/Si$, 25/1.5/25μm), a photoresist with a thickness of 5.3 μm (6000 rpm/s, 30s) is already adequate. Prior to the testing of DRIE etchings, an optimization of this photolithography with photoresist AZ4562 was performed to obtain a vertical photoresist profile and a precise trench width in accordance with the lithography mask design (5 μm).

The processing of photoresist AZ4562 was performed mostly by obeying the guidelines given by the manufacturer, which includes spin coating, prebake, exposure and development. What needs to be mentioned is the pre-coating of adhesion promoter PRIMER. This promoter needs to be coated

before photoresist AZ4562, otherwise long and thin arms of the comb fingers were found to move during development. After the whole processing, the sample wafer was cleaved and its cross section was observed and its sidewall profile was measured with a metallurgical microscope. In order to simplify the optimization process, only the UV exposure dose of the lithography was varied to find an optimal condition. The obtained trench profile as function of exposure dose is plotted in Figure 4-26a, and an example of cross section image is shown in Figure 4-26b.

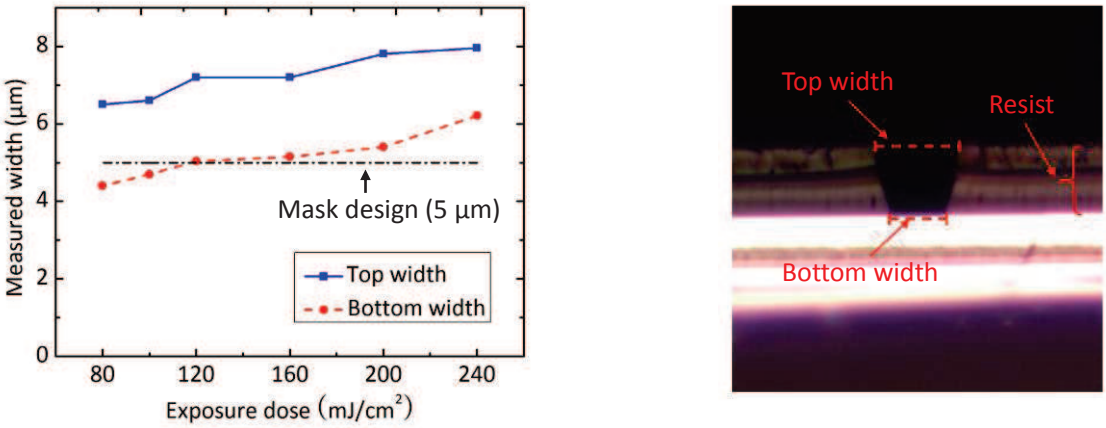

a) b)

Figure 4-26. (a) Plot of measured trench top and bottom widths versus exposure dose, (b) example of cross section image obtained with a metallurgical microscope.

The results show that there is always nearly a 2 µm difference between the top and bottom trench widths. Among different UV doses, the optimal result was found to be 100 mJ/cm^2. Then, through further optimization steps with this exposure dose, a better profile with 6 µm top width and 4.7 µm bottom width was successfully realized. For the following fabrication tests, we continued to use this recipe which needs 100 mJ/cm^2 exposure dose and 30-50s development time.

4.4.2 Development of Three Layer DRIE Etching

As mentioned above, DRIE etching of a Si/SiO_2/Si trilayer is not a conventional process. Our validation tests of this process have been splitted into four steps: firstly Si etching, then SiO_2 etching, then SiO_2/Si etching, and finally Si/SiO_2/Si etching. These tests were performed in collaboration with Benoit Belier, research engineer in IEF clean rooms facilities.

Si was firstly etched by a standard Bosch process which is composed by two alternating repeated processes: isotropic plasma Si etching in SF_6+O_2 gaz mixture and passivation process in a C_4F_8 plasma. The schematic diagram of this etching and Scanning Electron Microscope (SEM) image of obtained profile are shown in Figure 4-27. A 47.2 µm deep trench with a slightly larger width (6.7 µm) than designed and highly vertical sidewalls was obtained.

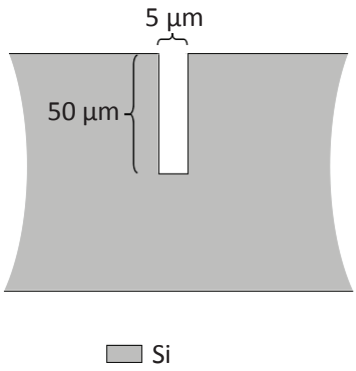

a) Schematic diagram of Si etching test

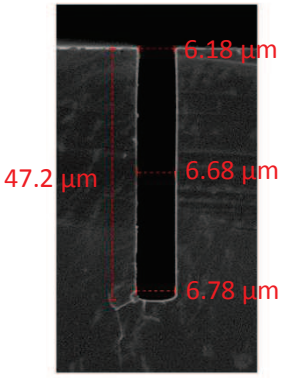

b) SEM image of obtained profile

Figure 4-27. (a) Schematic diagram and (b) SEM image of Si etching test performed by Bosch process.

The next experimental test was thermal SiO_2 layer etching. An oxidized Si wafer with a 1.07 µm thick SiO_2 film on the surface was etched in the same ICP equipment but with a different reactive gas (CHF_3). The schematic diagram and SEM image are shown in Figure 4-28.

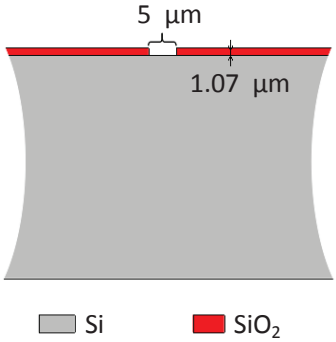

a) Schematic diagram of SiO_2 etching test

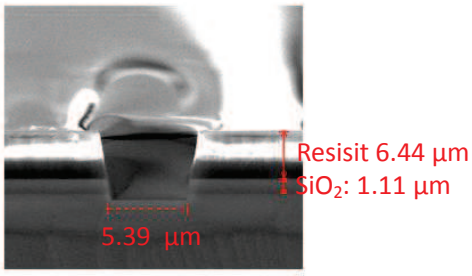

b) SEM cross section of the profile of SiO2 etch

Figure 4-28. (a) Schematic diagram and (b) SEM image of SiO_2 etching test.

Then, we combined these two etching processes by using only one photoresist layer. A deep Si etching was performed directly after SiO_2 etching. The corresponding images of this process are shown in Figure 4-29.

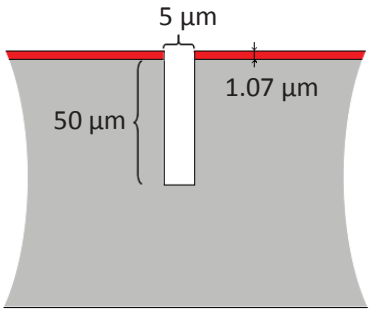

a) Schematic diagram of SiO_2+Si etching test

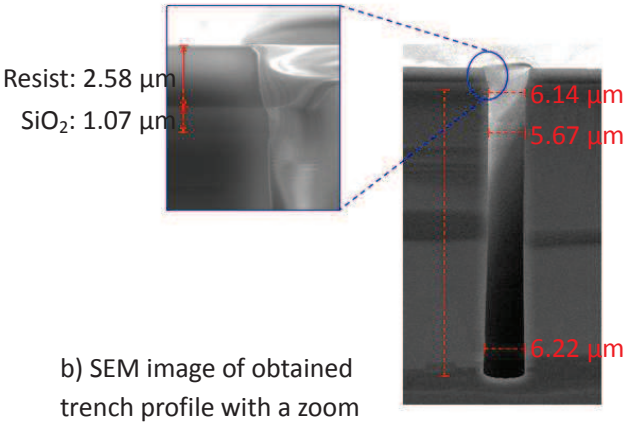

b) SEM image of obtained trench profile with a zoom view on the top surface

Figure 4-29. (a) Schematic diagram and (b) SEM image of SiO_2+Si etching performed in the same ICP equipment.

Finally we carried out the three layer etching of double SOI wafers (see results in Figure 4-30). Much effort was spent on the optimization etching time and applied power for these three independent etching steps. The second Si etching step etches same thickness of Si layer as the first one, but needs much more applied power.

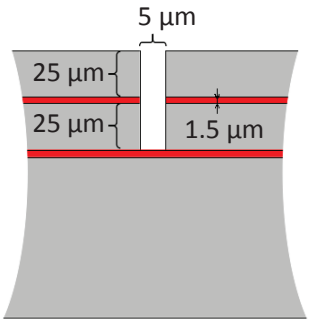

a) Schematic diagram of Si+SiO_2+Si etching test

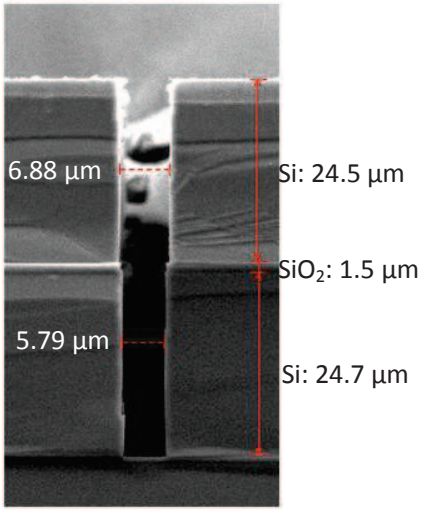

b) SEM image of Si+SiO_2+Si etching test

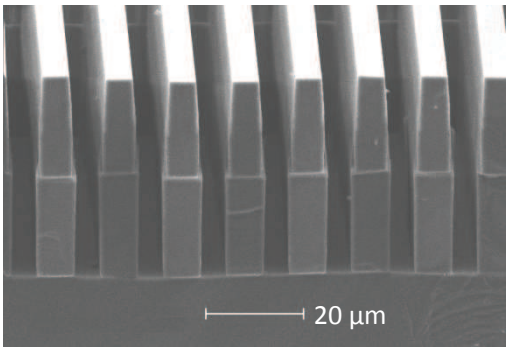

c) Bird view of etched comb fingers

Figure 4-30. (a) Schematic diagram and (b) SEM image of Si+SiO_2+Si etching in the same ICP equipment, (c) bird view of etched comb fingers.

In conclusion, we have tested and optimized the first topside lithography by using thick photoresist AZ4562. An optimal recipe for our experiment was chosen after tens of trials. A top width of 6 µm and bottom width of 4.7 µm for the photoresist trench was finally obtained. Then with this photoresist patterned masking layer, different wafers with different layer stacks were etched to validate the final goal of three layer etching masked by one photoresist film. All these etching tests were successfully performed. And a three layer trench (Si/SiO_2/Si) with desired thickness (25/1.5/25 µm) and almost same width everywhere (5.8-6.9 µm) was finally obtained.

4.5 Etching and Metallization on Highly Structured Surfaces

After the first patterning of the double SOI wafer, we need to open windows for contacts on the buried Si layer and metallize both the top and buried Si layer to allow electrical actuation. These fabrication steps need to be performed on a highly structured surface (trenches with 50 µm depth). Conventional spin coating of photoresist is known to have severe limitations for such a surface but, as the trenches which need to be protected are relatively narrow (5 µm), we nevertheless made a test by using a thick photoresist layer. Microscope image of a wafer that has endured a photolithography followed by a Si etch is shown in Figure 4-31. Ideally, all the areas shown in this image should have been coated by photoresist and not been damaged after etching. However results show that some areas were not well protected by photoresist. These experiments confirm that spin coating, even with a thick photoresist, is not suitable for local protection of areas with deep trenches.

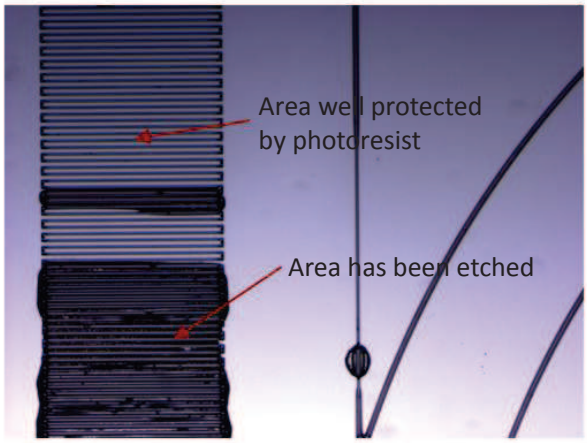

Figure 4-31. A test of spin coating photoresist on a highly structured surface.

In order to replace the conventional spin coating, we considered several possible methods. The first method is dry film photoresist masking lithography (Figure 4-32a). Dry film can be easily and fastly processed, and it can overhang highly structured surface with no bending nor collapse. But its disadvantage is a relatively large minimum pattern size that can be achieved (about 20 µm). Then, the second solution we considered is spray coating of diluted photoresist (Figure 4-32b). Spray coated photoresist could well cover the whole surface morphology of a non-planar surface. But unlike spin coaters, spray coaters can only work with highly diluted photoresists, so all photolithography parameters as well as Si etching parameters must be optimized again. Our clean room was equipped with a new spray coater at the middle of this thesis work, but to save time, the development of the spray coating method has not been launched during this thesis. Then, the third possible option is the use of shadow mask based lithography (Figure 4-32c). This shadow mask could be fabricated from a bare Si wafer by through wafer Deep Reactive Ion Etching (DRIE) or by using an apertured membrane. The main issue of this patterning technique is mask alignment. It can be done mechanically, for example by using capillaries or pins, but this solution is not suitable in our case where all trenches have the same too narrow width (5 µm) to get homogenous etching depths. Finally, a last possible method is delay masking technology, which makes use of two masking layers coated on the initial double SOI wafer (Figure 4-32d). Such different masking layers are able to define different etching depths with a single etching step. The difficulty of this method is the choice of mask layer 2, which

needs to be both thin and resistant to the following Si and SiO_2 etch. Common used masking materials for this process is a metal or SiNx. However, metallic masking layers are not allowed in our ICP equipment and PECVD SiNx has a poor resistance to SiO_2 etching conditions (buffered HF chemical etching).

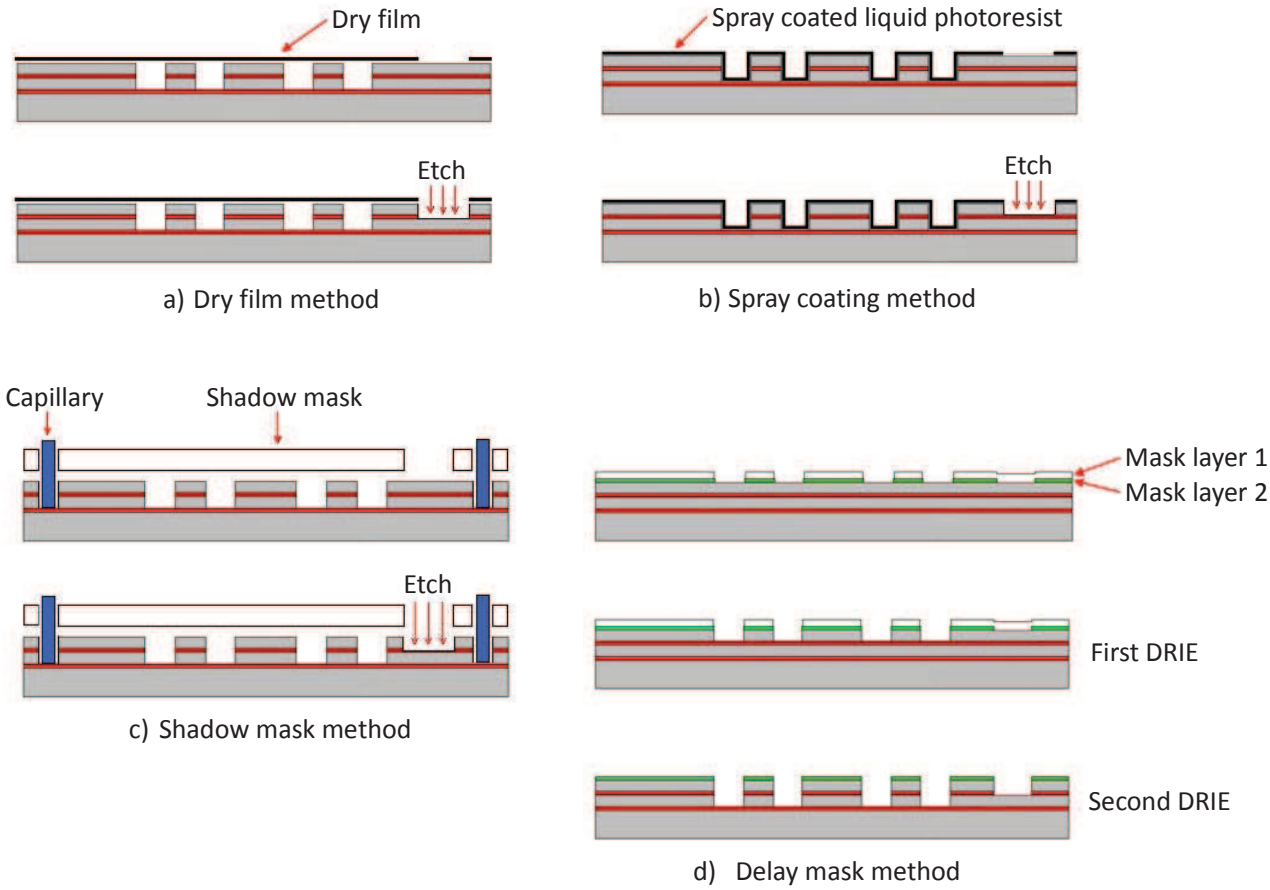

Figure 4-32. Different possible solutions for the fabrication technologies on highly structured surface.

Following this analysis, we have finally chosen the dry film photoresist. Its drawback of low patterning resolution is not critical for us, because the selected electrical contacts have a large planar size and a large misalignment tolerance.

Patterning by dry photoresist film technology has been previously studied in our research group for lithography and metal deposition by lift-off on a planar surface. Its development on highly structured surface is a contribution of this thesis work.

4.5.1 Lithography of Dry Film Photoresist on Non-planar Surface

The dry film photoresist used for this experimental work is MX5015 purchased from Dupont™ supplier. It is stored in rolls as shown in Figure 4-33a. As illustrated in Figure 4-33b, the dry photoresist film is protected by two plastic films: a polyethylene layer (that must be peeled off before lamination) and another polyester layer (that must be preserved during lamination). The selected dry film is the thinnest one (15µm) of the MX500 series and is able to achieve the best pattern resolution of about 20 µm..

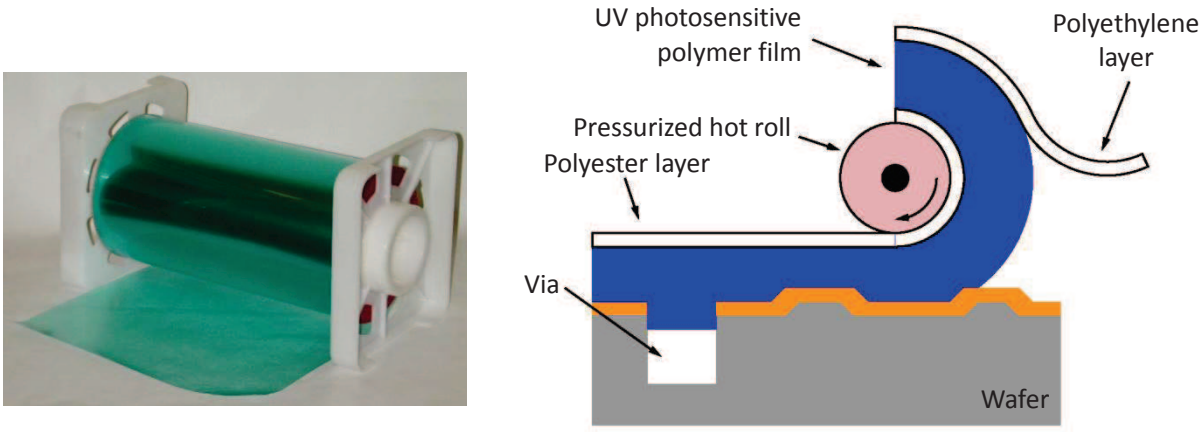

Figure 4-33. (a) Roll of dry photoresist film, (b) composition of the dry film and processing method of the different layers during lamination.

The lithography of dry film photoresist was carried out with the following procedure: 1) spin coating of adhesion promoter PRIMER on the wafer surface and wafer baking on a hotplate at 120 ℃ to solidify this promoter; 2) peeling off of the polyethylene layer from the dry film by a Scotch tape, and then lamination of the dry film on wafer surface by a pressurized hot roll as shown in Figure 4-33b above; 3) exposure of the wafer to UV light with a total dose of 80 mJ/cm^2; 4) peeling off the last polyester layer from the dry film, and dry film development in a diluted solution of MRD4000/75; 5) final rinsing and drying of the wafer. Let us emphasize that in case of lithography defects, the dry film could be totally removed in a bath of P1316 (Technic) at 60 ℃ .

An important fabrication step for dry film is the pre-coating of PRIMER. Previous work on this dry film in our research group has reported a high risk of air bubble captured during lamination and detachment of the whole film when a too long sink in the developer is performed. This issue could be totally avoided by pre-coating of PRIMER. This adhesion promoter is thought to largely increase the adhesion of dry film on Si wafer and to greatly reduce processing difficulties. Another concern about the dry film is its exposure to vacuum with some air captured inside underlying cavities. This occurs in our fabrication process during subsequent plasma etching and metallization steps. The dry film adhesion, integrity, hermiticity and fracture resistance performances are then very critical. Such a case under vacuum condition has been successfully performed with no fracture nor large delamination observed. This result proves that adhesion, stiffness and fracture strength of the dry film are suited to our requirements. Another issue is the handling of the polyester layer. According to our experimental results, it is recommended to keep it during exposure, because it can provide a good protection against mask contamination and its light absorption is negligible.

Dry film lamination has been performed on a highly structured surface (Fig. 4-34a) and was visualized by a microscope. The image in Figure 4-34b shows that a dry film can be laminated over deep and narrow trenches (50 µm depth and 5 µm width) without visible wrinkles or air bubbles. Figure 4-35 also shows that an apertured dry film is able to span over a very large cavity with its edges freely hanging at the periphery.

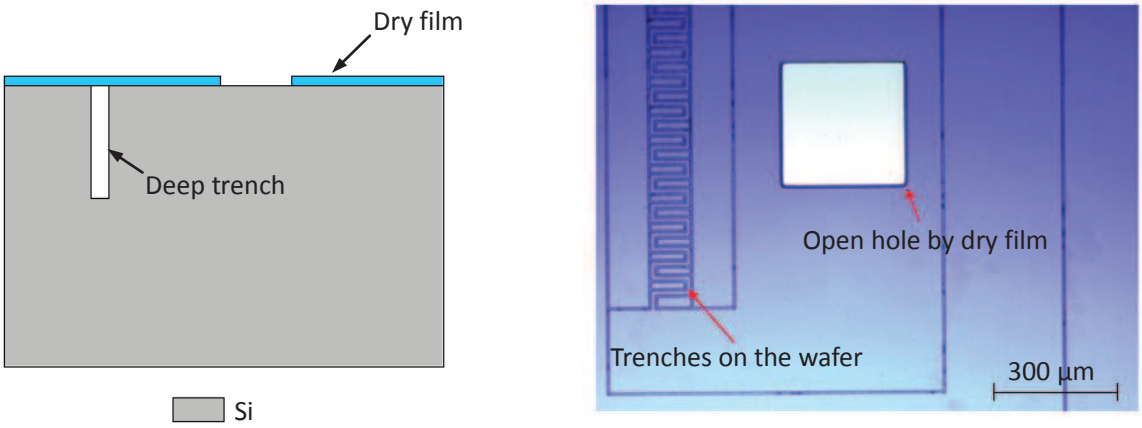

Figure 4-34. (a) Schematic drawing and (b) microscope image of a patterned dry film on a Si wafer with deeply etched trenches.

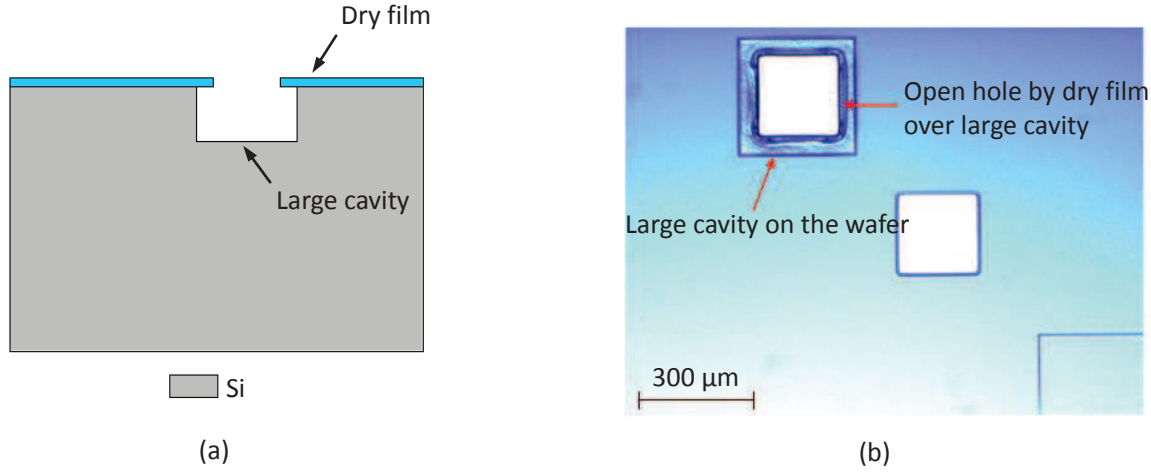

Figure 4-35. (a) Schematic drawing and (b) microscope image of an apertured dry film spanning over a large cavity.

4.5.2 DRIE and Metallization Using a Dry Photoresist Masking Film

After the experimental testing of lithography using dry film photoresist, the following fabrication tests were the opening of a window for the contact on the second Si layer and the metallization of two different Si layers having different heights.

Topside optical microscope image and SEM cross-section image of a Si DRIE with a dry film photoresist masking layer are shown in Figure 4-36. A 300×300 μm^2 cavity with a 25 µm depth and highly vertical sidewalls was demonstrated.

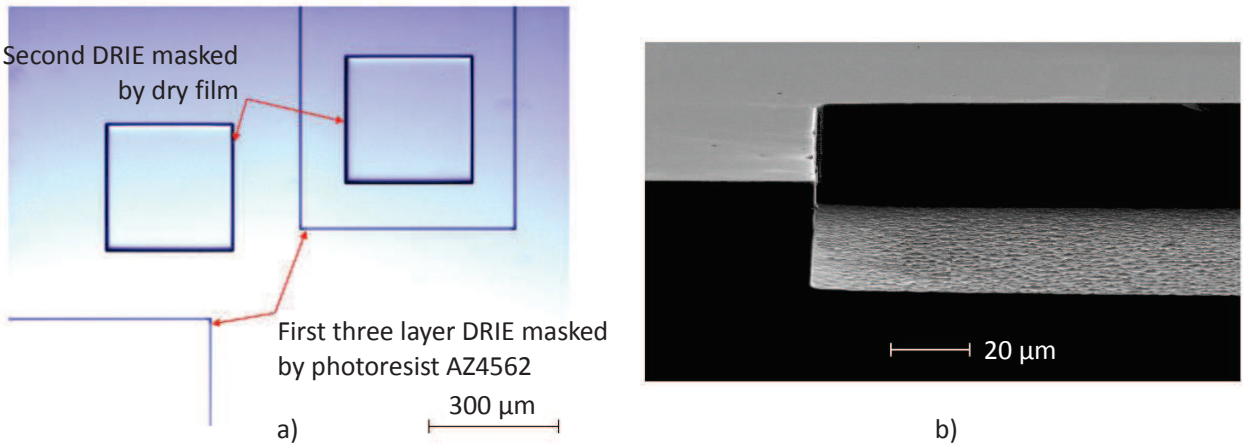

Figure 4-36. (a) Microscope image and (b) SEM image of DRIE test using a dry photoresist masking film.

The next test was the metallization of the two different Si layers of the DSOI wafer which are located at different heights. Dry film photoresist could bring us a great benefit by realizing metallization simultaneously at two different heights. This avoids one additional lithography and DRIE, and thus simplifies the fabrication process. The patterning of electrodes on the top Si layer was made by lift-off, while the bottom electrodes on second Si layer were fabricated by using the shadow masking principle (Figure 4-37a). The obtained results are shown in Figure 4-37b and 4-37c.

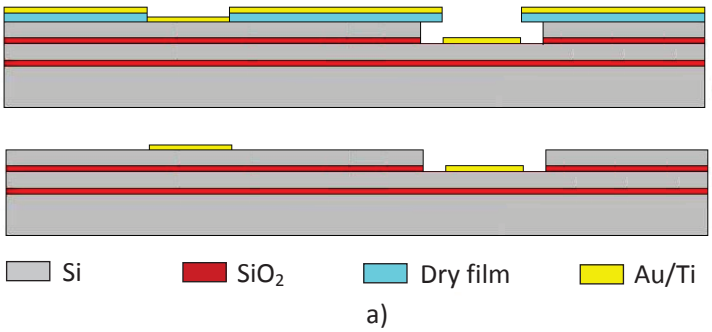

a)

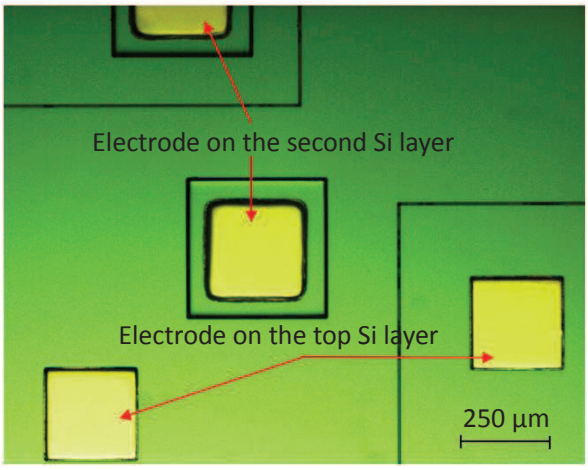

b)

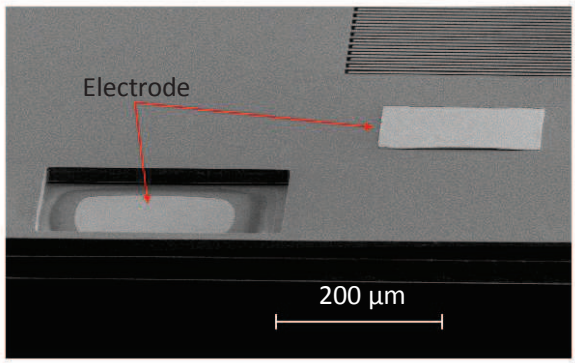

c)

Figure 4-37 (a) Technology principle, (b) microscope image and (c) SEM image of metallization at two different heights masked by dry film photoresist.

These electrodes are composed of an Au layer over a Ti layer. The pre-deposited Ti layer is intended to increase the mechanical adhesion of Au on the Si surface, and the Au layer is chosen for wire bonding and electrodes biasing. A careful inspection showed that, as expected, the electrodes deposited on the bottom (2nd) Si layer are slightly enlarged when compared to the dry film shadow mask window size but they are still within the cavity area. Such result is achieved when the sputtering target surface is parallel to the sample surface. When a co-sputtering system with a tilted target and a rotating sample holder are used, the lateral expansion of the electrodes was found to exceed the margin design (50 µm).

Electrodes deposited on the top Si layer by lift-off seem to have a well-defined edge. However, a zoomed view evidences some wrinkles on the edge, as shown in Figure 4-38b. These wrinkles are measured to have a 1-5 µm height. They are resulting from residues and the non inverted sidewall profile of the dry film after development (Figure 4-38b). Fortunately this issue is not critical for our design. Further improvement could result from an optimization of the exposure dose and a possible addition of an O_2 plasma etching after dry film lithography.

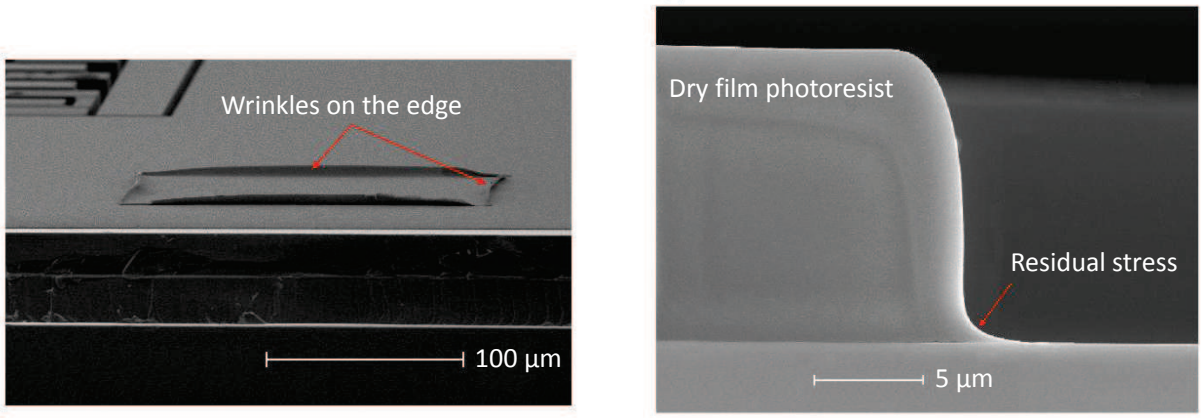

Figure 4-38. (a) Bird view and (b) cross section SEM image of a patterned dry film photoresist respectively showing electrode wrinkles and dry film residues on bottom edge.

To summarize this section, we have developed a quick and suitable patterning technology working on highly structured surfaces owing to the use of a dry photoresist masking film. A pre-coating of adhesion promoter PRIMER is essential for its processing as it totally eliminates air bubbles observed in previous study. The DRIE on non-planar surface and simultaneous metallizations at different heights have both been successfully developed by using dry film photoresist. These fabrication steps are the final ones of the proposed topside fabrication stage of our micro-mirror vertical scanner.

4.6 Release Step and Final Fabricated Device

After the top side processing is finished, the wafer is etched from backside to release all suspended structures. A detailed fabrication process flow of this release is shown in Figure 4-39.

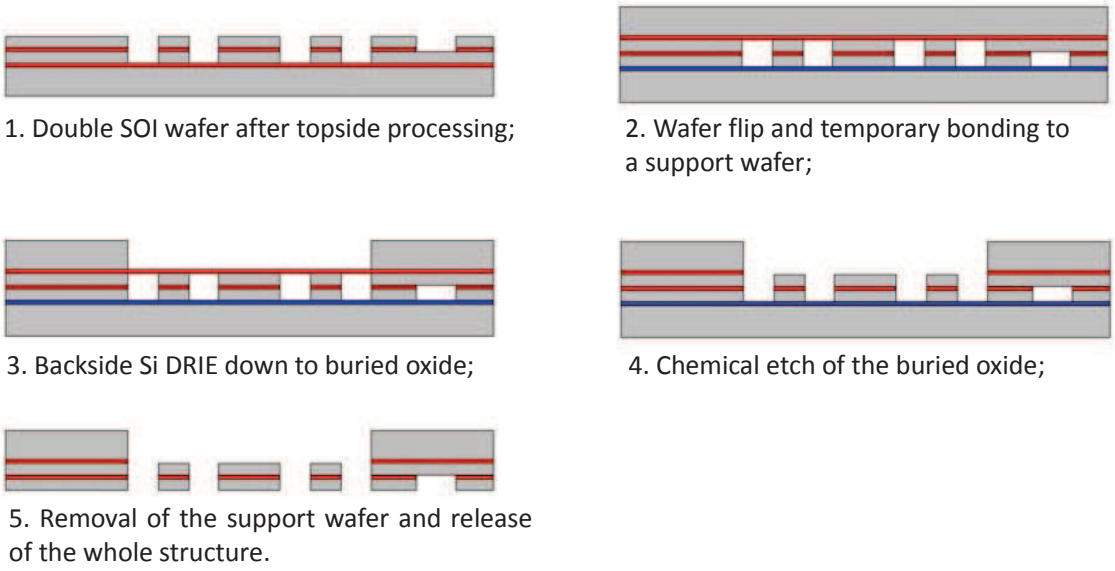

Figure 4-39. Fabrication process flow chart of backside etch and structure release.

After topside processing, the double SOI wafer was initially spin coated with a protective layer on the topside (standard liquid photoresist). This coating was intended to prevent scratches on the topside and more important, to get rid of contaminations coming from thermal grease that needed to be removed at the last step. Then the wafer was temporally bonded to a support wafer (oxidized Si wafer) by using thermal grease following exactly the same process as described in section 4.4 above (see Figure 4-39.2). Next, a backside DRIE was applied to etch the whole Si substrate down to the buried oxide layer (Figure 4-39.3). Then at step 4, the buried oxide was etched by Buffered Hydrofluoric acid (BHF). The sandwiched SiO_2 layer that will compose our three layer device was expected to be protected by the support wafer during this etching process. Nevertheless a slight lateral under-etching was observed. This etching is limited by the low etching rate of the confined film (limited diffusion). Finally the support wafer was removed by heating at 70 ℃ , and cleaned by isopropanol then by acetone. Let us emphasize that the wafer must be flipped during the last two solvent rinses, otherwise the thermal grease may fall down on the device surface and become very difficult to remove afterwards.

The experiment tests were firstly carried out on standard SOI wafers ($Si/SiO_2/Si$, 50/2/400 μm). A large cavity was vertically etched from the backside until buried oxide was reached (shown in Figure 4-40). Then serpentine springs made from the device layer of SOI wafer were freely suspended after release. Cross section and bird view SEM images of these springs are given in Figure 4-41a and b. It can be seen that these springs with different parameters were all horizontally suspended with no obvious bending and curving. Measurement of their spring constants are scheduled to evaluate the difference between computed theoretical values and experimental ones measured on a real device.

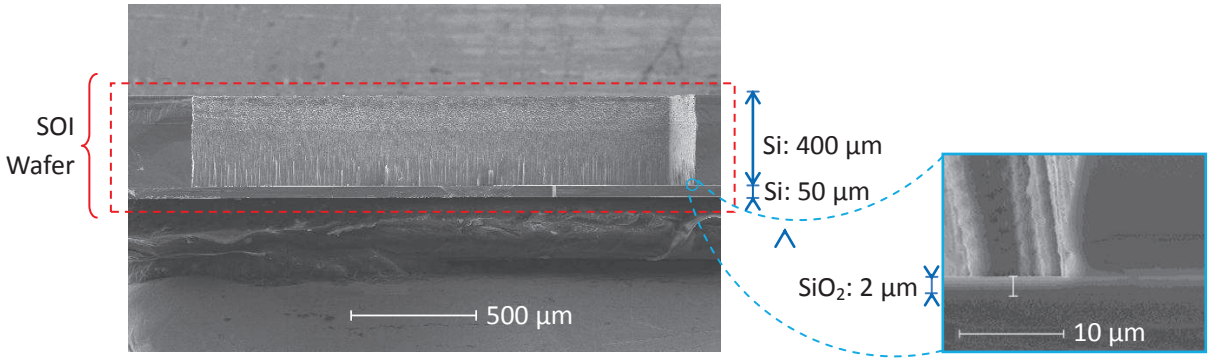

Figure 4-40. Backside DRIE on SOI wafer.

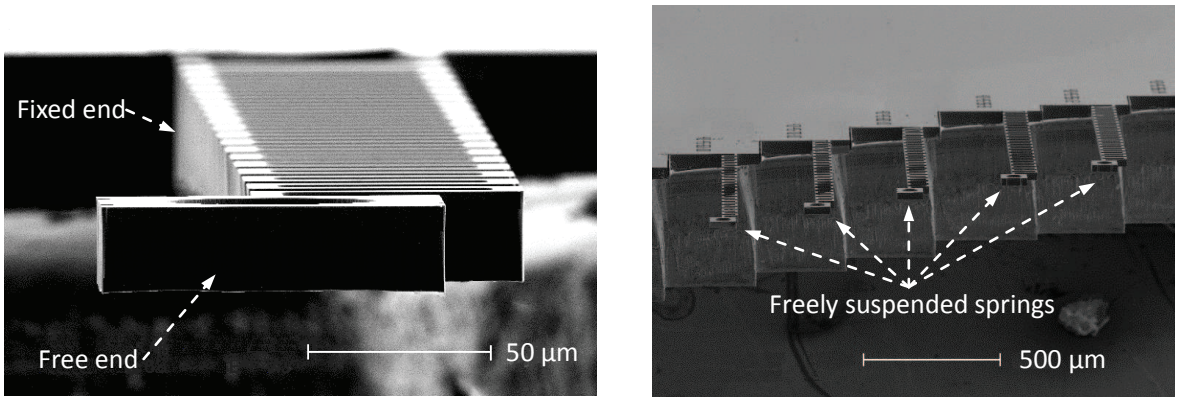

Figure 4-41. Released serpentine spring made from the device layer of SOI wafer.

At the end of this thesis, due to lack of well performed double side aligner and certain limitations of the proposed fabrication process and structure design, there is still some remaining issues of the final release step that has not been ideally solved. The production yield is quite low, and lateral stiction occurs when the device is dragged out from the liquid solution.

Anyhow, a full fabrication run of a movable mirror scanner based on double SOI technology was still finished. The microscope images and SEM images of fabricated device are shown in Figure 4-42 and Figure 4-43 respectively.

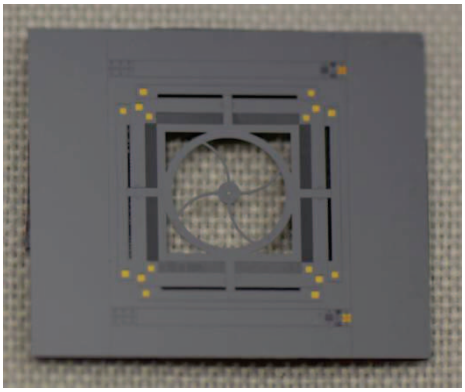

Figure 4-42. Microscope image of finished mirror scanner fabricated from a double SOI wafer.

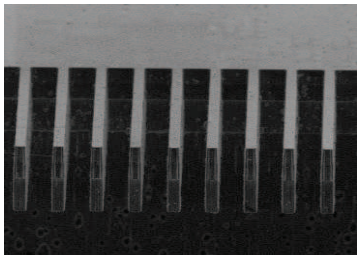

Vertical combs

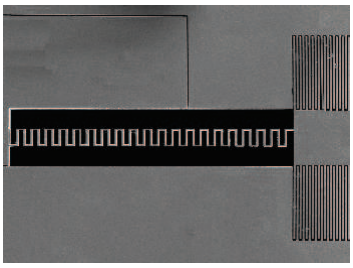

Serpentine spring

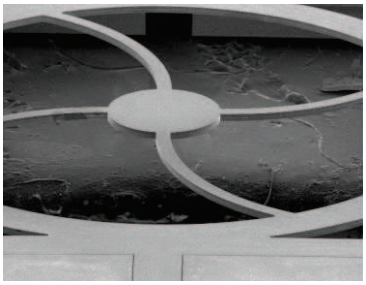

Central mirror with curved beams

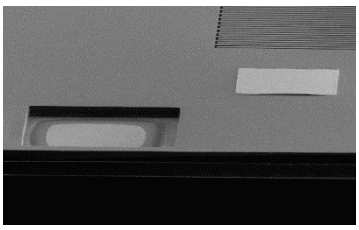

Electrodes on top and lower Si layer

Figure 4-43. SEM images of finished mirror scanner fabricated from a double SOI wafer.

4.7 Beam Splitter Fabrication

Besides the micro-mirror scanner discussed above, a beam splitter formed by semi-reflective multi-layer is also needed to constitute the Mirau micro-interferometer. This fabrication work was previously carried out in our research group by Hervé Bertin. Six pairs of SiNx and SiO_2 layers deposited by plasma enhanced chemical vapor deposition (PECVD) were chosen for this beam splitter. In the following we will summarize the processing steps and results obtained previously during the thesis of Hervé Bertin [Bertin-2013] and summarized in a published paper [Bertin-2013-2].

4.7.1 Tuning The Residual Stress by Annealing

The multilayer membrane requested for the Mirau interferometer must have a controlled reflectance coefficient in a broad wavelength range as well as a high flatness. The optical design and simulation work was already discussed in section 3-4. A reflectivity around 50% is achievable in the spectrum range of 550-800 nm. Then the latter requirement of flatness is typically solved by fabricating the membrane in slight tensile stress.

The total residual stress in a multilayer membrane is given by the weighted sum of the stress of each layer:

$$\sigma_{tot} = \frac{\sum \sigma_i \, t_i}{\sum t_i} \tag{4.1}$$

where σ_i and t_i are respectively the residual stress and thickness of layer i.

SiN_x and SiO_2 layers deposited on silicon in the multifrequency PECVD reactor of IEF at 300°C with a low excitation plasma frequency (380kHz) and with "standard" conditions are initially in a high compressive stress state. Stress values measured previously by the wafer curvature method using a FSM laser scanning system are -820 MPa for SiN_x films and -370 MPa for SiO_2 films.

It was shown from FTIR measurements of chemical bonds in low frequency PECVD films that annealing at temperatures above the deposition temperature produces a desorption of hydrogen and the formation of new SiN or SiO bonds [Bertin-2013] [Bertin-2013-2]. This is accompanied by a slight variation of stress in silica films and to a large compressive stress reduction and even the generation of a tensile stress above 650°C for silicon nitride films (Figure 4-44).

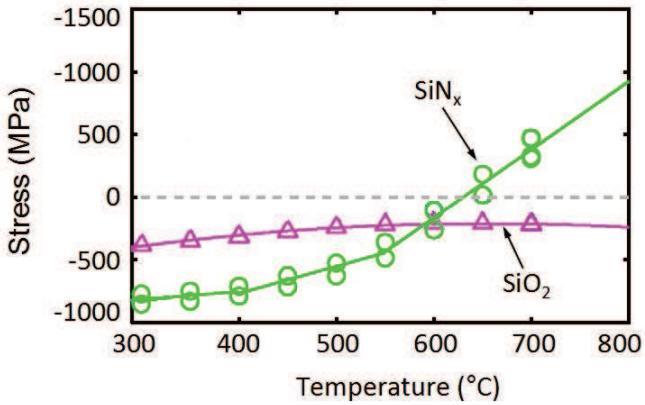

Figure 4-44. Variation of residual stress of PECVD SiN_x and SiO_2 layers as function of 1 hour annealing temperature.

These two different variations provide a possible solution for the tuning of the whole residual stress of multilayers composed of pairs of PECVD SiO_2 and Si_3N_4 films by performing a post-deposition annealing at temperatures above 650 ℃ .

Through analytical calculation using Formula 4.1 and the multilayer composition given in Table 3-3, the total residual stress is expected to change from -565.3 MPa before annealing to 103.7 MPa after annealing at 750 ℃ . Actually, Hervé Bertin showed that this calculation provides only a starting point for stress optimization because stress relaxation of films in a multilayer is different from that observed in single films. This arises notably from different hydrogen diffusion rates of hydrogen in silica and silicon nitride films and to hydrogen accumulation at interfaces. It remains nevertheless valid that high temperature annealing allows the fabrication of PECVD SiO_2/Si_3N_4 multilayers with a controlled tensile stress.

4.7.2 Fabrication Procedures of Beam Splitter

The fabrication process steps of a dielectric multilayer beam splitter wafer are indicated in Figure 4-45. Firstly, a low bow and low total thickness variation (TTV) Si wafer is cleaned and coated with alternating layers of SiN_x and SiO_2 by PECVD. The thickness of each layer is given in Table 3-3. Then the whole wafer is transferred into a furnace and annealed in nitrogen gaz at 750 ℃ for 1.5 hour. In the next step, the wafer is temporally bonded to a support wafer with thermal grease and etched by DRIE from the backside through a masking layer aperture until a remaining Si thickness of about 10-20 μm. After that, the support wafer is removed by heating at 70 ℃ (Figure 4-45.4). A second highly selective XeF_2 etch is then performed to remove all the remaining Si substrate.

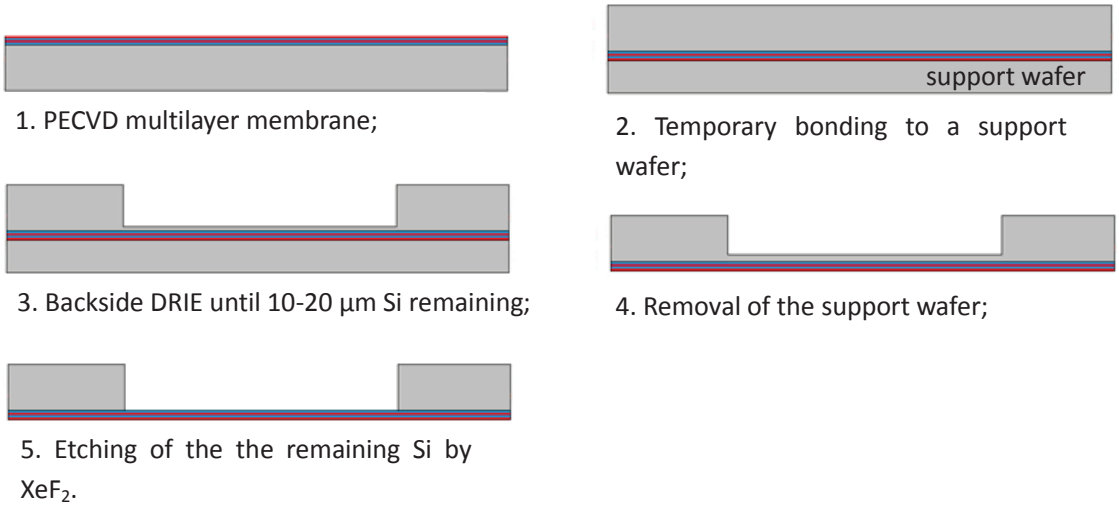

1. PECVD multilayer membrane;

2. Temporary bonding to a support wafer;

3. Backside DRIE until 10-20 µm Si remaining;

4. Removal of the support wafer;

5. Etching of the the remaining Si by XeF_2.

Figure 4-45. Fabrication process flow chart of dielectric multilayer beam splitter membrane.

It was demonstrated that this fabrication procedure has a quite high production yield. This is illustrated in Figure 4-46a which shows that octogonal membranes with different diameters could be successfully released on a 4 inches wafer (Figure 4-43a). These membranes were fabricated for a tunable Fabry-Pérot filters array. Their octagonal shape was chosen to maximize their coverage in this device but the presence of angles was shown to produce a stress inhomogeneity and a local out-of plane deformation of the membranes which depends on stress level and membrane size. For the Mirau interferometer circular membranes will be used.

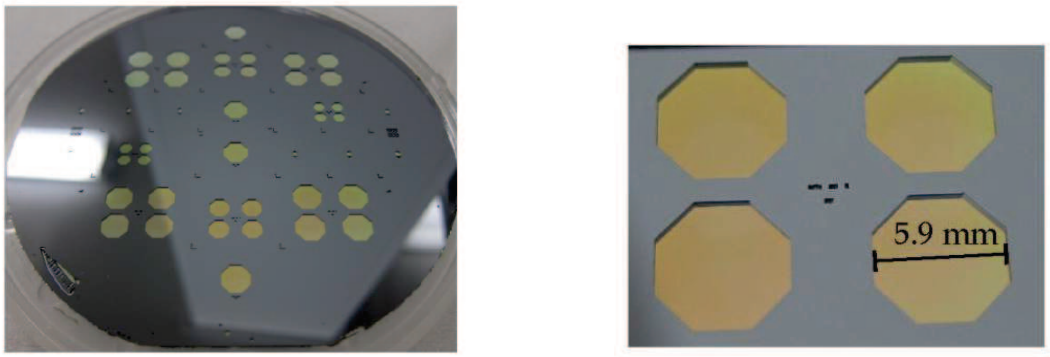

(a) Picture of a Si wafer with octagonal 12 layers membranes

(b) Close view of large area membranes

Figure 4-46. Released multilayer beam splitters with different membranes sizes on a silicon wafer.

4.8 Conclusion

An original process with only 5 lithographic mask levels is proposed for the fabrication of the reference mirror scanner in double SOI wafer technology. All critical patterns, notably the fingers of the self-aligned vertical electrostatic combs and the serpentine springs, are defined by the first UV photolithography and Deep Reactive Ion Etching (DRIE) etching step. All following fabrication steps are performed on highly structured or apertured surfaces. To overcome this difficulty after considering various options such as spray coating or delay masking layer, we choose to develop various patterning techniques based on the use of thin dry photoresist films. Lithography with dry photoresist film has limited lateral resolution (~20µm) and limited performance of resist wall, but this is not an issue for fabrication process of this scanner. Conversely, it allows a minimization of the number of fabrication steps and reduces the sensitivity of the process to particle contamination and warranties an homogeneous thickness of the photoresist film. .

The main critical fabrication steps were investigated one by one before attempting a full run of the fabrication process.

We first investigated the direct bonding of a Si wafer with an oxidized Si wafer surface and its subsequent thinning by Chemical Mechanical Planarization (CMP). These steps are required for the fabrication of a double SOI wafer. As direct wafer bonding and CMP of 100mm Si and SiO_2/Si wafers had not been previously investigated at IEF, specific characterization techniques were developed such as NIR transmission imaging of bonding defects and multilayer thickness measurement by Fourier transform infrared spectroscopy. Various surface preparations (with or without plasma activation), bonding conditions and high temperature annealing parameters were tested but the presence of large bonding defects could not be totally avoided. We attributed these defects to a not sufficiently controlled particle and organic contamination in the clean rooms. CMP of bonded wafers was nevertheless investigated and thinned wafers with a low rms surface roughness could be obtained. While good results were previously obtained at IEF on low area samples, the thickness homogeneity of thinned 100 mm wafers was found very poor and not acceptable for our needs. We finally choose to use commercially available double SOI wafers with 25µm thick top and bottom Si layers and 1.5µm buried oxide layer..

A major step of the mirror scanner fabrication process is the DRIE etching of the top Si/SiO_2/Si trilayer of the double SOI wafer. Such etching is not usual and not straightforward because of the very different plasma etching behavior of Si and SiO_2 and the possibility of notching effects. After different trench etching tests in Si, SiO_2, SiO_2/Si and double SOI wafers, a process able to pattern 5 µm wide and 50 µm deep trenches with vertical walls in a DSOI wafer could be defined. This process uses different parameter sets for each layer. It is not yet ideal as it produces narrower trench in the bottom Si layer but this result was considered sufficient for our requirements.

Two patterning techniques on highly structured surfaces based on dry photoresist films were successfully developed: DRIE etching of cavities with a dry film masking layer and simultaneous patterning of metal contacts at different heights. This later process is the most innovative and combines aligned lift-off and shadow masking techniques with a single dry film masking layer.

Finally, a run of the full fabrication process including backside DRIE eching and release by chemical etching of the revealed SiO_2 layer was performed. Fabricated serpentine spring test devices showed that the SOI wafers have a very low stress gradient (no spring curvature). Unfortunately the released scanner structures were found stuck by lateral stiction effect and the performances of the fabricated scanners could not be evaluated at the end of this thesis work.

5. Conclusion

We investigated the miniaturization of Mirau optical interferometers mainly for their implementation in full field optical surface profilometers. Beside a higher compactness, a lower cost owing to batch fabrication and an easier adaptation to various wavelength ranges, miniaturized Mirau interferometers offer the new ability to build interferometer arrays for parallel measurements. Analysis of published works shows that integration of Mirau interferometers was mostly done for their use with a single monochromatic light source and with an external adjustment of the optical path difference between the two interfering beams. The goal of this thesis was to go further by adding the ability of a large range and bidirectional optical path difference integrated tunability and by extending their wavelength range of operation. Because of the low inertia of micromachined structures, faster measurements by phase shifting, sinusoidal phase modulation of low coherence fringe scanning interferometry are expected.

The proposed configuration of integrated tunable Mirau interferometer is based on the 3D integration (vertical stacking) of a reference mirror vertical scanner wafer with a beam splitter wafer. They were both designed to be compatible for an operation of the Mirau interferometer in the visible-near infrared range.

In most previous works the reference mirror is supported by a transparent membrane. In this work, the reference mirror is suspended by stiff, but stress relaxing, curved arms in an open frame structure. The resulting mirror scanner is thus very largely independent on the wavelength range of operation. The Mirau interferometer tunability is achieved by suspending this frame with serpentine springs and by its actuation with vertical electrostatic comb drives. The major novelty of the proposed design is its ability of a large and bidirectional translation range owing to the use of composite $Si/SiO_2/Si$ self-aligned vertical electrostatic combs made from a double SOI wafer.

The beam splitter was designed to be made of a semi-reflective dielectric multilayer membrane. Optical simulations and calculations demonstrate that, by using a membrane made with 6 pairs of SiO_2/Si_3N_4 PECVD layers, a 50% beam splitter suitable for its use with a high numerical aperture objective (NA=0.6) and with narrow band LED illumination in the 550-800 nm wavelength range can be obtained. This beam splitter membrane has a sufficiently low thickness to get low spherical aberrations. However, the computed phase difference between reflected and transmitted light for this beam splitter is too high for low coherence Mirau interferometry with a broadband light source if a reference mirror holder with an open structure is used. Low coherence scanning interferometry with

this beam splitter can still be considered but with a limited light source spectrum bandwidth and thus with a degraded vertical resolution. A fully compensated Mirau interferometer might be achieved by adding a dielectric membrane but at the expense of a much more complex fabrication process. For broadband low coherence interferometry, another beam splitter multilayer membrane will have to be designed in the future.

An in depth mechanical and electromechanical modeling of the reference mirror scanner by analytical and finite elements simulations has been performed. Conventional electromechanical design of an electrostatic microactuator starts from the desired translation range and maximum admitted voltage to define the geometry of the electrostatic comb drives and the spring constants of the suspensions. Because the design is based on vertical electrostatic combs in double SOI technology, a different methodology was used. The starting points were design rules for the maximum aspect ratio of the electrostatic gaps and comb fingers, the maximum foot print of the springs and comb drives, and the maximum translation range (limited by the thickness of Si layers of available DSOI wafers). Calculations and simulations were then performed to evaluate the maximum vertical force that can be generated by electrostatic combs for a reasonable voltage (40-60V), then the required spring constants were determined and the geometry of the springs was optimized.

Serpentine springs were chosen for the frame suspensions and an optimization procedure combining analytical 2D calculations and 2D and 3D finite element simulations allowed to obtain a low vertical spring constant and a remarkably high ratio of lateral to vertical spring constant ratio (k_x+k_y=198 k_z).

Electrostatic FEM simulations showed that a ±20µm mirror translation range is achievable for an applied voltage of ±50V with a reasonable number of finger pairs (N=624) and the optimized suspension springs. In addition, the initial force without offset between the electrostatic fingers was found sufficiently high for bidirectional actuation and the generated force approximately constant in most of the translation range. These were mandatory requirements for a successful operation of the vertical electrostatic combs. The predicted total translation range (40µm) is among the highest values (if not the highest value) reported for a vertical scanner with vertical electrostatic combs in non resonant mode of operation. It should allow scanning interferometry measurements of highly structured surface what was not yet demonstrated with an integrated Mirau interferometer. It is also useful to compensate wafer bow, total thickness variations and possibly stress induced deformation of the scanner and beam splitter wafers which will lead to variable air gaps between the mirror and the beam splitter after wafer bonding. According to the translation considered, the scanner open loop resolution can reasonably be expected to be in the 0.4 nm-10nm range what is compatible with high resolution interferometric measurements by phase shifting interferometry or fringe scanning interferometry.

Global FEM simulations of the scanner mechanical structures demonstrated that the final design produces a negligible deformation of the mirror during translation. Dynamic mechanical simulations predict a resonant frequency of 464 Hz for the fundamental vibration mode. This value corresponds to a response time of approximately 6 ms which is suitable for fast phase shifting or fringe scanning measurements. However the resonant frequencies of the first 3 vibration modes (464-703 Hz) remain likely too low to get a good immunity to external disturbances. The displacement of the mechanical structure induced by weight is also non negligible (~2µm). These are the two main limitations of this current design.

This version of the scanner was designed for conservative maximum values (10) of the aspect ratios of the electrostatic gaps and fingers. If larger aspect ratios can finally be achieved in practice, a design with larger vertical spring constant will become possible what will lead to a better scanner with higher resonant frequencies and lower weight effect. This is also true if the design is limited to a lower translation range.

An innovative 5 mask levels fabrication process of the proposed scanner which requires only one accurate patterning step and which minimizes the total number of fabrication steps was defined. This could be achieved owing to the extensive use of dry photoresist film techniques to pattern highly structured surfaces and to perform multilevel metallization on such surfaces. Tests of the most critical fabrication steps were then performed:

First, tests of direct bonding and subsequent thinning by Chemical-Mechanical Polishing (CMP) of a oxidized Si wafer with a Si wafer were performed to investigate the feasibility of double SOI wafers fabrication in our clean room facilities. Several characterization techniques, such as multiple thickness measurements by Fourier Transform Infrared Spectrometry and defect inspection by Near-Infrared (NIR) imaging, were specifically developed for the evaluation of bonding and thinning processes. Results were not satisfactory enough because of a too large amount of particle and/or organic contamination in the clean rooms and of unsufficient performances of the polishing machine for 100 mm wafers. Commercially available DSOI wafers were thus used for the following experimental works.

Then, we investigated Deep Reactive Ion Etching (DRIE) of 51.5 µm deep trenches in a double SOI wafer by a Bosch like process. Such etching step is demanding as it defines all critical patterns dimensions (springs, gaps, vertical combs,..) of the scanner and is not obvious because of the largely different etching behavior of Si and SiO_2 and of possible charging effects. Although not yet fully optimized, a process leading to trenches with vertical walls, without notching but with a slight narrower trench in the bottom Si layer could be obtained by combining 3 etching steps with different parameters.

Finally, different patterning techniques by dry film photoresist technology were developed. Lithography and Si DRIE etching on highly structured SOI surface (51.5 µm high patterns) was successfully achieved with a dry film photoresist masking layer. Likewise we demonstrated for the first time the possibility to pattern metallic (Au/Ti) contacts simultaneously at different locations having a large height difference (25 µm) by combining lift-off patterning and shadow masking patterning with a single dry photoresist film.

Results of these preliminary tests were used to perform a full fabrication run of a mirror scanner. Unfortunately, a stiction of the released scanner structure, attributed to residues of thermal grease used for temporary bonding of a protecting wafer during the last DRIE etching step prevented scanner operation and evaluation of its performances.

Concerning the beam splitter membrane, the fabrication process is based on high temperature annealing of a PECVD multilayer for stress control and membrane release by DRIE and highly selective XeF_2 etching. This process was already developed in the research group for a micro-machined tunable Fabry-Pérot filters array by Hervé Bertin and large area beam splitter octagonal membranes are available. The same process will be used in the future for the fabrication of circular membranes with a high flatness and optimized dimensions for the Mirau interferometer.

Another fabrication run of the mirror scanner is in progress and we hope it will allow a full characterization of mirror scanners. Meanwhile we started to characterize the spring constants in all directions of our fabricated serpentine spring with commercial mechanical probes (Femto Tools company) recently acquired by the research group. If operational, a mirror scanner die associated with an available multilayer membrane die should allow a first evaluation in open loop mode of the designed tunable integrated Mirau interferometer by implementing it on one of the optical interferometric profilers existing in Institut d'Electronique Fondamentale.

To get a fully integrated Mirau interferometer, another fabrication step will also have to be developed: the assembly of mirror scanner wafer and beam splitter wafer with a well-controlled gap. This will require a low temperature and low stress wafer bonding step to avoid degradation of the metallizations. The use of adhesive wafer bonding with benzocyclobutene (BCB) combined with stops, already considered in a previous project for tunable micromachined Fabry-Pérot filter arrays, or of a low temperature Transient Liquid Phase (TLP) wafer bonding with an InAu or CuSn sealing ring, under development for other projects of the research team, could be used.

Finally, for close loop operation of the integrated tunable Mirau interferometer, a capacitive detection able to work at 50V will have to be implemented.

In summary an integrated tunable Mirau interferometer has been carefully designed from a mechanical, optical and electromechanical points of view and its fabrication has been partly but almost completely investigated. A large amount of work is still required to obtain a fully integrated device working in close loop mode and implemented on an optical profiler. Nevertheless, the design is robust and well supported by modeling, and the progress of the fabrication process is sufficient to consider that the realization of a fully integrated tunable Mirau interferometer suitable for optical profilometry or vibrometry should be possible in the near future. As mentioned above there is a margin of improvement of the performances of the designed tunable Mirau interferometer if the aspect ratio of Double SOI wafer DRIE etched patterns can be increased above 10, and if a beam splitter design with a better phase compensation can be obtained.

Appendix

Synthèse des travaux en langue française

Introduction

Au sens strict du terme, les microsystèmes électromécaniques (MEMS) exploitent les déformations et/ou les vibrations de microstructures suspendues réalisées par micro-usinage de surface ou de volume pour réaliser des capteurs ou des actionneurs intégrés. Depuis leur introduction au début des années 80, les MEMS ont trouvé une très large gamme d'applications dans tous les secteurs et le marché des MEMS a largement augmenté ces dernières années notamment en raison de leur introduction dans les produits de grande consommation (jeux vidéos, téléphones portables, composants télécoms, caméras de surveillance, transports…). Les MEMS optiques et les microsystèmes optoélectromécaniques (MOEMS) constituent un sous ensemble des MEMS qui combine des MEMS avec des technologies micro/nano optiques pour la manipulation de la lumière ou la transduction optomécanique [Motamedi-2005]. Les exemples de MEMS optiques les plus connus sont les matrices de micro-miroirs [Hombeck-1997] ou les réseaux de diffraction commutables (light gate valves) utilisées dans les vidéo projecteurs, les matrices de microbolomètres [Niklaus-2007] utilisés dans les caméras infrarouges et les composants optiques ajustables (lasers, filtres,…)[Chang-2000].

Le MEMS optique étudié dans cette thèse est un microinterféromètre Mirau ajustable et intégré 3D, c'est-à-dire réalisé par assemblage hybride vertical de tranches (wafers) de matériaux. Les interféromètres optiques macroscopiques de type Mirau sont des interféromètres à 2 faisceaux coaxiaux usuellement combinés avec un objectif de microscope pour réaliser le plus souvent des profilomètres (et vibromètres) optiques interférométriques (cf Chapitre I). Cette technique de profilométrie/vibrométrie sans contact, 3D et plein champ est la plus utilisée pour la caractérisation de la topographie, des déformations (et des vibrations) des microstructures avec une résolution verticale (sub) nanométrique et une résolution latérale (sub) micronique [Bosseboeuf-2003].

Les interféromètres Mirau conventionnels sont fabriqués avec des composants optiques et optomécaniques macroscopiques, et leur différence de chemin optique est typiquement variée à l'aide d'un actionneur piezoélectrique externe asservi. L'objectif de ces travaux de thèse est de réaliser des versions miniaturisées d'interféromètres Mirau ajustables pour leur intégration dans des profilomètres-vibromètres optiques interférométriques. Ces microinterféromètres Mirau ont comme avantages potentiels d'être plus compacts, de coût plus réduit (grâce à une fabrication collective), d'être réalisables sous forme de matrice pour des mesures en parallèle, et surtout de permettre un ajustement interne de la position du miroir de référence. La contribution essentielle de cette thèse est de proposer

une conception et un procédé de fabrication originaux de microinterféromètres Mirau supportés par des modélisations et des test de fabrication analysés en détail..

Cette thèse a été soutenue par une bourse du China Science Council (CSC). Les travaux ont été réalisés dans l'opération « MNOEMS et instrumentation » du département de recherche « Microsystèmes et Nanobiotechnologies » de l'Institut d'Electronique Fondamentale (IEF) avec un financement interne du département. L'IEF est une unité mixte de recherche du CNRS et de l'Université Paris-Sud située dans la région parisienne (Orsay, 91) et qui abrite les salles blanches de la Centrale de Technologie Universitaire (CTU) où ont été réalisés les tests de fabrication.

Ces travaux font suite à différents travaux sur les composants micro-optiques et les MEMS optiques réalisés dans l'opération comme le développement de procédés de lithographie UV, laser et électronique 3D pour la fabrication de composants micro-optiques, le développement de procédés de fabrication de microlentilles réfractives et diffractives, la conception d'un micro-objectif à miroirs de type Schwarzchild et la réalisation de micromiroirs sphériques convexe et concaves pour ce type d'objectif et enfin la conception et la réalisation partielle d'une matrice de filtres Fabry-Perot accordables pour l'imagerie multispectrale [Bertin-2003].

Cette synthèse en langue française résume les différents travaux et est organisée en 3 chapitres consacrés respectivement à une revue très rapide de l'état de l'art, à la conception et la modélisation optique et électromécanique du microinterféromètre, et aux tests de fabrication.

I. Etat de l'art des interféromètres Mirau

Un profilométre optique interférométrique est essentiellement un microscope optique équipé d'objectifs interférométriques permettant de réaliser des interférences entre un faisceau lumineux réfléchi sur la surface de l'échantillon à mesurer et un faisceau lumineux réfléchi sur un miroir de référence. L'acquisition par une caméra et le traitement d'un ou plusieurs interférogrammes obtenus en variant la différence de chemin optique entre les 2 faisceaux par translation du miroir, de l'objectif ou de l'échantillon permet de remonter au profil 3D de la surface (ou du mode de vibration si un éclairage stroboscopique est utilisé). Les objectifs interférométriques utilisés pour les faibles grandissements (<10×), les grandissements moyens (10× à 50×), et les grandissements élevés sont respectivement les objectifs interférométriques de type Michelson (Fig.I.1a), de type Mirau (Fig.I.1b) et de type Linnik (Fig.I.1c). Les objectifs interférométriques de type Mirau sont les plus utilisés car ils ont un champ de vue (50-500 µm) et une résolution latérale (0.5-2.5 µm) adéquats pour la caractérisation dimensionnelle de nombreux microdispositifs. De plus ils exploitent un faisceau optique coaxial, ont une structure compacte peu sensible aux vibrations et une structure planaire favorable à leur fabrication et leur intégration hybride verticale (multiwafers) en technologie MEMS. C'est pourquoi, parmi les 3 types d'interféromètres précités, les interféromètres Mirau ont reçu la plus grande attention pour leur développement aussi bien à l'échelle macroscopique qu'à l'échelle microscopique.

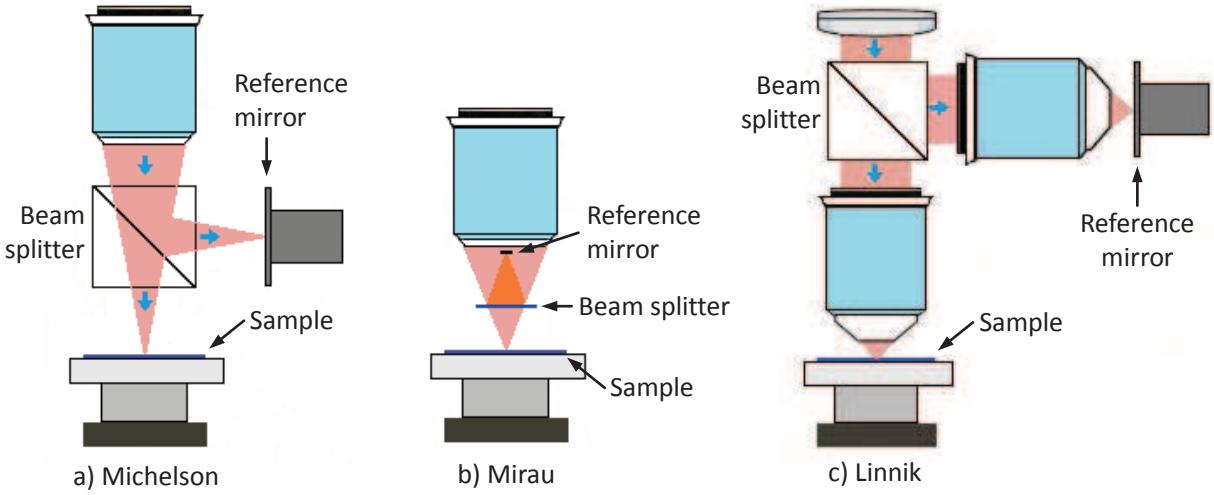

Figure I.1. Principaux objectifs interférométriques utilisés en profilométrie optique.

I.1 Développements récents des interféromètres Mirau macroscopiques

Les interféromètres Mirau pour le visible sont commercialisés et utilisés depuis longtemps pour leur mise en œuvre dans des profilomètre optiques interférométrqiues plein champ. Récemment de nouvelles versions d'interféromètre Mirau, décrits dans la suite, ont été proposés pour l'interférométrie en lumière polarisée (Fig.I.2a), pour l'interférométrie en immersion (Fig.I.2b) et pour d'autres gammes spectrales.

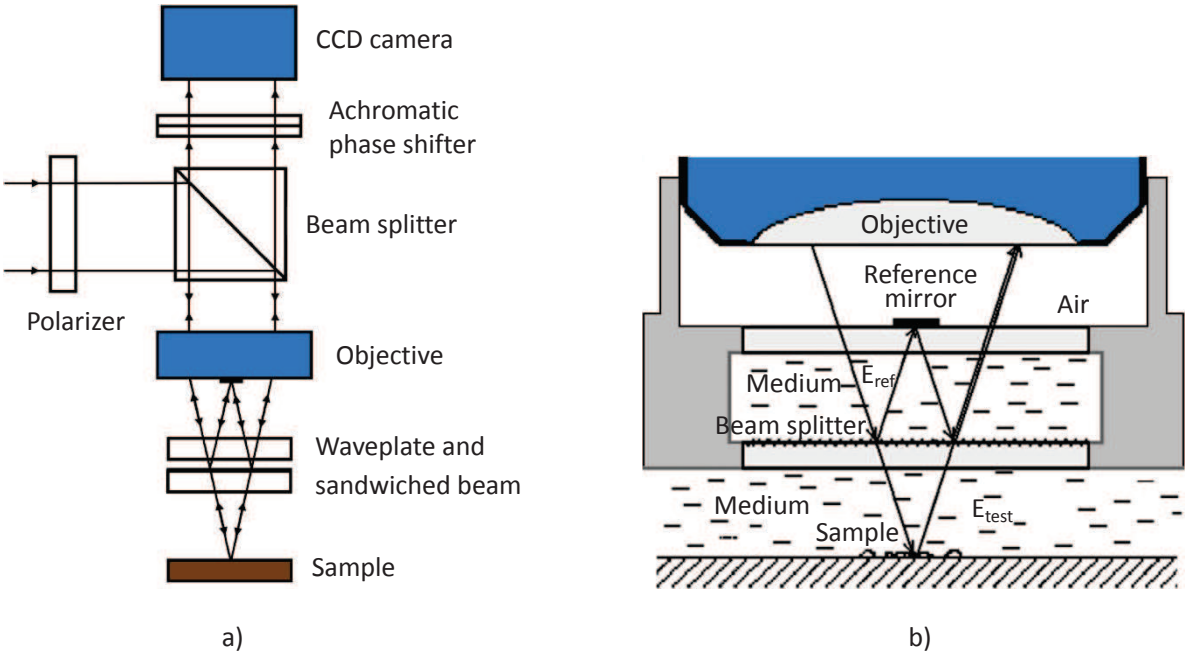

Figure I.2. (a) Profilomètre avec interféromètre Mirau adapté pour la lumière polarisée. (b) Objectif interférométrique Mirau à immersion.

Outre la possibilité d'un ajustement de l'intensité relative des 2 faisceaux (maximization du contraste des franges), l'intérêt d'un fonctionnement en lumière polarisée est de permettre l'acquisition simultanée d'interférogrammes différents décalés en phase en ajustant les lames d'onde et donc une acquisition très peu sensible aux perturbations externes (vibrations). Les objectifs interférométriques Mirau en immersion ont été développés essentiellement pour les applications biologiques [Lu-2012, Lyuko-2013] tout en augmentant la résolution spatiale grâce à l'indice optique >1 du liquide. Les 2 approches (polarisation et immersion) ont été combinées par Lyuko [Lyuko-2013].

Concernant le développement d'objectifs interférométriques pour d'autres gammes spectrales, nous pouvons signaler les travaux de Hamamoto et al. [Hammamoto-2005] qui ont développé une version d'interféromètre Mirau fonctionnant dans l'extrême UV (13.5 nm) pour l'inspection de masques de lithographie pour la microélectronique et les travaux de Chou [Chou-2010] et de l'IneSS qui montré la possibilité de mesurer le profil de surfaces enterrés en technologie silicium par un fonctionnement dans le domaine proche infrarouge où le silicum est transparent (>1.1 µm).

A l'IEF, nous avons développé en 2009 avec la société Fogale nanotech un objectif interférométrique DUV (=250 nm) mais de type Linnik avec contrôle de la polarisation pour la caractérisation des NEMS et en 2010-2012 un profilomètre multibandes spectrales dans le domaine visible-proche infrarouge (450 nm-2 µm) avec un grand champ de vue (jusqu'à 3 cm) et un objectif interférométrique de type Michelson pour la caractérisation de procédés de packaging au niveau du wafer et de profils d'interfaces enterrées.

I.2 Etat de l'art des Interféromètres Mirau intégrés

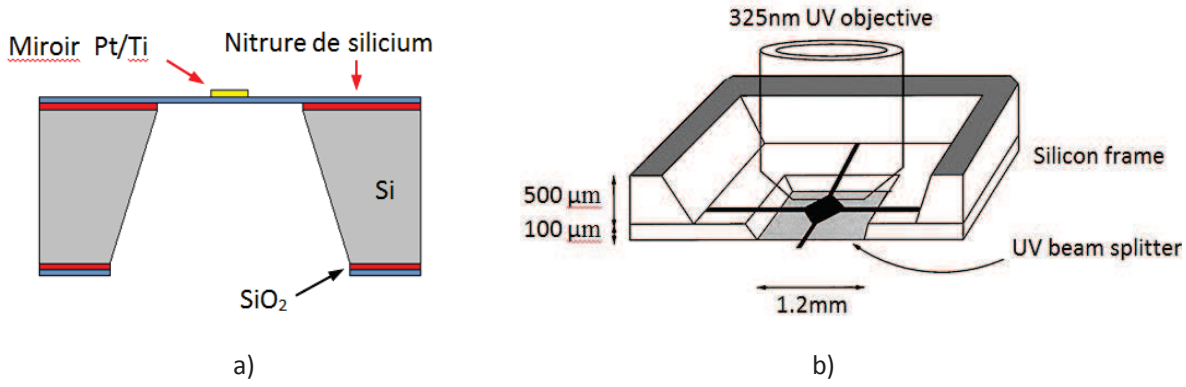

Figure I.3. (a) Miroir d'interféromètre Mirau microusiné et (b) Interféromètre Mirau UV microusiné.

Très peu de travaux ont été publiés sur la réalisation d'interféromètre Mirau intégrés. Chim, Beck et Kino ont été les premiers, il y a plus de 20 ans, à réaliser par microusinage un interféromètre Mirau partiellement intégré (Fig.I.3a) [Chim-1990, Chim-1991]. Le miroir de référence a été réalisé par dépôt et lithographie d'un film de Pt/Ti sur une membrane en nitrure de silicium fabriquée par gravure chimique anisotrope dans KOH de la face arrière du substrat de silicium. Cet interféromètre a été intégré dans un microscope et utilisé avec succès pour la mesure du profil 3D de surface de tranchées de résine et de circuits intégrés. Plus tard, Chang et Kino [Chang-1998] ont rapportés des résultats sur la construction d'un profilomètre avec un interféromètre Mirau intégré fonctionnant dans l'UV (=325 nm). Le micro-interféromètre Mirau réalisé est schématisé dans la Fig.I.3b. Il est constitué d'une part

d'un miroir de référence en forme de losange métallisé avec de l'aluminium et suspendu par 4 bras en nitrure de silicium, et d'autre part d'une membrane séparatrice de nitrure de silicium riche en silicium déposé chimiquement en phase vapeur (LPCVD) sur un autre wafer de silicium [Chang-1997]. Les 2 wafers ont été assemblés par soudure de substrats de silicium pour former un interféromètre Mirau opérationnel. Les 2 interféromètres Mirau de la Fig.I.3 ont été conçus pour une utilisation en lumière monochrome et ne sont pas ajustables.

La fabrication d'interféromètres Mirau intégrés n'a été considérée par la suite que très récemment par Albero et al. [Albero-2011]. Ces travaux développé dans la cadre du projet européen SMARTHIENS avaient pour objectif le développement d'une station interférométrique de test pour l'inspection parallèle de la production de MEMS [Gastinger-2009]. Dans ce projet deux interféromètres ont été étudiés, un interféromètre faiblement cohérent fondé sur une configuration Mirau [Albero-2011] pour les mesures statiques et un interféromètre laser fondé sur un interféromètre Twynman-Green [Oliva-2012] pour les mesures dynamiques. Le microscope interférométrique Mirau proposé est schématisé dans a Fig.I.4. L'interféromètre Mirau inséré dans le cadre en trait pointillé exploite une technologie d'assemblage verre-silicium (Fig.I.5).

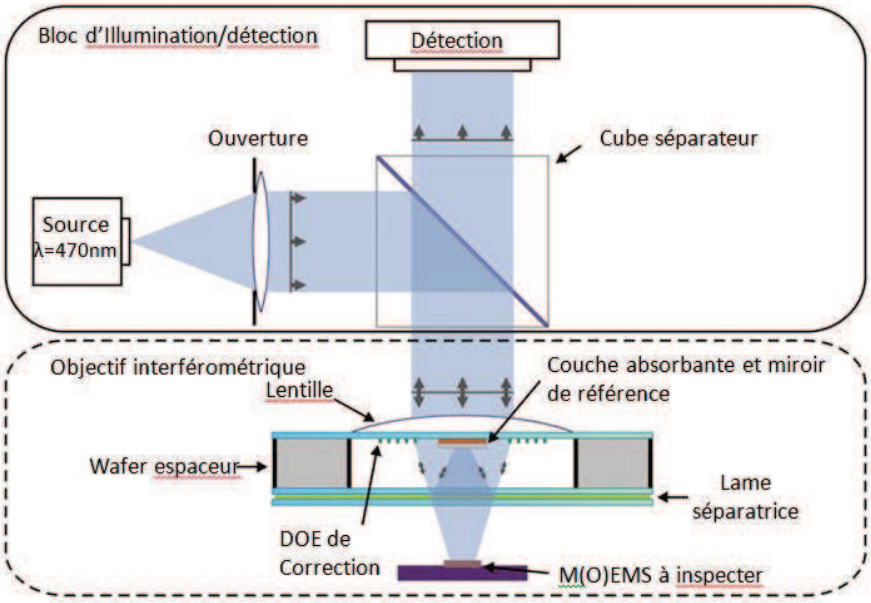

Figure I.4. Microscope interférométrique Mirau étudié dans le projet européen SMARTIEHS.

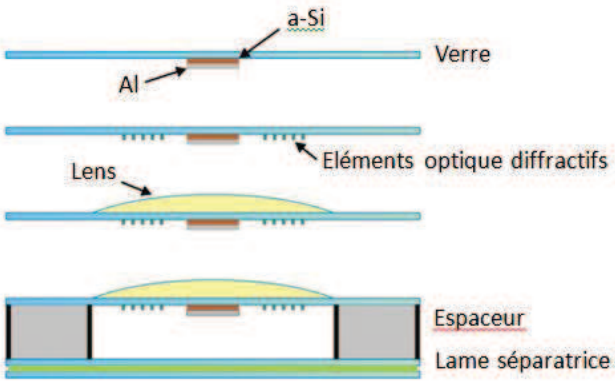

Figure I.5. Procédé de fabrication utilisé pour la fabrication de l'interféromètre Mirau.

Avant soudure, des microlentilles sont formées by fluage de résine sur le verre de silicium ou par fluage de verre dans un mule de silicium et des éléments optiques diffractifs ont été fabriqués par lithographie laser 3D pour corriger les aberrations optiques de la microlentille [Gorecki-2011].

Récemment, dans le cadre d'un autre projet européen (VIAMOS), l'institut FEMTO-ST, en collaboration avec le Fraunhofer ENAS, étudie actuellment un système de tomographie optique cohérente fondé sur une matrice d'interféromètres Mirau. Ce système est prévu d'être utilisé pour le diagnostic prématuré du cancer de la peau. Il exploitera une source à balayage de longueur d'onde et un actionneur intégré pour translater la matrice de miroirs (Fig.I.6). L'interféromètre Mirau ajustable est schématisé dans la Fig.I.7.

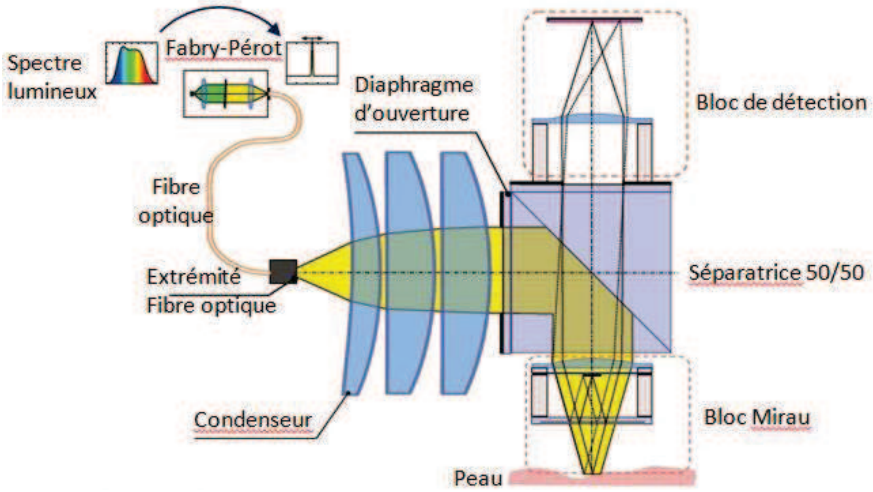

Figure I.6. Schéma du système de tomographie optique cohérente hétérodyne du projet VIAMOS.

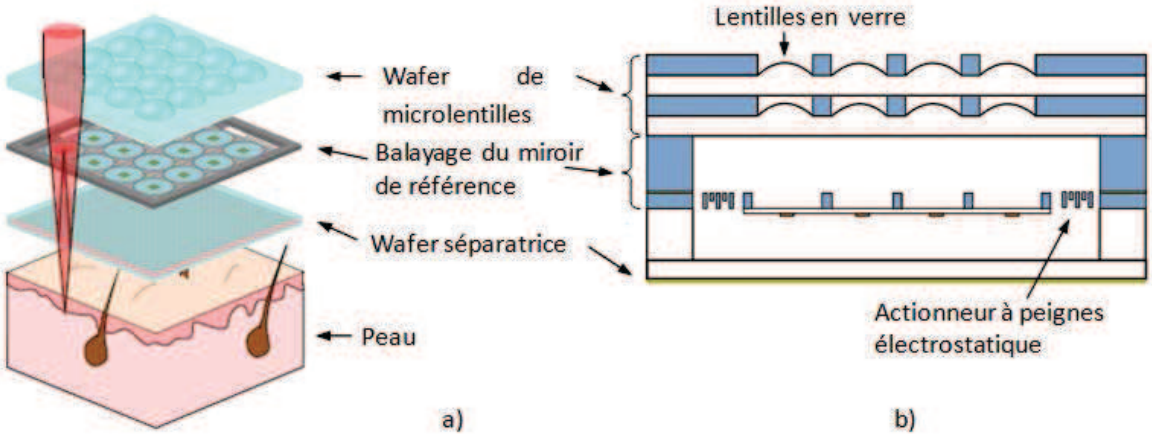

Figure I.7. Matrice d'nterféromètres Mirau intégrés avec système de balayage du projet VIAMOS.

L'architecture générale 3D de l'interféromètre ajustable a des similarités avec celle étudiée dans cette thèse mais avec des différences notables : Le système de balayage étudié à FEMTO-ST est essentiellement prévu pour des mesures en décalage de phase donc la gamme de balayage est assez réduite (0-1.5 µm) et a été prévu pour translater simultanément toute la matrice de miroirs. Cette solution permet d'utiliser qu'un seul faisceau optique mais nécessite une surface analysée relativement plane et de la taille de la matrice. Nous verrons que le système de balayage étudié dans cette thèse est

prévu pour chaque miroir et une gamme de translation de ±20 µm adéquate à la fois pour l'interférométrie à décalage de phase et l'interférométrie faiblement cohérente. Ceci permet l'utilisation d'une matrice d'interféromètre Mirau pour la mesure de grades surfaces non planes mais avec un pas de mesure assez grand et cette configuration nécessite des faisceaux multiples. Ce sont donc 2 approches complémentaires. Les technologies étudiées sont aussi très différentes. Dans le projet de FEMTO-ST les miroirs sont supportés par des membranes en verre fabriquées par soudure anodique verre-Si (Fig.I.8) alors que les miroirs sont autosupportés dans notre conception. Le système de balayage de FEMTO-ST utilise des peignes électrostatiques verticaux unidirectionels en technologie SOI alors que celui étudié dans cette thèse est fondé sur des peignes électrostatiques verticaux bidirectionnels en technologie double SOI. Finalement la séparatrice dans le projet VIAMOS est réalisée à partir d'un wafer de verre alors que dans notre conception elle est constituée d'une membrane multicouche.

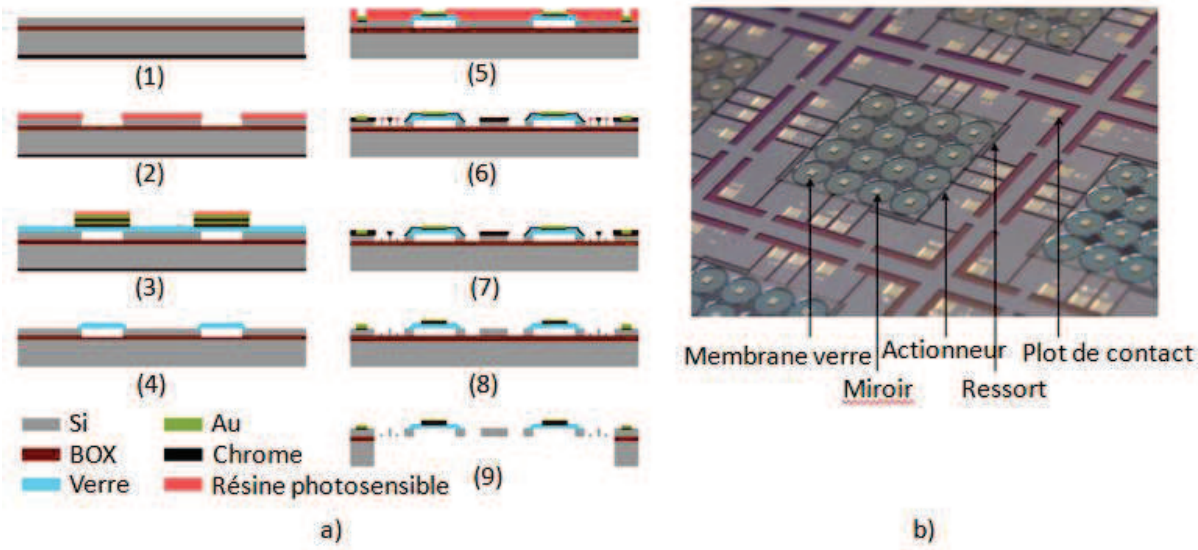

Figure I.8. (a) Procédé de fabrication et (b) image d'un réseau d'interféromètre Mirau ajustable intégré.

A notre connaissance le projet VIAMOS et les travaux réalisés dans cette thèse sont les seules et premières tentatives pour réaliser des interféromètres Mirau intégrés ajustables.

I.3 Autres microinterféromètres ajustable intégrés

A côté des interféromètres Mirau intégrés discutés précédemment, de nombreux autres types d'interféromètres intégrés ont été étudiés et développés par des chercheurs du monde entiers. Parmi les interféromètres intégrés les plus étudiés on peut citer les interféromètres Fabry-Pérot et les interféromètres Mach Zehnder à base de guides d'onde. Des interféromètres de Michelson en technologie MEMS avec une configuration planaire (intégration horizontale) exploitant des miroirs de Bragg Si-Air ont aussi été développés en France à l'ESIEE et au Canada à l'école Polytechnique de Montréal. La possibilité d'exploiter ce dernier type d'interféromètre pour la profilométrie à été démontré à l'ESIEE [Malak-2014]. Des informations un peu plus détaillées peuvent être trouvées dans le chapitre 2 de la version anglaise de cette thèse.

I.4 Conclusion

Les interféromètres Mirau sont des interféromètres à 2 faisceaux coaxiaux de structure. A l'échelle macroscopique, quelques nouveaux développements ont été réalisés récemment pour leur utilisation avec de la lumière polarisée et/ou dans des liquides ou pour des longueurs d'ondes non visibles. Les interféromètres Mirau se prêtent particulièrement bien à une intégration multiwafers en technologie MEMS. Il existe malgré tout très peu de travaux sur la réalisation de microinterféromètres Mirau intégrés et la plupart sont des interféromètres individuels fixes pour une utilisation en lumière monochrome. Ce n'est que très récemment que l'étude et la réalisation de versions ajustables et de matrices de microinterféromères Mirau ont été entreprises. Cette thèse est une de ces rares tentatives avec la particularité de viser une large course de balayage du miroir et une utilisation dans une large gamme spectrale.

II. Conception et modélisation d'interféromètres Mirau ajustables intégrés

L'objectif de cette thèse est d'étudier l'intégration en technologie MEMS d'un interféromètre Mirau ajustable. Ce chapitre décrit le cahier des charges choisi, la conception générale et les modélisations optiques et électromécaniques qui ont été effectuées pour dimensionner les microinterféromètres Mirau et pour atteindre cet objectif.

II.1 Cahier des charges visé

Ces travaux de thèse avaient pour ambition de réaliser des interféromètres intégrés avec des caractéristiques allant au-delà des interféromètres intégrés existants. Les caractéristiques visées sont les suivantes :

- Un fonctionnement possible dans le domaine visible et proche infrarouge en lumière monochrome et, si possible, avec une source large bande pour permettre des mesures de profilométrie de surface en interférométrie faiblement cohérente par balayage de franges.

- La possibilité de configurer l'interféromètre pour d'autres domaines de longueur d'ondes simplement en changeant la séparatrice.

- Un ajustement intégré de la différence de chemin optique par translation du miroir de référence avec une résolution verticale et une course suffisante pour permettre à la fois des mesures par interférométrie à décalage de phase (course > $\lambda/2$, résolution <1 nm) et des mesures par interférométrie faiblement cohérente (course >10 µm, résolution <5 nm). Cet ajustement devra être bidirectionnel avec une large course pour pouvoir annuler la différence de chemins optiques dues aux erreurs de compensation intrinsèques et aux variations de gap initiales entre le miroir at la séparatrice provenant des défauts de planéité, des variations d'épaisseur des wafers et des défauts d'assemblage.

- Un asservissement possible de la différence de chemin optique.

- La possibilité de réaliser des matrices de microinterféromètre Mirau avec un ajustement individuel de chacun des interféromètres.

- La possibilité d'intégrer dans la suite d'ajouter un objectif à miroirs de type Schwarzchild tpour réaliser un objectif interférométrique Mirau complètement intégré.

- Un procédé de fabrication avec le minimum d'étapes technologiques et compatible avec des tailles de wafers de 100 mm ou plus.

II.2 Conception générale

Bien que d'autres applications soient possibles, l'interféromètre Mirau intégré ajustable étudié dans cette thèse est destiné en premier lieu à être mis en œuvre dans un profilomètre-vibromètre plein champ interférométrique comme illustré dans la Fig.II.1.

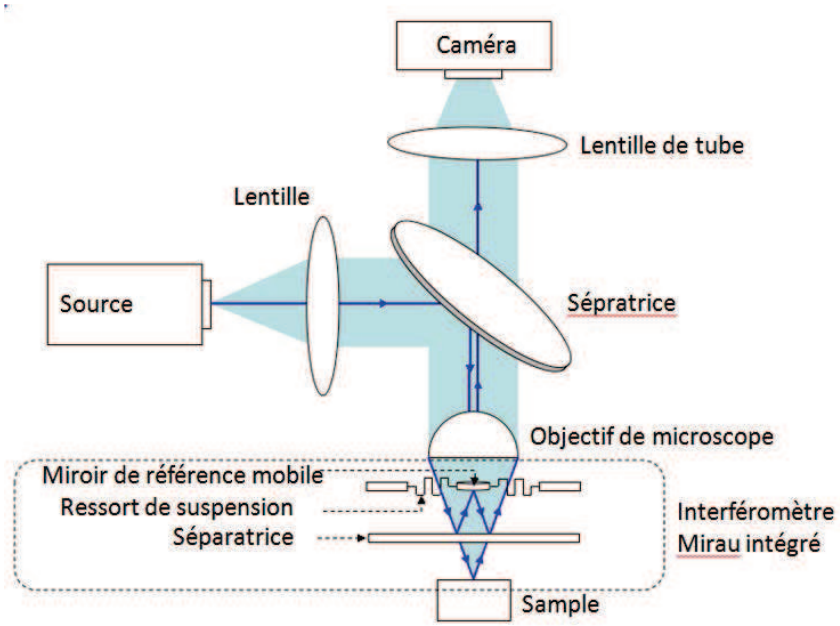

Figure II.1. Schéma d'un profilomètre optique intégrant un interféromètre Mirau intégré.

Ceci impose une épaisseur totale de l'interféromètre inférieure à la distance de travail de l'objectif. Notons qu'un des intérêts des interféromètres Mirau intégrés est leur faible épaisseur possible ce qui les rend potentiellement exploitables avec des objectifs de fort grossissement, de faible distance de travail et non compensés.

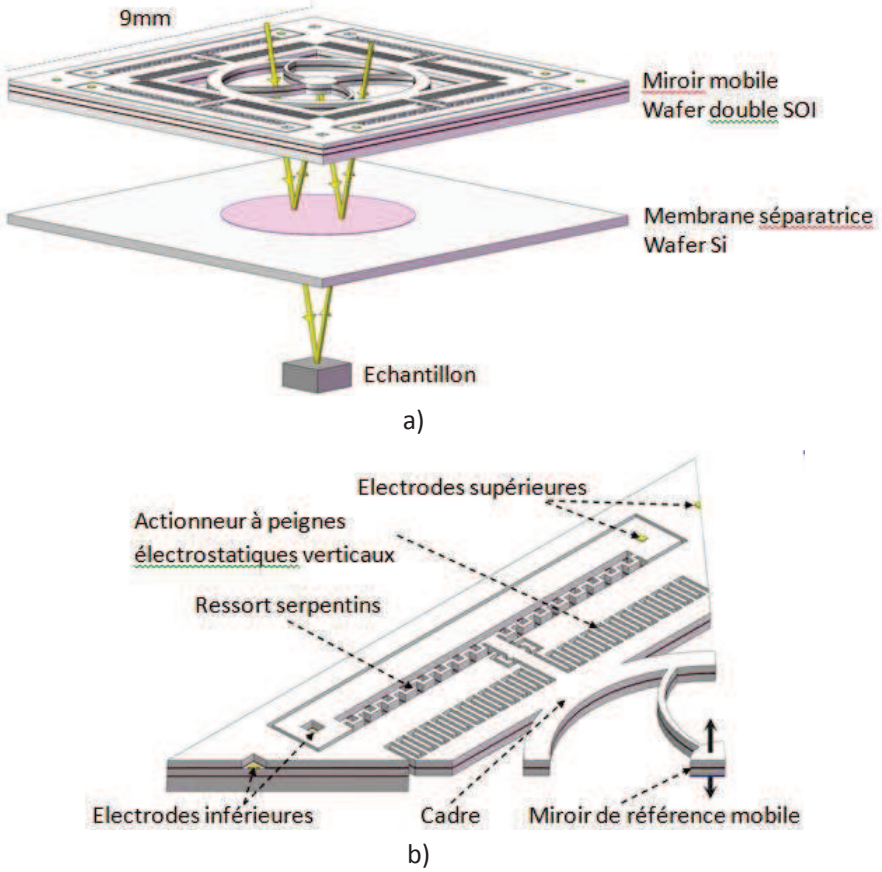

Figure II.2. (a) Configuration proposée de l'interféromètre Mirau intégré et (b) zoom sur 1/4 d'un miroir mobile.

La configuration choisie pour l'interféromètre Mirau afin de répondre au cahier des charges et à cette application est illustrée dans la Fig.II.2. L'interféromètre est prévu d'être réalisé par assemblage de 2 wafers. Le wafer supérieur, de type double SOI (Silicium sur Isolant), correspond aux puces de miroirs de référence mobiles et le second wafer en silicium supportent des membranes diélectriques multicouches semi-réfléchissantes qui servent de séparatrices et qui sont adaptées au domaine de longueurs d'onde d'utilisation.

Chaque miroir mobile est suspendu dans un cadre rigide ouvert et circulaire par 4 bras de suspensions incurvés pour permettre une relaxation des contraintes résiduelles. Le cadre est suspendu par des ressorts serpentins et actionné verticalement (mode piston) avec des peignes électrostatiques verticaux bidirectionnels. La configuration choisie des ressorts de suspension est prévue pour un actionnement purement vertical mais il serait possible de permettre un léger actionnement latéral et une inclinaison selon 2 axes perpendiculaires en choisissant une autre implantation des ressorts. Ce mode d'actionnement a été choisi car il permet avec une technologie relativement simple (pas d'ajout de matériau actif) une grande course avec une résolution élevée, un asservissement de la position par détection capacitive, une faible consommation et une faible dépendance avec la température. Un déplacement bidirectionnel est obtenu grâce à la possibilité d'appliquer des potentiels V1, V2, V3 et V4 différents sur les parties supérieures et inférieures des peignes électrostatiques qui sont isolées par une couche de silice enterrée (Fig.II.3) et par des tranchées d'isolation. Ainsi l'application d'une différence de potentiel entre V1 et V4 permet un déplacement de l'électrode mobile vers le haut et entre V2 et V3 un déplacement de cette électrode vers le bas. En première analyse, la course maximum

possible est donnée par la somme des épaisseurs de silicium, soit ±25 µm pour le wafer double SOI sélectionné (Si 25µm/SiO_2 1.5µm/Si 25µm/SiO_2 1µm/Si 380µm). Le même matériau faiblement contraint, épais et monocristallin (Si) étant utilisé pour les parties inférieures et supérieures des peignes ceci est favorable à une course importante, une bonne symétrie, une bonne reproductibilité et une fiabilité élevée de l'actionnement. Ce choix de technologie d'actionnement est une des innovations majeures du système de balayage choisi par rapport aux solutions proposées dans la littérature.

Les modélisations optique de l'interféromètre et électromécanique du système de balayage du miroir de référence sont résumées dans les parties suivantes

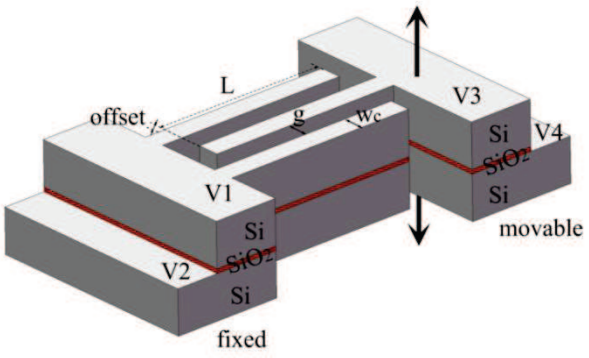

Figure II.3. Schéma d'une paire de doigts d'un peigne électrostatique vertical bidirectionnel.

II.3 Conception et modélisation optique de l'interféromètre Mirau intégré

Le dimensionnement optique du système de balayage du miroir de référence est assez simple : les dimensions du cadre et du miroir correspondent simplement à l'ouverture (6 mm) et au champ de vue (~800 µm) de l'objectif pour lequel est conçu l'interféromètre. La distance entre le miroir de référence et la séparatrice doit aussi être inférieure à la moitié de la distance de travail de l'objectif.

Notons que le miroir produit une obscuration centrale qui réduit l'ouverture numérique de l'objectif. En conséquence la résolution latérale et le contraste des franges sont diminués et la profondeur de champ et l'interfrange sont augmentés [Sheppard-1995, Dubois-2000]. Cette obscuration étant inévitable et ses effets bien connus la modélisation de l'influence de l'obscuration n'a pas été entreprise.

En même, pour être complet, il serait souhaitable d'évaluer l'effet des bras de suspension du miroir sur les performances optiques de l'objectif interférométrique intégrant le microinterféromètre. Des expériences passées de l'IEF avec un interféromètre Mirau macroscopique développé avec la société Fogale nanotech qui comportait des bras de suspension du miroir de référence de ~500 µm de largeur n'ont pas mis en évidence de limitations majeurs liées apportées par la présence des ces bras. La largeur des bras de suspension de l'interféromètre Mirau microusiné étant plus faible, nous avons considéré en première approximation que leur effet était négligeable.

La conception et la modélisation optique de la séparatrice est plus complexe car elle doit conserver un rapport approximativement constant du coefficient de transmission et de réflexion dans

des gammes de longueur d'onde et d'angle d'incidence les plus grande possibles tout en apportant le minimum d'aberrations optiques et de défaut de compensation de l'interféromètre.

La technologie retenue pour la séparatrice est une membrane constituée de couches alternées de films de silice et de nitrure de silicium déposées par PECVD et recuites pour obtenue une contrainte globale en tension afin d'obtenir une membrane plane. Cette technologie a été développée précédemment à l'IEF par H. Bertin [Bertin-2013] pour des filtres Fabry-Pérot micro-usinés [Bertin-2013-2]. La membrane conçue par H. Bertin est constituée de 12 couches (Tab.II.1) et a une réflectance en incidence normale de ~50% dans la gamme 550-850 nm. Pour son application dans l'interféromètre Mirau, la réflectance de cette membrane a été simulée pour une incidence de 36.87° (correspondant à l'angle maximum d'un objectif d'ouverture numérique de 0.6) en prenant les indices optique et la dispersion des films PECVD mesurées par ellispométrie spectroscopique. Le résultat (Fig.II.4) montre que cette membrane est utilisable dans la gamme 550-800 nm.

Table II.1. Empilement de couches de la séparatrice.

SiN_x (H)/ SiO_2 (L) (nm)
Air/L 108/ H 117/ L 19/ H 181/ L 205/ H 53/ L 228/ H 90/ L 116/ H 84/ L 112/ H 79/Air

Figure II.4. Réflectance optique de la séparatrice pour une incidence de 0° et 36.87° en fonction de la longueur d'onde.

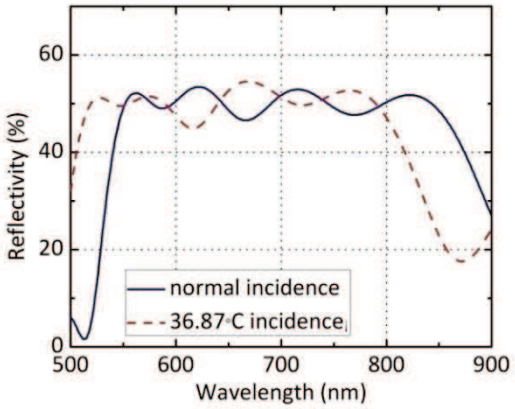

Pour obtenir des franges contrastées, la différence de chemin optique entre les faisceaux réfléchis sur le miroir de référence et ceux sur l'échantillon avant recombinaison doit être inférieure à la longueur de cohérence de la source. Les modélisations montrent que pour la membrane séparatrice précitée, la différence de chemin optique est entre 2.2 et 2.6 µm dans la gamme λ=500-800 nm. L'interféromètre Mirau pourra donc fonctionner sans ajustement avec des sources LED visibles et proche infrarouge. Il devrait aussi fonctionner pour la profilométrie à balayage de franges avec des LEDS blanches mais un ajustement du miroir de référence sera nécessaire et le contraste des franges sera dégradé.

La séparatrice introduit des aberrations sphériques mais pour la séparatrice choisie et une ouverture numérique de 0.6, les calculs montrent que rayon d'aberration calculé reste toujours inférieur à 1/5 du rayon du spot limité par la diffraction dans la gamme 500-800 nm. Les aberrations sphériques introduites par la séparatrice sont donc tout à fait tolérables.

II.4 Conception électromécanique du système de balayage du miroir de référence

Des modélisations approfondies mécanique et électromécanique analytiques et par éléments finis (logiciel ANSYS) du système de balayage du miroir de référence ont été effectuées. Dans cette synthèse en français nous ne présenterons que la démarche utilisée te les principaux résultats obtenus.

II.4.1 Peignes électrostatique verticaux en technologie double SOI

Nous avons considéré dès le départ une largeur minimum des gaps électrostatiques et des doigts des peignes électrostatiques égale à de 5 µm afin de limiter le rapport d'aspect hauteur/largeur inférieur à 10. De même nous avons limité à 50 le rapport d'aspect longueur/largeur des doigts des peignes (longueur L=400 µm, largeur w=8 µm). La tension maximum d'actionnement a été fixée à 50 V (valeur très inférieure au claquage dans l'air).

La force électrostatique verticale générée par une paire d'électrode sur un doigt mobile a été simulée par éléments finis pour tenir compte des effets de bord. Les résultats (Fig.II.5) montrent que lorsqu si la tension est appliquée entre les parties supérieures des électrodes fixes et la partie inférieure des doigts mobiles, la force est maximale et approximativement constante pour un offset entre ±2.5 et ±20 µm, s'annule lorsque le déplacement devient égal à l'épaisseur de silicium (25 µm) et reste encore égale à 1/4 de la force maximale lorsque les peignes sont alignés verticalement. Ce dernier résultat est important car il indique que la force verticale peut être suffisante pour obtenir un déplacement même en l'absence d'offset vertical. La force est proportionnelle à U^2/g où g est le gap transverse et U la tension appliquée. La force verticale /unité de longueur générée par une paire d'électrode est voisine de 1 mN/m.

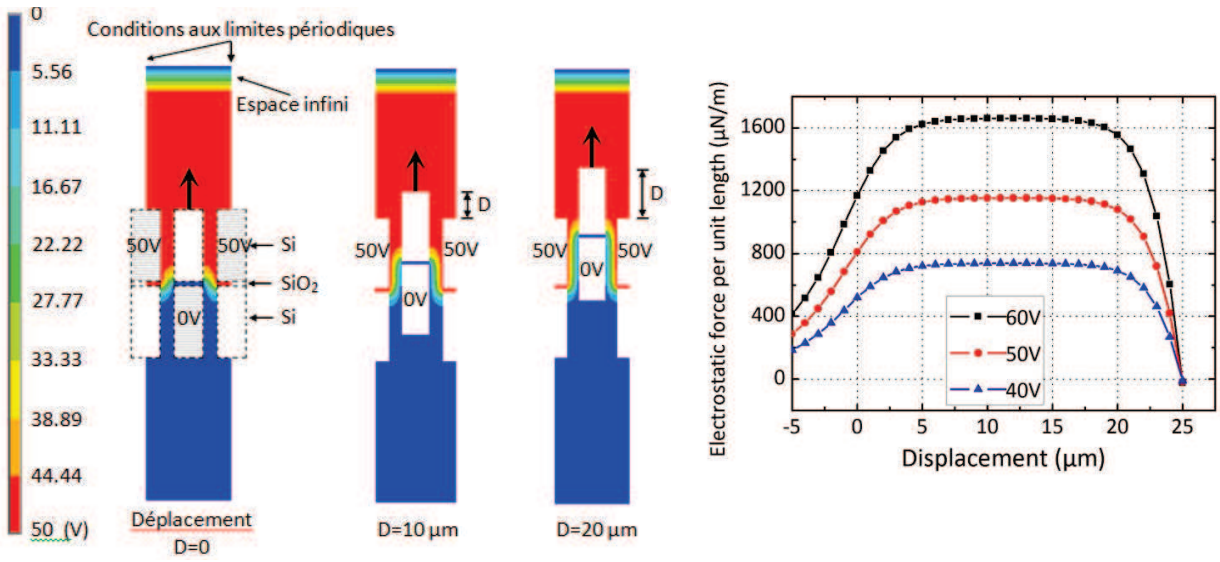

Figure II.5. Distribution du potentiel et force générée par unité de longueur en fonction du déplacement vertical de l'électrode centrale pour une paire d'électrodes.

II.4.2 Modélisation et dimensionnement des ressorts serpentins de suspension

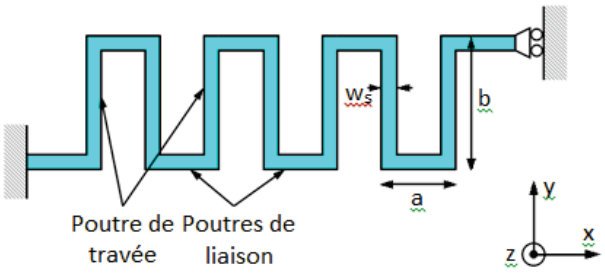

Figure II.6. Schéma d'un ressort de type serpentin.

Des ressorts de la forme d'un serpentin (Fig.II.6) ont été choisis pour les suspensions car ils peuvent être très flexibles pour un encombrement relativement réduit. Par symétrie de la conception générale du système da balayage avec 4 peignes électrostatiques verticaux (cf Fig.II.2) , dans le cas idéal, la force électrostatique globale est uniquement verticale. Néanmoins en présence d'un désalignement des peignes (gaps électrostatiques transverses asymétriques), les forces latérales peuvent devenir suffisantes pour produire une défaillance par collage électrostatique. Les calculs montrent que pour la géométrie des peignes choisies (gap g= 5 µm, longueur de recouvrement =400 µm, 1/2 hauteur=20 µm), la force latérale peut devenir 7 fois plus grande que la force verticale (cas d'un désalignement de 2.5 µm). Il faut donc concevoir des ressorts de suspension qui ont une rigidité verticale très faible devant leur rigidité transverse ou longitudinale. La valeur minimum du rapport $(k_x+k_y)/k_z$ (somme des constantes de raideur dans le plan/constante de raideur hors plan) pour l'ensemble de la structure (Fig.II.7) nécessaire pour éviter un collage électrostatique latéral (déplacement <1/3 du gap initial) a été estimé à 125.9. Pour limiter les défaillances par collage électrostatique, des butées circulaires isolées électriquement ont été rajoutées sur les bras reliant les ressorts au cadre circulaire central (Fig.II.7).

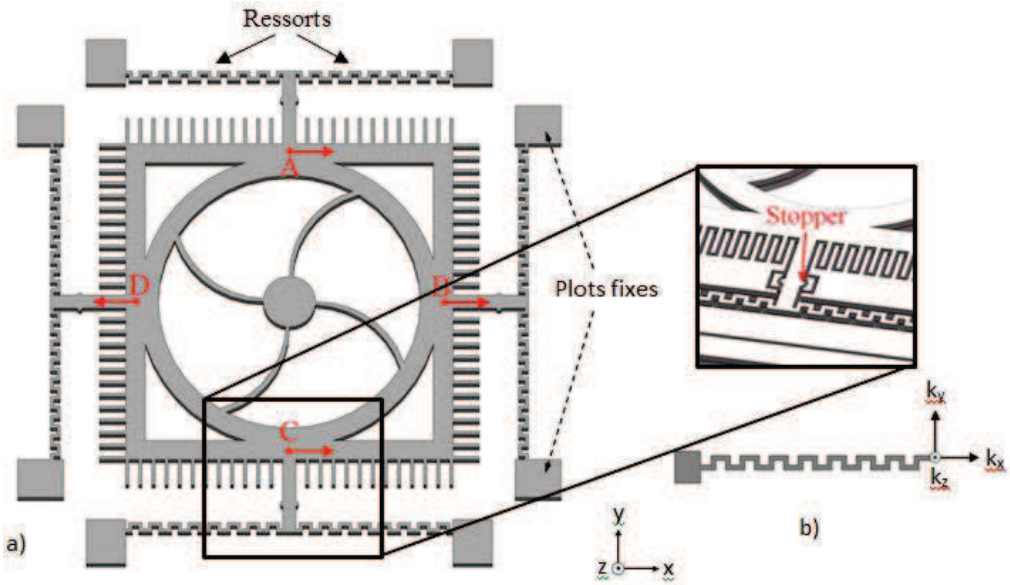

Figure II.7. Géométrie globale de la partie suspendue du système de balayage du miroir de référence.

Les constantes de raideurs des ressorts serpentins encastrés guidés dans les 3 directions x,y et z ont été modélisées analytiquement avec le modèle de Fedder [Fedder-1994] et par simulations par

éléments finis 2D et 3D en tenant compte de l'anisotropie mécanique du silicium d'orientation (100) [Hopcroft-2010]. Les modélisations par éléments finis ont montré que les constantes de raideur des ressorts calculées sans la couche d'oxyde enterrée ne sont que très légèrement sous estimées (<3.2%) par rapport aux constante de raideurs des ressort composites ($Si/SiO_2/Si$). Un bon accord (écart<3.2%) a été trouvé entre les différentes méthodes de modélisation pour la constante de raideur hors plan kz mais les raideurs dans le plan longitudinales kx et transverses ky calculées analytiquement peuvent être surestimées de 16% et 28.5% respectivement. Ces différentes méthodes de modélisation ont été combinées dans une boucle pour maximiser le rapport $(k_x+k_y)/k_z$. Pour la structure globale avec 4 ressorts (Fig. II.7) un rapport $k_z/(k_x+k_y)$ très élevé (221.6) et supérieur à la valeur minimum nécessaire (égale à 125.9, voir ci-dessus) a pu être obtenu.

II.4.3 Modélisation de la structure globale

Une modélisation par élément finis de la structure globale a été réalisée pour déterminer le déplacement du miroir en fonction de la tension appliquée, l'effet du poids, les déformations éventuelles, les contraintes générées ainsi que les fréquences de résonance et les modes de vibrations associés de la structure mécanique. Pour cela un modèle 3D de conception par ordinateur (CAO) a été importé dans le logiciel de simulations par éléments finis ANSYS.

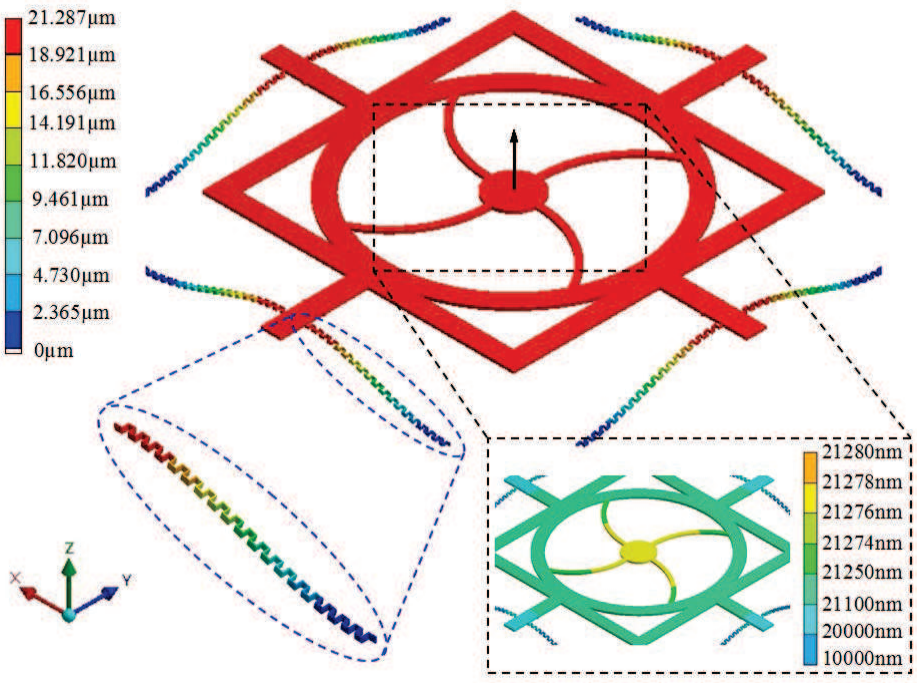

Figure II.8. Cartographie des déplacements de la structure mobile pour une tension de 50 V.

Les résultats (Fig.II.8) montrent le déplacement du miroir est très principalement induit par la flexion des ressorts. Pour le déplacement maximum (21.3 µm), les déformations du cadre et du miroir (<2 nm) sont très faibles (respectivement <30 nm et <2 nm) et les contraintes maximum au voisinage des encastrements (40 MPa) restent très inférieures à la limite de rupture du silicium (~4 GPa). Malgré une structure très ajourée, le poids produit une dissymétrie de 1 µm de l'actionnement vertical pour une course de ±20 µm. Cet effet pourrait être réduit en réduisant les gaps électrostatiques et en augmentant la rigidité verticale des ressorts. Le déplacement n'est que très approximativement linaire

avec la tension appliquée (Fig.II.9) avec une pente de ~0.4 µm/V. En deçà de 1µm la résolution devrait être meilleure que 0.4 nm et atteindre ~10 nm en bout de course. Ces valeurs sont respectivement compatibles avec une utilisation pour l'interférométrie à décalage de phase et pour l'interférométrie à balayage de franges en lumière faiblement cohérente. Cependant, un asservissement du déplacement par mesure capacitive de la position sera nécessaire pour linéariser la réponse.

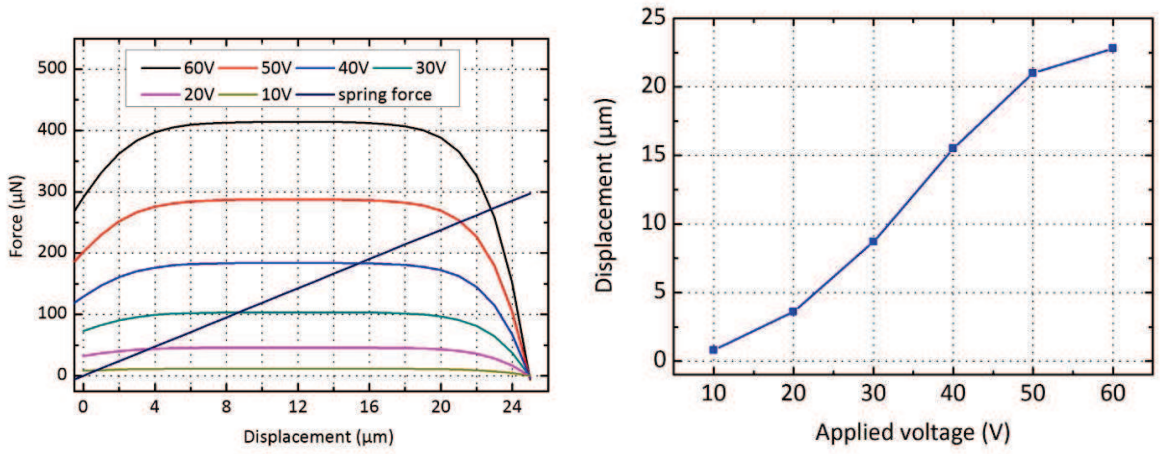

Figure II.9. (a) Positions d'équilibre entre la force électrostatique et la force de rappel des ressorts, (b) Déplacement en fonction de la tension appliquée.

Il faudrait idéalement que les fréquences de résonance soient supérieures à quelques kHz pour limiter l'influence des perturbations acoustiques et autres sources de vibrations. Une fréquence de résonance élevée du mode piston est aussi souhaitable pour obtenir un temps de réponse faible. La fréquence de résonance du mode fondamental (piston) a été évaluée à 464.6 Hz par simulations dynamiques par éléments finis en assez bon accord avec une modélisation analytique simple (451.8 Hz) et donc à priori insuffisantes pour une bonne immunité à l'environnement. Ceci correspond à un temps de réponse d'environ 6 ms ce qui est déjà intéressant pour des mesures rapides. Des modélisations de l'amortissement visqueux dans l'air de la structure mécanique seront nécessaires dans l'avenir pour déterminer s'il faut absolument s'affranchir de ces résonances mécaniques. Ces performances dynamiques pourraient être améliorées en augmentant la constante de raideur verticale des ressorts et en réduisant les gaps électrostatiques. Ceci serait aussi favorable à la diminution de l'effet du poids.

II. 5 conclusion

L'interféromètre Mirau intégré a été conçu pour un fonctionnement dans un domaine spectral assez large et pour permettre un ajustement bidirectionnel de la différence de chemin optique avec une grande course et une résolution (sub) nanométrique. L'architecture originale proposée repose sur un miroir de référence suspendu et actionné par des peignes électrostatiques en technologie double SOI et une séparatrice constituée d'une membrane diélectrique multicouche.

Les modélisations optiques montrent que l'interféromètre Mirau intégré conçu devrait être utilisable avec un objectif d'ouverture numérique élevée (NA=0.6) dans le domaine visible-proche infrarouge et ne devrait pas produire d'aberrations optiques majeures. L'utilisation d'une séparatrice formée d'une multicouche produit de façon inhérente un défaut de compensation qui peut en partie

être corrigé par une translation du miroir de référence. Le défaut résiduel devrait être suffisamment faible pour permettre un fonctionnement en lumière faiblement cohérente dans le visible mais avec une dégradation du contraste des franges.

Les modélisations électrostatiques, mécaniques et électromécaniques ont permis de dimensionner un système de balayage qui devrait avoir une résolution (sub)nanométrqiue et qui devrait permettre d'atteindre une course de ±20µm en appliquant une tension de 50 V sur le couple d'électrodes adéquat.

III. Tests de fabrication du système de balayage du miroir de référence et de la séparatrice

La conception du système de balayage bidirectionnel du miroir de référence repose sur l'utilisation de peignes électrostatiques verticaux en technologie double SOI pour ajuster la position du miroir. Le procédé de fabrication doit permettre de polariser indépendamment les parties supérieures et inférieures de ces peignes et de délimiter et libérer la structure complète su système de balayage (cadre du miroir, peignes, suspensions et ressorts serpentins).

De nombreux procédés de fabrication de peignes électrostatiques verticaux ont été proposé dans la littérature. L'examen de ces travaux montre que les points les plus difficiles sont l'obtention d'un offset vertical initial pour permettre d'initier l'actionnement, l'obtention d'une course d'actionnement élevée, le contrôle précis de l'alignement des parties fixes et mobiles des peignes électrostatiques et le contrôle des contraintes mécaniques résiduelles dans les différents matériaux constituant les peignes et les autres parties de la structure mobile. La technologie double SOI que nous avons choisie permet de résoudre ces différents problèmes avec un procédé de fabrication comportant un nombre d'étapes de fabrication réduit par rapport à la plupart des travaux publiés. Ce procédé est décrit dans la suite ainsi que les différents tests technologiques qui ont été menés pour le développer.

III.1 Procédé de fabrication proposé

Le procédé de fabrication du système de balayage du miroir comporte 6 étapes (Fig.III.1).

La deuxième étape (Fig.III.1-2) consiste à définir la géométrie de la structure mobile (miroir, peignes, ressorts,…) par gravure ionique réactive profonde (DRIE) des 3 couches $Si/SiO_2/Si$ superficielles avec une couche de masque en résine. Pour assurer une bonne homogénéité de la gravure, des motifs de remplissage ont été prévus pour obtenir des tranchées de largeur identique (5 µm) sur toute la surface. Cette étape est la seule qui nécessite une lithographie et une gravure de motifs avec précision.

Ensuite des ouvertures pour les contacts sur la couche de silicium enterrée sont gravées par DRIE et gravure chimique dans BHF (Fig.III.1-3). La surface étant fortement structurée (tranchées de 51.5 µm de profondeur) le masquage est réalisé par un film de résine photosensible laminé.

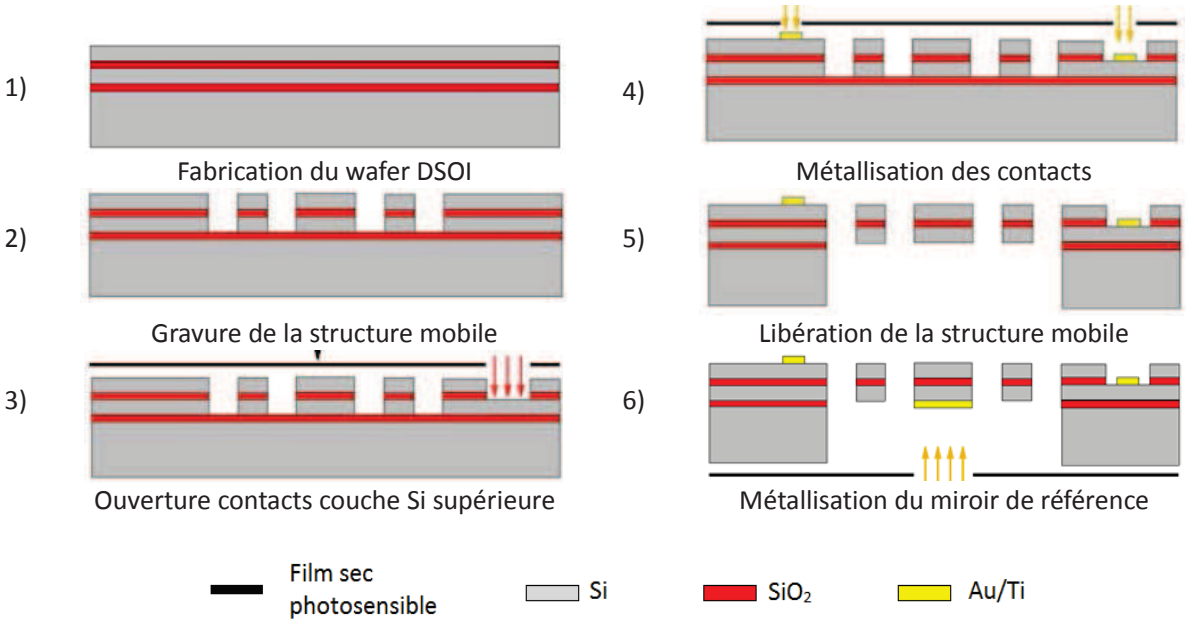

Figure III.1. Vues en coupe des étapes de fabrication du système de balayage du miroir.

L'étape suivante (Fig.III.1-4) consiste à déposer des plots de contact (Au/Ti) par lift-off et shadow masking simultanément sur les 2 films de silicium constituant les peignes électrostatiques. Comme précédemment, le masquage est réalisé par un film de résine photosensible laminé.

La structure mobile est ensuite libérée par gravure DRIE de la face arrière du wafer et gravure chimique dans BHF de la 2ème couche de slice enterrée (Fig.III.1-5).

Finalement, la face arrière du miroir est métallisée par évaporation et shadow masking avec un film de résine sec photosensible (Fig.III.1-6).

Ce procédé innovant, qui permet la fabrication de peignes électrostatiques verticaux auto-alignés de grande course, ne nécessite que 3 gravures DRIE, 2 métallisations et 5 lithographies sans alignement critique dont une seule comporte des motifs de petites dimensions.

Différents testx des étapes les plus critiques de ce procédé et d'un procédé complet ont été réalisés dans la centrale de technologie IEF-Minerve avec l'aide du personnel technique de cette centrale et des ingénieurs et techniciens procédés du département microsystèmes et Nanobiotechnologies.

III.2 Tests de fabrication de double wafer SOI

Les doubles wafers SOI n'étant pas standards, nous avons initialement essayé de fabriquer ce type de wafers à l'IEF par le procédé schématisé dans la Fig. III.2.

Des tests de soudure directe ont ainsi été réalisés avec des wafers oxydés thermiquement à 1000°C par voie humide (épaisseur silice 170 nm) et des wafers de silicium ayant subi un nettoyage RCA classique avec une oxydation finale dans un bain de HCL:H_2O_2:H_2O produisant une surface hydrophile (même interface de soudure que pour un wafer double SOI). Un banc d'imagerie infrarouge été construit et mis en place pour inspecter les défauts de soudure.

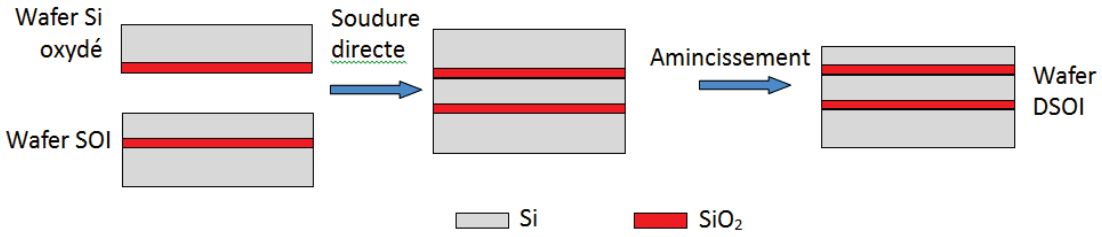

Figure III.2. Schéma de principe du procédé de fabrication de double wafers SOI.

Les tests de soudure ont classiquement été réalisés par contact manuel après nettoyage et séchage, éventuellement complété par un contact sous pression (force d'appui 6000-8000N) et à température modérée (400-500°C) dans une machine de soudure de wafer, et finalement suivi d'un recuit dans un four sous azote à haute température (800-1000°C, 1-2 heures).

Des tests avec une activation de surface par plasma d'oxygène avant soudure ont aussi été réalisés car ce traitement de surface est connu pour favoriser la formation de groupement silanol à la surface et d'abaisser la température de recuit nécessaire pour obtenir une énergie d'adhérence élevée [Wiegand-2000].

D'une manière générale, les assemblages de wafers ont pu être réalisés mais des défauts de soudure rédhibitoires attribués à des poussières inorganiques et organiques ont systématiquement été observés et n'ont pas pu être évités. Un exemple de résultat est présenté dans la Fig.III.3.

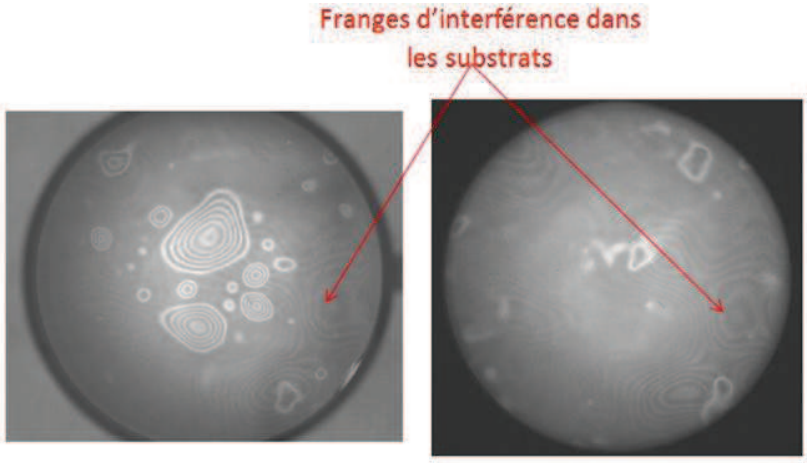

Figure III.3. Images infrarouge de wafers Si et SiO_2/Si assemblés (a) après soudure initiale (b) après recuit haute température.

Des essais d'amincissement par polissage mécanochimique (CMP) ont tout de même été entrepris sur des wafers assemblés de type SOI avec une polisseuse MecaPol de la société PRESI. L'amincissement se déroule en 3 étapes : 1) amincissement de ~200 µm pas rodage avec du papier abrasif (grains d'alumine) ; 2) polissage avec particules de diamant de 9, 3, 1 et 0.25 µm et 3) polissage mécanochimique final avec pulvérisation d'une solution de NaOH, de silice colloidale et eau (solution Nalco).

Une procédure de mesure de l'épaisseur de silicium aminci superficiel par spectrométrie infrarouge à transformée de Fourier a été mis au point pour caractériser le procédé. Elle consiste à ré-échantillonner le spectre d'absorption pour obtenir un échantillonnage régulier et à effectuer une transformée de Fourier pour analyser les franges d'interférences produites dans le substrat et dans la couche de silicium superficielle. Dans le cas d'un substrat de Si simple on observe dans le spectre FFT des pics réguliers dont la distance est liée à l'épaisseur. Dans le cas d'un substrat SOI, des pics d'intervalle proportionnel à l'épaisseur du film de silicium se superposent (Fig. III.4a et b).

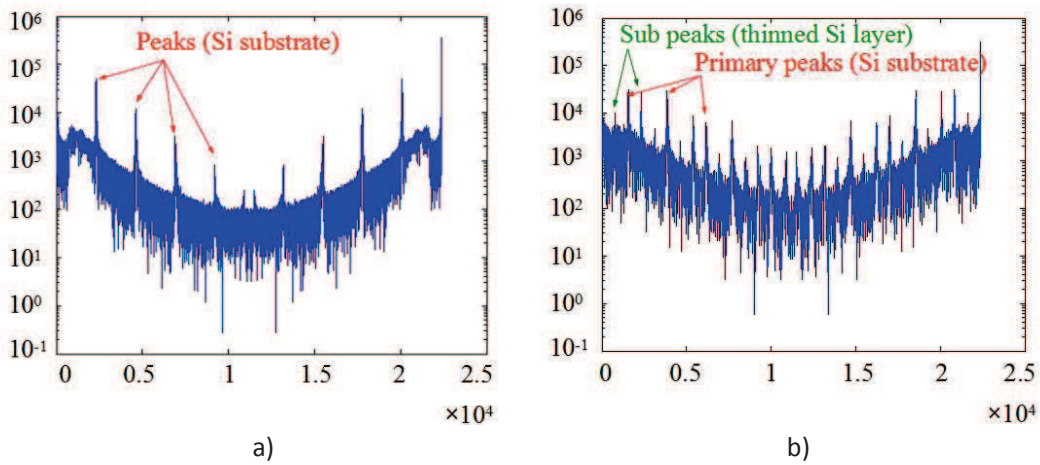

Figure III.4. Analyse FFT du spectre d'absorption infrarouge d'un substrat SOI (a) simulation pour un substrat Si 300 µm, (b) mesure pour un substrat Si 300 µm/SiO_2 170nm/Si 200 µm.

Cette méthode a été validée par comparaison avec des mesures à l'aide d'un comparateur.

Les quelques tests d'amincissement effectués ont montré que l'homogénéité de l'amincissement était médiocre (variation de 18% de l'épaisseur enlevée) et que le polissage pouvait de façon inattendue produire un biseau d'épaisseur restante. L'état de surface après polissage est de très bonne qualité avec une rugosité quadratique moyenne mesurée par profilométrie interférométrique à décalage de phase ≤3 nm (valeur identique à celle mesurée par cette technique sur un wafer non poli). Il a été également observé que le polissage d'un wafer de silicium nu produisait une surface avant plane mais une courbure creuse de la face arrière.

Ces essais ont montré qu'il n'était pas possible à l'heure actuelle de réaliser à l'IEF des wafers SOI ou double SOI de bonne qualité. Les autres tests de fabrication ont donc été réalisés avec des wafers commerciaux.

III.3 Gravure profonde de substrat double SOI

La maitrise de la gravure profonde de tranchées de rapport d'aspect ≥10 dans un substrat double SOI est une condition impérative pour pouvoir réaliser le système de balayage de miroir avec le procédé proposé. Dans le cas du silicium, il est relativement aisé de réaliser une tranchée de rapport d'aspect élevé avec des parois verticales en utilisant le procédé Bosch (Fig. III.5a) (alternance de cycle gravure dans un plasma SF_6 et de passivation des parois par polymérisation dans un plasma C_4F_8). Le cas d'une gravure profonde de l'empilement $Si/SiO_2/Si$ est plus complexe en raison des effets de ' notching ' (gravure latérale à l'interface Si/SiO_2 dûe à des effets de charges électriques) et de la faible

vitesse de gravure de la silice par rapport au silicium et à la résine de masquage. Après différentes optimisations de la gravure de Si, SiO_2, SiO_2/Si et Si/SiO_2/Si des résultats à perfectionner mais déjà satisfaisants (Fig.III.5b et c) ont été obtenus en combinant des gravures de paramètres différents.

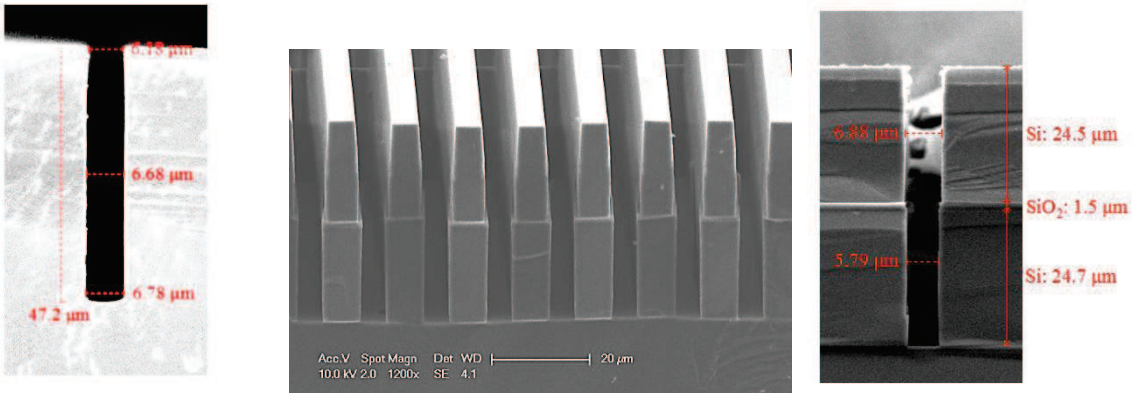

a) b) c)

Figure III.5. images en coupe de microscopie électronique (a) d'une tranche gravée dans Si, (b) de dents de peignes gravées dans Si/SiO_2/Si et (c) d'une tranchée gravée dans Si/SiO_2/Si.

III.4 Métallisation et gravure de surfaces fortement structurées

Dans le procédé de fabrication proposé, après la 1ère étape de gravure , toutes les étapes suivantes doivent être réalisées sur des surfaces fortement structurées (tranchées de 51.5 µm de profondeur) et même ajourée (dernière étape). Il n'est alors plus possible d'utiliser des résines photosensibles étalées à la tournette pour réaliser les étapes de photolitographie. Les solutions connues pour surmonter ce problème sont d'utiliser des résines électrodéposées ou déposées par nébulisation, d'utiliser des masques stencils, ou d'utiliser des films secs photosensibles laminés. C'est cette dernière solution qui a été choisie dans cette thèse. Cette technologie de délimitation de motifs a une résolution limitée (~20 µm) mais est très polyvalente. Une des contributions de cette thèse a été de développer des procédés innovants de délimitation de motifs avec des films secs photosensibles.

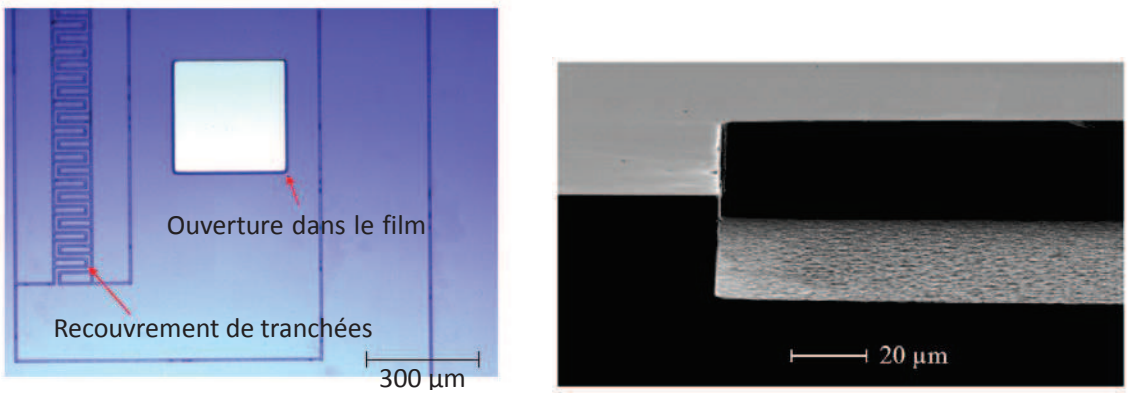

Figure III.6. Exemple de lithographie sur une surface comportant des tranchées et résultat d'une gravure de Si avec un film sec comme couche de masquage.

Tous les tests ont été effectués avec des films secs de 15 µm de la société Dupont™. Ces films permettent excellent recouvrement de tranchées de 5 µm (Fig.III.6a) et ont été utilisés avec succès comme masque de gravure DRIE (Fig.III.6b) (2ème étape du procédé de fabrication). Cette étape de

gravure comme toutes les étapes de gravure DRIE du procédé est réalisée après assemblage temporaire du substrat avec un wafer support avec de la graisse thermique.

Nous avons également démontré la possibilité de délimiter des métallisations de plots de contact simultanément à la surface par lift-off et au fond d'une cavité en utilisant localement le film sec comme masque stencil (Fig.III.7) (étape 4 du procédé de fabrication). Ceci permet de supprimer une étape de lithographie avec alignement et une métallisation.

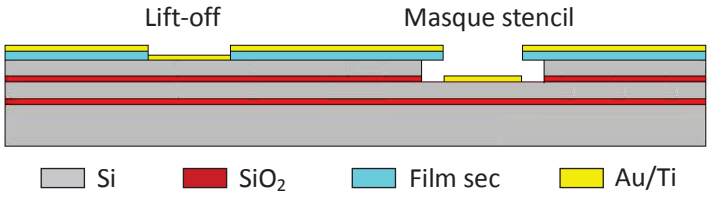

a)

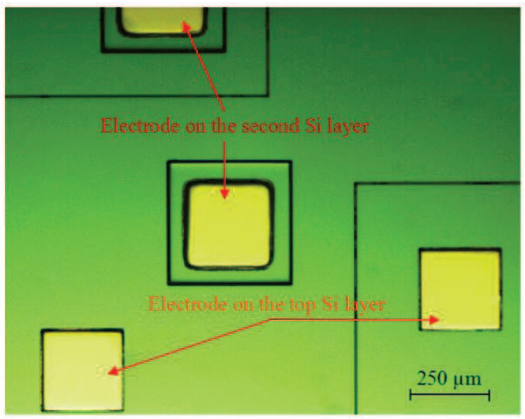

b)

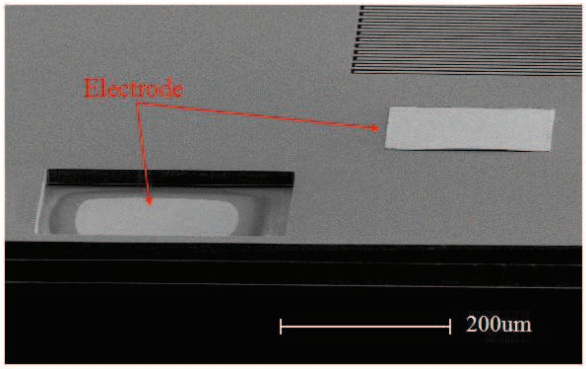

c)

Figure III.7. Métallisation multiniveaux avec un film sec photosensible comme couche de masquage. (a) Principe. (b) Vue de dessus en microscopie optique. (C) Image MEB sous incidence oblique.

III.5 Libération de la structure mobile

Après délimitation de la géométrie de la structure mobile du système de balayage du miroir et la métallisation des contacts, la structure mobile doit être libérée du substrat. Cette étape est réalisée par gravure DRIE d'une ouverture dans la face arrière du substrat double SOI (Fig.III.8a) puis de la silice enterrée par gravure chimique (Fig.III.8b). Pendant ces étapes la face avant est protégée par un substat de silicium qui est assemblé temporarirement. La dernière étape (Fig.III.8c) consiste à retirer ce wafer.

a) b) c)

Figure III.8. Etapes du procédé de libération de la structure mobile.

La Fig.III.9a montre un ressort serpentin de test libéré d'un wafer SOI par ce procédé de libération et la Fig.III.9b l'extrémité d'un ressort de test libéré d'un wafer double SOI. Le résultat dans ce dernier cas est moins satisfaisant à cause d'une contamination résiduelle de graisse thermique. Dans les 2 cas les structures libérées sont très planes ce qui démontre qu'il est intéressant d'utiliser les couches de silicium de wafers SOI ou double SOI comme couches structurelle en raison de leur faible gradient de contraintes résiduelles.

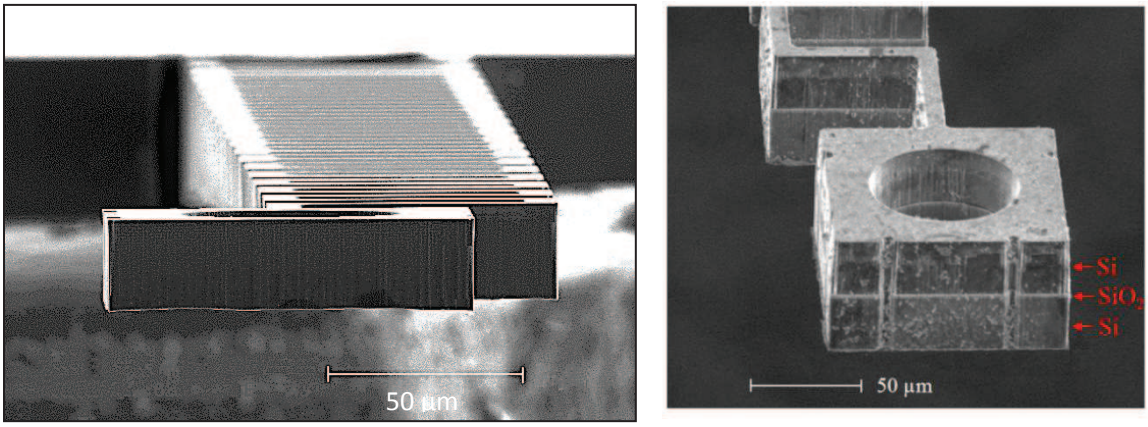

a) b)

Figure III.9. Ressorts serpentins libérés d'un wafer SOI et d'un wafer double SOI.

La Fig.III.10. montre le résultat d'un test du procédé quasiment complet (sans la métallisation du miroir). Ce résultat n'est pas encore optimisé ni opérationnel: nous avons observé un collage de la structure dû à des résidus de graisse thermique issus de l'assemblage temporaire utilisé pour la dernière étape de libération. Néanmoins il démontre la possibilité de préserver l'intégrité de la structure mécanique sans rupture.

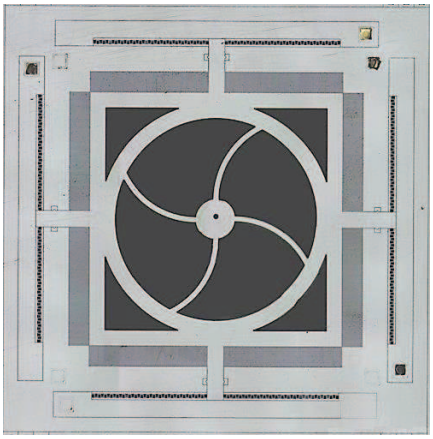

Figure III.10. Image de la structure mobile en technologie double SOI ayant subi les étapes principales du procédé de fabrication. Taille de la puce 9 mm x 9 mm.

III.6 Fabrication de la séparatrice

Rappelons que la séparatrice de l'interféromètre Mirau intégré est une membrane diélectrique, multicouche et semi-réfléchissante dans le domaine visible proche-infrarouge (500-850 nm). Le procédé de fabrication de ce type de membranes a été développé précédemment à l'IEF par H. Bertin [Bertin-2013] [Bertin-2013-2] lors de sa thèse sur les matrices de microinterféromètres Fabry-Perot. ajustables. Il repose sur le dépôt alterné de couches de nitrure de silicium et de silice déposées sur silicium par PECVD dont la contrainte est ajustée en tension par recuit haute température : Initialement, après dépôt, les films sont contraints en compression et la désorption d'hydrogène forme de nouvelles liaisons SiO et SiN et engendre une contrainte en tension qui dépend de la température du recuit (Fig.III.11.) et de sa durée.

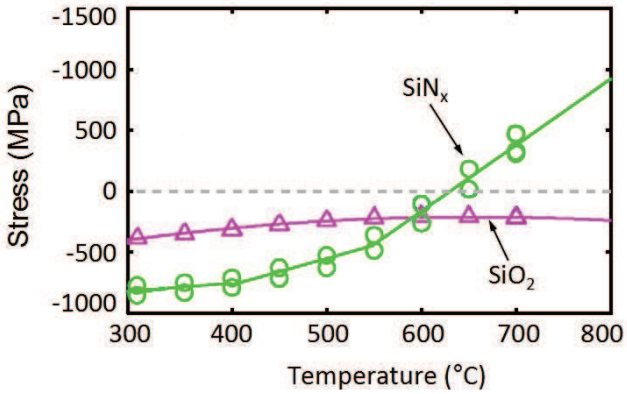

Figure III.11. Variation de la contrainte mécanique résiduelle dans des films déposé par PECVD en fonction de la température de recuit (durée 1 heure).

Les membranes sont libérées par gravure DRIE d'une cavité en face arrière du substrat de silicium jusqu'à une épaisseur de ~10 µm suivie d'une gravure très sélective et isotrope du silicium restant dans du difluorure de Xenon (XeF_2). Ce procédé a un rendement très élevé et il a été démontré qu'il permettait de fabriquer des membranes de 8 à 12 couches jusqu'à une taille de 5.9 mm. Ceci est illustré dans le cas de membranes octognales dans la Fig.III.12.

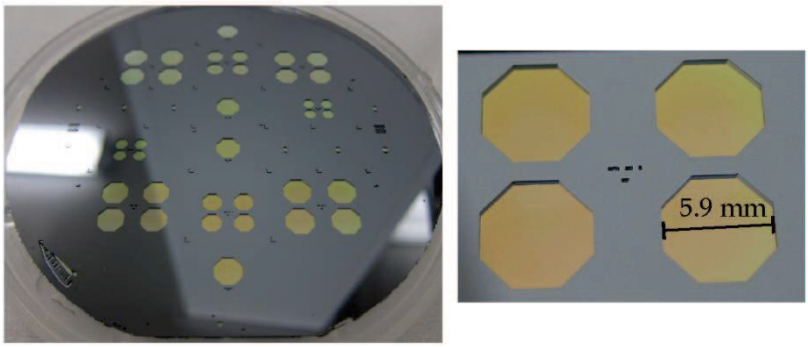

Figure III.12. Membranes séparatrices multicouches Si_3N4/SiO_2 déposées par PECVD.

III.7 Conclusion

Un procédé original de fabrication d'un système de balayage de miroir en technologie double SOI a été conçu et testé. Ce procédé nécessite seulement 5 niveaux de masque, 3 gravures et deux métallisations. Il comporte une seule étape où la lithographie et la gravure doivent être précises, les autres étapes étant très tolérantes du point de vue des dimensions et de l'alignement. Le procédé repose sur l'usage de films secs photosensibles pour permettre les opérations de gravure et de métallisation sur des surfaces très fortement structurées. Il a en partciculier été démontré la posssibilté de déposer simultanément par lift-off et masque stencil des plots fe métallisation sur des niveaux de hauteurs très différentes (25 µm). La fabrication complète du système n'a pas pu être menée à bien faute de temps et d'un problème de contamination mais l'essentiel du procédé a été validé.

Les membranes séparatrices multicouhes de l'interféromètre Mirau seront fabriquées par un procédé développé précédemment à l'IEF et validé pour des membranes de 8 à 12 couches et de taille jusqu'à ~6 mm.

IV. Conclusion générale et perspectives

Une architecture et un procédé de fabrication originaux d'interféromètres Mirau ajustable intégrés 3D ont été étudiés. L'architecture proposée est modulaire et robuste, et présente les avantages d'un fonctionnement dans une large gamme de longueur d'onde (500-850 nm) et d'un ajustement bidirectionnel, de grande course (±20 µm) , haute résolution (gamme (subs) nanométrique) et rapide (6 ms) de la différence de chemin optique. La principale limitation de l'interféromètre Mirau proposé est un défaut de compensation trop variable avec la longueur d'onde qui limite ses performances en interférométrie faiblement cohérente. Un autre inconvénient est sa sensibilité au poids et aux vibrations sonores mais ceci pourrait être résolu en réduisant les largeurs de gap électrostatique et en augmentant la rigidité verticale des ressorts.

Des travaux resteraient à faire pour aboutir à un interféromètre Mirau ajustable intégré performant. La prermière étape à réaliser serait de finaliser le développement du procédé de fabrication, en particulier l'assemblage des wafers de scanners et de séparatrices, et de tester le comportement mécanique et électromécanique du système de balayage du miroir de référence. Une modélisation plus fine des performances optiques serait aussi souhaitable. Par la suite l'étude de l'asservissement en position du miroir par détection capacitive intégrée devra être menée. Enfin l'interféromètre Mirau complet devra être testé pour l'application initialement visée: la profilométrie et la vibrométrie interférométrique. A plus long terme, l'interféromètre pourra être combiné avec un objectif à miroirs sphérique de type Schwarzchild microusiné afin de réaliser un objectif interférométrique entièrement intégré.

List of Figures

List of Tables

References

[Albero-2011] J. Albero, S. Bargiel, N. Passilly, et al. "Micromachined array-type Mirau interferometer for parallel inspection of MEMS." Journal of Micromechanics and Microengineering 21.6 (2011): 065005.

[Aslihan-2010] A. Aslihan, D. Brown, W.O. Davis, et al. "Comb-actuated resonant torsional microscanner with mechanical amplification." Journal of Microelectromechanical Systems, 19.4 (2010): 936-943.

[Ataman-2006] C. Ataman, H. Urey and A. Wolter. "A Fourier transform spectrometer using resonant vertical comb actuators." Journal of micromechanics and microengineering, 16.12 (2006): 2517.

[Ataman-2006] C. Ataman, H. Urey, and A. Wolter. "A Fourier transform spectrometer using resonant vertical comb actuators." Journal of micromechanics and microengineering 16.12 (2006): 2517.

[Avazi-2000] F. Ayazi and K. Najafi. "High aspect-ratio combined poly and single-crystal silicon (HARPSS) MEMS technology." Journal of Microelectromechanical Systems, 9.3 (2000): 288-294.

[Azevedo-2008] R.G. Azevedo, W. Huang, O.M. O'Reilly, A.P. Pisano. "Dual-mode temperature compensation for a comb-driven MEMS resonant strain gauge." Sensors and Actuators A: Physical 144.2 (2008): 374-380.

[Baranski-2013] M. K. Baranski. " Optical design and development of building blocks for a new generation of vertically integrated on-chip confocal microscopes." PhD Thesis, Université de Franche Comté, 2013.

[Benhaddou-2000] D. Benhaddou, P.C. Montgomery, D. Montaner, J. Bonnafe. "Buried interface characterization in optoelectronic materials by interference microscopy." Journal of modern optics 48.3 (2001): 533-547.

[Bertin-2013] H. Bertin. "Etude de matrices de filtres Fabry Pérot accordables en technologie MOEMS intégré 3D: Application à l'imagerie multispectrale." PHD thesis, Université Paris Sud, (2013).

[Bertin-2013-2] H. Bertin, A. Bosseboeuf, P. Coste, M Péalat and N. Roux. "Large area and broadband semi-reflective Bragg mirror membrane manufactured by PECVD." Journal of Micromechanics and Microengineering 23.7 (2013): 074005.

[Bosseboeuf-2003] A. Bosseboeuf, and S. Petitgrand. "Characterization of the static and dynamic behaviour of M(O)EMS by optical techniques: status and trends." Journal of Micromechanics and Microengineering 13.4 (2003): S23-S33.

[Bosseboeuf-2007] A. Bosseboeuf, and S. Petitgrand. "Interference microscopy techniques for microsystem characterization." Optical inspection of microsystems, CRC press, Taylor& Francis Group, (2007): 217-243.

[Caglar-2006] A. Caglar and H. Urey. "Modeling and characterization of comb-actuated resonant microscanners." Journal of Micromechanics and Microengineering, 16.1 (2006): 9.

[Carlen-2005] E.T. Carlen, K.H. Heng, S. Bakshi, A. Pareek, C.H. Mastrangelo. "High-aspect ratio vertical comb-drive actuator with small self-aligned finger gaps." Journal of Microelectromechanical Systems 14.5 (2005): 1144-1155.

[Carr-2006] E. Carr, S. Olivier, and O. Solgaard. "Large-stroke self-aligned vertical comb drive actuators for adaptive optics applications." Proceeding of SPIE, MEMS/MOEMS Components and Their Applications III, 61130T, 2006.

[Chang-1997] F.C. Chang and G.S. Kino. "Nitrogen-rich silicon nitride thin films for deep-ultraviolet Mirau interferometry." Optics letters 22.8 (1997): 492-494.

[Chang-1998] F.C. Chang and G.S. Kino. "325-nm interference microscope." Applied optics 37.16 (1998): 3471-3479.

[Chang-2000] C.J. Chang-Hasnain. "Tunable VCSEL." IEEE Journal on Selected Topics in Quantum Electronics, Vol.6, No.6, (2000): 978-987.

[Chim-1990] S.C. Chim, P.A. Beck, and G.S. Kino. "A novel thin film interferometer." Review of Scientific Instruments 61.3 (1990): 980-983.

[Chim-1991] S.C. Chim and G.S. Kino. "Phase measurements using the Mirau correlation microscope." Applied Optics 30.16 (1991): 2197-2201.

[Chiou-2005] J.C. Chiou and Y.J. Lin. "A novel large displacement electrostatic actuator: pre-stress comb-drive actuator." Journal of Micromechanics and Microengineering 15.9 (2005): 1641.

[Choo-2007] H. Choo, D. Garmire, J. Demmel, R.S. Muller. "Simple fabrication process for self-aligned, high-performance microscanners—Demonstrated use to generate a 2-D ablation pattern." Journal of Microelectromechanical Systems, 16.2 (2007): 260-268.

[Chou-2010] X.Chou, Y. Liu, K. Niu, J. Liu, C. Xue, W. zhang. "Internal profile measurement of GaAs microstructures based on near-infrared light phase-stepping interferometry." Optics and Lasers in Engineering 48.12 (2010): 1200-1205.

[Chung-2008] J.W. Chung and W. Hsu. "Fabrication of a polymer-based torsional vertical comb drive using a double-side partial exposure method." Journal of Micromechanics and Microengineering 18.3 (2008): 035014.

[Creath-1988] K. Creath. "Phase-measurement interferometry techniques." Progress in optics 26.26 (1988): 349-393.

[Dubois-2000] A. Dubois, J. Selb, L. vabre, A.C. Boccara. Phase measurements with wide-aperture interferometers. Applied Optics 39.14 (2000): 2326

[Dubois-2004] A. Dubois. Effects of phase change on rfelction in phase-measuring interference microscopy. Applied Optics 43.7 (2004): 1503[Dziuban-2007] J.A. Dziuban. " Bonding in microsystem technology." Vol. 24. Springer, 2007: 130.

[Ebermann-2010] M. Ebermann, N. Neumann, K. Hiller , E. Gittler, M. Meinig, S. Kurth. "Recent advances in expanding the spectral range of MEMS Fabry-Perot filters." MOEMS-MEMS. International Society for Optics and Photonics, (2010).

[Fedder-1994] G.K. Fedder. Simulation of microelectromechanical systems. PHD thesis, University of California, 1994.

[Gallagher-2012] E. Gallagher, W. Moussa and M. McDermott. "A review of fabrication processes for vertical comb drives." Microsystem technologies 18.4 (2012): 381-397.

[Gastinger-2009] K. Gastinger, K.H. Haugholt, M. Kujawinska, et al. "Optical, mechanical, and electro-optical design of an interferometric test station for massive parallel inspection of MEMS and MOEMS." SPIE Europe Optical Metrology. International Society for Optics and Photonics, (2009).

[Gelais-2009] R. St-Gelais, J. Masson, and Y.A. Peter. "All-silicon integrated Fabry–Pérot cavity for volume refractive index measurement in microfluidic systems." Applied physics letters 94.24 (2009): 243905.

[Ghodssi-2011] R. Ghodssi and P. Lin. MEMS materials and processes handbook. Vol. 1. Springer, 2011. P107.

[Gorecki-2011] C. Gorecki, S. Bargiel, J. Albero, et al. "Micromachined array-type Mirau interferometer for MEMS metrology." Solid-State Sensors, Actuators and Microsystems Conference (TRANSDUCERS), 2011 16th International. IEEE, (2011).

[Hamamoto-2005] K. Hamamoto, Y. Tanaka, H. Kawashima, et al. "Actinic Mask Inspection Using an EUV Microscope–Preparation of a Mirau Interferometer for Phase-Defect Detection–." Japanese journal of applied physics 44.7S (2005): 5474.

[Hariharan-2003] P. Hariharan. Optical interferometry. Academic press, Elsevier science (2003).

[Hombeck-1997] L.J. Hornbeck. "Digital light processingTM for high-brightness, high-resolution applications." Proceeding of SPIE. Vol 3013, (1997).

[Hopcroft-2010] M.A. Hopcroft, W.D. Nix, and T.W. Kenny. "What is the Young's Modulus of Silicon?." Journal of Microelectromechanical Systems, 19.2 (2010): 229-238.

[Hourdakis-2006] E. Hourdakis, B.J. Simonds and N.M. Zimmerman. "Submicron gap capacitor for measurement of breakdown voltage in air." Review of scientific instruments 77.3 (2006): 034702-034702.

[Jen-2012] Y.J. Jen, M.J. Lin, S.K. Yu, C.C Chen. "Extended broadband achromatic reflective-type waveplate."Optics letters 37.20 (2012): 4296-4298.

[Jeong-2005] K.H. Jeong and P.L. Luke. "A novel microfabrication of a self-aligned vertical comb drive on a single SOI wafer for optical MEMS applications." Journal of Micromechanics and Microengineering 15.2 (2005): 277.

[Jeong-2012] J.W. Jeong, S. Kim, and O. Solgaard. "Split-frame gimbaled two-dimensional MEMS scanner for miniature dual-axis confocal microendoscopes fabricated by front-side processing." Journal of Microelectromechanical Systems 21.2 (2012): 308-315.

[Kaajakari-2009] V. Kaajakari. "Practical MEMS: Design of microsystems, accelerometers, gyroscopes, RF MEMS, optical MEMS, and microfluidic systems." Las Vegas, NV: Small Gear Publishing (2009).

[Lahiri-2012] M. Lahiri and E. Wolf. "Theory of refraction and reflection with partially coherent electromagnetic beams." Physical Review A 86.4 (2012): 043815.

[Lahiri-2013] M. Lahiri, and Emil Wolf. "Propagation of electromagnetic beams of any state of spatial coherence and polarization through multilayered stratified media." Journal of Optical Society of America A 30.12 (2013): 2547-2555.

[Lullin-2014] J. Lullin, S. Bargiel, E. Courjon, S. Perrin, C. Gorecki. "Monolithic integration of a glass membrane on silicon micro-actuator for micro-interferometry." Optical MEMS and Nanophotonics (OMN), 2014 International Conference on. IEEE, 2014.

[Katsidis-2002] C.C. Katsidis and D.I. Siapkas. "General transfer-matrix method for optical multilayer systems with coherent, partially coherent, and incoherent interference." Applied optics 41.19 (2002): 3978-3987.

[Gastinger-2009] K. Gastinger, K.H. Haugholt, M. Kujawinska, M. Jozwik, C. Schaeffel, S. Beer. "Optical, mechanical, and electro-optical design of an interferometric test station for massive parallel inspection of MEMS and MOEMS." SPIE Europe Optical Metrology. International Society for Optics and Photonics, (2009).

[Keating-2007] A. Keating, J. Antoszewski, K. Silva, et al. "Fabry-Perot MEMS microspectrometers spanning the SWIR and MWIR." Defense and Security Symposium. International Society for Optics and Photonics, (2007).

[Keller-1997] C.G. Keller and R.T. Howe. "Hexsil tweezers for teleoperated micro-assembly." Proceedings of IEEE, Tenth Annual International Workshop on Micro Electro Mechanical Systems, 1997.

[Khalil-2011] D. Khalil, Y. Sabry, H. Omran, M. Medhar, A. Hafez, B. Saadany. "Characterization of MEMS FTIR spectrometer." SPIE MOEMS-MEMS. International Society for Optics and Photonics, (2011).

[Kim-1996] M.T. Kim. Influence of substrates on the elastic reaction of films for the microindentation tests. Thin Solid Films, 1996, 283(1): 12-16.

[Kim-2006] J. Kim, H. Choo, L. Lin, R.S. Muller. "Microfabricated torsional actuators using self-aligned plastic deformation of silicon." Journal of Microelectromechanical Systems, 15.3 (2006): 553-562.

[Kino-1990] G.S. Kino and S.C. Chim. "Mirau correlation microscope."Applied Optics 29.26 (1990): 3775-3783.

[Krauter-2014] J. Krauter, T. Boettcher, W. Lyda, et al. "Optical design of a vertically integrated array-type Mirau-based OCT system." SPIE Photonics Europe. International Society for Optics and Photonics, (2014).

[Lee-2003] A.P. Lee, C.F. McConaghy, G. Sommargren, P. Krulevitch and E.W. Campbell. "Vertical-actuated electrostatic comb drive with in situ capacitive position correction for application in phase shifting diffraction interferometry." Journal of Microelectromechanical Systems, 12.6 (2003): 960-971.

[Lee-2004] D. Lee, U. Krishnamoorthy, K. Yu, O. Solgaard. "Single-crystalline silicon micromirrors actuated by self-aligned vertical electrostatic combdrives with piston-motion and rotation capability." Sensors and Actuators A: Physical 114.2 (2004): 423-428.

[Liao-2005] L. Liao, D. Samara-Rubio, M. Morse, A. Liu, D. Hodge, D. Rubin, U.D. Keil, and Thorkild Franck. "High speed silicon Mach-Zehnder modulator." Optics Express 13(8), (2005): 3129-3135.

[Lin-2005] W.T. Lin., J. C. Chiou, and C. Tsou. "A self-aligned fabrication method of dual comb drive using multilayers SOI process for optical MEMS applications."Microsystem technologies 11.2-3 (2005): 204-209.

[Liu-2013] Y. Liu, J. Xu, S. Zhong, Y. Wul. "Large size MEMS scanning mirror with vertical comb drive for tunable optical filter." Optics and Lasers in Engineering 51.1 (2013): 54-60.

[Lu-2013] S. Lu, C. Chang, and C. Kao. "Full-field optical coherence tomography using immersion Mirau interference microscope."Applied optics 52.18 (2013): 4400-4403.

[Lyulko-2013] O.V. Lyulko, G. Randers-Pehrson and D.J. Brenner. "Simultaneous immersion Mirau interferometry." Review of Scientific Instruments 84.5 (2013): 053701.

[Malacara-2007] D. Malacara, ed. Optical shop testing. Vol. 59. John Wiley & Sons, (2007).

[Malak-2013] M. Malak, F. Marty, H. Nouira, G. Vailleau and T. Bourouina. "All-silicon Michelson instrument on chip: Distance and surface profile measurement and prospects for visible light spectrometry."Applied Physics Letters 102.14 (2013): 141102.

[Manzardo-1999] O. Manzardo, H.P. Herzig, C.R. Marxer and N.F. de Rooij. "Miniaturized time-scanning Fourier transform spectrometer based on silicon technology." Optics letters 24.23 (1999): 1705-1707.

[Masson-2010] J. Masson, R.St-Gelais, A. Poulin, Y.A.Peter. "Tunable fiber laser using a MEMS-based in plane Fabry-Pérot filter." Quantum Electronics, IEEE Journal of 46.9 (2010): 1313-1319.

[Milanovic-2004] V. Milanovic. "Multilevel beam SOI-MEMS fabrication and applications." Journal of Microelectromechanical Systems 13.1 (2004): 19-30.

[Milne-2007] J.S. Milne, A. Keating, J. Antoszewski, et al. "Extending the tuning range of SWIR microspectrometers." Defense and Security Symposium. International Society for Optics and Photonics, (2007).

[Montgomery-1997] P. Montgomery, D. Benhaddou, and D. Montaner. "Interferometric roughness measurement of Ohmic contact/III–V semiconductor interfaces."Applied physics letters 71.13 (1997): 1768-1770.

[Montgomery-1999] P. Montgomery and D. Montaner. "Deep submicron 3D surface metrology for 300 mm wafer characterization using UV coherence microscopy." Microelectronic Engineering, 45, 291, (1999).

[Montgomery-2008] P. Montgomery, F. Anstotz, G. Johnson and R. Kiefer. "Real time surface morphology analysis of semiconductor materials and devices using 4D interference microscopy." Journal of Materials Science: Materials in Electronics, 19 (Suppl. 1) pp. 194-198, 2008 p. 28.

[Montgomery-2010] P. Montgomery, et al. "Towards real time 3D quantitative characterisation of in situ layer growth using white light interference microscopy." Journal of Physics: Conference Series. Vol. 253. No. 1. IOP Publishing, (2010).

[Montgomery-2011] P. Montgomery, F. Anstotz, and J. Montagna. "High-speed, on-line 4D microscopy using continuously scanning white light interferometry with a high-speed camera and real-time FPGA image processing." SPIE Optical Metrology. International Society for Optics and Photonics, 2011.

[Moriceau-2010] H. Moriceau, F. Rieutord, F. Fournel, et.al. "Overview of recent direct wafer bonding advances and applications." Advances in Natural Sciences: Nanoscience and Nanotechnology 1.4 (2010): 043004.

[Motamedi-2005] M.E. Motamedi. " MOEMS: micro-opto-electro-mechanical systems." SPIE Press, (2005).

[Neumann-2008] N. Neumann, M. Ebermann, S. Kurth, K. Hiller. "Tunable infrared detector with integrated micromachined Fabry-Perot filter." Journal of Micro/Nanolithography, MEMS, and MOEMS 7.2 (2008): 021004-021004.

[Neumann-2009] N. Neumann, M. Ebermann, S. Kurth, K. Hiller. "Novel MWIR microspectrometer based on a tunable detector." SPIE MOEMS-MEMS: Micro-and Nanofabrication. International Society for Optics and Photonics, (2009).

[Niklaus-2007] F. Niklaus, C. Vieider, hristian, H. Jakobsen. "MEMS-based uncooled infrared bolometer arrays: a review." Photonics Asia 2007. International Society for Optics and Photonics, (2007).

[Oda-2012] K. Oda, H, Takao, K. Terao, et al. "Vertical comb-drive MEMS mirror with sensing function for phase-shift device." Sensors and Actuators A: Physical 181 (2012): 61-69.

[Oliva-2012] M. Oliva, D. Michaelis, P. Dannberg, et al. "Twyman–Green-type integrated laser interferometer array for parallel MEMS testing." Journal of Micromechanics and Microengineering 22.1 (2012): 015018.

[Palik-1998] E.D. Palik, edited. Handbook of optical constants of solids. Vol. 3. Academic press, 1998.

[Petitgrand-2004] S. Petitgrand and A. Bosseboeuf. "Simultaneous mapping of out-of-plane and in-plane vibrations of MEMS with (sub) nanometer resolution." Journal of Micromechanics and Microengineering 14.9 (2004): S97.

[Quack-2009] N. Quack, P. Rust, S. Blunier, et al. "A comb drive actuated vertically moving micromirror for tunable mid-infrared Resonant Cavity Enhanced Detectors." Microelectronic Engineering 86.4 (2009): 1243-1246.

[Sandner-2008] T. Sandner, A. Kenda, W. Scherf, C. Drabe and H. Schenk. "Translatory MEMS actuators for optical path length modulation in miniaturized Fourier-transform infrared spectrometers." Journal of Micro/Nanolithography, MEMS, and MOEMS 7.2 (2008): 021006-021006.

[Sandner-2008] T. Sandner, A. Kenda, W. Scherf, C. Drabe and H.Schenk, et al. "Translatory MEMS actuators for optical path length modulation in miniaturized Fourier-transform infrared spectrometers." Journal of Micro/Nanolithography, MEMS, and MOEMS, 7.2 (2008): 021006-021006.

[Santbergen-2013] R. Santbergen, A. HM Smets and M. Zeman. "Optical model for multilayer structures with coherent, partly coherent and incoherent layers."Optics express 21.102 (2013): A262-A267.

[Sasaki-2004] M. Sasaki, D. Briand, W. Noell, N.F. de Rooij and K.Hane. "Three-dimensional SOI-MEMS constructed by buckled bridges and vertical comb drive actuator." Selected Topics in Quantum Electronics, IEEE Journal of 10.3 (2004): 455-461.

[Schmit-2007] J. Schmit and P. Hariharan. "Improved polarization Mirau interference microscope." Optical Engineering 46.7 (2007): 077007-077007.

[Shahosseini-2013] I. Shahosseini, E. Lefeuvre, J. Moulin, E. Martincic, M. Woytasik and G. Lemarquand. "Optimization and microfabrication of high performance silicon-based MEMS microspeaker." Sensors Journal, IEEE 13.1 (2013): 273-284.

[Sheppard-1995] C.J.R. Sheppard and K. G. Larkin. "Effect of numerical aperture on interference fringe spacing." Applied optics 34.22 (1995): 4731-4734.

[Sieger-2013] M. Sieger, F. Balluff, X. Wang, S. Kim, L. Leidner, G. Gauglitz and B. Mizaikoff. "On-Chip Integrated Mid-Infrared GaAs/AlGaAs Mach–Zehnder Interferometer." Analytical Chemistry, 85 (6), (2013): 3050–3052.

[Singh] N. Singh. "LPCVD of Polysilicon." Oxford instruments, plasma technology. www.oxfordplasma.de/pla_news/polysili.pdf

[Tang-1992] W.C. Tang, M.G. Lim and R.T. Howe. "Electrostatic comb drive levitation and control method." Journal of Microelectromechanical systems 1.4 (1992): 170-178.

[Tapilouw-2013] A.M. Tapilouw, L. Chen, Y. Jen, S. Lin and S. Yeh. "Orthogonal polarization Mirau interferometer using reflective-type waveplate." Optics letters 38.14 (2013): 2502-2504.

[Torres-1999] J.M. Torres and R.S. Dhariwal. "Electric field breakdown at micrometre separations." Nanotechnology 10.1 (1999): 102.

[Toshiyoshi-1996] H. Toshiyoshi, and H. Fujita. "Electrostatic micro torsion mirrors for an optical switch matrix." Journal of Microelectromechanical systems, Vol 5, No. 4, (1996): 231-237.

[Tran-1996] A.T.T.D. Tran, Y.H. Lo, Z.H. Zhu, D. Haronian, E. Mozdy. "Surface micromachined Fabry-Perot tunable filter."Photonics Technology Letters, IEEE 8.3 (1996): 393-395.

[Troparevsky-2010] M.C. Troparevsky, A.S. Sabau, A.R. Lupini, Z. Zhang. "Transfer-matrix formalism for the calculation of optical response in multilayer systems: from coherent to incoherent interference." Optics express 18.24 (2010): 24715-24721.

[Tsai-2004] J.M. Tsai, H.Y Chu, J. Hsieh, W. Fang. "The BELST II process for a silicon high-aspect-ratio micromachning vertical comb actuator and its applications." Journal of Micromechanics and Microengineering 14.2 (2004): 235.

[Tsou-2005] C. Tsou, W.T. Lin, C.C. Fan, B.C.S Chou. "A novel self-aligned vertical electrostatic combdrives actuator for scanning micromirrors." Journal of micromechanics and microengineering 15.4 (2005): 855.

[Turner-1998] K.L. Turner, S.A. Miller, P.G. Hartwell, et al. "Five parametric resonances in a microelectromechanical system." Nature 396.6707 (1998): 149-152.

[U.K-24] U. Krishnamoorthy, D. Lee, and O. Solgaard. "Self-aligned vertical electrostatic combdrives for micromirror actuation." Journal of Microelectromechanical Systems, 12.4 (2003): 458-464.

[VIAMOS] http://www.viamos.eu/

[Wei-2008] T. Wei, Y. Han, Y.Li, H. Tsai and H.Xiao. "Temperature-insensitive miniaturized fiber inline Fabry-Perot interferometer for highly sensitive refractive index measurement." Optics Express 16.8 (2008): 5764-5769.

[Wiegand-2000] M. Wiegand, M. Reiche, and U. Gösele. "Time-Dependent Surface Properties and Wafer Bonding of O_2-Plasma-Treated Silicon (100) Surfaces." Journal of The Electrochemical Society 147.7 (2000): 2734-2740.

[Wooldridge-2013] J. Wooldridge, A. Muniz-Piniella, M. Stewart, T.A.V. Shean, P.M. Weaver and M.G. Cain. "Vertical comb drive actuator for the measurement of piezoelectric coefficients in small-scale systems." Journal of Micromechanics and Microengineering 23.3 (2013): 035028.

[Wu-2005] M. Wu and W. Fang. "Design and fabrication of MEMS devices using the integration of MUMPs, trench-refilled molding, DRIE and bulk silicon etching processes." Journal of Micromechanics and Microengineering 15.3 (2005): 535.

[Wu-2006] M. Wu and W. Fang. "A molded surface-micromachining and bulk etching release (MOSBE) fabrication platform on (111) Si for MOEMS." Journal of Micromechanics and Microengineering 16.2 (2006): 260.

[Yurtsever-2014] G. Yurtsever, B. Považay, A. Alex, B. Zabihian,W. Drexler and R. Baets. "Photonic integrated Mach-Zehnder interferometer with an on-chip reference arm for optical coherence tomography." Biomedical Optical Express 5(4), (2014):1050-1061.

[Zhang-2005] Q.X. Zhang, A.Q. Liu, J. Li, A.B. Yu. "Fabrication technique for microelectromechanical systems vertical comb-drive actuators on a monolithic silicon substrate." Journal of Vacuum Science & Technology B 23.1 (2005): 32-41.

[Zickar-2007] M. Zickar, M. Mita, M. Ataka, H. Fujita. "Low cross talk design and simple fabrication process of electrostatic vertical comb drive actuators for positioning application." IEEJ Transactions on Electrical and Electronic Engineering 2.3 (2007): 289-294.